Project No. 11-3039

Technical Development for S-CO2 Advanced Energy Conversion

Reactor Concepts

Dr. Mark Anderson
University of Wisconsin - Madison

In collaboration with:
Texas A&M University

Brian Robinson, Federal POC
Jim Sienicki, Technical POC

NEUP Nuclear Energy University Programs
U.S. Department of Energy

Project Number: NU-11-WI-UWM-0303-03 (Project 11-3039)
Project Title: Technical Development for S-CO2 Advanced Energy Conversion
Report: 2014 Annual Report (Final Report)
2014 Final Report
Due: November 10, 2014

Milestone Status:

M1: ActivityNU-11-WI-UWM_-0303-031: Monthly Spend Plan – **Completed 11/10/14**

M1NU-11-WI-UWM_-0303-032: FY2013 Go/No-Go Review - (Project 11-3039) Technical Development for S-CO2 Advanced Energy Conversion - **Completed 9/30/2013**

M1NU-11-WI-UWM_-0303-033: Final Report - (Project 11-3039) Technical Development for S-CO2 Advanced Energy Conversion - **Completed 11/10/2014**

M3NU-11-WI-UWM_-0303-034: Design and construction of HEX - **Completed 6/30/2012**

M3NU-11-WI-UWM_-0303-035: Calibration of HEX facility - **Completed 7/31/2013**

M3NU-11-WI-UWM_-0303-036: Design and construction of seal testing facility – **Completed 10/20/2013**

M3NU-11-WI-UWM_-0303-037: Obtain test data for S-Co2 through orifice - **Completed 10/20/2013**

M3NU-11-WI-UWM_-0303-038: Implement coupled algorithm into open foam - **Completed 10/20/2014**

Student Information:

Matt Wolf – Received Master's degree in Nuclear Engineering from UW- June 2014
Jacob Mahaffey – Continuing on to PhD-UW
John Dyreby – Received PhD in Mechanical Engineering UW- Sept 2014
Haomin (Kirk) Yuan – Continuing on to PhD- UW
Sandeep Pidaparti - Continuing on to PhD- Georgia Tech

Abstract

This report is divided into four parts. First part of the report describes the methods used to measure and model the flow of supercritical carbon dioxide (S-CO_2) through annuli and straight-through labyrinth seals. The effects of shaft eccentricity in small diameter annuli were observed for length-to-hydraulic diameter (*L/D*) ratios of 6, 12, 143, and 235. Flow rates through tooth-cavity labyrinth seals were measured for inlet pressures of 7.7, 10, and 11 MPa with corresponding inlet densities of 325, 475, and 630 kg/m^3. Various leakage models were compared to this result to describe their applicability in supercritical carbon dioxide applications. Flow rate measurements were made varying tooth number for labyrinth seals of same total length. Flow rate measurements were also made for a stepped labyrinth seal similar to shaft seal found in Sandia National Laboratories research facility.

The effect of eccentricity on flow through small diameter annuli was found to be minimal for the lengths typically found in labyrinth type shaft seals. There is an expected flow increase when moving a shaft from a concentric position to an eccentric position which is driven by a change in the fluid friction. This flow increase was found to be small for short annular orifices. An observed increase in flow rate of 3% was observed for short length annular orifices and was increased to 8.5% when the orifice length was increased beyond a distance equal to the developing entrance length and frictional effects were manifested.

Flow rate measurements for a straight through labyrinth seal with three teeth were made at inlet pressures of 7.7, 10, and 11 MPa with corresponding inlet densities of 325, 475, and 630 kg/m^3. Various labyrinth seal leakage models were applied to the data calculated to compare applicability. Applying the Homogeneous Equilibrium Model (HEM) with an experimentally determined discharge coefficient to predict the mass flow rate gave results with less than 5%

error for the higher pressure cases of 10 and 11 MPa and less that 14% error for the lower pressure case of 7.7 MPa. The HEM model works well when the inlet condition chokes prior to entering the two phase region and begins to deviate when two-phase effects become more prevalent. Other models were unable to predict property changes along with poor response to changes in geometry due to their lack of complexity. A Stepped labyrinth seal was designed to mimic the geometry used in the supercritical flow research loop at Sandia National Laboratories. This provided a more complex geometry to further test the capabilities of the facility and validate models. The results showed that the data could be used to scale to larger diameters and apply to more practical geometries. Three-tooth and four-tooth cases were tested an inlet pressure of 10 MPa with a corresponding inlet density of 325 kg/m^3. It was found that increasing the tooth number decreased the flow by 5% from the three-tooth case to the four-tooth case.

Second part of the report describes the computational study performed to understand the leakage through the labyrinth seals using Open source CFD package OpenFOAM. Fluid Property Interpolation Tables (FIT) program was implemented in OpenFOAM to accurately model the properties of CO_2 required to solve the governing equations. To predict the flow behavior in the two phase dome Homogeneous Equilibrium Model (HEM) is assumed to be valid. Experimental results for plain orifice (L/D ~ 5) were used to show the capabilities of the FIT model implemented in OpenFOAM. Error analysis indicated that OpenFOAM is capable of predicting experimental data within ±10% error with the majority of data close to ±5% error. Following the validation of computational model, effects of geometrical parameters and operating conditions are isolated from each other and a parametric study was performed in two parts to understand their effects on leakage flow.

Results of the geometrical parametric study indicated that the carryover coefficient of a seal is independent of pressure drop across the seal and is only a function of geometry. A model for carryover was developed as a function of *c/s* (clearance to pitch ratio) and w_{cavity}/c (cavity width to clearance). It has been identified that the major non-dimensional parameter influencing the discharge through an annular orifice is w_{tooth}/c (tooth width to clearance) and a model for C_d (discharge coefficient) can be developed based on the results. Flow through labyrinth seals can be considered as a series of annular orifices and cavities. Using this analogy, leakage rate can be modeled as a function of the discharge coefficient under each tooth and the carryover coefficient, which accounts for the turbulent dissipation of kinetic energy in a cavity. The discharge coefficient of first tooth in a labyrinth seal is similar to that of an annular orifice, whereas, the discharge coefficient of the rest of the tooth was found to be a function of the C_d of the previous tooth and the carryover coefficient. To understand the effects of operating conditions, a 1-D isentropic choking model is developed for annular orifices resulting in upper and lower limit curves on a T-s diagram which show the choking phenomenon of flow through a seal. This model was applied to simulations performed on both annular orifices and labyrinth seals. It has been observed that the theory is in general valid for any labyrinth seal, but the upper and lower limit curves on T-s diagram depend on number of constrictions. As the number of constrictions increase these two curves move further away from the critical point.

Third part of the report provides the details of the constructed heat exchanger test facility and presents the experimental results obtained to investigate the effects of buoyancy on heat transfer characteristics of Supercritical carbon dioxide in heating mode. Turbulent flows with Reynolds numbers up to 60,000, at operating pressures of 7.5, 8.1, and 10.2 MPa were tested in a round tube. Local heat transfer coefficients were obtained from measured wall temperatures over a large set of experimental parameters that varied inlet temperature from 20^{o} C to 55^{o} C,

mass flux from 150 to 350 kg/m^{2}s, and a maximum heat flux of 65 KW/m^2. Horizontal, upward and downward flows were tested to investigate the unusual heat-transfer characteristics to the effect of buoyancy and flow acceleration caused by large variation in density. In the case of upward flow, severe localized deterioration in heat transfer was observed due to reduction in the turbulent shear stress and is characterized by sharp increase in wall temperature. In the case of downward flow, turbulent shear stress is enhanced by buoyancy forces leading to an enhancement in heat transfer. In the case of horizontal flow, flow stratification occurred leading to a circumferential variation in wall temperature. Thermocouples mounted 180^o apart on the tube revealed that the wall temperatures on the top side are significantly higher than the bottom side of the tube. Buoyancy factor calculations for all the test cases indicated that buoyancy effects cannot be ignored even for horizontal flows at Reynolds number as high as 20,000. Experimentally determined Nusselt numbers are compared to existing correlations available in literature. Existing correlations predicted the experimental data within ±30% with maximum deviation around the pseudo-critical point.

Final part of this report presents the simplified analysis performed to investigate the possibility of using wet cooling tower option to reject heat from the supercritical carbon dioxide Brayton cycle power convertor for AFR-100 and ABR-1000 plants. A code was developed to estimate the tower dimensions, power and water consumption, and to perform economic analysis. The code developed was verified by comparing the calculations to a vendor quote. The effect of ambient air and water conditions on the sizing and construction of the cooling tower as well as the cooler is studied. Finally, a cost-based optimization technique is used to estimate the optimum water conditions which will improve the plant economics. A comparison of different cooling options for the S-CO_2 cycle indicated that the wet cooling tower option is a much more feasible and economical option compared to dry air cooling or direct wet cooling options.

Table of Contents

Abstract 2

List of Figures 12

List of Tables 19

Introduction 20

1 Background 22

1.1 Supercritical Working Fluids 22

1.1.1 The S-CO_2 Brayton Cycle Turbomachinery 24

1.2 Previous Work 27

1.2.1 Annular Seals 27

1.2.2 Eccentric Flow Increase 28

1.2.3 Eccentric Entrance Length 30

1.2.4 Leakage Models 31

1.2.5 Measured Seal Leakage 41

2 Data Collection 43

2.1 Test Facility 43

2.1.1 Test Section 50

2.1.2 Seal Geometries 52

2.2 Test Conditions 57

2.3 Data Collection 58

2.3.1 Assembly Procedure/Eccentricity Measurement 58

2.3.2 Data Collection Procedure 61

3 Computational model 62

3.1 Governing Equations 63

4 Experimental Results 72

4.1 Shaft Eccentricity 72

4.1 Straight through Labyrinth Seals 76

4.1.1 Property Variation and HEM Model 76

4.1.2 Tooth Number Optimization 79

4.1.3 Leakage Models 82

4.2 Stepped Labyrinth Seal 85

4.3 Empirical Discharge Coefficient 92

5 Numerical Results 94

5.1 Validation of computational model 97

5.1.1 Effect of radius of curvature 101

5.2 Effect of geometrical parameters 102

5.2.1 Effect of Radial clearance 102

5.2.2 Effect of Tooth width 104

5.2.3 Effect of tooth height 107

5.2.4 Effect of Shaft Diameter 108

5.2.5 Correlation for Carry over coefficient 109

5.2.6 Effect of radial clearance 110

5.2.7 Effect of Tooth Height 111

5.2.8 Effect of cavity width 113

5.2.9 Effect of Shaft Rotation on annular orifices and labyrinth seals 116

5.3 Effect of Operating Conditions 122

5.3.1 Results for Annular orifice 130

5.3.2 Results for Labyrinth Seal 138

6 Heat transfer characteristics of supercritical CO_2 146

6.1 Experimental facility overview 146

6.2 Validation of the test facility 149

6.3 Experimental and data analysis procedure 150

6.3.1 Uncertainty analysis 151

6.4 Results and Discussion 152

6.4.1 Effect of operating pressure 152

6.4.2 Effect of flow configuration 153

6.4.3 Effect of inlet temperature 156

6.4.4 Effect of heat flux 159

6.4.5 Buoyancy criteria 160

6.4.6 Evaluation of existing correlations 167

7 Wet Cooling tower option for S-CO_2 Cycle 169

7.1 Introduction to cooling towers 169

7.1.1 Classification of cooling towers 169

7.1.2 Components of a cooling tower 172

7.2 Cooling tower theory 174

7.3 Design procedure 180

7.3.1 Estimation of optimum mw/ma 181

7.3.2 Merkel number 182

7.3.3 Estimation of floor area 183

7.3.4 Estimation of fill height 187

7.3.5 Water consumption rate 189

7.3.6 Power requirements 190

7.3.7 Estimation of cooling tower cost 191

7.3.8 Factors affecting cooling tower size 192

7.4 Design Calculations 193

7.4.1 Verification of the code 194

7.4.2 Effect of ambient air conditions 196

7.4.3 Control of water conditions 198

7.4.4 Effect of design water conditions 201

7.5 Cost based optimization 209

Conclusion 1

References 9

Appendix A 15

8 Uncertainty Analysis 15

8.1 Pressure Transducers 15

8.2 Temperature 16

8.3 Mass Flow Rate and Density 17

8.4 Discharge Coefficient Uncertainty 18

8.5 Uncertainty Summary 19

APPENDIX B 20

APPENDIX C 21

APPENDIX D 22

List of Figures

Figure 1. Sandia National Laboratory engineering diagram of labyrinth seal (A). The seal is made of brass and has four teeth that approach the steps on the rotating shaft. The compressor wheel (B) shows the four steps on the shaft.

Figure 2. Calculated windage loss for the S-CO_2 SNL turbo-alternator-compressor as a function of rotor cavity pressure [2].

Figure 3. Conventional pocket damper seal [10].

Figure 4. Piercy's result for increase in volumetric flow rate due to eccentricity in narrow fully-developed annular flow. The dashed line shows effects in the laminar region and the solid line shows effects in the turbulent region.

Figure 5. Detail of SNL main compressor, labyrinth seals, ball bearings, and location of other major components [14].

Figure 6. Sandia National Laboratory engineering diagram of labyrinth seal (A). The seal is made of brass and has four teeth that approach the steps on the rotating shaft. The compressor wheel (B) shows the four steps on the shaft [14].

Figure 7. Measured (brown) and predicted (red) leakage flow rate through the SNL four tooth stepped labyrinth seal [14].

Figure 8. Conceptual layout of the UW-Madison test facility.

Figure 9. Single Stage HydroPac compressor used in UW-Madison facility.

Figure 10. Heated and insulated buffer tank used to reduce pressure fluctuations from compressor shifting.

Figure 11. Precooler heat exchanger utilizing chilled water.

Figure 12. Preheater consisting of three heated and insulated pipes in parallel controlled via PID in Labview.

Figure 13. Conditions for various locations on the loop (Figure 8), shown on a temperature-specific entropy diagram during typical experiment conditions.

Figure 14. Cross Section of pressure vessel showing a) seal location/configuration, b) collet sub-assembly, c) shaft, d) seal, e) spacer drill bushing, f) test section flange [15].

Figure 15. Cross Section of test section flange showing seal configuration [15].

Figure 16. Seals and cavities used in the straight-through labyrinth tests, do=9.525 mm, di, seal=3.175 mm, di, cavity=4.763 mm and length = 1.27 mm.

Figure 17. 3-D model of seal curvature taken with Zygo NewViewTM white light interferometer.

Figure 18. Stepped labyrinth design showing pertinent dimensions.

Figure 19. Stepped labyrinth seal.

Figure 20. Shaft used to activate all four teeth within the stepped labyrinth design.

Figure 21. Shafts used in stepped labyrinth geometry, a) 4 land shaft b) 3 land shaft.

Figure 22. Temperature-specific entropy plot for CO2 with the test section inlet conditions shown for inlet pressures of 7.7 MPa (green), 10 MPa (blue), and 11 MPa (red) at corresponding inlet densities of 325, 475, and 630 kg/m3 in three-tooth labyrinth seal tests.

Figure 23. Assembly procedure of shaft-seal sub-assembly [15].

Figure 24. Result of image processing code used to measure eccentricity at shaft-seal interface.

Figure 25. Measured mass flow rate of CO2 through three tooth labyrinth seal as a function of pressure ratio for an upstream stagnation pressure of 10 MPa and an upstream stagnation density of 475 kg/m3.

Figure 26. OpenFOAM syntax for differential equations, picture taken from [36]

Figure 27. Density ratios for two phase CO_2 and water

Figure 28. Specific heat ratios for two phase CO_2 and water

Figure 29. Duct flow approximation flow area determination. Dividing lines show division where radial clearance was taken, a) concentric case b) eccentric case.

Figure 30. Duct flow approximation results for DH=0.1956 mm.

Figure 31. Experimental mass flow rate for annuli of varying L/D_h with a DH=0.195 mm and inlet conditions of Pin = 10 MPa and ρin=325 kg/m3.

Figure 32. Temperature-specific entropy diagram for 3 tooth straight through labyrinth showing inlet conditions (filled markers) and outlet conditions (hollow markers).

Figure 33. Discharge coefficient results for three-tooth straight through labyrinth seal at varying inlet conditions.

Figure 34. Measured flow rate for three-tooth straight through labyrinth for inlet conditions P=10 MPa and $\boldsymbol{\rho}$=325 kg/m^3. The blue line shows calculated flow rate using isentropic HEM

model and the red line shows the calculated flow rate applying a constant discharge coefficient to the isentropic HEM model.

Figure 35. Variation in tooth number for the same total length. One Tooth a: short length, depicts maximum flow rate. One Tooth b: Tooth occupies entire length and depicts the flow rate approached as tooth number is further increased [20].

Figure 36. Variation in tooth number for the same total length. Variation in pressure ratio shows an optimal tooth number of three [20].

Figure 37. Measured flow rate for variation in tooth number for the same total length compared to calculated flow rate using Open Foam simulation [7]. Minimum leakage is found at a tooth number of three. Inlet Pressure is 10 MPa with corresponding inlet density of 325 kg/m^3.

Figure 38. Comparison of measured flow rate to CFD calculated flow rate for varying tooth number with same total length.

Figure 39. Measure flow rates through straight through 3-tooth labyrinth seal for inlet pressure of 10 MPa and inlet density of 325 kg/m^3 compared to various labyrinth seal leakage models.

Figure 40. Incompressible and ideal gas condition check for Martin and Egli model over prediction. Inlet pressure of 6.8 MPa with corresponding inlet temperature of 200^{o}C.

Figure 41. Measure flow rates through straight through 3-tooth labyrinth seal for inlet pressure of 11 MPa and inlet density of 630 kg/m^3 compared to various labyrinth seal leakage models.

Figure 42. Four-tooth stepped labyrinth geometry for inlet pressure of 10 MPa and inlet density of 640 kg/m^3. Compared to calculated SNL leakage flow rate which is within 20% of measured flow rate.

Figure 43. Area normalized mass flow rate comparison of four-tooth stepped labyrinth seal to SNL leakage calculation for inlet conditions of 10 MPa and 640 kg/m^3

Figure 44. Area normalized leakage for four-tooth stepped labyrinth seal compared to calculated flow rate from SNL compressor facility.

Figure 45. Three-tooth and four-tooth stepped labyrinth seal flow rate measurement for inlet pressure of 10 MPa and inlet density of 640 kg/m^3.

Figure 46. Mass flow rate experimental measurements and calculations for three and four tooth stepped labyrinth seal including the SNL Martin leakage equation and the HEM model with constant discharge coefficient.

Figure 47. Experimentally determined discharge coefficient for three and four tooth stepped labyrinth seal at an inlet condition of 10 MPa with corresponding inlet density of 640 kg/m^3.

Figure 48. A sample computational mesh used for simulations

Figure 49. Variation of leakage rate prediction with number of nodes

Figure 50. Variation of discharge coefficient with number of nodes

Figure 51. Leakage rate for inlet condition of 9 MPa, 372 kg/m^3 (case 1 in Table D.3)

Figure 52. Leakage rate for inlet condition of 9 MPa, 498 kg/m^3 (case 2 in Table D.3)

Figure 53. Leakage rate for inlet condition of 10 MPa, 372 kg/m^3 (case 3 in Table D.3)

Figure 54. Leakage rate for inlet condition of 10 MPa, 498 kg/m^3 (case 4 in Table D.3)

Figure 55. Leakage rate for inlet condition of 11 MPa, 372 kg/m^3 (case 5 in Table D.3)

Figure 56. Error analysis for plain orifice data

Figure 57. Effect of radius of curvature on leakage rate

Figure 58. Variation of leakage rate with Radial clearance

Figure 59. Variation of discharge coefficient with radial clearance

Figure 60. Variation of leakage rate with tooth width

Figure 61. Variation of C_d with tooth width

Figure 62. C_d of annular orifices having same w/c

Figure 63. Variation of leakage rate with tooth height

Figure 64. Variation of C_d with tooth height

Figure 65. Variation of C_d with shaft diameter

Figure 66. Measurement of divergence angle in the cavity

Figure 67. Effect of clearance on γ

Figure 68. Effect of tooth/cavity height on γ

Figure 69. Effect of cavity height on leakage rate

Figure 70. Effect of cavity width on leakage rate

Figure 71. Variation of γ with cavity width

Figure 72. Velocity profile at the entrance of each tooth

Figure 73. Influence of shaft rotation on C_d of annular orifices

Figure 74. Variation of γ with shaft speed

Figure 75. Variation of the C_d with shaft speed for labyrinth seals

Figure 76. Pressure variation along centerline in the radial clearance region

Figure 77. Temperature variation along centerline in the radial clearance region

Figure 78. Leakage rate prediction using 1-D isentropic model for case 2 in Appendix C

Figure 79. Inlet conditions used for testing 1-D isentropic model

Figure 80. Isentropic flow behavior for S_{in}=-1.0 KJ/kg-K

Figure 81. Isentropic flow behavior for S_{in}=-1.338 KJ/kg-K

Figure 82. Isentropic flow behavior for S_{in}=-1.5 KJ/kg-K

Figure 83. Downstream velocity and local sound speed of an annular orifice as a function of outlet pressure

Figure 84. Choking theory for isentropic flow

Figure 85. Leakage rate for inlet condition of 9 MPa and 372 kg/m^3

Figure 86. Leakage rate for inlet condition of 9 MPa and 498 kg/m^3

Figure 87. C_d for cases 4 and 5 in Table D.1 of Appendix D

Figure 88. Leakage rate for inlet condition of 10 MPa and 372 Kg/m^3

Figure 89. Leakage rate for inlet condition of 10 MPa and 498 Kg/m^3

Figure 90. C_d for case 3 in Table D.1 and case 2 in Appendix B

Figure 91. Leakage rate for inlet condition of 11 MPa and 372 Kg/m^3

Figure 92. Leakage rate for inlet condition of 11 MPa and 498 Kg/m^3

Figure 93. C_d for cases 1 and 2 in Table D.1 of Appendix D

Figure 94. C_d for case 6 in Table D.1 of Appendix D

Figure 95. Choking point calculations for annular orifice (Flow curve)

Figure 96. Leakage rate for inlet condition of 9 MPa and 372 Kg/m^3

Figure 97. Leakage rate for inlet condition of 9 MPa and 498 Kg/m^3

Figure 98. Leakage rate for inlet condition of 9 MPa and 630 Kg/m^3

Figure 99. C_d for an inlet pressure of 9 MPa (cases 3, 4 and 5 in Table D.1)

Figure 100. Leakage rate for inlet condition of 10 MPa and 372 Kg/m^3

Figure 101. Leakage rate for inlet condition of 10 MPa and 498 Kg/m^3

Figure 102. C_d for an inlet pressure of 10 MPa

Figure 103. C_d for an inlet pressure of 11 MPa

Figure 104. C_d for an inlet pressure of 7.7 MPa

Figure 105. Choking point calculations for labyrinth seal (Flow curve)

Figure 106. Downstream velocity of labyrinth seal and local sound speed as a function of outlet pressure

Figure 107. Schematic of the experimental facility and the test section

Figure 108. Wall temperature and Nusselt Number for water validation test

Figure 109. Effect of operating pressure on heat transfer for downward flow, G – 195 kg/m^{2}s, $Q"_{PS}$ – 13.5 kW/m^2

Figure 110. Effect of flow configuration on heat transfer for p – 8.1 MPa, G – 195 kg/m^{2}s, $Q"_{PS}$ – 24 kW/m^2, T_{in} – 46°C

Figure 111. Effect of inlet temperature on the wall temperatures for p – 7.5 MPa, G – 320 kg/m^{2}s, $Q"_{PS}$ –24 kW/m^2

Figure 112. Effect of heat flux on downward flow heat transfer for p – 7.5 MPa, G- 195 kg/m^{2}s

Figure 113. Normalized Nusselt number versus Jackson's buoyancy parameter, *Bu*

Figure 114. Normalized Nusselt number versus Jackson's buoyancy parameter, Bo_j

Figure 115. Calculated Nusselt number using Mokry et al. correlation

Figure 116. Calculated Nusselt number for downward flow

Figure 117. Proposed schematic of the cooler and induced draft cooling tower

Figure 118. Concept of different fill types

Figure 119. Control volume of counterflow fill configuration

Figure 120. Air side control volume

Figure 121. Counterflow cooling diagram

Figure 122. Delta cooling towers Inc. one cell plan [80]

Figure 123. Effect of heat load

Figure 124. Effect of range

Figure 125. Effect of approach

Figure 126. Effect of wet-bulb temperature

Figure 127. Variation of requirements for AFR-100 at optimum $\dot{m}_w/\dot{m}_a$ conditions

Figure 128. Effect of $\dot{m}_w/\dot{m}_a$ on the power consumption and make-up water requirements

Figure 129. Effect of water conditions on the cooler variables

Figure 130. Effect of water conditions on the tower floor area in Idaho Falls

Figure 131. Effect of water conditions on the fill height in Idaho Falls

Figure 132. Effect of water conditions on the total power consumption in Idaho Falls

Figure 133. Effect of water conditions on the cooling tower cost in Idaho Falls

Figure 134. Effect of water conditions on the cooler cost

Figure 135. Effect of water conditions on plant capital cost in Idaho Falls

Figure 136. Effect of water conditions on plant capital cost for all three locations

List of Tables

Table I. Experimental flow increase due to eccentricity for DH=0.195 mm and inlet conditions of Pin =10 MPa and ρin= 325 kg/m3

Table II. Empirical discharge coefficient results

Table III. Choking and saturation pressures for various operating conditions

Table IV. Reference cooler design conditions for AFR-100 and ABR-1000 plants

Table V. Tower Merkel number calculation example

Table VI. Manufacturer data for different cell types

Table VII. Comparison of calculations to the manufacturer quotation

Table VIII. Monthly design ambient air conditions

Table IX. Cost-based optimization results for AFR-100 and ABR-1000 plants

Table X. Comparison of different cooling options for ABR-1000

Table XI. Pressure transducer uncertainty and configuration summary.

Table XII. Temperature uncertainty and configuration summary.

Table XIII. Mass flow and density uncertainties and configuration summary.

Table XIV. Summary of key parameter uncertainties.

Introduction

The widespread use and success of the Rankine cycle has, until recently reduced interest in developing alternative methods of power conversion. There is now increased research into alternatives to the steam Rankine cycle because of the higher thermal efficiencies that are possible at the high temperatures associated with next generation nuclear power and concentrating solar power. One potential alternative power cycle which takes advantage of these higher temperatures to achieve greater efficiency is the supercritical carbon dioxide Brayton cycle. As a result, the development of a fundamental understanding of the behavior of S-CO_2 as a working fluid in these cycles has become an important area of research for the turbo machinery community [1-4].

The operating conditions associated with the S-CO_2 Brayton cycle provide both potential advantages and interesting engineering concerns. The wide variation in properties across the S-CO_2 system demands a thorough understanding of the working fluid and its behavior under a variety of conditions. This need is compounded by the relatively small turbo machinery dimensions that are possible in the S-CO_2 Brayton cycle. Windage losses caused by the high density S-CO_2 can have a large effect, reducing efficiencies due to the high speed of the turbine [5, 6].

Several aspects of the S-CO_2 Brayton Cycle still require significant research and development, and this work addresses few of these areas. The behavior of S-CO_2 as it flows through restrictions such as valves, turbo machinery seals, and pipe ruptures is not well understood, but the development of models describing these phenomena is integral to the practical implementation of the S-CO_2 Brayton Cycle. For example, approximations for flow rates and pressure drops associated with annular orifices and labyrinth seals are necessary in computer

models used for predicting the performance of the power cycle. Models, such as Computational Fluid Dynamics (CFD), that are validated by this data can then be used to model more complex geometries [7].

The most relevant and basic flow situation related to this problem is flow through circular and annular orifices [8]. Therefore, flow through an annular space must be understood in order to model and optimize more complex seals such as labyrinth seals. When the annular geometry is understood the more complex labyrinth geometry can be observed and then optimized. The first objective of this study is to collect and use experimental data to model and optimize simple, small diameter shaft seals to aid in the practical design and use within S-CO_2 environments. The second objective is to develop computational model to understand the flow behavior through seals in more detail. Open source CFD package OpenFOAM is used for this task. The effect of geometrical parameters and operating conditions are isolated and studied individually.

Another biggest challenge in development of the cycle is that the detailed heat transfer mechanisms are still not completely understood. Due to drastic variation in thermophysical properties, heat transfer to supercritical fluids is quite different compared to ideal fluids. Qualitative explanation of different heat transfer mechanisms to supercritical fluids is provided by Licht et al. [62]. In a pipe flow, both axial and radial variation in density results in strong buoyancy effects deteriorating or enhancing the heat transfer depending on flow configuration and operating conditions [43-62]. Hence, the third objective of this work is to investigate such buoyancy effects on heat transfer to supercritical fluids (CO_2 in this case) and identify the conditions under which buoyancy effects are significant.

Rejecting the heat from power generation plants is also a big issue. There are numerous ways to achieve this task. One of the traditional options is to circulate cooling water from a nearby water

sources like river, lake, pond etc. which acts as an ultimate heat sink. The use of this direct wet cooling option is severely restricted due to the new environmental policies and scarcity of water resources in some locations. Alternatively, the dry air cooling option can be used with air as ultimate heat sink. However, recent calculations [67] suggested that the use of dry air cooling option would increase the cost of electricity by 40% compared to the direct wet cooling option. Hence, dry air cooling would be an expensive option for the AFR-100 or ABR-1000. The final task of the current work is to analyze the possibility of using the evaporative cooling tower option to reject the heat from these proposed power plants.

1 Background

1.1 Supercritical Working Fluids

A supercritical fluid is a substance whose temperature and pressure lie above the critical point. The critical point is found at the top of the vapor dome on the boundary of the two-phase region. This point is defined mathematically as the condition when the first and second derivatives of pressure with respect to volume at constant temperature are zero [9]. Within the supercritical region there is no distinct separation between the liquid and gas phases. This causes unusual behavior especially near the critical point where physical properties such as density and specific heat vary greatly.

The advantages of these property changes as applied to power cycles have been investigated for quite some time. Using supercritical fluid in power cycles allows for greatly increased power output and compression efficiency. This can be done by operating the compressor portion of the power cycle near the critical region where the density varies greatly with temperature. There is a considerable amount of work necessary to compress a low density fluid and this reduces the turbine output. By operating near the critical point and making use of the high

density of the fluid within the compressor the backwork ratio can be lowered, increasing efficiency. This effect can be seen in the Rankine cycle where compression takes place in the liquid region where the density is higher and shaft work can be reduced. Operating in this region invites some disadvantages; to achieve this liquid state the cycle must include evaporation and condensation stages. This complicates the cycle by requiring more equipment to facilitate the phase change. Also more complexity is introduced to problems that arise from cavitations within the system which can damage materials and reduce efficiency.

Several power cycles that operate within the supercritical region have been heavily researched. The front-runner working fluids are supercritical water (SCW), supercritical helium, and supercritical carbon dioxide (S-CO_2). Each poses different engineering advantages and challenges in terms of materials and operating conditions.

SCW is operated in a Rankine cycle where the high pressure side operates above the critical point. This allows the phase transition on the high pressure side to be avoided which eliminates many complications. This has a large effect on the total efficiency of the cycle which improves from 33% to 44% in a nuclear power cycle [4]. This is achieved by operating the turbine at a pressure of 25 MPa and a temperature of 500^{o}C.

Supercritical helium is operated in a Brayton Cycle and can achieve a much higher thermal efficiency of 51% [5]. This may seem like a considerable improvement but to achieve this the helium cycle needs to achieve temperature between 800 and 900^{o}C. With current materials technology these temperatures are hard to handle. This makes the helium cycle a technology that requires more research and development.

S-CO_2 can be used as a working fluid in a Brayton cycle entirely above the critical point. This allows for the negative effects associated with fluid phase changes within the cycle to be avoided. The critical pressure is much lower than that of water which allows for a wider range of inlet pressures. Typical conditions for moderate heat sources (400°-650°C) include compressor inlet pressure of 7.5 MPa and outlet pressure of 22 MPa for power levels below 50 MW_e. Wright compares the S-CO_2 cycle to other advanced power cycles and find's it has a competitive 44-46% thermal efficiency for an inlet temperature of 550°C and reduces capital costs by approximately 23% [6]. If inlet temperature is pushed to 700°C efficiencies can approach 50%.

1.1.1 The S-CO_2 Brayton Cycle Turbomachinery

To obtain these high thermal efficiencies with the S-CO_2 Brayton cycle it is important to have properly designed turbomachinery. The main goal of this investigation is to examine the problem of leakage through the shaft seals used within the cycle both experimentally and computationally. With a moving shaft it is not possible to have a hermetic seal across a large pressure gradient, meaning there will be leakage from the high pressure compressor region into the low pressure generator cavity. This causes frictional windage losses within the generator cavity that reduce the efficiency of the system.

The frictional losses from this leakage into the generator cavity are highly related to the density in the cavity. One way to reduce the flow into the generator cavity is to separate the compressor region by including a series of expansions and contractions called a labyrinth seal. As the labyrinth seal does not provide a perfect seal there is some leakage that is expected. If this leakage is not addressed the pressure within the generator cavity will increase to match the pressure in the compressor region. On method of eliminating this pressure from the generator

cavity is to incorporate a secondary system to draw out the residual working fluid from the generator cavity. This may be done by placing pumps within the system to remove the excess S-CO_2 from the generator cavity. This introduces losses due to the work required to operate the pumps. With this method in mind it is of interest to minimize leakage through the optimization of shaft seals.

Windage losses are particularly important to consider in smaller facilities with power less than 1 MW. This is because the surface area to volume ratio of such machines tends to be high. This is the case for the Sandia National Labs 250 KW_e facility where the compressor wheel is depicted in Figure 1. This facility will be used as a practical comparison to the experiment detailed in this work.

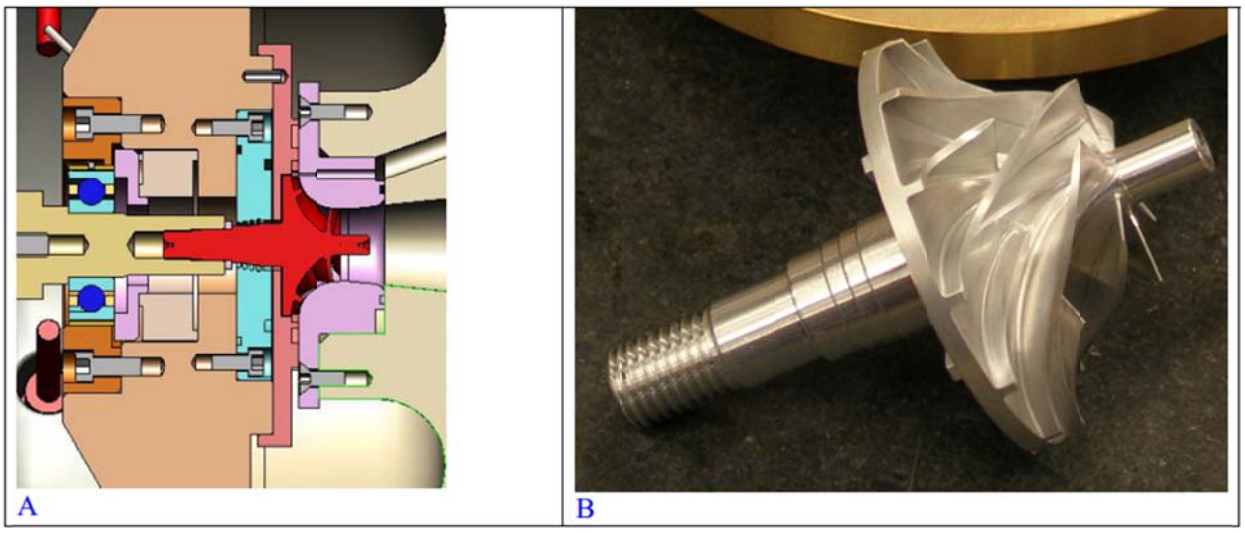

Figure 1. Sandia National Laboratory engineering diagram of labyrinth seal (A). The seal is made of brass and has four teeth that approach the steps on the rotating shaft. The compressor wheel (B) shows the four steps on the shaft [2].

Figure 2 illustrates the rotor windage loss and how it varies as a function of the cavity pressure. This was calculated for the SNL research facility cavity and shows that for cavity pressures near the compressor inlet pressure of 7.7 MPa the losses are considerable [2]. At cavity pressures near 7.5 MPa the losses are on the order of 35-40 kW which nearly equals the capability of the

motor control system and the pumping power for the compressor used. This led design to operate the cavity at pressures of 1.78 MPa to reduce the losses due to cavity pressure to 4% of the generated power down from 35%. The optimization of shaft seals limits the amount of power needed to operate pumps which are used to achieve these low cavity pressures. The investigation into this problem shown here depicts the need for the optimization of shaft seals to limit the leakage into the cavity. Fortunately it is expected that the fractional pumping power for large commercial systems is much smaller than for the SNL proof-of-principle test loop. This is largely because more conventional sealing technologies can be used. Another reason is that in a larger system the generated power will grow as the radius squared, while the leakage flow rate grows proportional to the radius, thus it will be much easier to keep the fractional windage losses low in larger systems.

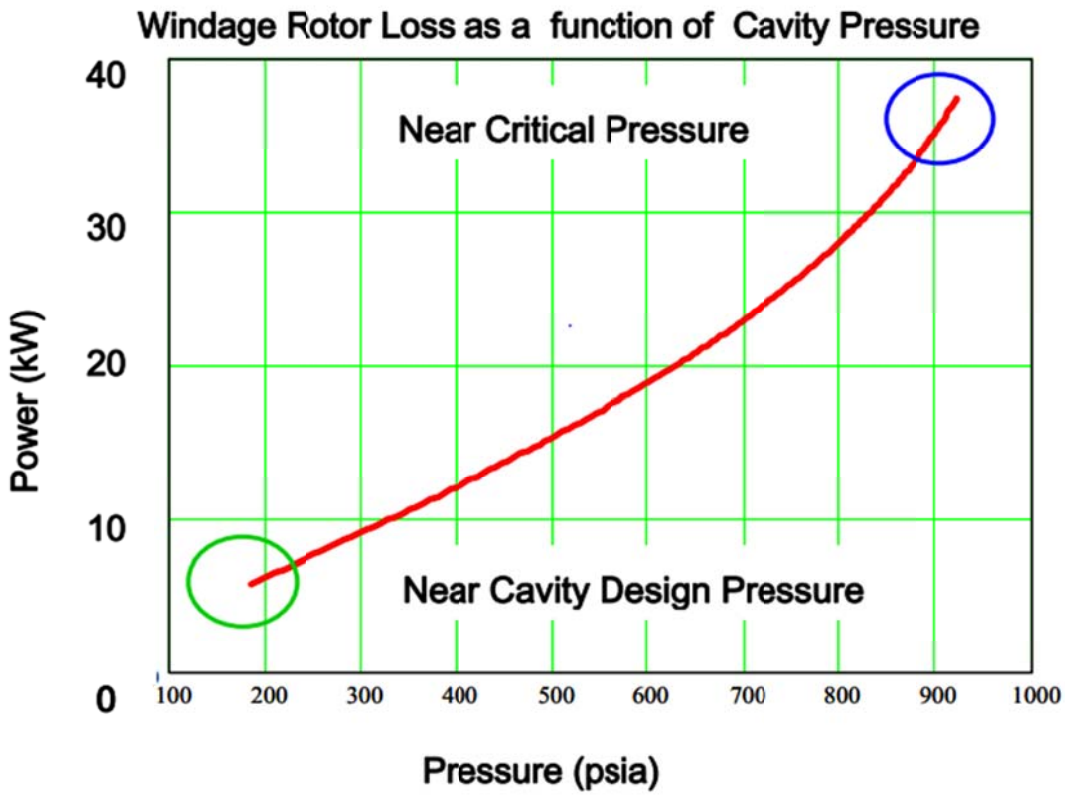

Figure 2. Calculated windage loss for the S-CO_2 SNL turbo-alternator-compressor as a function of rotor cavity pressure [2].

1.2 Previous Work

1.2.1 Annular Seals

The high demands of the power industry have caused turbomachinery to be designed with higher efficiency and higher shaft speeds in mind. This results in a need to reach optimal balance between a turbomachine's leakage characteristics and its rotordynamic performance, while dealing with ever-tightening clearances. Research on one particular component used in such machines, the annular shaft seal, has been instrumental in achieving the operating speeds and efficiency levels that are necessary to attain today. Annular shaft seals limit fluid flow across regions of unequal pressure. These seals have desirable leakage prevention performance and are designed with a non-contacting nature. This non-contacting design allows rotor speeds to be increased significantly. One of the simplest designs that employ these characteristics is the annular labyrinth seal. Labyrinth seals are made up of a series of contractions and expansions referred to as teeth and cavities. The ratio of the radial clearance to the shaft diameter is usually on the order of 1:100. The annular constrictions formed by the teeth cause the working fluid to throttle and then expand repeatedly, reducing the total pressure of the fluid from one cavity to the next and limiting the overall axial leakage rate. The labyrinth seal is one of the simplest and widest used shaft seals but it suffers from some undesirable rotordynamic effects related to instability. Also labyrinth seals offer only limited damping of shaft vibrations. To account for this more complex seal designs have been created and one of these designs is the pocket damper seal.

The pocket damper seal is made up of teeth dividing the seal into active and inactive cavities. The cavities are then partitioned into pockets at points along the circumference of the seal; this can be seen in Figure 3. What this does is resist the flows ability to move in the radial direction and increases the shaft stability provided by the seal [10].

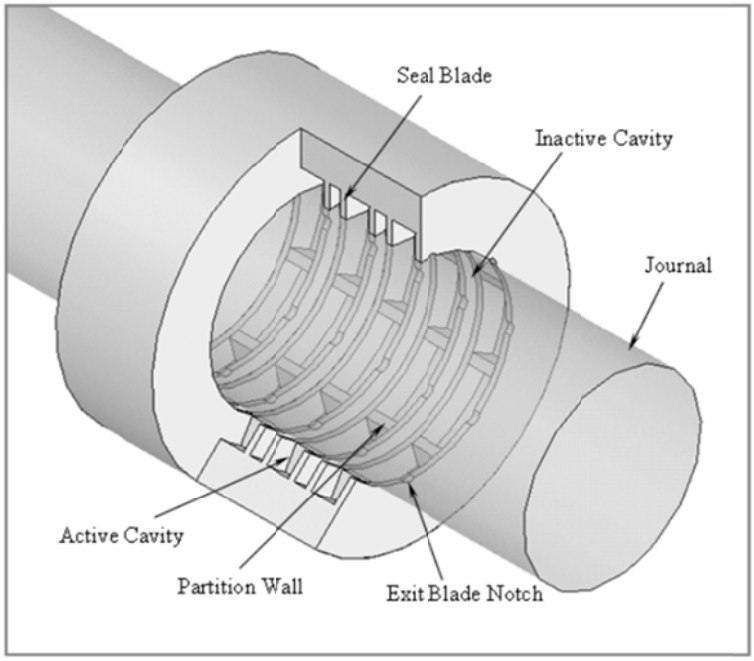

Figure 3. Conventional pocket damper seal [10].

Before more complex seals like the pocket damper seal can be examined the simpler examples like the straight-through labyrinth geometry must be investigated. Modeling the flow through these simpler seals allows validation of models which can then be applied to more complex geometries. Labyrinth seals are an easily fabricated and adjustable design which allows for a large number of parameters to be tested. By looking at different geometrical parameters, such as cavity depth and tooth width in labyrinth seals, the design of more complex geometries can be performed more efficiently. The investigation of labyrinth seals is in itself valuable as they provide a cheap and effective seal. Labyrinth seals may also be combined with other designs in more complex geometries. All these factors point to a need for research into the flow of S-CO_2 through labyrinth seals

1.2.2 Eccentric Flow Increase

In assembling a labyrinth seal the shaft position within the seal has a large effect on the geometry of the flow. The concern for this work, with respect to eccentricity, is knowing the

assembled eccentricity and understanding what effect that has had on the measured flow rate. Two factors that contribute to this are described here to better understand the effect of eccentricity and how it applies to labyrinth seals. Piercy et al. developed an analytical solution for flow through a pipe with an eccentric core [11]. When running the experiment, the researchers found it difficult to precisely center the cores within the pipes and thus inadvertently observed the effect of eccentricity on the flow. For long annular spaces, an analytical solution was presented for the increase in volumetric flow associated with the eccentric case relative to the concentric case. The exact solution is shown in Figure 4 for the limiting case of narrow annuli with a diameter ratio approaching one. The diameter ratio is defined as the ratio of the core or shaft diameter to the outer diameter. The relative eccentricity is defined as the distance between the shaft center and seal center divided by the difference in seal diameter and the shaft diameter. This result was subsequently verified by Tao [12] and White [13], and predicts an increase in the flow from the concentric to the eccentric case of 25% for narrow gap annulus under turbulent conditions. This result suggests that the effect of eccentricity on turbulent fully developed flow in annular geometries is substantial and therefore eccentricity might be important in the design of shaft seals used in S-CO_2 flow.

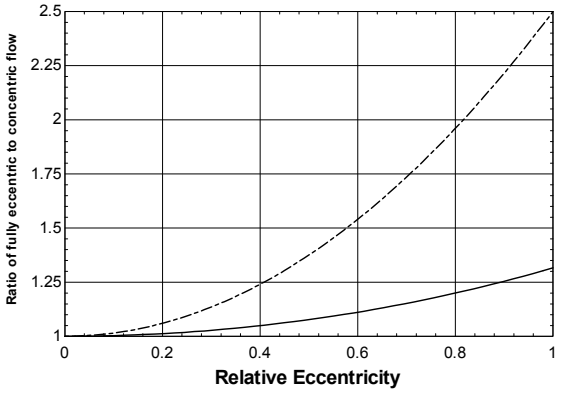

Figure 4. Piercy's result for increase in volumetric flow rate due to eccentricity in narrow fully-developed annular flow. The dashed line shows effects in the laminar region and the solid line shows effects in the turbulent region.

1.2.3 Eccentric Entrance Length

The increase in flow due to eccentricity is a frictional effect. The entrance length where flow has yet to fully develop has a relatively high effect because of this. This effect is compounded by the particularly short lengths expected in seal design. Jonsson's study [14] of the eccentric effect in turbulent conditions noted a large change in the entrance length from concentric to the eccentric case. He describes the entrance length at the location where flow reaches within 2% of the fully developed pressure drop. This length was measured with circumferential pressure taps installed along the length of the test section. At four lengths along the annulus six pressure taps were spaced evenly around the circumference of the test sections outer wall. The experimental measurements show that under some conditions, the eccentric entrance length is triple that of the concentric entrance length. This increase in entrance length is caused by the additional length required to transport fluid from the narrow part to the wider part of the annulus. These results are further compounded by the fact that these data show that the effect from eccentricity increases as the diameter ratio approaches one [15]. The results indicate there is a distance past the concentric entrance length where the eccentric case is still experiencing the increased friction associated with the entrance region. The increase in the developing distance and associated increase in the shear stress then tends to offset to some extent the decrease in the friction factor associated with the eccentric geometry. For very long annular gaps (i.e., ones with lengths that are much longer than the eccentric entrance length) the increase in flow due to eccentricity will reach a maximum value. However, for relatively short annular gaps (i.e., ones with lengths that are comparable to the eccentric entry length) the increase in flow will be less significant.

1.2.4 Leakage Models

Straight Through Labyrinth Seals

A considerable amount of work has been done to model leakage flow in labyrinth seals. In this study several models which are used within the industry shall be compared to the experimental data gathered. These models assume incompressible ideal gas behavior but will be observed to evaluate their performance with S-CO_2. The conditions seen in the operation of an S-CO_2 Brayton cycle are far from ideal or incompressible, but these models are designed for labyrinth seal leakage and if they perform well can provide a simple method for predicting leakage when given only the minimum amount information about the seal and the conditions it is under.

Vennard and Street [16] carried out an energy balance on a one dimensional flow element to obtain the Euler equation shown in Equation (1). Applying isentropic assumptions and integrating yields the velocity expression in Equation (2). Where the subscript *i* denotes the *ith* cavity and γ denotes the ratio of specific heat values.

$$\frac{dP}{\rho} + u \cdot du + g \cdot dz = 0 \tag{1}$$

$$\frac{u_i^2 - u_{cav}^2}{2} = \int_{P_{i+1}}^{P_i} \frac{dP}{\rho} = \frac{P_i}{\rho_i} \cdot \frac{\gamma}{\gamma - 1} \cdot \left[1 - \left(\frac{P_{i+1}}{\rho_i} \right)^{\frac{\gamma-1}{\gamma}} \right] \tag{2}$$

$$u_i = \sqrt{\frac{P_i}{\rho_i} \cdot \frac{2 \cdot \gamma}{\gamma - 1} \cdot \left[1 - \left(\frac{P_{i+1}}{\rho_i} \right)^{\frac{\gamma-1}{\gamma}} \right]} \tag{3}$$

$$\dot{m}_i = \frac{P_i \cdot A_i}{\sqrt{\gamma \cdot R \cdot T_i}} \cdot \sqrt{\frac{2 \cdot \gamma^2}{\gamma - 1} \cdot \left[\left(\frac{P_{i+1}}{P_i}\right)^{\frac{2}{\gamma}} - \left(\frac{P_{i+1}}{P_i}\right)^{\frac{\gamma-1}{\gamma}} \right]} \tag{4}$$

For seal constrictions it is assumed that the upstream condition is a stagnation condition. This means the flow velocity in the cavity upstream of the constriction can be neglected relative to the velocity of the flow through the constriction. After rearranging and again applying isentropic assumptions the St. Venant leakage equation is shown in Equation (4). This equation was first used by Schultz [17] for the calculation of leakage through pocket damper seals. It is an iterative method which calculates the pressure drop at each cavity.

Martin presented the first leakage equation specifically intended for labyrinth seals. His formula, which assumes incompressible ideal gas behavior, is shown in Equation (5). Martin's Equation is derived based on an approach of determining the number of teeth, *n*, required to achieve a given pressure drop, then relating that number to the work done in dropping the pressure. The work done is then related to the flow-rate through the kinetic energy of the fluid.

$$\dot{m} = \frac{A \cdot P_{in}}{\sqrt{R \cdot T}} \sqrt{\frac{1 - \left(\frac{P_{out}}{P_{in}}\right)^2}{n - ln\left(\frac{P_{out}}{P_{in}}\right)}} \tag{5}$$

Egli [18] used Martin's Equation as a starting point and suggested the use of a flow correction factor and a kinetic energy carry-over coefficient, which he determined empirically.

$$\dot{m} = \mu_i^{empirical} \frac{A \cdot P_{in}}{\sqrt{R \cdot T}} \sqrt{\frac{1 - \left(\frac{P_{out}}{P_{in}}\right)^2}{n - ln\left(\frac{P_{out}}{P_{in}}\right)}} \tag{6}$$

Egli's flow coefficient is not based on the clearance area of the seal or the area at the vena contracta, but the area of the jet of fluid at some point after it passes through the constriction.

The use of the jet area comes from the assumption that at some point along the jet, shortly after the constriction, the pressure in the jet is equal to the cavity pressure in the downstream cavity (the cavity being entered). The need for a kinetic energy carry-over coefficient is evident from Egli's description of the flow through the constrictions of a labyrinth seal: "as the steam flows through the labyrinth, a pressure drop occurs across each throttling. After each throttling, a small part of the kinetic energy of the steam jet will be reconverted into pressure energy, a second part will be destroyed and transferred into heat, and the remaining kinetic energy will enter the following throttling." The carry-over coefficient therefore represents the portion of kinetic energy carried over from one cavity to the next. Egli reasons that since the jet emerging from the constriction increases with increasing axial distance, the percentage of kinetic energy carried over from one throttling to the next must decrease with increasing spacing between the blades or with decreasing clearance. Using Egli's method, the flow through a labyrinth seal can be shown to follow the proportionality of Equation (7) and this proportionality can be approximated to $n^{0.5}$.

$$\dot{m} \propto \frac{1}{\sqrt{n - ln\left(\frac{P_{out}}{P_{in}}\right)}} \tag{7}$$

Another modification on Egli's equation is the Hodkinson's equation [19] which is shown in Equation (8). Where Egli used an empirical coefficient to account for kinetic energy carry-over, Hodkinson developed a semi-empirical expression for this coefficient based on an assumption regarding the gas jet's geometry. His assumption pertained to the shape of the fluid jet as it expands after the constriction. A conical expansion at a small angle from the tip of the upstream tooth moves through with a small portion entering the next cavity undisturbed.

Hodkinson makes note that Egli does not take into consideration the higher velocity through the final constriction and then derives a carry-over factor based on a linear increase in the pressure drop with each constriction. He incorporates his idea of a conically shaped stream and does not take into account vena contracta effects. For the conical angle he uses a stream angle with a tangent of 0.02 which best described his data.

$$\dot{m}_\iota = \mu_i^{Hodkinson} \frac{A \cdot P_{in}}{\sqrt{R \cdot T}} \sqrt{\frac{1 - \left(\frac{P_{out}}{P_{in}}\right)^2}{n - ln\left(\frac{P_{out}}{P_{in}}\right)}} \tag{8}$$

$$\mu_i^{Hodkinson} = \sqrt{\frac{1}{1 - \left(\frac{n-1}{n}\right) \cdot \left(\frac{\frac{c_i}{l_i}}{\left(\frac{c_i}{l_i}\right) + 0.02}\right)}} \tag{9}$$

The carry over coefficient defined in Equation (9) cannot increase indefinitely. There is a numerical limit which Hodkinson defines since if clearances continue to increase, the fluid will blow straight through and the seal will act like one with a single constriction. At very large pressure drops, Hodkinson notes that the carry-over coefficient becomes unnecessary since at the acoustic velocity the seal leakage is more or less determined by the clearance of the final tooth. At pressures further from the critical ratio or with a liquid in place of a gas, the carry-over effects become significant.

Developing his own carry-over coefficient Vermes [20] modified Martin's leakage equation. This equation is developed based on boundary layer theory and is shown in Equation (10).

$$\dot{m}_i = \mu_i^{Vermes} \frac{A \cdot P_{in}}{\sqrt{R \cdot T}} \sqrt{\frac{1 - \left(\frac{P_{out}}{P_{in}}\right)^2}{n - ln\left(\frac{P_{out}}{P_{in}}\right)}} \tag{10}$$

$$\mu_i^{Vermes} = \sqrt{\frac{1}{1 - \left(\frac{1}{(1 - \alpha_i)}\right)}} \tag{11}$$

$$\alpha_i = \frac{8.52}{\frac{l_i - t_i}{c_i} + 7.23} \tag{12}$$

Neumann [Childs 21] developed the empirical leakage expression of Equation (13) which contains a semi-empirical leakage flow coefficientC_f. The coefficient accounts for the further contraction of flow after it has passed through the plane of the physical constriction.

$$\dot{m}_i = C_{f,i} \cdot \mu_i^{Neumann} \cdot \sqrt{\frac{P_i^2 - P_{i+1}^2}{R \cdot T}} \tag{13}$$

$$C_{f,i} = \frac{\pi}{\pi + 2 - 5 \cdot \beta_i + 2 \cdot \beta_i^2} \tag{14}$$

$$\beta_i = \left(\frac{P_i}{P_{i+1}}\right)^{\frac{\gamma - 1}{\gamma}} - 1 \tag{15}$$

$$\mu_i^{Neumann} = \sqrt{\frac{n}{n \cdot \left((1-\alpha_i)\right) + \alpha_i}} \tag{16}$$

$$\alpha_i = 1 - \frac{1}{\left(1 + 16.6 \cdot \frac{c_i}{l_i}\right)^2} \tag{17}$$

Zimmerman and Wolf [22] treated the problem of straight through labyrinth seals by applying a method which treated the initial constriction differently. As the carry-over coefficient is not present in the first constriction it is more effective at reducing the flow than at least some of the downstream constrictions. They state that this holds true even though the "effectiveness" of each constriction increases as the flow moves downstream. This method applies the St. Venant equation to the first constriction and then applies Martin's equation with a carry-over coefficient to the remainder of the seal, Equation (18).

$$\dot{m}_\iota = \frac{P_i \cdot A_i}{\sqrt{\gamma \cdot R \cdot T_i}} \cdot \sqrt{\frac{2 \cdot \gamma^2}{\gamma - 1} \cdot \left[\left(\frac{P_{i+1}}{P_i}\right)^{\frac{2}{\gamma}} - \left(\frac{P_{i+1}}{\rho_i}\right)^{\frac{\gamma-1}{\gamma}}\right]} \qquad for\ i = 1 \tag{18}$$

$$\dot{m}_\iota = \mu_i^{Hodkinson} \frac{A \cdot P_{in}}{\sqrt{R \cdot T}} \sqrt{\frac{1 - \left(\frac{P_{out}}{P_{in}}\right)^2}{n - ln\left(\frac{P_{out}}{P_{in}}\right)}} \qquad for\ i > 1$$

Scharrer [23] developed a two control volume model in which he used the non-constant kinetic energy carry-over coefficient developed by Vermes. He then applied this to Neumann's equation and is shown in Equation (19).

$$\dot{m}_\iota = C_{f,i} \cdot \mu_i^{Vermes} \cdot \sqrt{\frac{P_i^2 - P_{i+1}^2}{R \cdot T}} \tag{19}$$

Esser and Kazakia [24] used Neumann's Equation and carried out a computational fluid dynamics analysis of the behavior of the fluid jet through planar constriction. They concluded that a constant value for the flow coefficient would be more accurate and is shown in Equation (20)

$$\dot{m}_\iota = C_{f,i} \cdot \mu_i^{Neumann} \cdot \sqrt{\frac{P_i^2 - P_{i+1}^2}{R \cdot T}} \quad \text{Where } C_{f,i} = 0.716 \tag{20}$$

Another analysis performed by Kurohashi [25] focused on calculating the circumferential pressures developed in a seal when the journal is displaced, but also presented a method for calculating axial leakage. The equation developed is based on Neumann's Equation but derived a kinetic energy carry-over coefficient which is shown in Equation (22).

$$\dot{m}_\iota = C_{f,i} \cdot \mu_i^{Kurohashi} \cdot \sqrt{\frac{P_i^2 - P_{i+1}^2}{R \cdot T}} \tag{21}$$

$$\mu_1^{Kurohashi} = \sqrt{\frac{1}{1 - \alpha_1 + \alpha_1^2}}$$
$$\mu_{i>1}^{Kurohashi} = \sqrt{\frac{1}{1 - 2 \cdot \alpha_1 + \alpha_1^2}} \tag{22}$$

$$\alpha_i = \frac{\left(\frac{c_i}{l_i}\right)}{\left(\frac{c_i}{l_i}\right) \cdot C_{f,i} + tan(6^o)} \tag{23}$$

Sriti [26] began with Neumann's Equation and further developed it to better match their experimental results. Equation (24) uses a single multiplier coefficient which accounts for both flow contraction and kinetic energy carry-over effects.

$$\dot{m}_i = \lambda \cdot \left(1.57 \cdot \frac{c_i}{l_i}\right) A_i \cdot \sqrt{\frac{P_i^2 - P_{i+1}^2}{R \cdot T}} \tag{24}$$

$$\lambda = \begin{cases} 0.8 \cdot Re^{-0.014} & for\ Re\ \leq 1250 \\ 3.65 \cdot Re^{-0.22} & for\ Re\ > 1250 \end{cases} \tag{25}$$

The models described previously in this chapter are designed for labyrinth seals in ideal and incompressible flow. They apply different kinetic carry-over coefficients and flow coefficients to better account for the effects of each subsequent throttling. These simple models were compared to data taken to assess their applicability as first approximations within S-CO_2 flow.

One-Dimensional Isentropic Homogeneous Equilibrium Model (HEM)

As the models previously described are not designed for the non-ideal and compressible flow of S-CO_2, this work also applied an isentropic model that accounts for two-phase flow and the real gas properties of CO_2. The Homogeneous Equilibrium Model (HEM) is an isentropic model that assumes the velocities, temperatures, and pressures of the phases are equal [27]. When applied to single phase conditions the HEM collapses to that of a single phase isentropic model. Using the capabilities of this facility the upstream pressure and density are measured along with the downstream pressure and density. These are used then to calculate the downstream velocity

using the energy balance in Equation (26). This is then used with the annular area to define the mass flow rate in Equation (27).

$$h_{in} = h_{out} + \frac{u_d^2}{2} \tag{26}$$

$$\dot{m}_{HEM} = \rho_{out} \cdot u_{out} \cdot A_{annular} \tag{27}$$

To apply this to two-phase flow the fluid is treated as a single phase fluid with mixture properties [28]. These mixture properties are here defined as average properties based on mass averages defined in Equation (28) and Equation (29). Where *x* is the quality and the *g* and *f* subscripts denote gas and fluid properties respectively.

$$\rho_{mix} = \frac{1}{\frac{x}{\rho_g} + \frac{1-x}{\rho_f}} \tag{28}$$

$$h_{mix} = x \cdot h_g + (1-x) \cdot h_f \tag{29}$$

Due to the assumptions made by the HEM the flow predicted by this model will always be the maximum possible flow through an annular geometry. This means that the calculation will always over predict the measured flow rate for a given geometry and condition. To account for this an empirically determined discharge coefficient may be defined as shown in Equation (30).

$$C_d = \frac{\dot{m}_{measured}}{\dot{m}_{HEM}} \tag{30}$$

Leakage Model Summary

A number of leakage models have been described here which can be applied to the flow of S-CO_2 through labyrinth seal geometries. One dimensional models designed for labyrinth seal flow that assume ideal and incompressible flow, were chosen to validate their depiction of the geometrical complexity in labyrinth seals. The isentropic HEM was also described as it allows for the characterization of the real gas properties that are present in S-CO_2.

The ideal and incompressible models gain value from their description of the geometry in labyrinth seals. By accounting for carry-over effects, with the inclusion of a carry-over coefficient and/or flow coefficient, they better account for changes in tooth number, cavity depth, and cavity width, etc. Several models allow for the pressure drop to be calculated quickly across the entire seal in one step, where others allow for the pressure drop through each constriction to be calculated. Although these models offer geometrical complexity they do not account for the real gas properties of S-CO_2 or the two phase conditions experienced in the S-CO_2 Brayton cycle. Care must be used when applying these models near the critical point and two-phase dome.

The HEM accounts for these real gas properties and uses mixture properties to better capture two-phase effects. This allows the model to better predict when the flow will choke and what the critical mass flow rate is. The HEM does not however account for changes in geometry as it is solely based on the annular flow area at the entrance of the seal. Changes in tooth number, tooth dimensions, or cavity dimensions cannot be captured by the model. This means that an empirically determined discharge coefficient which can be used to account for the models over prediction of the flow needs to be measured for each change in geometry. The HEM is then best applied when experimental data is available for the geometry of interest.

1.2.5 Measured Seal Leakage

As the S-CO_2 Brayton cycle is still in the research and development phase there has been little work performed in the measurement of seal leakage under supercritical conditions for carbon dioxide. One case of interest is the research facility at Sandia National Laboratories (SNL) where a small scale 250 KW_e Brayton cycle loop was built to study the key issue of compression near the critical point of CO_2. In this study an investigation into the effectiveness of the stepped labyrinth seal that was used was performed and compared to predictions made by a Martin Equation using a constant discharge coefficient ($C_d = 0.61$) detailed in Equation (24), where A is the flow area.

$$\dot{m} = C_d \cdot A \cdot \sqrt{P_{in} \cdot \rho_{in} \left(\frac{\left(1 - \frac{P_{out}}{P_{in}}\right)^2}{n - ln\left(\frac{P_{out}}{P_{in}}\right)} \right)} \tag{31}$$

This equation was applied to a stepped labyrinth located between the compressor wheel and the generator cavity. The layout and position of the seal can be seen in Figures 5 and 6.

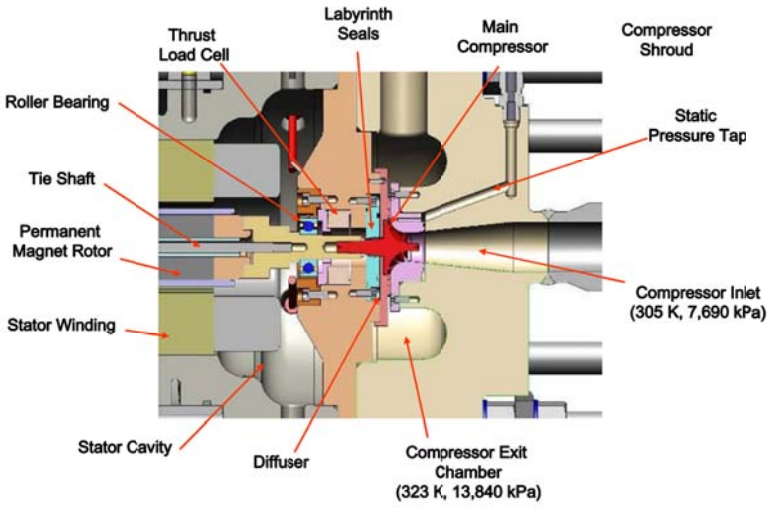

Figure 5. Detail of SNL main compressor, labyrinth seals, ball bearings, and location of other major components [2].

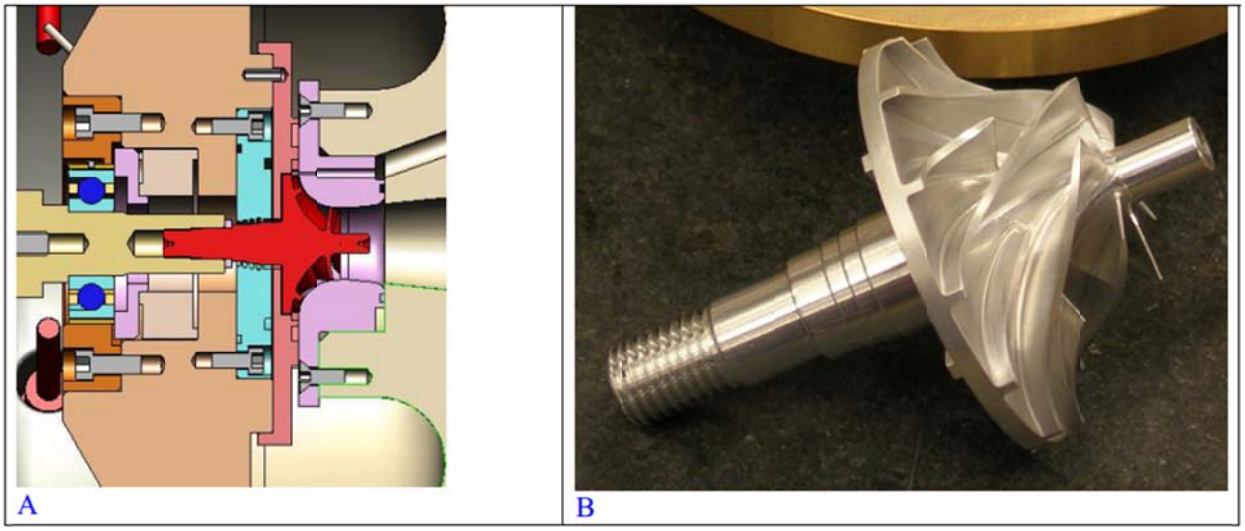

Figure 6. Sandia National Laboratory engineering diagram of labyrinth seal (A). The seal is made of brass and has four teeth that approach the steps on the rotating shaft. The compressor wheel (B) shows the four steps on the shaft [2].

The seal performance was tested during operation conditions with a compressor inlet pressure of 7.7 MPa and a compressor outlet pressure of 13.8 MPa. As the inlet conditions of the seal could not be measured the pressure at the inlet to the seal is somewhere between these two pressures. Although not knowing this inlet pressure SNL states that an internal study would suggest that the pressure is closer to the compressor inlet pressure. The outlet pressure was maintained at 3.62 MPa by Haskel pumps which are used to reduce pressure within in the rotor cavity. The results measured are shown in Figure 7. SNL found that the simple Martin Equation predicted the leakage reasonably well for the conditions tested. Some findings of note were that the leakage flow rate is not sensitive to shaft speed and the flow is primarily sensitive to flow area, inlet pressure and density, and very weakly to the rotor cavity pressure.

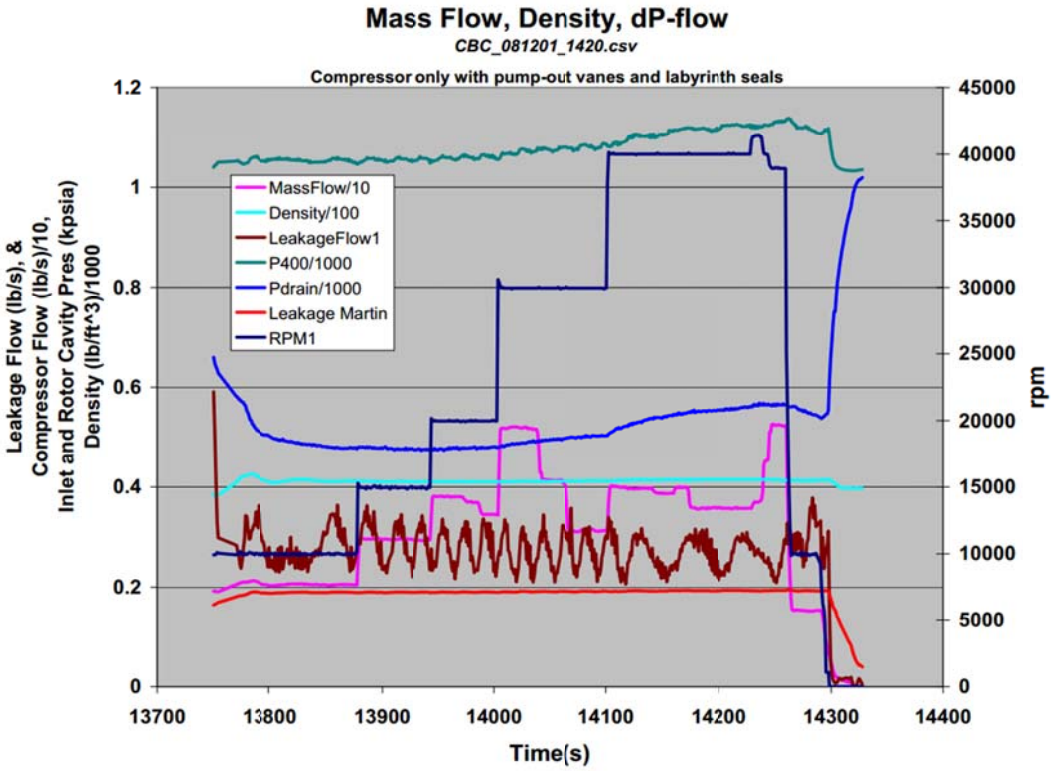

Figure 7. Measured (brown) and predicted (red) leakage flow rate through the SNL four tooth stepped labyrinth seal [2].

2 Data Collection

2.1 Test Facility

The UW-Madison Seal Test Facility is logically depicted in Figure 8. It was used to measure flow rate in seal geometries under S-CO_2 conditions. The facility allows for a wide variety of geometries and inlet conditions to be achieved. All plots and calculations were performed with Engineering Equation Solver (EES) [29].

To energize the system a single-stage, linear actuated compressor manufactured by HydroPac (Model No.: C02.4-40-2050LX/SSCO2) is used [30]. The HydroPac compressor has a maximum discharge pressure of 16.55 MPa (2400 psia) and a minimum suction pressure of 1.38 MPa (200 psia), which allows the facility to achieve a range of orifice inlet pressures that are both above

and below the critical pressure. A photograph of the HydroPac compressor is shown in Figure 9. The compressor has gas cylinders on either side of the oil cylinder so as to allow for compression on each stroke.

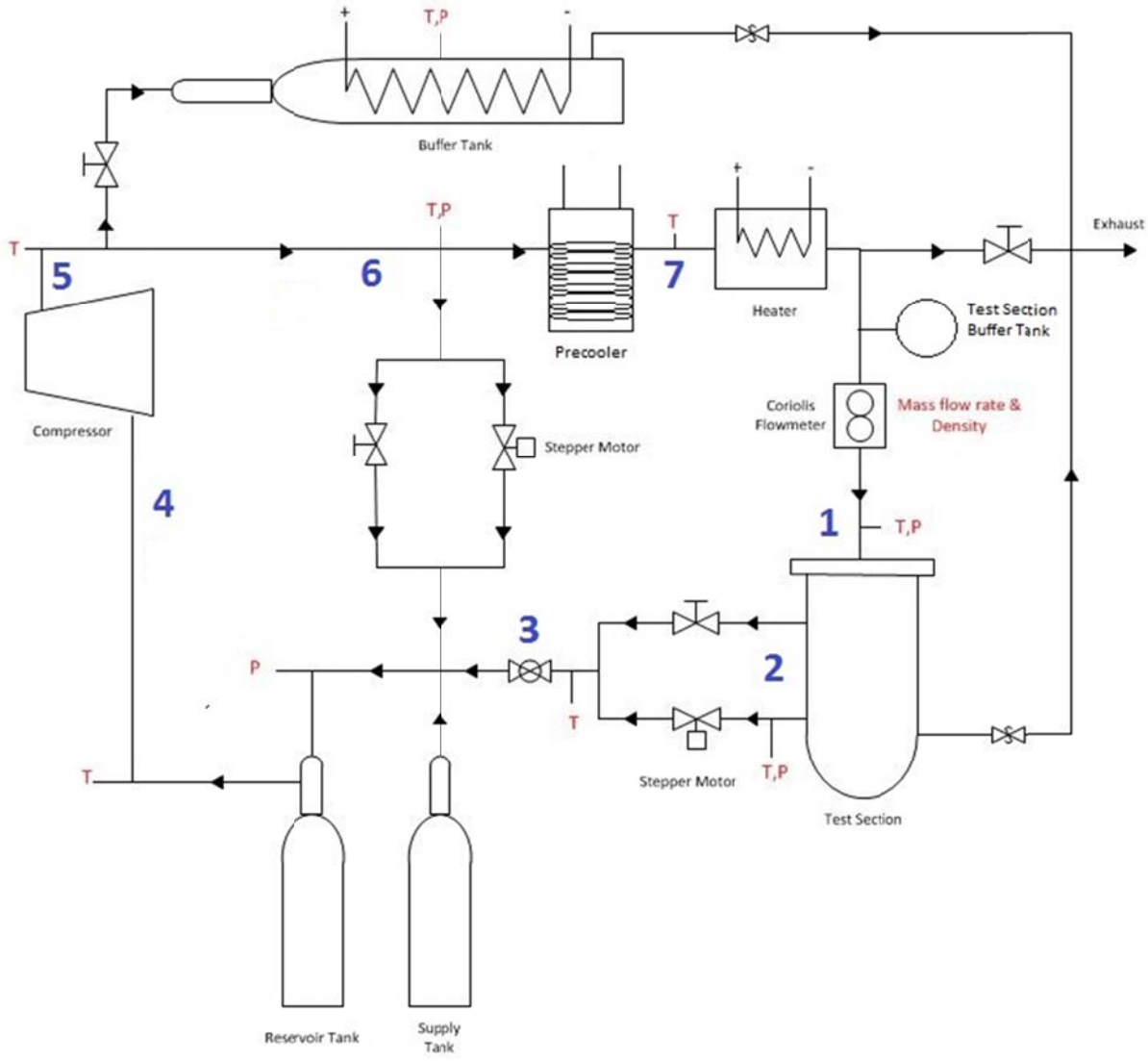

Figure 8. Conceptual layout of the UW-Madison test facility.

The facility is comprised of a test section loop and a bypass loop. Control of the bypass loop is achieved by the adjustment of two valves located, this regulates the flow of fluid through this section and forces more fluid to pass through the test section.

Figure 9. Single Stage HydroPac compressor used in UW-Madison facility.

As there is an amount of time where the compressor is shifting between strokes a pressure fluctuation is observed at the outlet of the compressor. These fluctuations are reduced by including a 0.123 m^3 heated buffer tank at the exit of the compressor to dampen this effect. To further reduce the fluctuations a restriction valve located at the entrance to the test section loop minimizes the fluctuations to 7 kPa. At the compressor inlet a reservoir tank is used to limit pressure fluctuations and help maintain a constant flow into the compressor. The pressure within the pressure vessel downstream of the seal geometry is controlled via two manual valves. By adjusting both the valves at the bypass loop and the valves at the outlet of the test section the upstream and downstream pressures can be manipulated to allow for a wide range of conditions to be tested.

The buffer tank requires heating in order to maintain a discharge pressure above the critical pressure. The buffer tank is wrapped with four HTS Amptek Duo-Tape® heater tapes [31], each capable of providing 1.25 kW. The temperature of the tank is controlled using these heaters with a Proportional Integral Derivative (PID) controller implemented in Labview™. Feedback for the PID controller is provided by three thermocouples welded to the surface of the buffer tank. During normal operation, the fluid in the buffer tank is maintained at a temperature that is between 70°C and 100°C in order to reduce the mass of CO_2 required in the system to reach high pressures (7.7 MPa-16.55MPa) in the supercritical region. The buffer tank is shown here insulated in Figure 10.

Figure 10. Heated and insulated buffer tank used to reduce pressure fluctuations from compressor shifting.

As the temperature of the fluid is greatly increased due to the buffer tank heaters a precooler is required to reduce the temperature of the fluid prior to entering the test section. The precooler is a shell and tube heat exchanger with the CO_2 passing through a helically wound pipe inside of a canister through which water flows. The device is controlled by varying the amount of chilled water that flows through the precooler can, this is done with a ball valve located at the water inlet. The precooler heat exchanger is shown in Figure .

Figure 11. Precooler heat exchanger utilizing chilled water.

The fluid temperature is then raised to the desired temperature by passing through three pipe heat exchangers that are situated in parallel shown in Figure 12. This allows for a greater control of the inlet temperature after the precooler. HTS Amptek Duo-Tape® heater tape with a heating capacity of 1.25 kW is wrapped around the tubing through which the fluid flows and then insulated. The inlet temperature of the test section is controlled with a PID controller implemented in Labview™. The surface temperature of the pipe heat exchangers was used to control the PID's via thermocouples welded to the pipe surface. By manipulating the temperature of these heat exchangers the temperature at the test section inlet can be controlled and fluctuations reduced to 0.1°C.

Figure 12. Preheater consisting of three heated and insulated pipes in parallel controlled via PID in Labview.

To maintain proper operating conditions within the facility temperature and pressure measurements are throughout the system at locations indicated in Figure 8. The test section inlet pressure, inlet density, mass flow rate, and outlet pressure are the primary measurements used to characterize the flow conditions and resulting flow rate through the seal geometry. The key pressure measurements are measured with Siemens Sitrans P pressure transducers located at the inlet and outlet of the test section [31]. These pressure measurements are made where the velocity of the fluid is negligible. The test section mass flow rate and inlet density are measured with an Endress Hauser Cubemass DCI Coriolis mass flow meter [32].

A description of the conditions typically viewed at various points around the loop during a standard experiment can be seen in Figure 13. This Figure shows a temperature-specific entropy diagram with points labeled with respect to Figure 8.

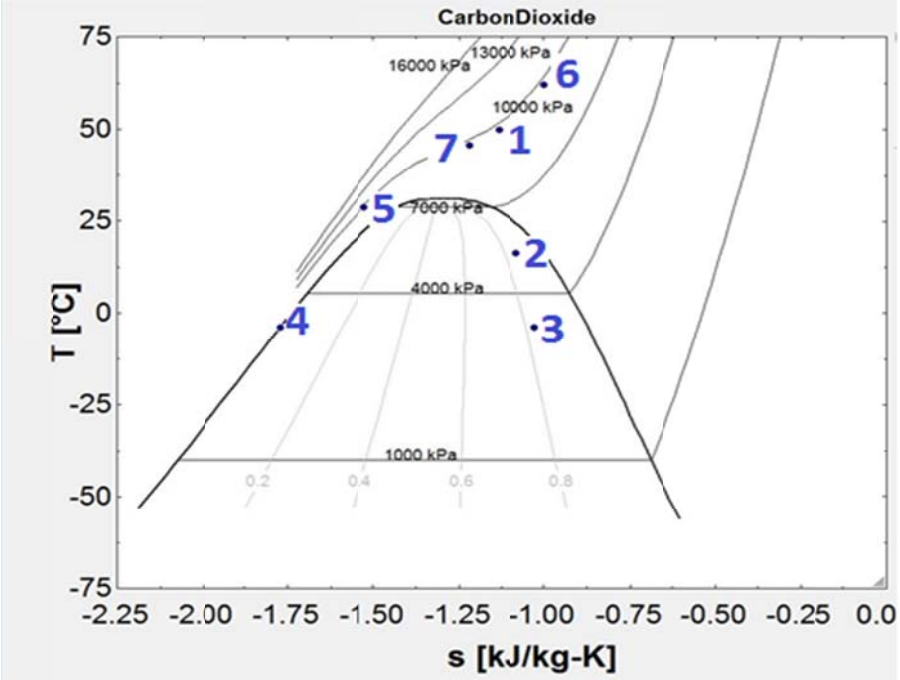

Figure 13. Conditions for various locations on the loop (Figure 8), shown on a temperature-specific entropy diagram during typical experiment conditions.

The inlet conditions to the test section are held constant throughout a test at the desired orifice inlet condition in the supercritical region, represented by point 1 in **Error! Reference source not found.**. There is a reduction in the pressure and temperature as the CO_2 flows through the orifice within the test section from the inlet (point 1) to the outlet (point 2) of the test section. The pressure at point 2 is controlled with the valves at the outlet of the test section. Another reduction in the pressure and temperature occurs from point 2 to point 3 across the valves used to control the test section outlet pressure. Between point 3 and point 4, the CO_2 from the test section loop and the CO_2 from the bypass loop mix causing the CO_2 entering the compressor at point 4 to be in liquid phase under many conditions, as shown in Figure 13. The compressor is

designed to take in single-phase (either liquid or gas) or two-phase CO_2. From point 4 to point 5, the CO_2 is compressed and mixed with high temperature CO_2 from the buffer tank (point 6), which results in an increase in both the pressure and temperature of the CO_2. The pressure and temperature of the CO_2 is reduced as it passes through the restriction valve at the entrance to the test section loop, and the temperature is further reduced in the precooler, resulting in point 7 shown in Figure 13. Finally, the temperature is increased to the desired test section inlet temperature (point 1) in the preheater.

2.1.1 Test Section

The test section can be seen in Figure 14, which shows the inlet at the top and dual outlet ports from the side. The pressure vessel allows for stagnation conditions to occur immediately following the orifice and the upper flange (Figure 15) is where the orifice is secured. Press fit drill bushings are used to provide the correct outer diameter for the orifices and the clamp shown in Figure 14 holds the seals in place. This method allows for variation in seal geometry by changing the length and diameters of the bushings and allows for the stacking of seals. The collet holder sub-assembly (Figure 14b) is used to hold the shaft in place. A BK Precision Collet™ (Model N.:NBC8-3.5AA) is used to hold the miniature shaft sizes. The collet holder sub assembly is attached to the test section allowing the shaft to be placed through the fixed orifice as shown in Figure 14.

This design allows for a wide range of geometries to be tested. The length of seals and cavities may be varied along with the diameter of the shaft. This ability can be seen in Figure 15. Figure 15 shows a cross section of the test section flange with a configuration of seals stacked within in the flow channel.

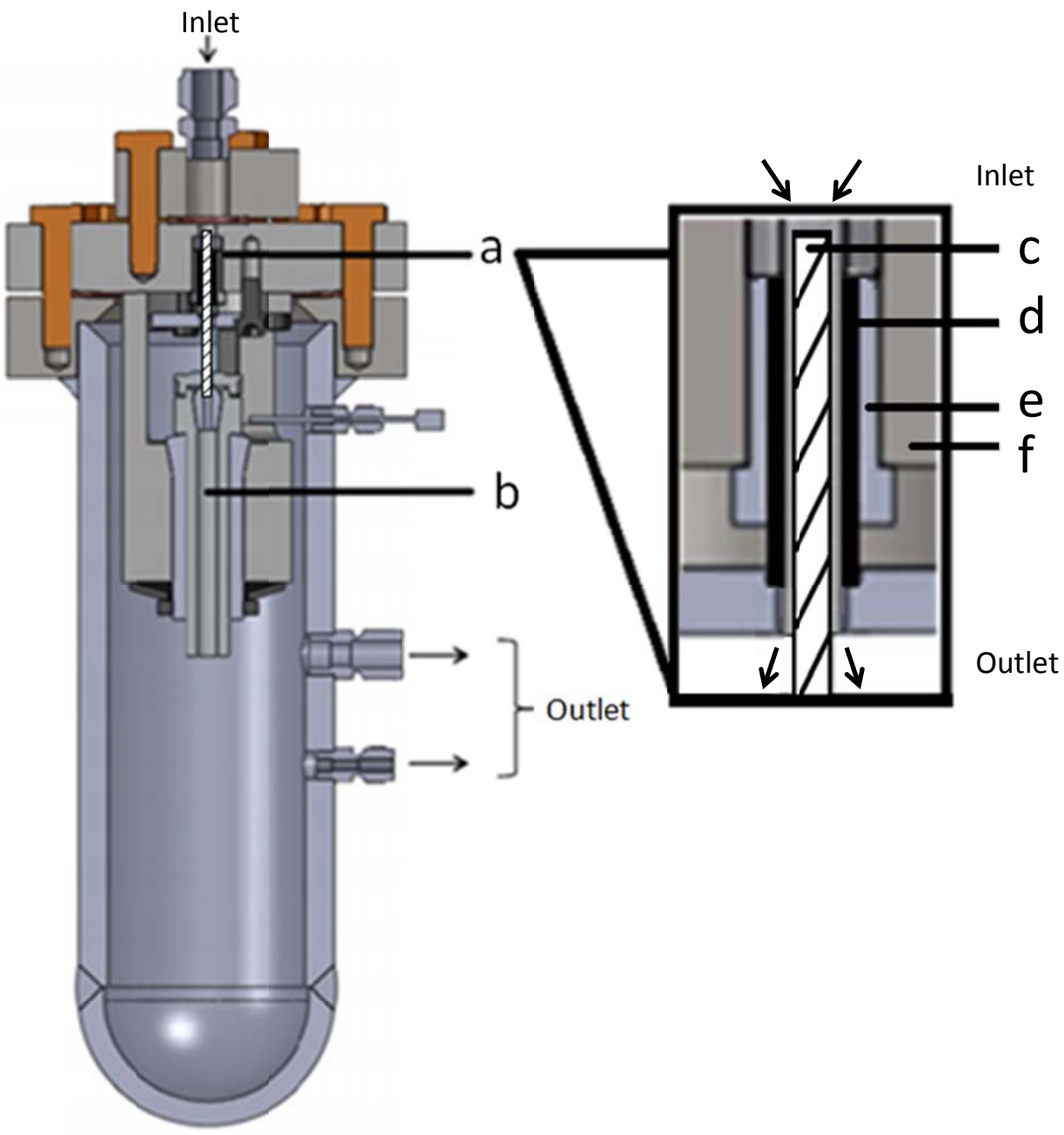

Figure 14. Cross Section of pressure vessel showing a) seal location/configuration, b) collet sub-assembly, c) shaft, d) seal, e) spacer drill bushing, f) test section flange.

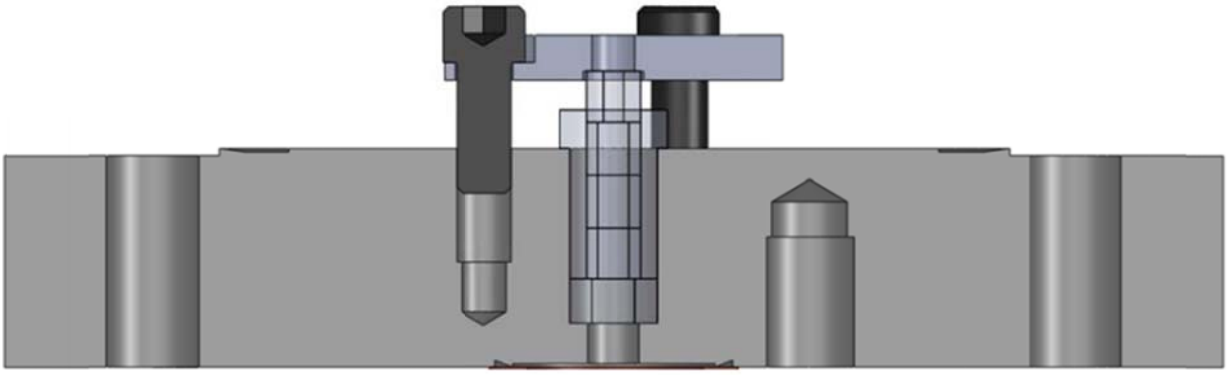

Figure 15. Cross Section of test section flange showing seal configuration.

2.1.2 Seal Geometries

Three types of geometries were tested for this study. Annular geometries were tested to observe the effect of shaft eccentricity and to determine discharge coefficients for a single annular constriction. Straight-tooth labyrinth seals were tested to observe the effects of inlet conditions and tooth number. A stepped-tooth labyrinth seal was also designed to observe more practical geometries and compare test results to the data found with the SNL research facility.

To construct different geometries orifices with different inner diameters were stacked onto each other. These orifices as shown in Figure 16 were machined to tight tolerances to provide an accurate description for modeling purposes. For the annular geometries the seals were had inner diameters of 3.175 mm and lengths of 1.272, 2.341, 27.890, and 45.825 mm. The diameter was measured optically using a microscope with 0.9 micron uncertainty.

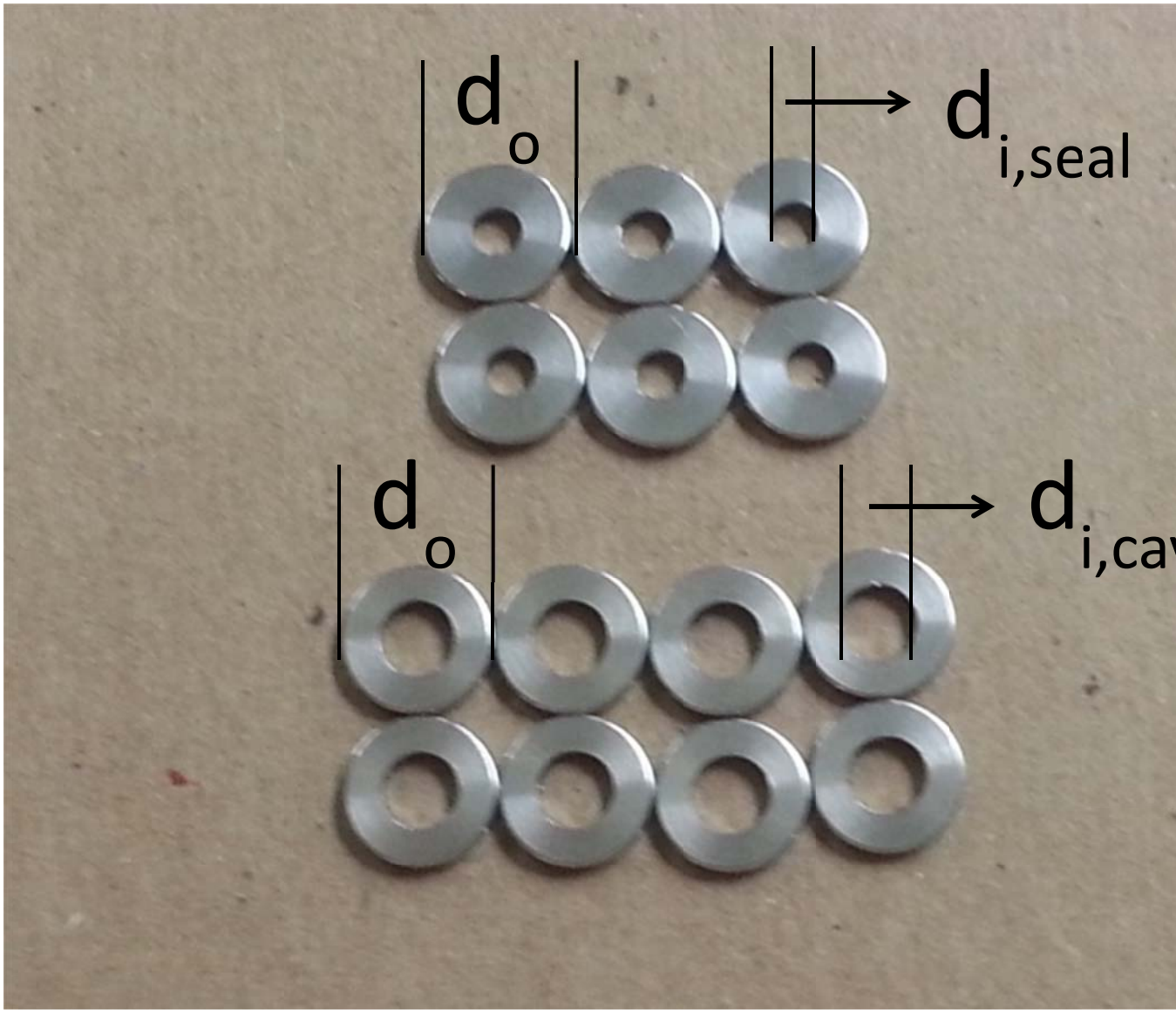

Figure 16. Seals and cavities used in the straight-through labyrinth tests, d_o=9.525 mm, $d_{i,\ seal}$=3.175 mm, $d_{i,\ cavity}$=4.763 mm and length = 1.27 mm.

To determine the inlet and outlet curvatures of the seals and cavities a Zygo NewView™ white light interferometric microscope [34]. Figure 17 shows the results of examining a single seal using the Zygo interferometer. The results clearly indicate that all seals and cavities had a very sharp inlet and exit curvature. This test was repeated after measurements were made with the seals and there was no change seen.

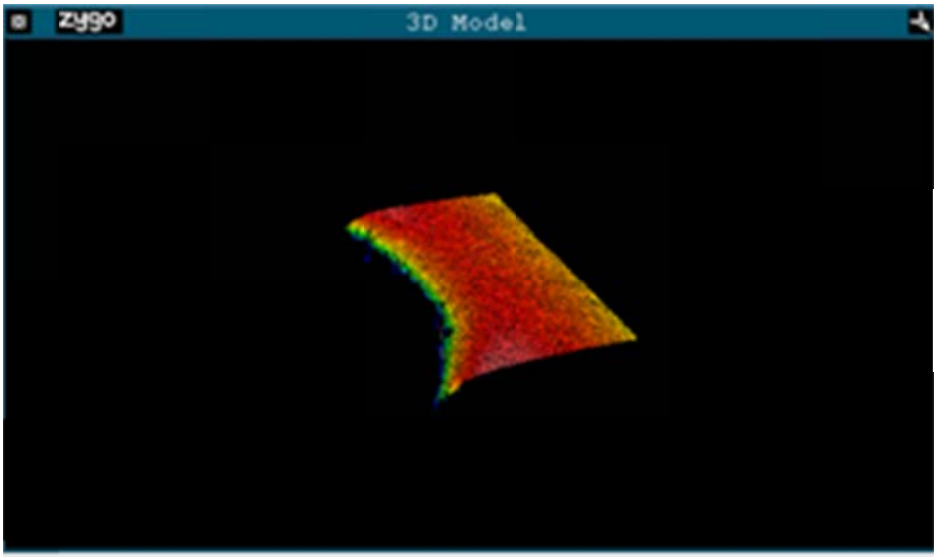

Figure 17. 3-D model of seal curvature taken with Zygo NewView™ white light interferometer.

A stepped labyrinth seal was designed to mimic the shaft seal used within the Sandia National Labs research loop. The dimensions were scaled down to allow for the seal to fit within the flange of test section. This meant reducing the inlet diameter of 13.97 mm to 9.398 mm. A cross section of the seal designed can be seen in Figure 18 along with a physical picture in Figure 19.

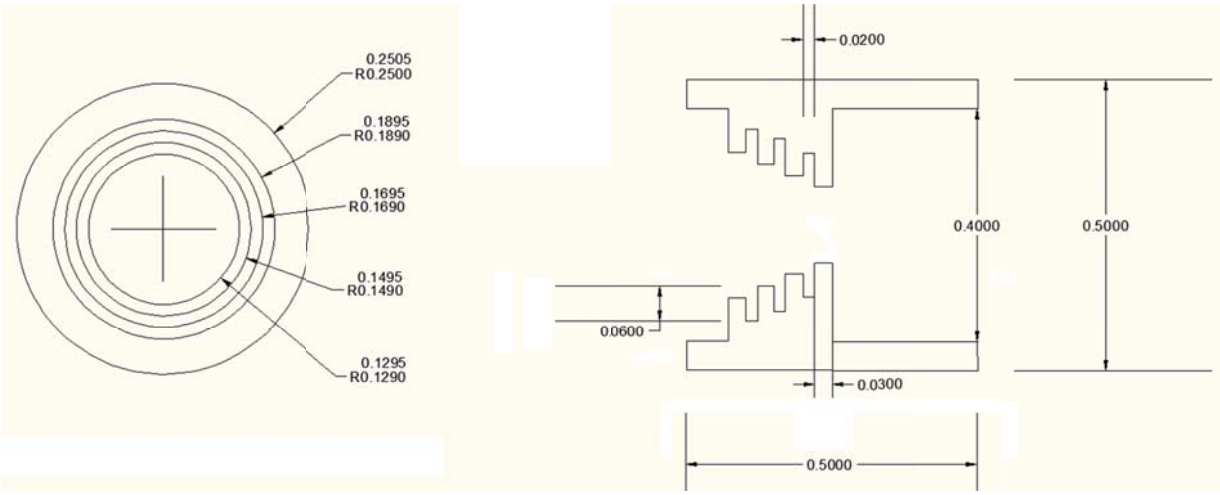

Figure 18. Stepped labyrinth design showing pertinent dimensions.

Figure 19. Stepped labyrinth seal.

The seal was designed to allow for stagnation conditions at the entrance to the seal so a gap prior to the seal is included to provide a large change in flow area as the fluid enters the seal. Two shafts were designed to be inserted into the seal. One shaft provides four lands to activate all teeth within the seal and the second shaft only provides three lands, thus activating only three of the seal teeth. This can be seen in Figure 20 and Figure 21. This will allow for the effect of teeth addition to be observed. The shafts are inserted into the seal from downstream and held in place via the collet sub-assembly detailed in the following sub-chapter.

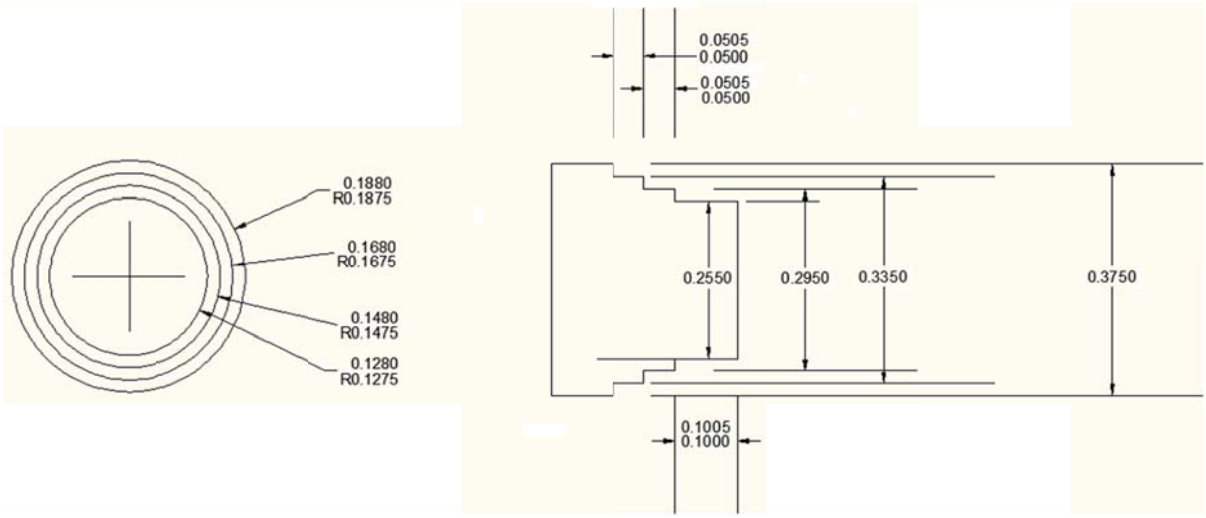

Figure 20. Shaft used to activate all four teeth within the stepped labyrinth design.

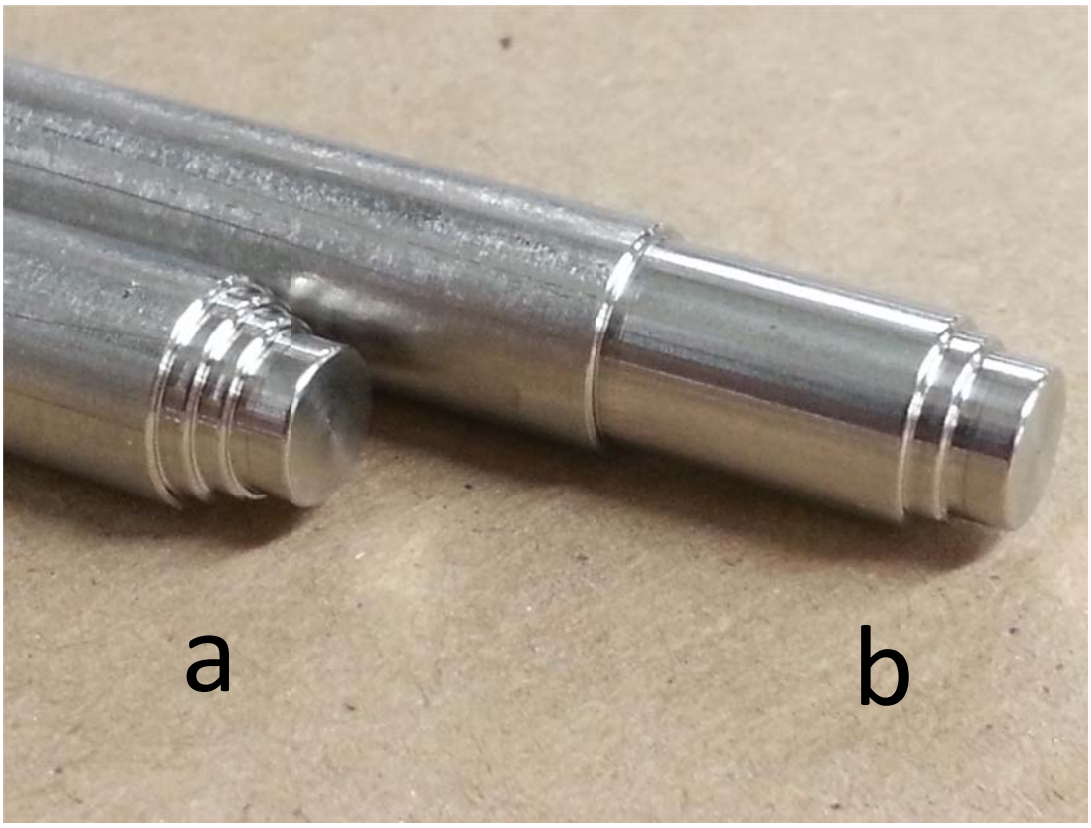

Figure 21. Shafts used in stepped labyrinth geometry, a) 4-land shaft b) 3-land shaft.

2.2 Test Conditions

The objective of this study is to observe the flow of S-CO_2 through various shaft seal geometries over a wide range of conditions. Even though the S-CO_2 Brayton cycle operates well above the two phase region it is of use to study flow through seal geometries and what effect transitioning to two phase exit conditions has on the leakage. For the examination of the shaft eccentricity effect the inlet condition was kept at 10 MPa and 325 kg/m^3. This allowed a better control over conditions at the inlet and exit and it avoided the two phase region but allowed observations to be made of the eccentric effect in the supercritical region. Figure 22 shows the range of inlet conditions performed for the three-tooth labyrinth seal to demonstrate the effects of property variation.

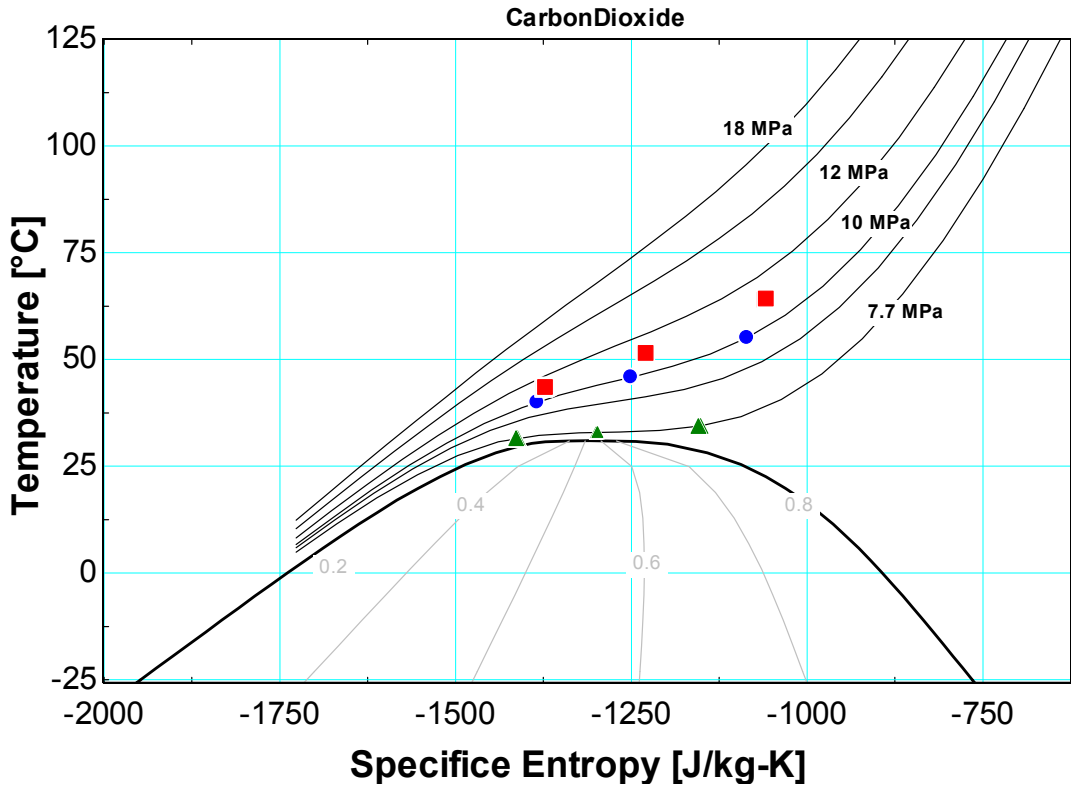

Figure 22. Temperature-specific entropy plot for CO_2 with the test section inlet conditions shown for inlet pressures of 7.7 MPa (green), 10 MPa (blue), and 11 MPa (red) at corresponding inlet densities of 325, 475, and 630 kg/m^3 in three-tooth labyrinth seal tests.

2.3 Data Collection

2.3.1 Assembly Procedure/Eccentricity Measurement

The eccentricity of the assembled test section comprised of the components shown in Figure 23 was measured using optical methods and assembled as follows. The seal to be tested was clamped into the test section flange and a plug gauge of the same diameter was used to align the collet holder sub-assembly onto the flange. The plug gauge was then removed and the shaft was installed through the full length of seal. This was considered to be the minimum eccentricity assembly as it was as close to concentric as possible. In order to obtain the maximum eccentricity assembly, the previous process was repeated but after the shaft was installed the collet holder sub assembly was loosened and the shaft moved until it touched the side of the seal.

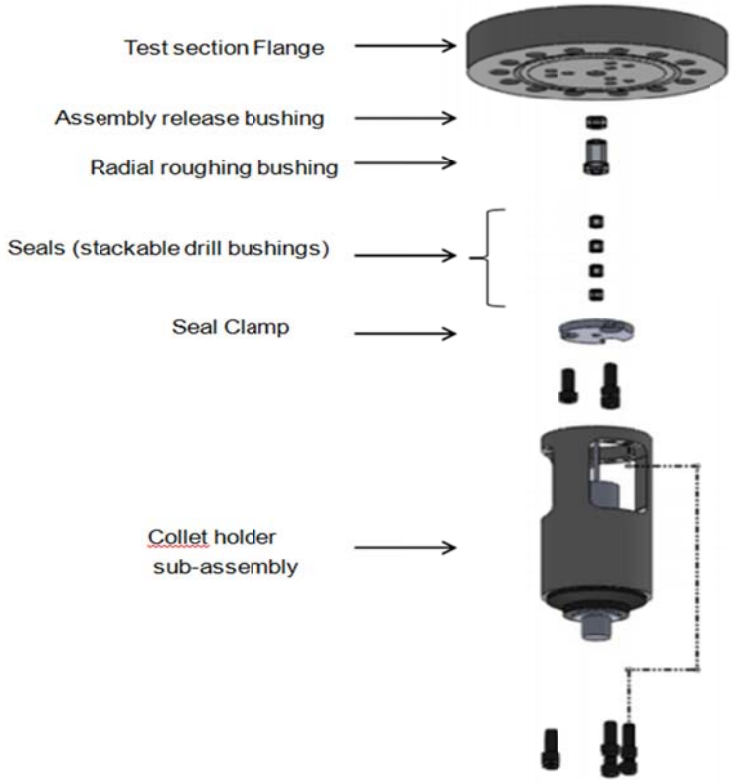

Figure 23. Assembly procedure of shaft-seal sub-assembly.

The eccentricity of these assembled cases is measured using a long focal length microscope and camera. The test section is mounted horizontally onto an optics table in front of a high magnification, long focal length lens attached to a Nikon D7000 digital camera that allows for images of the assembled shaft seal interface to be taken. Since the shaft and seal faces are not aligned, an image cannot be taken with both the seal face and the shaft face in focus simultaneously. To address this, two images were taken. The first image had the seal edge in focus and the second had the shaft face in focus. Both images were taken using back lighting to provide distinct edges for each object. These two images are then processed using a script in MATLAB™ r2012b [34]. This processing determines the outlines of the two shapes (the shaft and seal), overlays them, and measures the distances from their respective centers. This distance is then taken to be the eccentricity of the test.

The image processing converts the measurements to a binary image. The binary images are then processed using the standard MATLAB™ function *regionprops()* which locates contiguous objects within the image and applies an equivalent diameter to the area. This equivalent diameter is defined as the diameter of a circle having the same area as the region. This method was used with all images and was tested by repeatedly taking images of a known diameter shaft and comparing the value calculated from the image with the value measured using a micrometer. These values were consistently within 1% of each other. An example of the resulting image can be seen in Figure 24 which shows final images for both the concentric case and the eccentric case for one of the tests.

The combined uncertainty in the measurement of the eccentricity throughout the assembly procedure is approximately 5%. This uncertainty stems from two major contributions: the

alignment of the camera with the mounted test section flange, and the finite number of pixels in the images that were taken.

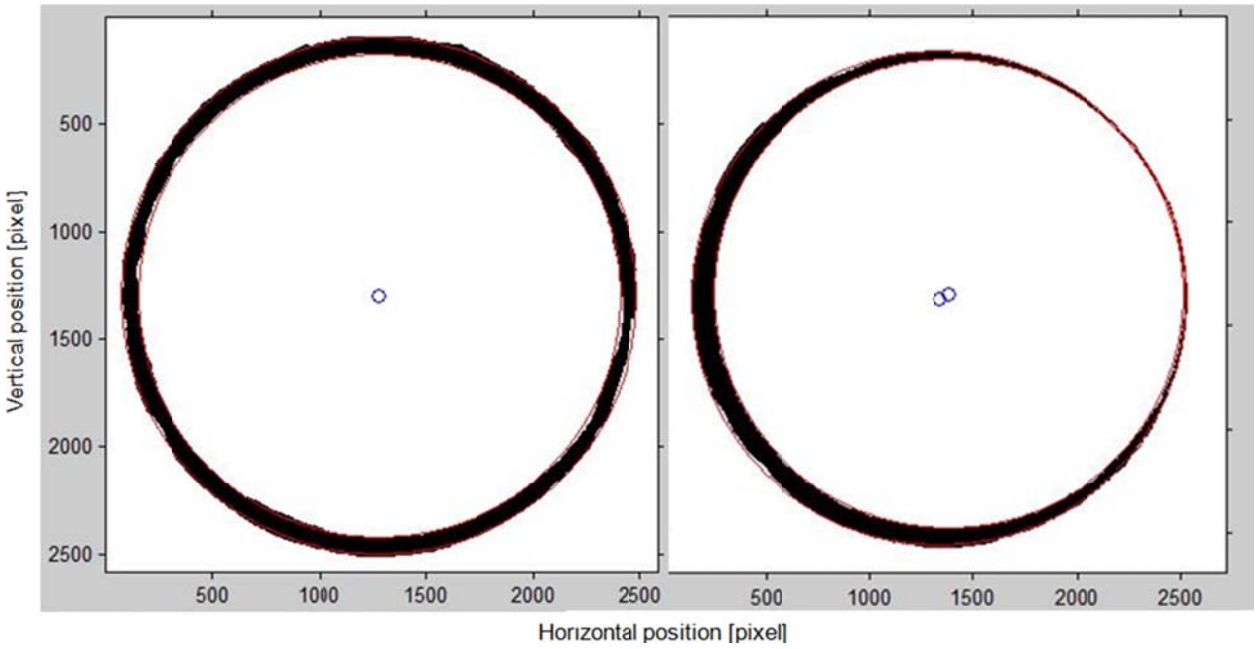

Figure 24. Result of image processing code used to measure eccentricity at shaft-seal interface.

Through this assembly procedure and measurement, a consistent minimum eccentric assembly between 0 and 0.25 could be achieved, as observed by repeated assembly, disassembly, and measurement. All tests labeled concentric have this level of eccentricity. Due to the distance of the seal from the collet tip, the total indicated run-out plays a factor in the eccentricity experienced throughout the seal (i.e., at axial locations other than where the images were obtained). This runout is defined as the difference in position of the shaft center along its axis relative to the center of the collet. For the concentric case it is possible that the shaft eccentricity is different where it enters the seal on the collet side than it is where it exits (the measurement location). The current design prohibits measurement of eccentricity from the collet and therefore in the eccentric case, the collet side may be more concentric than the inlet side of the flange. For the shorter lengths the difference in eccentricities for the entrance to the

exit can be 0.1 and 0.25 for the longer seal lengths. This difference in eccentricities from the entrance to the exit of the annulus slows the flow and reduces the maximum expected flow increase between the concentric and eccentric cases. The expected flow increase as determined in Equation 1 is 25%, but with this difference in eccentricities the expected flow increase between the concentric and eccentric case is reduced to 15%. This is caused by the reduction in eccentricity caused by the run-out of the shaft.

2.3.2 Data Collection Procedure

Figure shows the measured mass flow rate for a typical data set collected for the flow of S-CO_2 through a specific orifice at a given inlet condition. In Figure , the measured mass flow rate is shown as a function of the pressure ratio; pressure ratio is defined as the ratio of the test section outlet pressure to the test section inlet pressure.

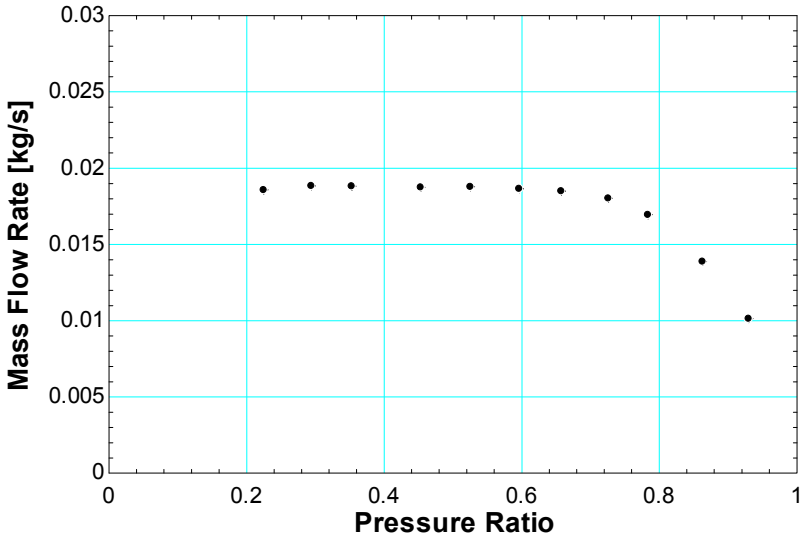

Figure 25. Measured mass flow rate of CO_2 through three tooth labyrinth seal as a function of pressure ratio for an upstream stagnation pressure of 10 MPa and an upstream stagnation density of 475 kg/m^3.

For each data set, the test section inlet condition was held constant and data were collected as the test section outlet pressure was incrementally increased from an initial value that

corresponded to a pressure ratio of approximately 0.3. At each outlet pressure, the experiment was allowed to reach steady state and data were collected for 30 seconds. Steady state was defined as a period of 60 seconds during which the downstream pressure fluctuated by no more than 20.7 kPa (3 psi) and the upstream temperature, based on the thermocouple immersed in the fluid at the test section inlet, fluctuated by no more than 0.1°C. In Figure , each data point represents the average measured mass flow rate for data collected over the 30 seconds at a rate of 1000 Hz while the experiment was at steady state.

3 Computational model

The computational model was developed in the open source software OpenFOAM 2.1.1. OpenFOAM is a C++ based CFD (Computational Fluid Dynamics) toolbox for development of customized numerical solvers based upon the applications of users. The applications developed in OpenFOAM fall under two categories: solvers, that are designed to solve a specific problem in continuum mechanics; and utilities, that are designed to perform tasks that involve data manipulation. The OpenFOAM distribution contains numerical solvers and utilities covering a wide range of applications, details of these can found in chapter 3 of OpenFOAM user manual [36] under standard solvers and standard utilities section.

One of the solvers of interest for this study is rhoSimplecFoam [36] which is a steady-state SIMPLEC based solver designed for laminar and turbulent RANS (Reynolds averaged Navier-Stokes) flows of compressible fluids. This solver solves a set of modified continuity, momentum, and energy equations programmed in C++ and necessary to represent a scenario in hand. The closure to these equations is provided by modeling properties of the fluid being simulated. One of the distinguished features of OpenFOAM is its syntax for tensor operations and partial

differential equations that closely resemble the equations being solved. Equation (32) is represented by the code shown in Figure 26.

$$\frac{\partial \rho U}{\partial t} + \nabla . \varphi U - \nabla . \mu \nabla U = -\nabla p \tag{32}$$

```
solve
(
      fvm::ddt(rho,U)
    + fvm::div(phi,U)
    - fvm::laplacian(mu,U)
      ==
    - fvc::grad(p)
);
```

Figure 26. OpenFOAM syntax for differential equations, picture taken from [36]

A new solver termed as hrhoSimplecFoam has been developed in OpenFOAM which solves the same set of partial differential equations as rhoSimplecFoam but provides closure to the governing equations by using the user defined CO_2 properties instead of standard thermodynamic models used by the original solver.

This chapter provides an in-depth explanation of the solver hRhoSimplecFoam. First, the theoretical governing equations being solved by the application will be discussed. Next, details will be provided about the user defined CO_2 properties modeled into the application, wherein the problem setup is explained as well. Finally, a table is generated showing the seal geometries and the operating conditions used in this study (Appendix B, C, D).

3.1 Governing Equations

The Navier-Stokes (NS) equations are the basic governing equations for a viscous, heat conducting fluid flow problem and consist of equations for the conservation of mass and momentum. The momentum equation is a vector equation obtained by applying Newton's laws of motion to a fluid element. It is supplemented by the mass conservation equation, also called

the continuity equation. For a fluid flow problem involving the transfer of energy such as heat transfer problem the energy equation must be used in addition to the NS equation [37].

The continuity equation (33), momentum equation (34) and energy equation (35) for a compressible fluid can be written as follows

$$\frac{\partial \rho}{\partial t} + \frac{\partial}{\partial x_j}\left[\rho u_j\right] = 0 \tag{33}$$

$$\frac{\partial}{\partial t}\left(\rho u_i\right) + \frac{\partial}{\partial x_j}\left[\rho u_i u_j + p\delta_{ij} - \tau_{ji}\right] = 0, \;\; i = 1,2,3 \tag{34}$$

$$\frac{\partial}{\partial t}(\rho e_o) + \frac{\partial}{\partial x_j}\left[\rho u_j e_o + u_j p + q_j - u_i \tau_{ij}\right] = 0 \tag{35}$$

For a Newtonian fluid, assuming that Stokes law is valid, the viscous stress is given by:

$$\tau_{ij} = 2\mu S_{ij}^* \tag{36}$$

Where the trace-less viscous strain-rate is defined by:

$$S_{ij}^* \equiv \frac{1}{2}\left(\frac{\partial u_i}{\partial x_j} + \frac{\partial u_j}{\partial x_i}\right) - \frac{1}{3}\frac{\partial u_k}{\partial x_k}\,\delta_{ij} \tag{37}$$

The heat-flux, q_j, is given by Fourier's law as:

$$q_j = -\lambda \frac{\partial T}{\partial x_j} \equiv -C_p \frac{\mu}{Pr}\frac{\partial T}{\partial x_j} \tag{38}$$

Where the laminar Prandtl number, *Pr* is defined by:

$$Pr \equiv \frac{C_p \mu}{\lambda} \tag{39}$$

The total energy, e_o, is defined by:

$$e_0 \equiv e + \frac{u_k u_k}{2} \tag{40}$$

Since, flow through seals is highly turbulent, turbulence modeling is important to capture the real scenario. There are numerous ways to model turbulence in a flow ranging from a simple linear eddy viscosity model to large eddy simulation (LES) and direct numerical simulation (DNS). In this study, two equation turbulence models which are one of the most common types of turbulence models are used. By definition, two equation models include two extra transport equations to represent the turbulent properties of the flow. Most often one of the transported variables is the turbulent kinetic energy, *K*. The second transport variable varies depending on what type of two-equation model is being used. Common choices are the turbulent dissipation, ε, or the specific dissipation, ω [37].

The equation for the ensemble averaged velocity is shown in equation 41.

$$u_i = \overline{u_i} + u_i' \tag{41}$$

The over-bar implies that the velocity is averaged, while the prime, ‘, implies the fluctuating component to the velocity. This same format is used for various other properties. A new set of equations can be developed for turbulent flows by modifying equations (33) through (35). The conservation of mass equation (33) remains the same for turbulent flow as well, while the momentum equation becomes:

$$\frac{\partial}{\partial t}(\rho\overline{u_i}) + \frac{\partial}{\partial x_j}\left(\rho\overline{u_i u_j}\right) = -\frac{\partial p}{\partial x_i} + \frac{\partial}{\partial x_j}\left[\mu\left(\frac{\partial \overline{u_i}}{\partial x_j} + \frac{\partial \overline{u_j}}{\partial x_i} - \frac{2}{3}\delta_{ij}\frac{\partial \overline{u_i}}{\partial x_j}\right)\right] + \frac{\partial}{\partial x_j}(-\rho\overline{u_i' u_j'}) \tag{42}$$

These equations are known as the Reynolds averaged Navier-Stokes equations (RANS).

The basis for all two equation models is the Boussinesq eddy viscosity assumption, which postulates that the Reynolds stress tensor, τ_{ij}, is proportional to the mean strain rate tensor, S_{ij}, as shown in equation (43).

$$\tau_{ij} = 2\mu_t S_{ij} - \frac{2}{3}\rho k \delta_{ij} \tag{43}$$

Where, μ_t is a scalar property called the eddy viscosity which is normally computed from the two transport variables. The same equation can be written more explicitly as:

$$-\overline{\rho u_i' u_j'} = \mu_t \left(\frac{\partial U_i}{\partial x_j} + \frac{\partial U_j}{\partial x_i}\right) - \frac{2}{3}\left(\rho k + \mu_t \frac{\partial u_k}{\partial x_k}\right)\delta_{ij} \tag{44}$$

The drawback of two equation models is the Boussinesq assumption which is a significant simplification. There might be some complex flows, like flows that are strongly accelerated, strongly rotating flows where Boussinesq assumption is simply not valid. Throughout this study, the standard *k-ε* turbulence model with enhanced wall treatment was chosen. Transport equations for standard k-epsilon model can be derived as [40],

$$\frac{\partial}{\partial t}(\rho k) + \frac{\partial}{\partial x_i}(\rho k u_i) = \frac{\partial}{\partial x_j}\left[\left(\mu + \frac{\mu_t}{\sigma_k}\right)\frac{\partial k}{\partial x_j}\right] + P_k + P_b - \rho\varepsilon - Y_M + S_k \tag{45}$$

$$\frac{\partial}{\partial t}(\rho \varepsilon) + \frac{\partial}{\partial x_i}(\rho \varepsilon u_i) = \frac{\partial}{\partial x_j}\left[\left(\mu + \frac{\mu_t}{\sigma_\varepsilon}\right)\frac{\partial \varepsilon}{\partial x_j}\right] + \frac{C_{1\varepsilon}\varepsilon}{k}(P_k + C_{3\varepsilon}P_b) - \frac{C_{2\varepsilon}\rho\varepsilon^2}{k} + S_\varepsilon \tag{46}$$

The turbulent viscosity is modeled as,

$$\mu_t = \frac{\rho C_\mu k^2}{\varepsilon} \tag{47}$$

Production of k can be written as,

$$P_k = -\rho\overline{u_i' u_j'}\frac{\partial u_j}{\partial x_i} \tag{48}$$

$$P_k = \mu_t S^2 \tag{49}$$

Where S is the modulus of the mean rate-of-strain tensor, defined as:

$$S \equiv \sqrt{2S_{ij}S_{ij}} \tag{50}$$

The model constants used for these equations are,

$$C_{1\varepsilon} = 1.44, \quad C_{2\varepsilon} = 1.92, \quad C_{3\varepsilon} = -0.33, \quad C_{\mu} = 0.09, \quad \sigma_k = 1.0, \quad \sigma_{\varepsilon} = 1.3$$

For turbulent flows, the velocity distribution near the wall can be divided into three distinct regions: the laminar sub layer, buffer region, and log-law region. Due to the no-slip condition at the wall, turbulent flows are greatly affected by the presence of the laminar sub layer. To accurately capture the aspects of this laminar sub-layer an enhanced wall treatment provided by OpenFOAM is used. More details of the near wall treatment can be found in the OpenFOAM user guide [36]. The non-dimensional parameter y^+ needs to be employed for use of the wall treatment. The parameter is defined as:

$$y^+ = \frac{u^* y}{\nu_w} \tag{51}$$

Where y is the distance from the wall, and ν_w is kinematic viscosity at the wall. The friction velocity, u^* is defined by:

$$u^* = \sqrt{\frac{\tau_w}{\rho}} \tag{52}$$

It has been suggested by many CFD experts in the past that value of y^+ should be less than 5 in order to use the enhanced wall function. Using a certain y^+ the distance of first node from the wall can be estimated approximately and a mesh can be generated accordingly.

All the governing equations derived earlier are in general valid for any Newtonian fluid. To provide closure for a particular fluid, an equation of state (EOS) to model properties of the fluid has to be specified. Most commercial packages like FLUENT provides a direct link to the National

Institute of Standards and Technology (NIST) thermodynamic and transport properties. OpenFOAM uses the ideal fluid equations to model the properties of CO_2 which are invalid in the supercritical region or in the two phase dome. In order to accurately model the properties of CO_2 in OpenFOAM a FIT (Fluid property Interpolation Tables) algorithm was implemented which utilizes a modified version of biquintic spline interpolation method [39].

Span and Wagner, (1994) [38] developed a new equation of state for CO_2 which is expressed in the form of the Helmholtz energy, *A*, with the two independent variables density, *ρ*, and temperature, *T*. They expressed the dimensionless Helmholtz energy $\varphi = A/(RT)$ in two parts: the ideal-gas part and the residual real fluid behavior which is expressed as in equation (53).

$$\varphi(\delta,\tau) = \varphi^o(\delta,\tau) + \varphi^r(\delta,\tau) \tag{53}$$

Where $\delta = \frac{\rho}{\rho_c}$ is the reduced density and $\tau = \frac{T_c}{T}$ is the inverse reduced temperature. Both the density and the temperature were reduced with their critical values. All the thermodynamic properties of a pure substance can be obtained by combining the derivatives of Equation (53). The Helmholtz energy of the ideal gas is given by equation (54).

$$A^o(\rho,T) = h^o(T) - RT - Ts^0(\rho,T). \tag{54}$$

Ideal gas enthalpy, h^0, and the entropy, s^0, can be derived from an equation for the ideal-gas heat capacity, $C_p^{\,0}$. The final form of ideal gas Helmholtz energy equation can be written as in equation (55).

$$A^o = \int_{T_o}^{T} C_p^o dT + h_0^o - RT - T\int_{T_o}^{T} \frac{(C_p^o - R)}{T}\, dT - RT\left[ln\left(\frac{\rho}{\rho_o}\right)\right] - TS_0^o \tag{55}$$

Where, subscript indicates the properties at reference state. The final equation for ideal gas part is,

$$\varphi^o = \frac{A^o}{RT} \tag{56}$$

$$\varphi^o(\delta,\tau) = ln(\delta) + a_1^o + a_2^o\tau + a_3^o\, ln(\tau) + \sum_{i=4}^{8} a_i^o\, ln[1 - exp(-\tau\theta_i^o)] \tag{57}$$

Since, there is no theoretical approach to accurately model the residual part of the Helmholtz energy which is valid in the whole fluid region of a pure substance Span and Wagner modeled the residual part in an empirical way by optimizing its functional form and fitting its coefficients to a large database of experimental results. The actual empirical form of the residual part is quite complicated and the bank of terms which were used in the optimization of the final EOS contained a total of 860 terms. More details about the coefficients in equation (57) and the residual part can be found in [38].

From the Helmholtz energy other properties can be calculated based on following thermodynamic relationships in reduced form

$$\frac{P(\delta,\tau)}{\rho RT} = 1 + \delta\varphi_\delta^r \tag{58}$$

$$\frac{s(\delta,\tau)}{R} = \tau(\varphi_\tau^o + \varphi_\tau^r) - \varphi^o - \varphi^r \tag{59}$$

$$\frac{u(\delta,\tau)}{RT} = \tau(\varphi_\tau^o + \varphi_r^r) \tag{60}$$

$$\frac{C_v(\delta,\tau)}{R} = -\tau^2(\varphi_{rr}^o + \varphi_{rr}^r) \tag{61}$$

$$\frac{h(\delta,\tau)}{RT} = 1 + \tau(\varphi_\tau^o + \varphi_r^r) + \delta\varphi_\delta^r \tag{62}$$

$$\frac{C_p(\delta,\tau)}{R} = -\tau^2(\varphi_{rr}^o + \varphi_{rr}^r) + \frac{\left(1+\delta\varphi_\delta^r - \delta\tau\varphi_{\delta\tau}^r\right)^2}{1+2\delta\varphi_\delta^r + \delta^2\varphi_{\delta\delta}^r} \tag{63}$$

Where, $\varphi_\delta = \left[\frac{\partial\varphi}{\partial\delta}\right]_\tau$, $\delta_{\delta\delta} = \left[\frac{\partial^2\varphi}{\partial\delta^2}\right]_\tau$, $\varphi_\tau = \left[\frac{\partial\varphi}{\partial\tau}\right]_\delta$, $\varphi_{\tau\tau} = \left[\frac{\partial^2\varphi}{\partial\tau^2}\right]_\delta$, $\varphi_{\delta\tau} = \left[\frac{\partial^2\varphi}{\partial\delta\,\partial\tau}\right]$.

FIT libraries are based on a piecewise biquintic interpolation of Helmholtz free energy. From Helmholtz free energy and all its derivatives as described in equations (58 through 63), all the other thermodynamic properties are calculated. If the Helmholtz free energy and its derivatives are known at the control points then the interpolated surface can be written as,

$$A(\rho, T) = \sum_{i=0}^{5} \sum_{j=0}^{5} a_{ij} \rho^i T^j \tag{64}$$

This representation will result in 36 unknown coefficients and these coefficients can be calculated from a set of equations obtained at the control points. The transport properties like k, α, μ etc. are interpolated independently. The results of the FIT algorithm for CO_2 were compared to REFPROP (Software for fluid properties developed by NIST) and agreed well with a typical error on the order of ~0.01%.

To solve the mass, momentum, and energy equations, the pressure based solver was used along with the SIMPLEC (Semi-Implicit Method for Pressure Linked Equations Corrected) algorithm for pressure-velocity coupling. A second order Gauss upwind scheme was used to solve the governing equations for the simulations performed on annular orifices and labyrinth seals. For simulations performed on plain orifices a first/second order accurate Gauss van leer scheme was used for better accuracy. More details about these schemes can be found out in a CFD book or the OpenFOAM user guide [36]. The boundary conditions selected for this study were a constant pressure at the inlet and outlet of the seal. A constant enthalpy/temperature boundary condition is used at the inlet.

When the flow expands into the saturation dome, the properties of CO_2 depend on quality and both the phases will be out of equilibrium to some extent traveling at different velocities with different temperatures. In this case the problem becomes complicated and in

order to capture the two phase flow field accurately, a separate set of equations have to be developed for both the phases taking into account the properties of each phase. However, for this thesis these complications are eliminated by assuming that there is no slip between phases and that both the phases are in thermal equilibrium. These are the basic assumptions of the "Homogeneous equilibrium model" explained in literature review section. Based on previous work using steam, authors in the past reported that they obtained good results using HEM except for very low quality steam. So, then the question is: "How valid is the HEM for CO_2?"

To answer this question, let us look at Figures (27 and 28). The density ratio of liquid to gas is much smaller for CO_2 compared to that of water in the pressure range of interest. This would imply that slip between liquid and gas is much smaller for CO_2 and relative velocity between phases is not as important as that of water. Hence, it is reasonable to assume that both the phases are travelling at same velocities.

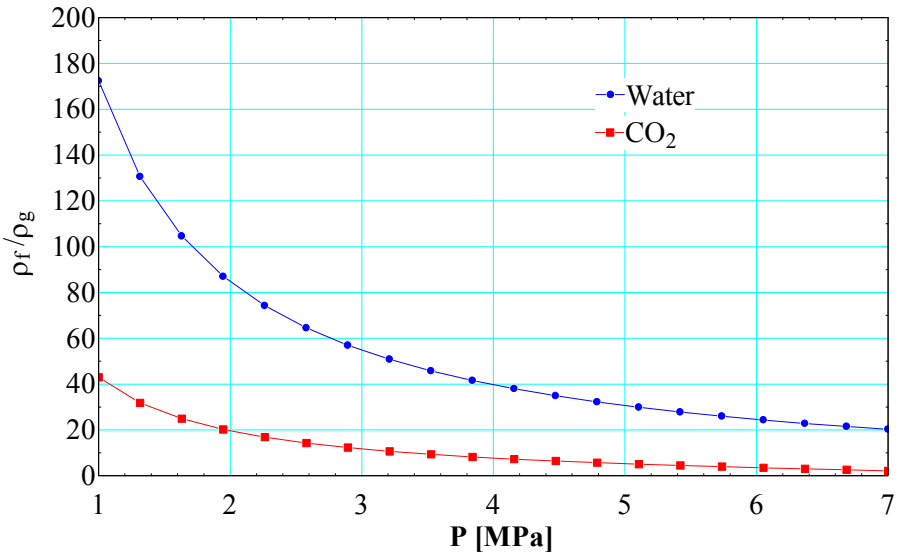

Figure 27. Density ratios for two phase CO_2 and water

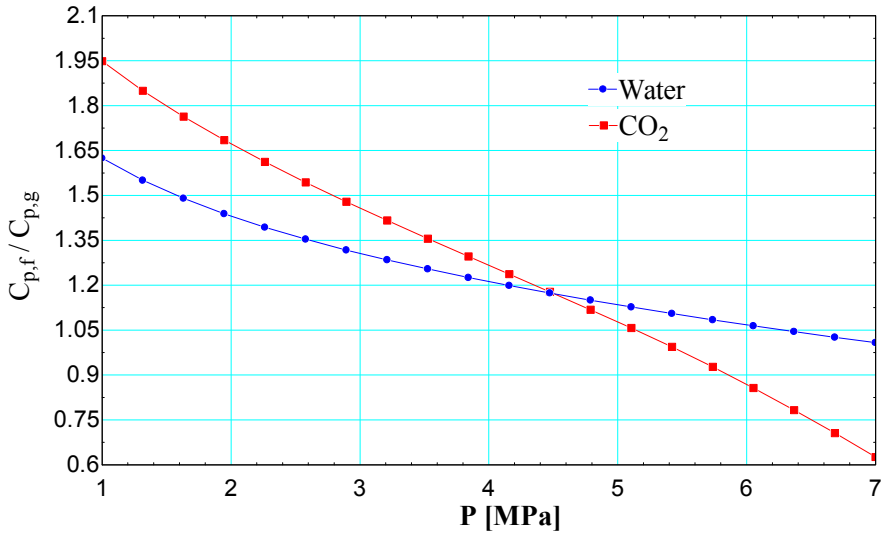

Figure 28. Specific heat ratios for two phase CO_2 and water

Similarly, the ratio of the gas specific heat to the liquid specific heat for CO_2 is comparable to that of water. These two plots indicate that if the HEM works reasonably well for water, it should work much better for CO_2. This is in fact true and will be shown in chapter 5 where some numerical results are compared to the experimental data for plain orifices.

4 Experimental Results

4.1 Shaft Eccentricity

To qualitatively understand the behavior of the entrance length effect and to provide a basic physical model the annular geometry was approximated using two simple duct flow models. The concentric case was modeled using a single rectangular duct with height that is equal to the concentric radial clearance of the tested annular geometry. The eccentric case was modeled by separating the flow area into two regions, one narrow and the other wide, as illustrated in Figure 29. The wide region has a height that provides the same hydraulic diameter of the upper 180^o segment centered at the maximum clearance point shown in Figure 29b. The narrow region has a height that provides the same hydraulic diameter of the lower 180^o segment in

Figure 29b. The model thus consists of two ducts, each with half the width of the concentric case but with heights larger than and smaller than that of the concentric case. The total flow area for the concentric case and the eccentric case is identical. These models were performed using the Engineering Equation Solver (EES) [29].

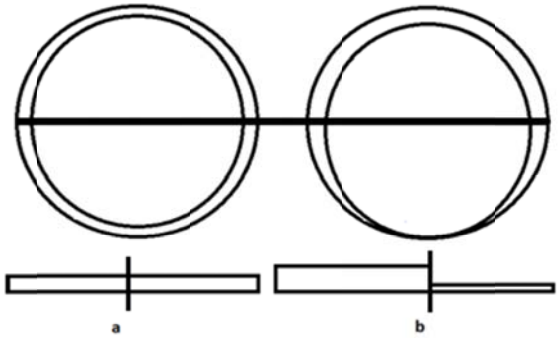

Figure 29. Duct flow approximation flow area determination. Dividing lines show division where radial clearance was taken, a) concentric case b) eccentric case

The ducts are connected in parallel. The pressure drop is the same for both ducts. The flow rates for the eccentric case were calculated and totaled. The Zidrang and Sylvester friction factor correlation in Equation (65) was used to calculate the flow rates [9].

$$f_{fd,h} = \left\{-2.0 \cdot log_{10}\left[\frac{2e}{7.54D_H} - \frac{5.02}{Re_{D_H}}\left(\frac{2e}{7.54 \cdot D_H} + \frac{13}{Re_{D_H}}\right)\right]\right\} \tag{65}$$

The increase in flow associated with the concentric case compared to the eccentric case was computed for varying values of the length to hydraulic diameter, as shown in Figure 30. The results agree with expectations in that there is a reduced impact of eccentricity at shorter lengths where the entrance effect is larger.

Figure 31 shows the mass flow rate data for each of the four lengths that were tested for an inlet pressure of 10 MPa and an inlet density of 325 kg/m^3. In each of the plots both the

concentric and eccentric mass flow rates are shown. Table I shows the average percent increase over the pressure ratios measured between the concentric and eccentric case observed for each length. The measurements show a small increase in flow between the eccentric and concentric case for the short length annular orifice. As the length of the orifice is increased past the experimentally determined turbulent fully developed length, described by Jonsson [13] as being approximately 120 hydraulic diameters, a greater effect of 5% increase is seen between the two cases. For the longest case that was tested, the eccentric case is observed to have an 8.5% higher flow than the concentric case.

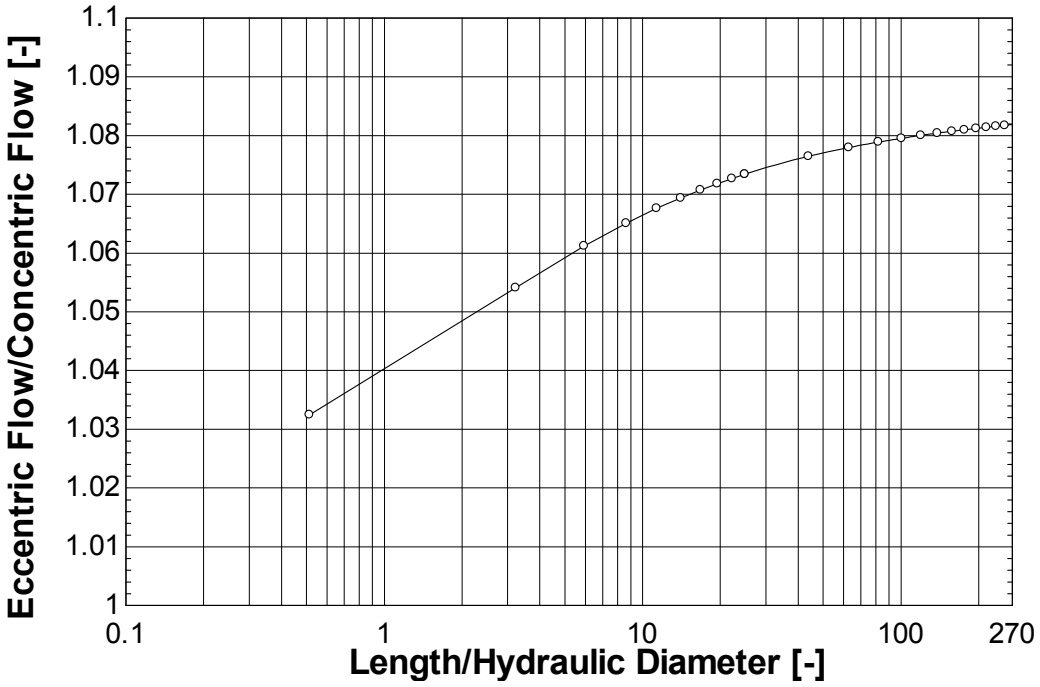

Figure 30. Duct flow approximation results for D_H=0.1956 mm.

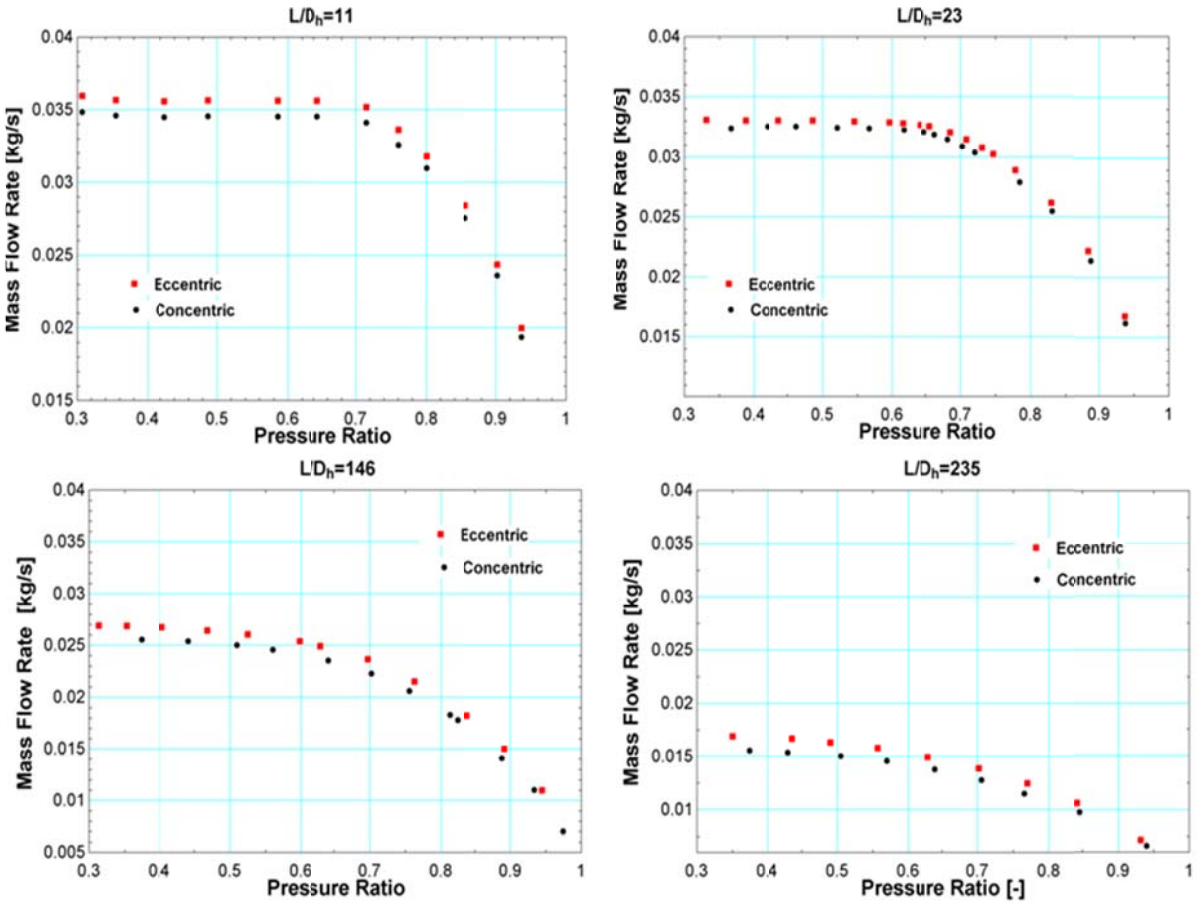

Figure 31. Experimental mass flow rate for annuli of varying L/D_h with a D_H=0.195 mm and inlet conditions of P_{in} = 10 MPa and ρ_{in}=325 kg/m^3.

These data show that for SCO_2 at short lengths, where the entrance effect is significant, the increase in flow due to eccentricity may not be significant. The maximum expected fully developed increase in flow from eccentricity in the turbulent region as predicted by Piercy's model is 25%, this expected value was reduced to 15% due to the effective eccentricity present in the assembly of the test section. As the increase at the longest length tested (235 L/D_H) was 8.5%, this shows that fully developed flow was achieved within the annulus and that there is a clear dependence on length for the increase in flow due to eccentricity. As the lengths used in shaft seal design are much shorter than fully developed lengths a minimal effect from eccentricity may be seen. This has the result of possibly reducing the capital cost from the tolerance on eccentricity in the design of shaft seals for use with S-CO_2.

L/D_H	Eccentric Flow Increase [%]	Re [-]
6	3	370,000
12	3	360,000
143	5	240,000
235	8.5	211,0000

Table I. Experimental flow increase due to eccentricity for D_H=0.195 mm and inlet conditions of Pin =10 MPa and ρ_{in}= 325 kg/m^3

4.1 Straight through Labyrinth Seals

4.1.1 Property Variation and HEM Model

Flow in a straight-through labyrinth geometry was measured at varying inlet conditions. These conditions mimic the wide range of possible conditions within the S-CO_2 Brayton cycle along with spanning the sharp property changes that occur near the critical point. The temperature-entropy diagram in Figure 32 shows the inlet conditions (solid markers) along with each outlet condition (hollow markers), assuming isentropic expansion, that comprise a data set. Data was taken for inlet pressures of 7.7, 10, and 11 MPa at corresponding inlet densities of 325, 475, and 630 kg/m^3 for a three-tooth labyrinth seal.

The objective of these tests is to attempt to characterize the leakage for a seal given an inlet pressure, outlet pressure, and inlet density. This was done by observing the predictions made by the HEM model using an annular area. The results are shown in Figure 33. The discharge coefficient can be used as a description of how well the HEM model predicts the form of the measured flow rate. If the HEM predicts the choking point at the given condition the discharge coefficient will remain constant at all pressure ratios. This result is not predicted but would allow an empirically determined constant discharge coefficient to be applied to an HEM model

and accurately predict the flow rate through a labyrinth seal at any pressure ratio for a given inlet condition. If the model does not predict the behavior well the discharge coefficient will vary with the pressure ratio. A change in pressure ratio would then require a different value of discharge coefficient to be applied to the HEM flow rate.

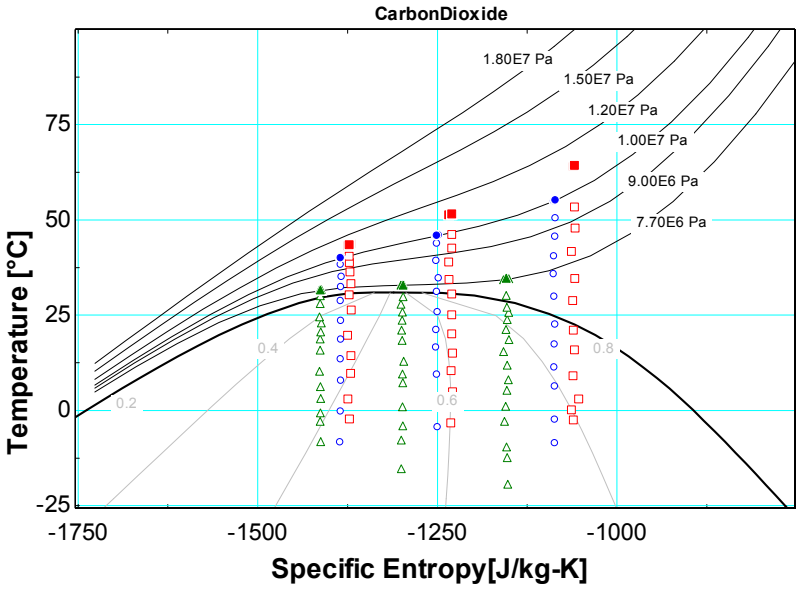

Figure 32. Temperature-specific entropy diagram for a 3 tooth straight-through labyrinth showing inlet conditions (filled markers) and outlet conditions (hollow markers) assuming isentropic expansion.

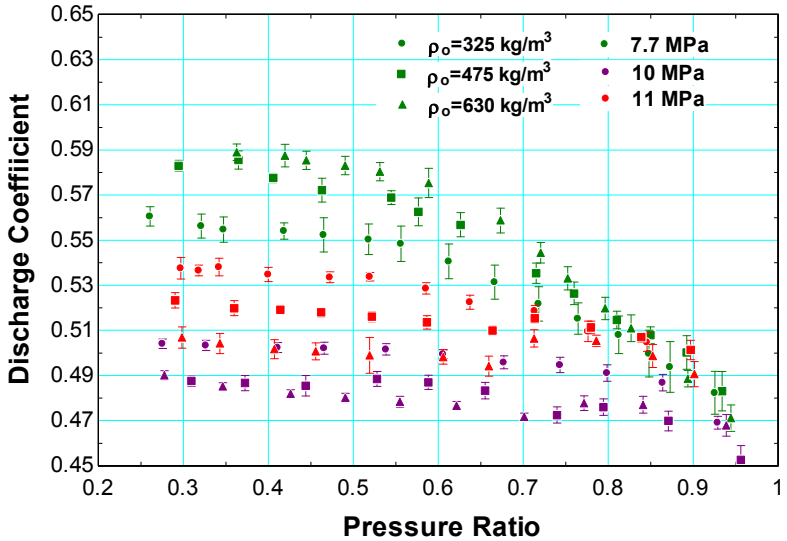

Figure 33. Discharge coefficient results for three-tooth straight through labyrinth seal at varying inlet conditions.

For the inlet pressures of 10 and 11 MPa the discharge coefficient in Figure 33 can be seen to only vary slightly with a change in pressure ratio. This means that the model accurately predicts the choking point for those conditions. This is because for these two conditions the flow chokes before entering the two phase region. As can be seen from Figure 33, the 7.7 MPa case varies considerably more than the higher pressure cases. This is because the model chokes before the measured flow rate and causes the discharge coefficient to increase until the measured flow rate chokes. If the model choked after the measured flow rate the inverse of this would be true and the discharge coefficient would decrease until the measured flow rate choked.

The reason this difference is more prevalent in the 7.7 MPa case is that it chokes well into the two-phase region as can be seen in Figure 34. This is shown at the pressure ratio where the mass flow rate ceases to increase with a decrease in pressure ratio. This occurs because the fluid has reached the sound speed and changes in pressure drop cease to affect the flow rate through the seal. The number of assumptions that the HEM model makes begins to become apparent as two-phase conditions become more dominant. This could be remedied by employing a more sophisticated model that makes fewer assumptions about the flow within the seal.

The value of the experimentally determined discharge coefficient can be seen in Figure 34. Averaging the discharge coefficients and applying it to the HEM model with a value of 0.51 results in a prediction of the measured flow rate for the 10 and 11 MPa cases with less than 5% error. For the 7.7 MPa case, which is less well predicted by the HEM, applying the same constant discharge coefficient of 0.51 predictions are made with less than 13% error. This allows for the leakage of a seal to be easily calculated using a simple model based on inlet conditions and a predetermined discharge coefficient.

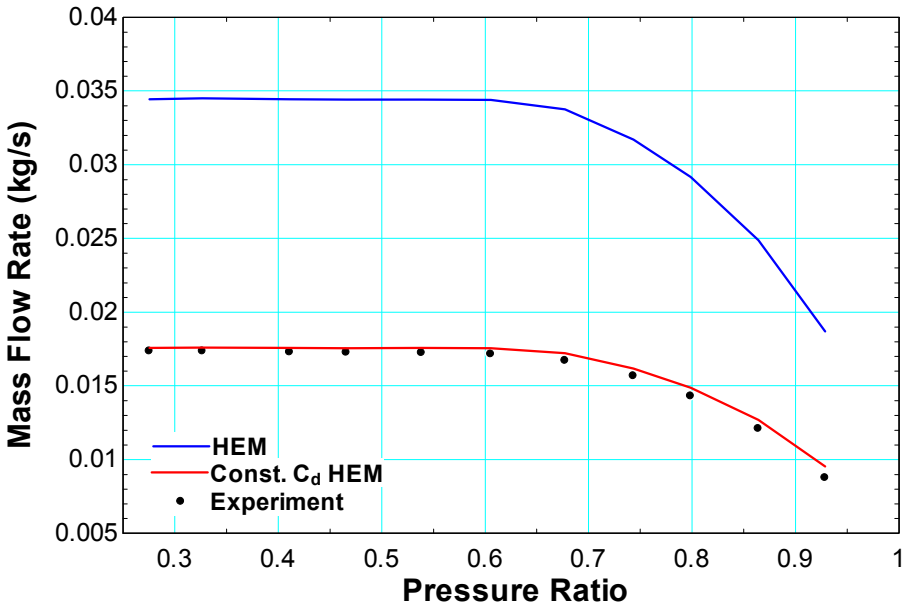

Figure 34. Measured flow rate for three-tooth straight through labyrinth for inlet conditions P=10 MPa and ρ=325 kg/m^3. The blue line shows calculated flow rate using isentropic HEM model and the red line shows the calculated flow rate applying a constant discharge coefficient to the isentropic HEM model.

4.1.2 Tooth Number Optimization

In many shaft seal engineering designs there is a limited amount of space available to include a shaft seal. This means that a seal needs to be optimized for a given total length to provide the least leakage. Yuan [20] performed a Computational Fluid Dynamics (CFD) investigation of the mass flow rate through a labyrinth seal increasing the number of teeth for the same total length. What is expected is that as the number of constrictions increases the decreasing distance between constrictions eliminates the benefit of the expansion into the cavity. There is less kinetic energy transferred to pressure and heat energy in the expansion and more communicated to the downstream cavity. This reduces the effectiveness of the seal. As the distance between constrictions decreases the flow eventually mimics that of a long annular orifice. This prediction can be seen in Figures 35 and 36.

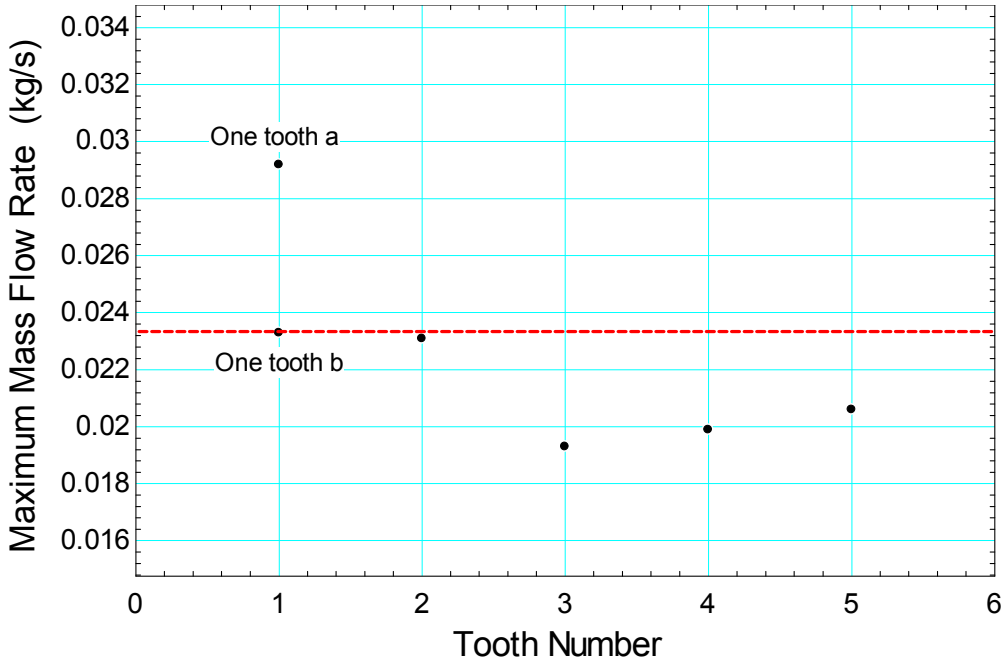

Figure 35. Variation in tooth number for the same total length. One Tooth a: short length, depicts maximum flow rate. One Tooth b: Tooth occupies entire length and depicts the flow rate approached as tooth number is further increased [7].

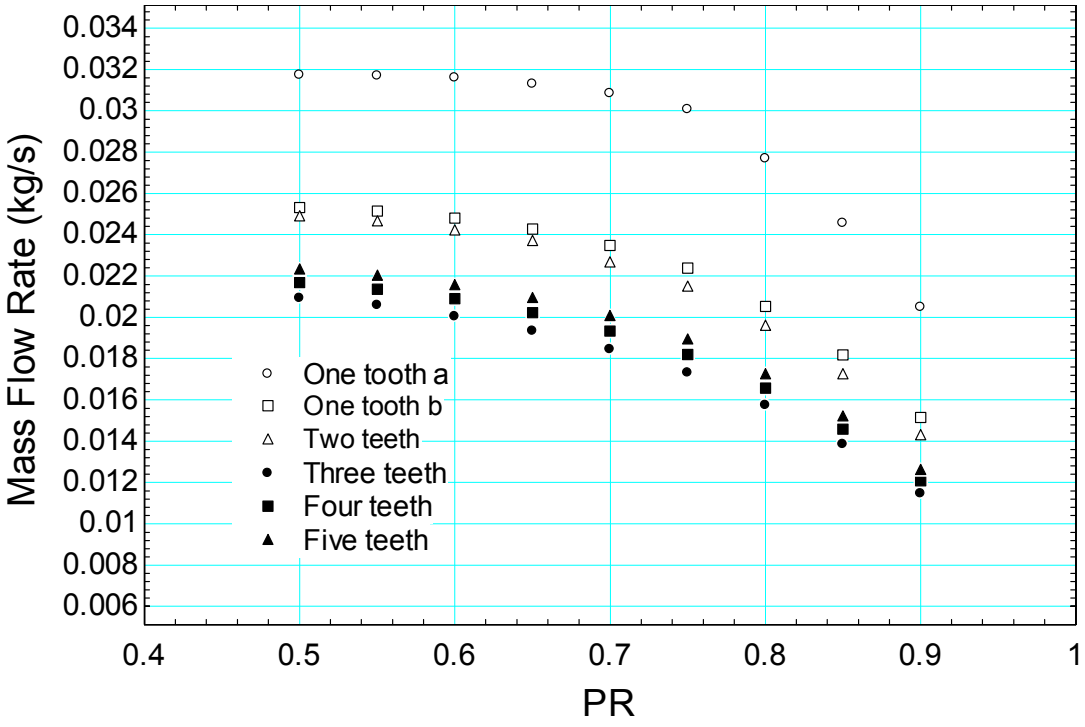

Figure 36. Variation in tooth number for the same total length. Variation in pressure ratio shows an optimal tooth number of three [7].

To examine this, measurements were made for straight-through labyrinth seals with tooth numbers of 2, 3, and 5. A cavity diameter of 4.783 mm and seal diameter of 3.175 mm were used with lengths of 1.782 mm to achieve a total length of 11.43 mm, with a shaft diameter of 3.000 mm. An inlet condition of 10 MPa and 325 kg/m^3 was used to provide a single phase test condition that was easily controlled. The measured flow rates are shown in Figure 37 and clearly show the expected result. Figure 38 shows that there is a clear optimization given a limited space to design a straight-through labyrinth seal and the model accurately predicts this. The increase in tooth number past this optimal reduces the effectiveness of the seal by reducing the amount of kinetic energy dispersed during the expansion into the cavity.

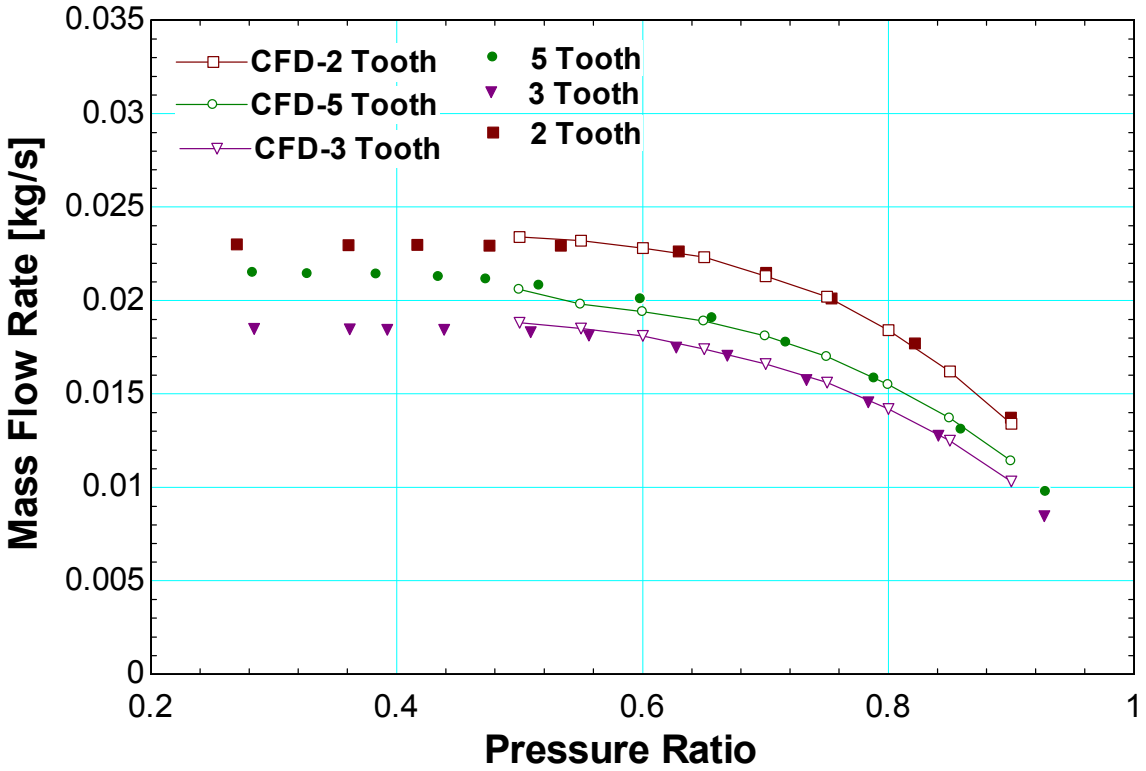

Figure 37. Measured flow rate for variation in tooth number for the same total length compared to calculated flow rate using Open Foam simulation [7]. Minimum leakage is found at a tooth number of three. Inlet Pressure is 10 MPa with corresponding inlet density of 325 kg/m^3.

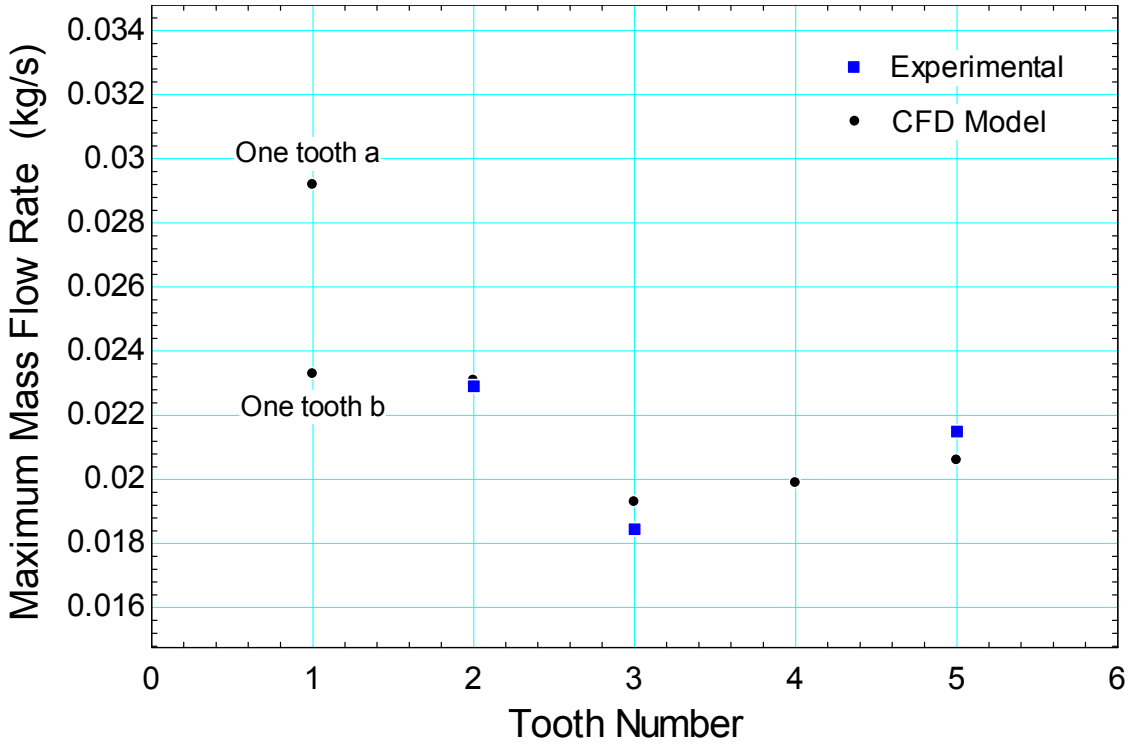

Figure 38. Comparison of measured flow rate to CFD calculated flow rate for varying tooth number with same total length.

4.1.3 Leakage Models

The leakage models described in Section 1.2.4 will here be compared to the measured flow rate of the three-tooth straight through labyrinth seals. Along with the seven labyrinth seal leakage models applied the HEM and constant discharge coefficient HEM model are included in this comparison. Figure 36 shows the results for three-tooth labyrinth seal at inlet pressure of 10 MPa and inlet density of 325 kg/m^3.

The results in Figure 39 are varied and describe the lack of complexity seen in these models. Several models including the Martin, Egli, and Sriti produce results that are above that of the HEM prediction. The HEM prediction is the ideal case for a single annular constriction and should be the highest possible flow rate. This illustrates the models inability to describe the property effects occurring in the supercritical and two-phase region for CO_2. These models were developed for incompressible ideal gas flow and cannot account for this. This inconsistency was

investigated by exploring the result for steam properties at a low pressure and high temperature where the state is considered ideal and incompressible.

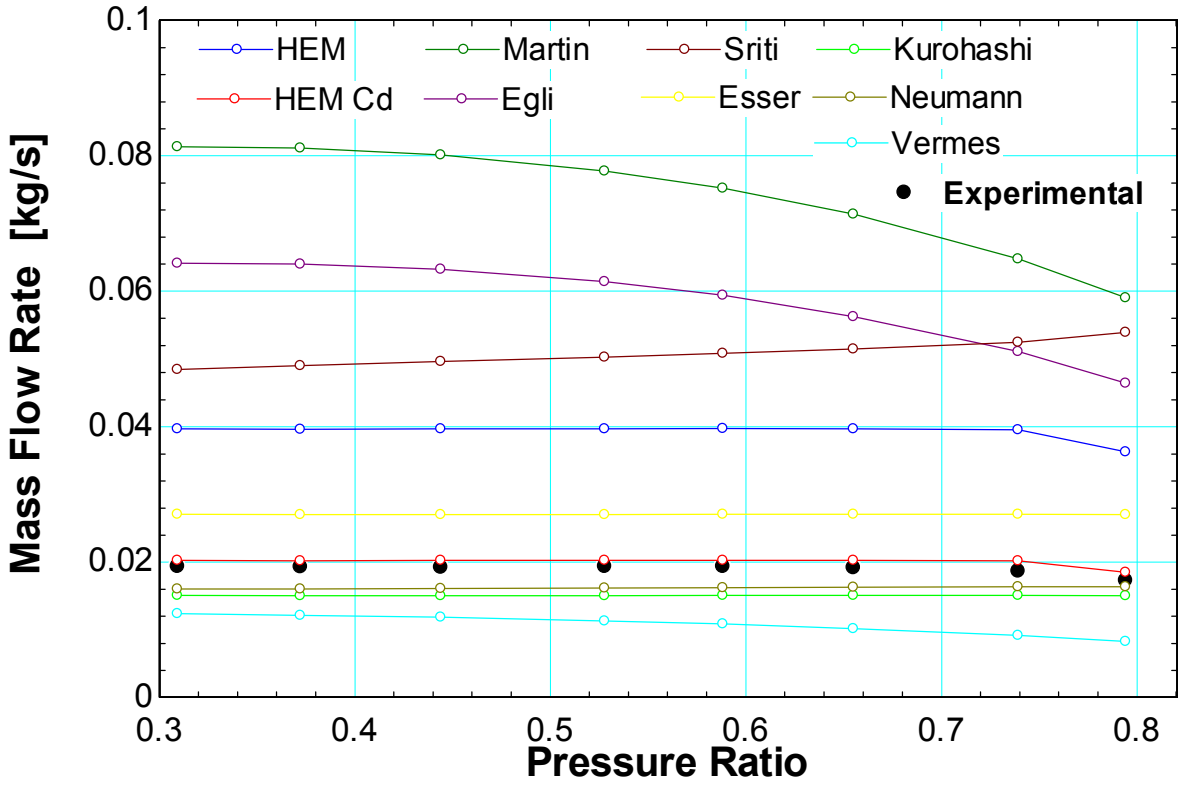

Figure 39. Measure flow rates through straight through 3-tooth labyrinth seal for inlet pressure of 10 MPa and inlet density of 325 kg/m^3 compared to various labyrinth seal leakage models.

This can be seen in Figure 40 where the mass flow rate for the Egli, Martin, and isentropic single phase model are shown for a steam inlet pressure of 6.83 MPa and corresponding inlet temperature of 200^{o}C. This shows that the real gas properties of S-CO_2 are causing the unrealistic prediction of the Egli and Martin Equations in Figure 39. Figure 41 shows the results for the inlet condition of 11 MPa and 630 kg/m^3 for the same three-tooth labyrinth seal geometry. The results are similar to the 10 MPa case with several models greatly under predicting the flow and some vastly over predicting it. As with the 10 MPa case the HEM model, with an experimentally determined discharge coefficient, is the most accurate and determines both the maximum flow rate and the pressure ratio at which the flow chokes. The assumptions

made by the labyrinth seal leakage models make them unable to predict the behavior of carbon dioxide for these conditions and the greater sophistication in regards to the flow coefficients and carry-over coefficients do not increase their accuracy.

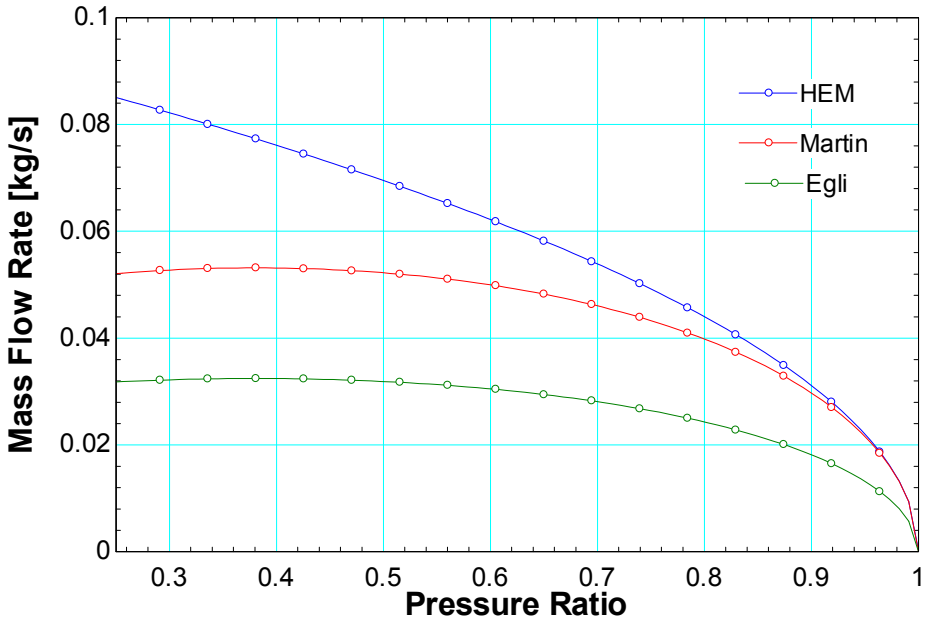

Figure 40. Incompressible and ideal gas condition check for Martin and Egli model over prediction. Inlet pressure of 6.8 MPa with corresponding inlet temperature of 200°C.

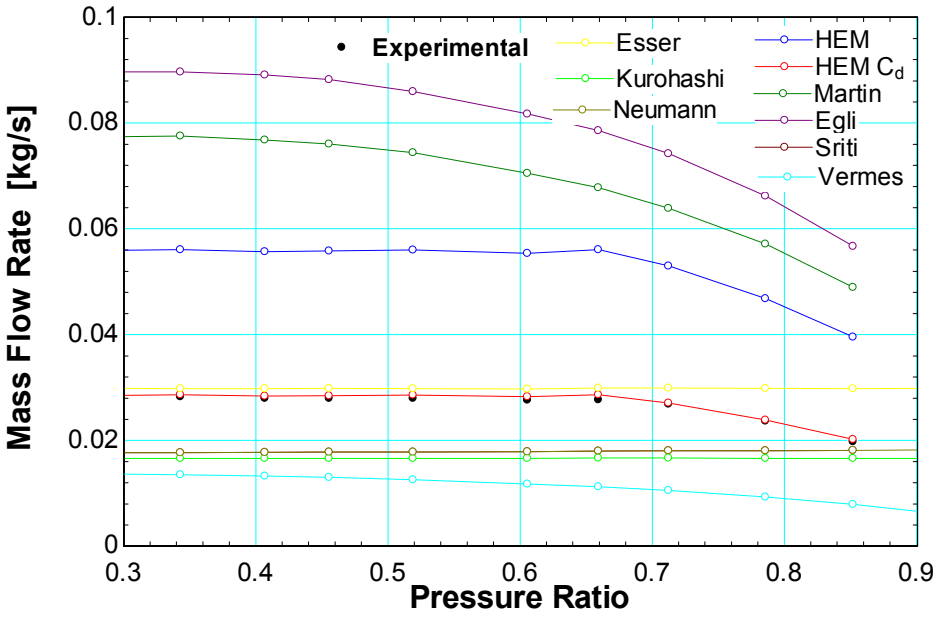

Figure 41. Measure flow rates through straight through 3-tooth labyrinth seal for inlet pressure of 11 MPa and inlet density of 630 kg/m^3 compared to various labyrinth seal leakage models.

The one-dimensional, ideal, incompressible models described here were unable to accurately predict the measured flow rate for the three tooth labyrinth seal at the different conditions tested. These models were tested despite their applicability to the non-ideal and compressible conditions of the S-CO_2 as they provide a simple one step calculation based only upon the inlet pressure, inlet density, outlet pressure, and flow geometry of the seal. This means that a simple model might be applied quickly and with minimal information. They apply different carry-over and flow coefficients based on the seal geometry to approximate the fluid dynamics within the seal. These added complexities did little to improve the accuracy of the predicted flow rate. This shows a necessity to model the correct fluid properties in the CO_2. The HEM model achieves this and with a constant empirical discharge coefficient it provided the best results which were within 5% of the measured flow rate for both conditions.

4.2 Stepped Labyrinth Seal

Flow rate measurements were made for a stepped labyrinth seal with three and four teeth at inlet pressure of 10 MPa and inlet density of 640 kg/m^3. This was done to test the seal geometry being used in practical research facilities for the S-CO_2 Brayton cycle. Results for the four-tooth case can be seen in Figure 42. The inlet conditions were chosen based upon the test conditions seen for the SNL seal [2].

The geometry tested has 15% the flow area of the SNL geometry and does not immediately reflect agreement. Looking at the mass flow rate normalized to the area shows better agreement. Figure 43 shows the mass flow rate normalized with the annular flow area. The values differ by 25% but one of the main points made in the SNL report is that the inlet condition to the seal was not known. This means that the inlet pressure could be anywhere between the compressor inlet pressure of 7.7 MPa and the compressor outlet pressure of 13.83

MPa. The inlet density of the seal could also be higher than the compressor inlet density which was maintained at 640 kg/m^3. The tests completed here were for a constant inlet density of 640 kg/m^3 which is the minimum.

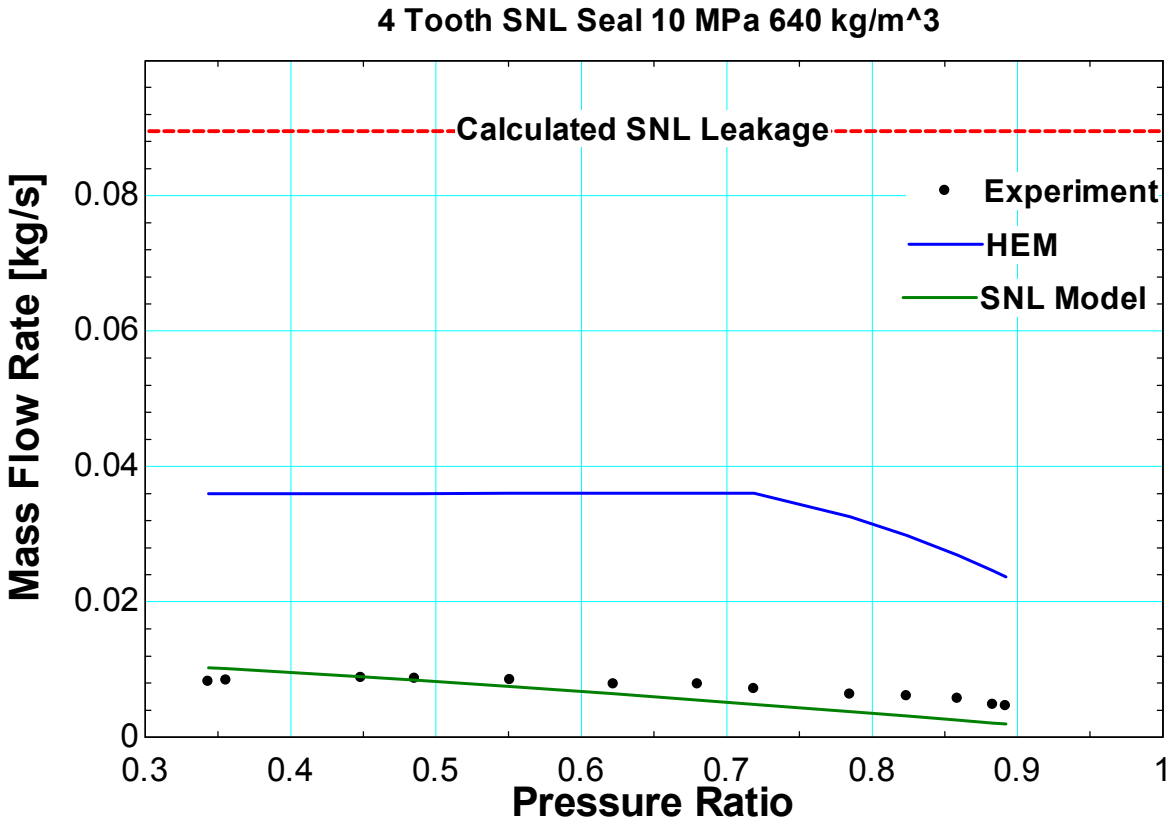

Figure 42. Four-tooth stepped labyrinth geometry for inlet pressure of 10 MPa and inlet density of 640 kg/m^3. Compared to the calculated SNL leakage flow rate which is within 20% of the measured flow rate.

To investigate this, the inlet pressure was varied maintaining an outlet pressure of 3.61 MPa and an inlet density of 640 kg/m^3. This was done to investigate the uncertainty in the seal inlet pressure, expressed by SNL, and can be seen in Figure 44. The unknown inlet condition for the seal within in the SNL research facility is due to the inability to measure the conditions at the entrance to the seal. Pressure and temperature measurements were made for the compressor inlet and outlet. These values of 7.7 MPa and 13.8 MPa respectively mean that the pressure at the seal entrance could be anywhere between these two values.

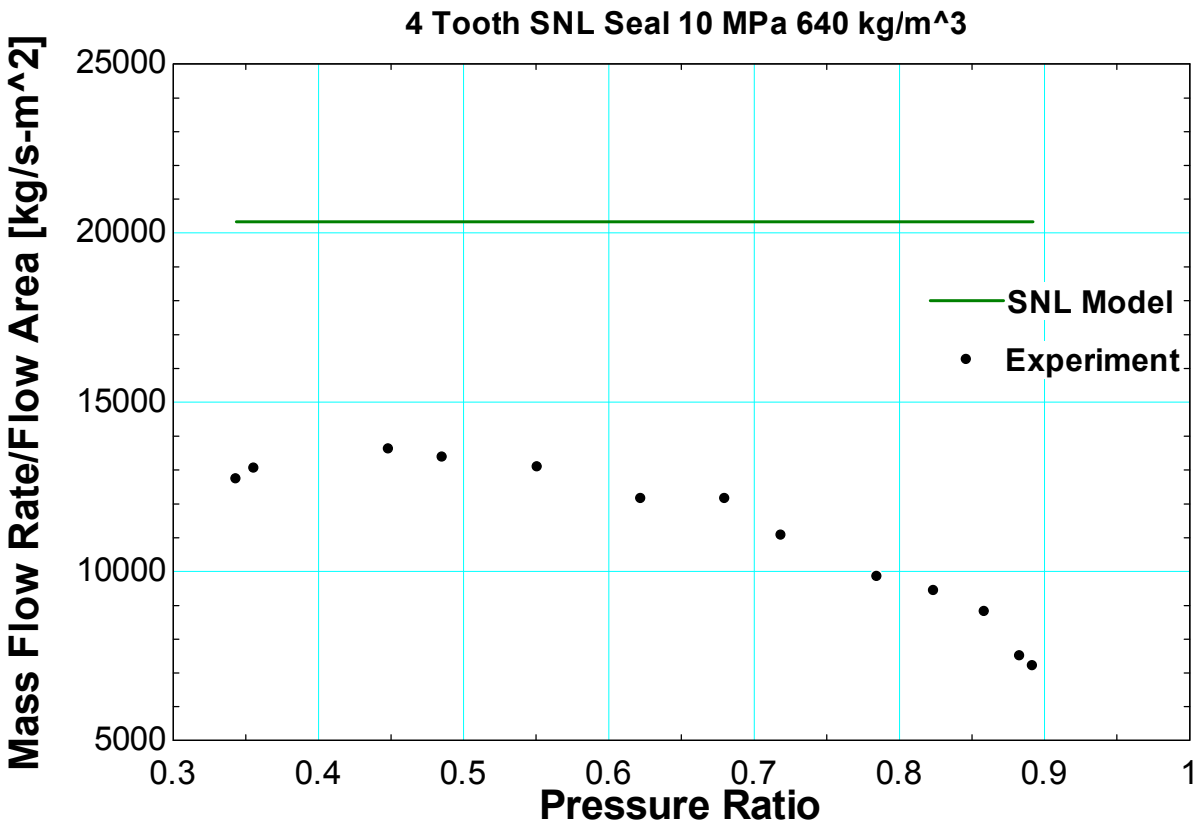

Figure 43. Area normalized mass flow rate comparison of four-tooth stepped labyrinth seal to SNL leakage calculation for inlet condition of 10 MPa and 640 kg/m^3.

The flow rate shown in Figure 44 is normalized to the flow area of the two different seals. The seal tested at UW-Madison required a smaller outer diameter to be placed within the test section flange. The inlet pressure was varied between the SNL reported compressor inlet and outlet pressures maintaining an inlet density of 640 kg/m^3. This was done to see at what pressure the flow seen in the SNL research facility is approached. Here it can be seen that the flow rate approaches the leakage seen in the SNL geometry at an inlet pressure of 12.5 MPa and would suggest that the difference in the measured flow rates is due to the difference in inlet conditions seen at the seal. Whether this difference is only in the pressure or the density or a combination of both is unknown but most likely due to both.

An internal study performed at SNL reported that the inlet condition experienced at the seal entrance is most likely closer to the compressor inlet pressure of 7.7 MPa due to the pump out

vanes on the back of the compressor wheel. These vanes are designed to reproduce the pressure profile of the compressor wheel front face at the back face. The labyrinth seal entrance is located at this back face and thus would experience an inlet pressure much lower than the maximum pressure at the compressor outlet of 13.8 MPa. The results here suggest that the inlet conditions of the seal are closer to the upper value of 13.8 MPa.

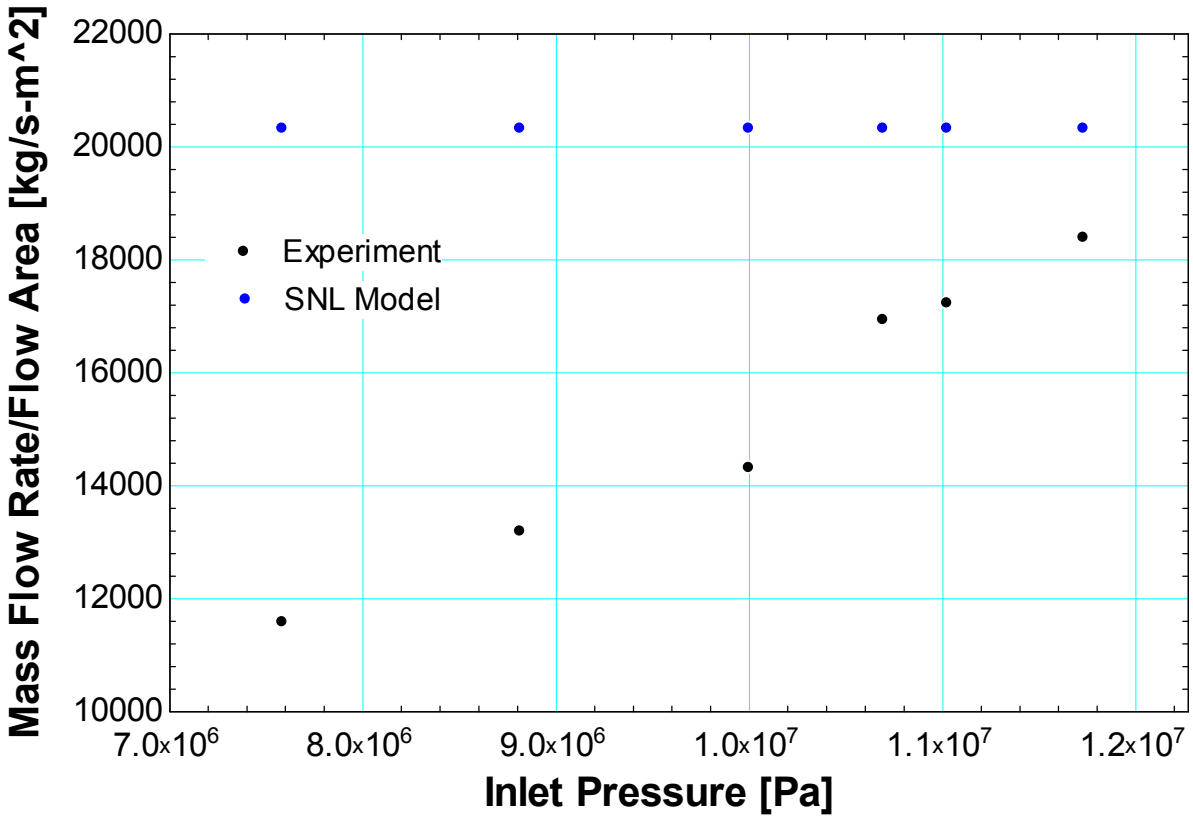

Figure 44. Area normalized leakage for four-tooth stepped labyrinth seal compared to calculated flow rate from SNL compressor facility.

To investigate the effect of increasing tooth number in the stepped geometry a three-tooth stepped labyrinth seal was tested by inserting a different shaft into the seal. In Figure 45 it can be seen that a decrease in flow rate from the three to the four tooth case of 5% was found. This would imply that there is a benefit from increasing the number of tooth present in the stepped labyrinth geometry. It can also been seen from Figure 42 and Figure 45 that the SNL Model which is a modified Martin equation does a reasonable job of predicting the flow rate within the

stepped labyrinth geometry. It gives an approximate flow rate within 30%, which agrees with the results found in the SNL investigation. As with the three-tooth straight-through geometry though, the model does not have sufficient ability to capture the geometry and property effects that are present.

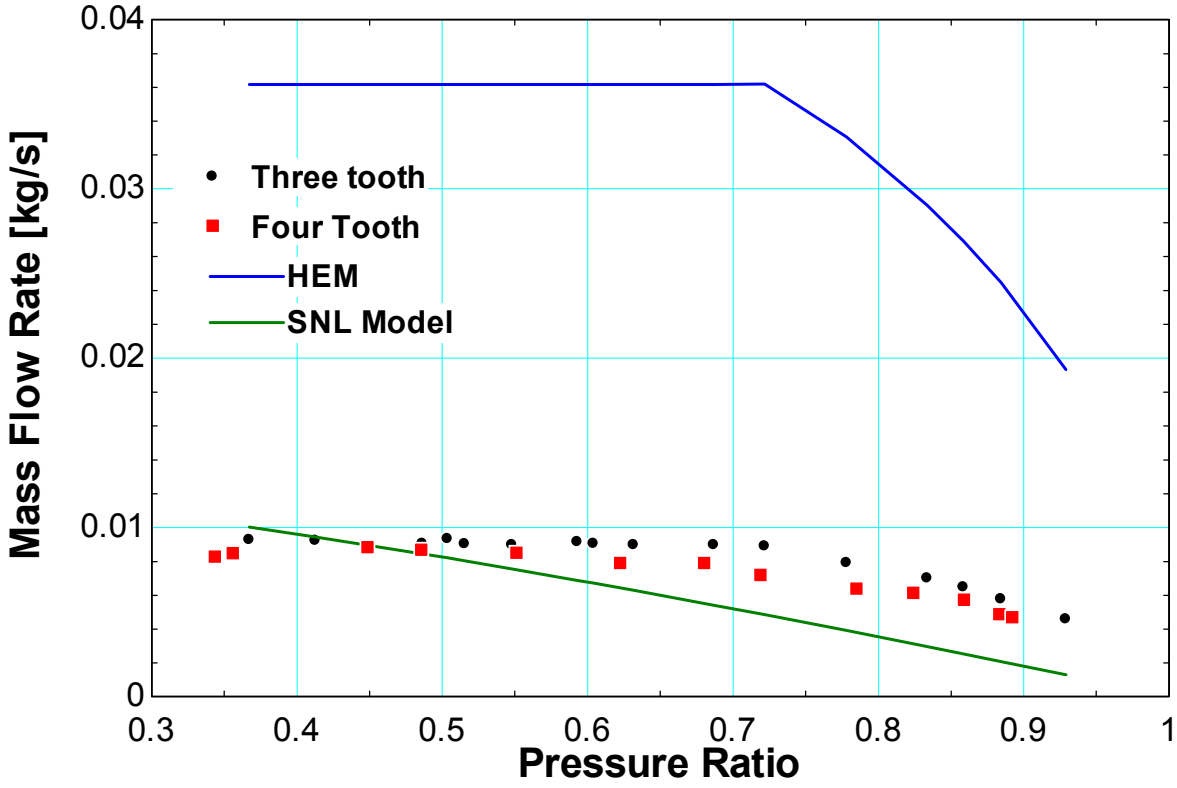

Figure 45. Three-tooth and four-tooth stepped labyrinth seal flow rate measurement for inlet pressure of 10 MPa and inlet density of 640 kg/m^3.

The Martin equation may be appropriate for a first step approximation to understand the scale at which a labyrinth seal may leak within a system. Figure 46 shows that it may also be used to predict the change in leakage due to increasing the number of teeth in the stepped labyrinth seal tested. A better approximation may be possible by using an effective flow area for higher pressure ratios. The HEM using an empirical constant discharge coefficient is shown in blue on Figure 46. The HEM with constant discharge coefficient predicts the form of the mass flow rate well giving a good estimation of the choking point along with the critical flow rate. This can be

seen in Figure 47 which shows the discharge coefficients for the three and four tooth stepped labyrinth geometries. This is for the inlet condition of 10 MPa with corresponding inlet density of 640 kg/m^3. The difference in discharge coefficient is due to the change in leakage from increasing the tooth number which the HEM model cannot predict.

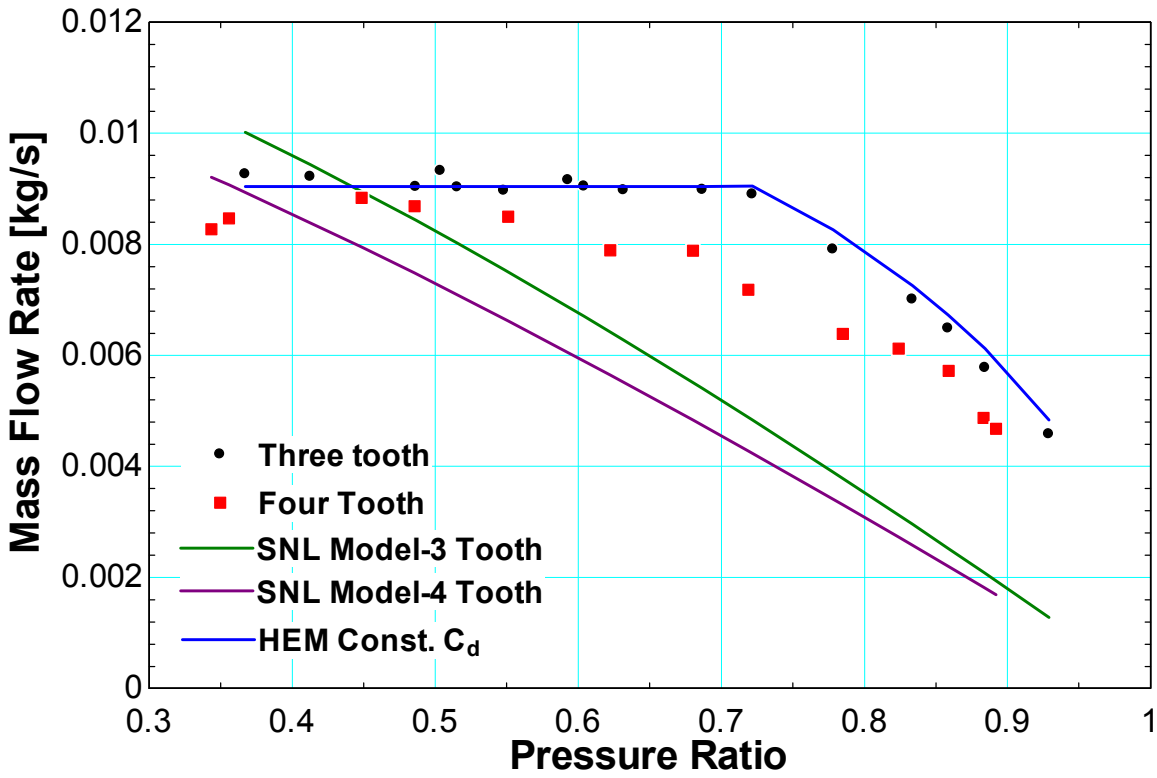

Figure 46. Mass flow rate experimental measurements and calculations for three and four tooth stepped labyrinth seal including the SNL Martin leakage equation and the HEM model with constant discharge coefficient.

The stepped labyrinth seal geometry tested here was tested to investigate the more complex geometries seen in practical research facilities such as the facility at Sandia National Labs. The geometry within this test facility was mimicked with a smaller flow area and was tested at conditions seen in the SNL facility. The results show that this facility can be used to replicate conditions seen in practical loops and that these smaller geometries can be scaled to larger geometries. The Martin leakage equation used by SNL was compared to the HEM model using a constant empirical discharge coefficient. The Martin equation although it is designed for ideal

and incompressible flow was shown to predict the flow rate within 30% and accurately predict the change in leakage due to an increase in the number of seal teeth from three to four.

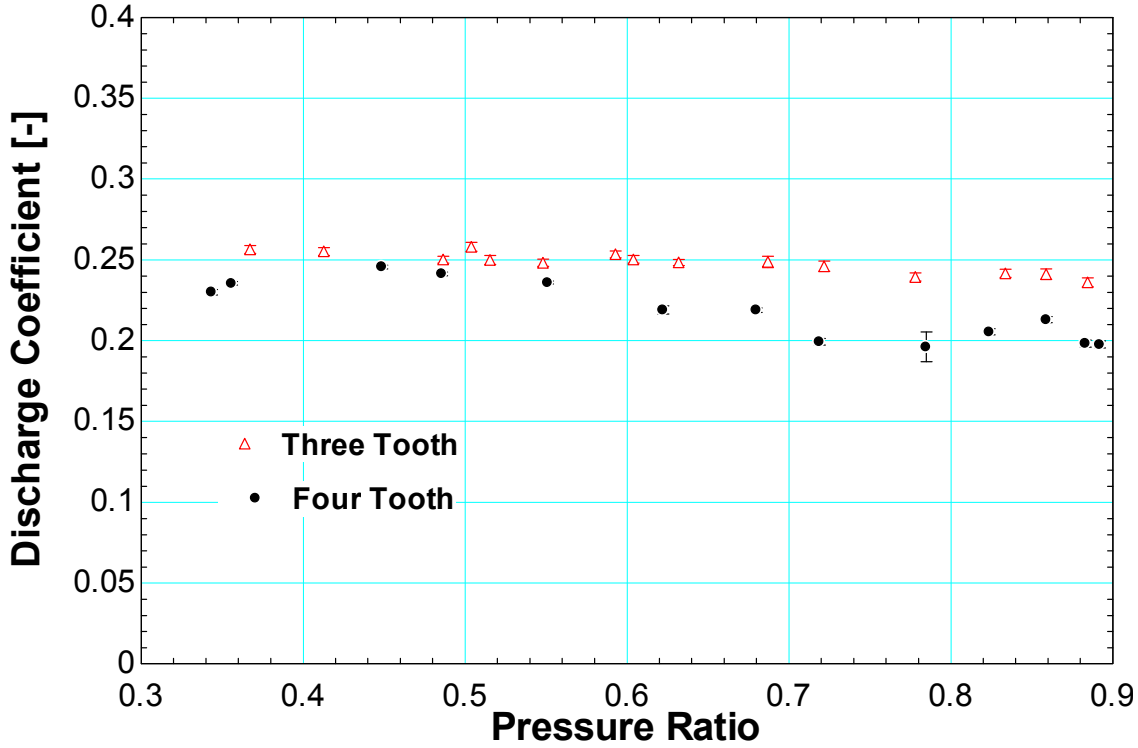

Figure 47. Experimentally determined discharge coefficient for three and four tooth stepped labyrinth seal at an inlet condition of 10 MPa with corresponding inlet density of 640 kg/m^3.

The HEM model with constant empirical discharge coefficient was shown to accurately predict the flow rate within 10%. It does not predict the decrease in flow rate increasing the tooth number from three to four because its only geometrical parameter is the flow area defined by the annular entrance. To account for this lack of complexity an empirical discharge coefficient is defined for each geometry. This shows that these one-dimensional models can be effectively used to perform first approximations of the flow through seals in S-CO_2. To achieve greater accuracy less assumptions must be made and a more detailed description of the geometry must be employed. Computational Fluid Dynamics (CFD) provides a robust and detailed approach to seal leakage which allows for more accurate results [7]. This experiment provides data for the validation of these complex models. It is of value though to assess these simple one-

dimensional models as they require very little information and are quickly calculated. Thus giving a useful first approximation and in the case of the HEM model a description of the critical flow rate and choking point.

4.3 Empirical Discharge Coefficient

The isentropic HEM has been applied to the data collected here for straight-through and stepped labyrinth seal. It provides a model that accounts for the real gas properties of CO_2 and uses mixture properties to model two-phase effects. The HEM assumes that the velocities, temperatures, and pressures between the phases are equal and when calculated for a single phase condition collapses to a one-dimensional isentropic model. These assumptions cause the model to always over predict the measured flow rate. To account for this an empirical discharge coefficient is applied to the model which then provides an accurate description of the leakage through a seal.

The results for the empirical discharge coefficient for the geometries tested are listed in Table II. The labyrinth seal results show that for the high inlet pressures of 10 and 11 MPa a constant discharge coefficient was found with an error of less than 4%. For the lower pressure tests of 7.7 MPa, it is necessary to define a range of pressure ratios with different constant discharge coefficients to maintain an error of 5%. This occurs because the higher pressure cases choke prior to or early in the two-phase region and the HEM correctly predicts the critical pressure ratio and critical mass flow rate. The lower pressure case chokes well into the two-phase region where the difference in properties between the phases is much greater. The HEM mixture properties do not accurately accommodate this and the accuracy of the model deteriorates. The model predicts a different choking point than is found in the measured data and this is reflected by a non-constant behavior in the discharge coefficient. To provide a more accurate

description of the flow rate a different discharge coefficient can be applied to two different ranges of pressure ratios. These regions are defined by the choking point predicted by the HEM. As the model chokes prior to the data, at pressure ratios higher than the model calculated critical pressure ratio the discharge coefficient is the same as predicted for the higher inlet pressure cases. Below this pressure ratio the discharge coefficient begins to deviate and a different average discharge coefficient is applied.

Geometry	Total Length [mm]	Inlet Pressure [MPa]	Pressure Ratio [-]	Discharge Coefficient [-]	Error [%]
Straight-Through					
One-Tooth	1.27	10,11	0-0.93	0.79	2.1
Three-Tooth	3.81	7.7	0-0.7	0.56	5.2
Three-Tooth	3.81	7.7	0.7-0.93	0.51	2
Three-Tooth	3.81	10,11	0-0.93	0.51	2
Two-Tooth	11.43	10	0-0.93	0.7	3
Three-Tooth	11.43	10	0-0.93	0.55	3.8
Five-Tooth	11.43	10	0-0.93	0.6	8.5
Stepped					
Three-Tooth	10.67	10	0-0.93	0.25	2.3
Four-Tooth	10.67	10	0-0.93	0.22	8.1

Table II. Empirical discharge coefficient results.

As the flow geometry becomes more complex the ability of the HEM to predict the choking point of measured flow also deteriorates. This can be seen in the increased error found for the more complex geometries of the five-tooth straight-through labyrinth seal and the four-tooth stepped labyrinth seal. As the length of the seal increases and the tooth number increases the amount of friction within the seal increases. This effect causes the flow to choke at a lower pressure ratio which the HEM cannot predict.

The HEM with an empirical discharge coefficient gives a prediction for all measured flow rates within 15%. This error is reduced to less than 10% for all labyrinth seals with three or less teeth

and inlet pressures of 10 or 11 MPa. For low inlet pressures where choking occurs well into the two-phase region a separate discharge coefficient for pressure ratios above and below the critical pressure ratio is suggested. This distinction allows for two empirical discharge coefficients with errors of 5% to be applied across the full range of pressure ratios. These results describe the usefulness of the HEM, with an empirical discharge coefficient, in predicting the flow of S-CO_2 through labyrinth seal geometries. It provides a good approximation for simple seals that is quickly and easily calculated.

5 Numerical Results

This chapter is divided into three parts: In the first part numerical results obtained for plain orifices are compared to experimental results, the second part explains the effect of geometrical parameters, and the third part deals with the effect of operating conditions.

The flow is assumed to be axisymmetric and hence a two dimensional (axial-radial) simulation is utilized. Axisymmetric assumption is considered to be good enough to represent flow field as long as the effects of boundary layer in the θ (Azimuthal) direction are negligible. The shaft is represented by a straight wall along the bottom of the domain. Long entrance and exit regions are used before and after the annular orifice to allow for the flow to equilibrate before it enters the tooth clearance. This would represent real geometry which would be used in experiments. A sample mesh (for case 2 in Appendix B) is shown in Figure 48. The mesh is created using the blockMeshDict utility provided by OpenFOAM which translates a set of well-defined coordinates and blocks into a mesh. In Figure 48 it can be seen that, the computational mesh is much finer in the clearance region. Care has been taken to make sure that value of Y^+ for nodes very close to the tooth and shaft walls is less than 5 in order to resolve the laminar sublayer. The mesh is also generated to follow the flow and hence is non-orthogoanl to the surface of tooth outside

clearance region. Error due to this non-orthogoanlity is minimized by performing non-orthogonal corrections after every iteration. Before validating the computational model, it was necessary to perform a grid independence study to make sure that results obtained from the computational studies are independent of mesh. Since, OpenFOAM doesn't have the capabilities to refine the mesh based on the gradient in variables, the mesh was subjected to various levels of manual refinement.

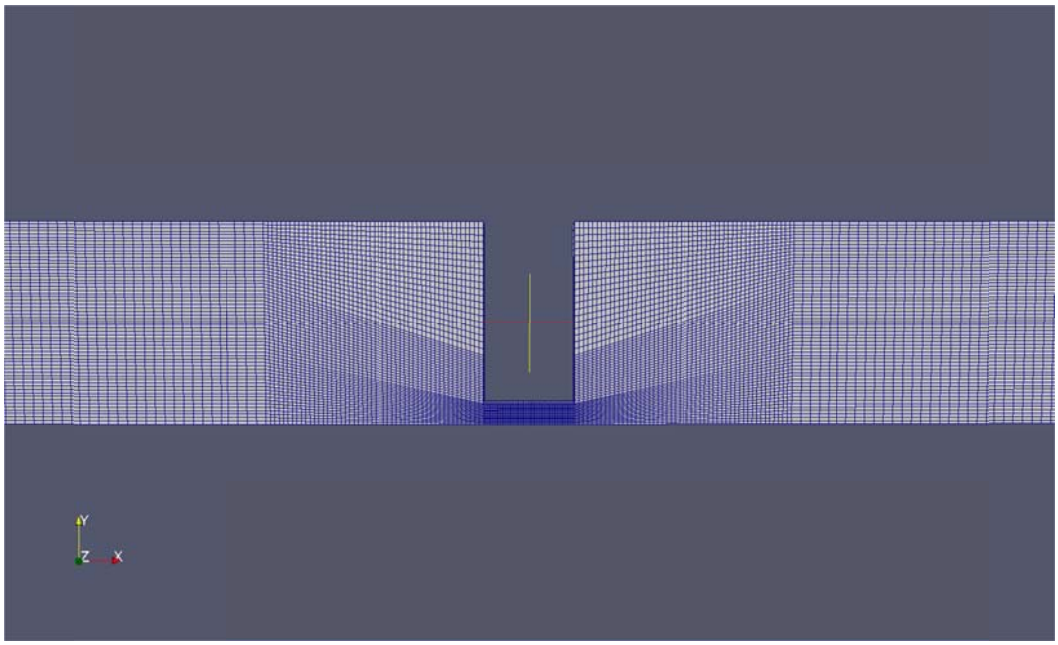

Figure 48. A sample computational mesh used for simulations

Results of the grid independence studies are presented in Figures (49 and 50). The leakage rate prediction error between the mesh with 20000 nodes and the orthogonal mesh with 50000 nodes was about 3 % for higher pressure ratios and less than 0.6 % for lower pressure ratios. This error at higher pressure ratios might slightly effect the prediction of C_d as shown in Figure 49. The error between the mesh with 30000 nodes and that of orthogonal mesh is about 1 % for higher pressure ratios and less than 0.3 % for lower pressure ratios. Hence, the mesh with 30000 nodes is employed for computational studies on the annular orifice.

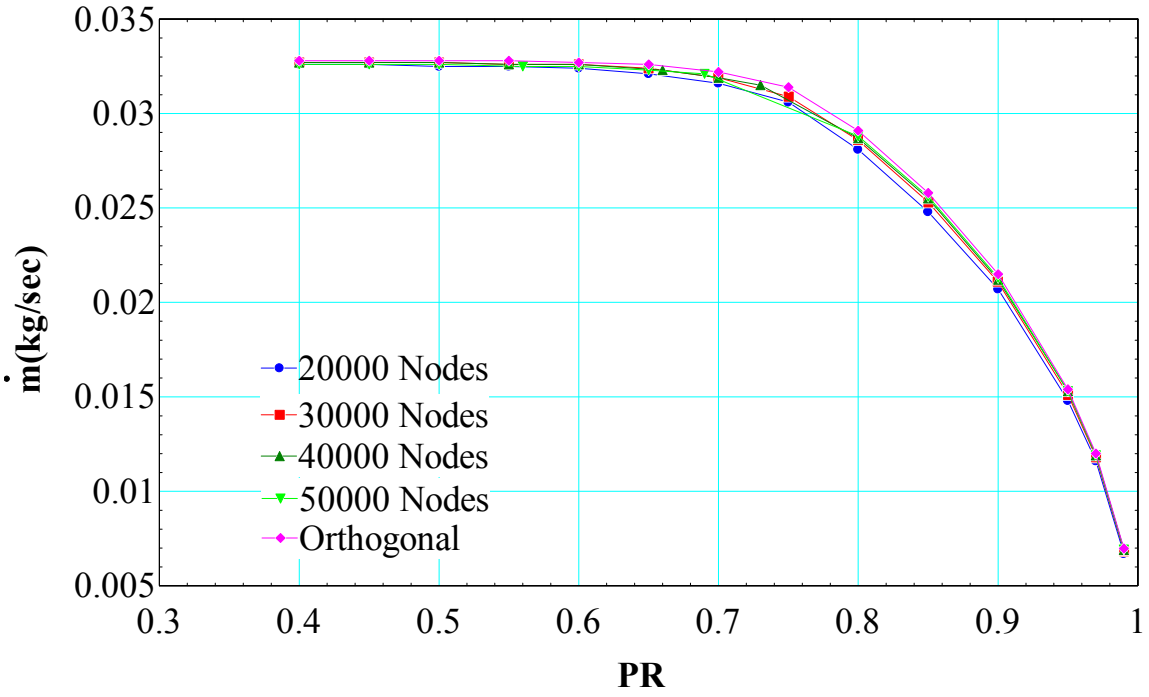

Figure 59. Variation of leakage rate prediction with number of nodes

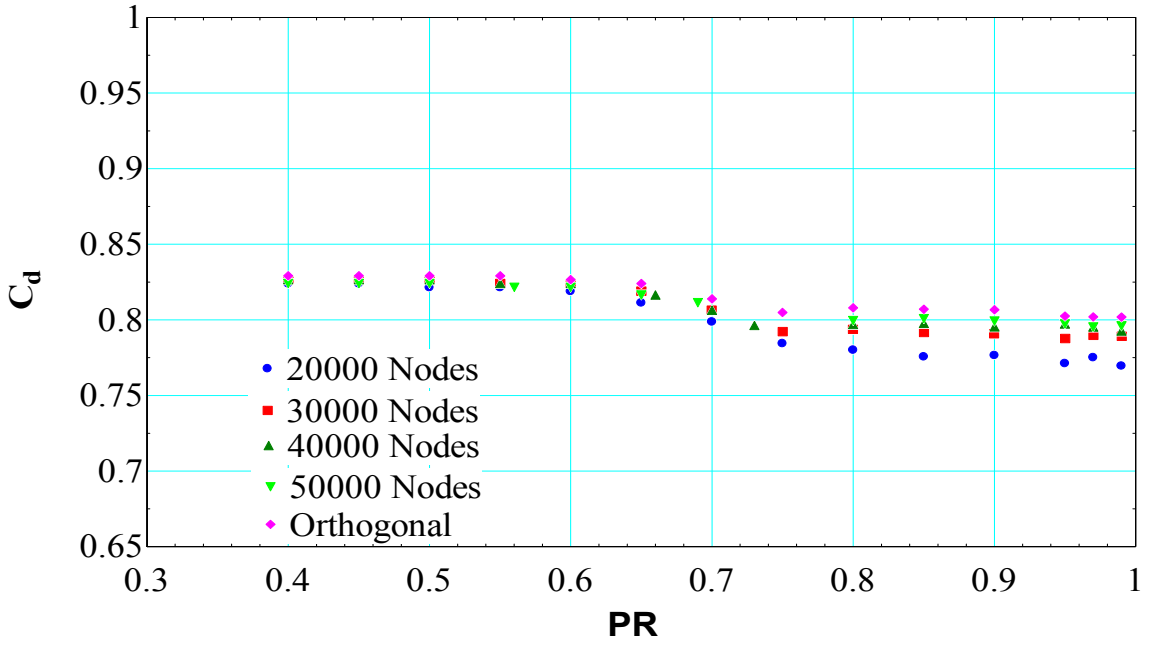

Figure 50. Variation of discharge coefficient with number of nodes

5.1 Validation of computational model

Experimental data is used to show the capabilities of model developed in OpenFOAM. The data used is that of a plain orifice having an inner diameter of 1.006 mm and a length of 5 mm resulting in *L/D*~5. The radius of curvature of the inlet edge has been carefully measured and it has been found that the edge can be considered as a sharp edge. Hence, a sharp edge has been used for these computational studies. However, it is very important to measure the radius of curvature accurately as it has a significant effect on the leakage rate as shown later in this section. Simulations are performed for this particular orifice for different operating conditions (Table D.3) and leakage rate results are presented in Figures 51 through 55.

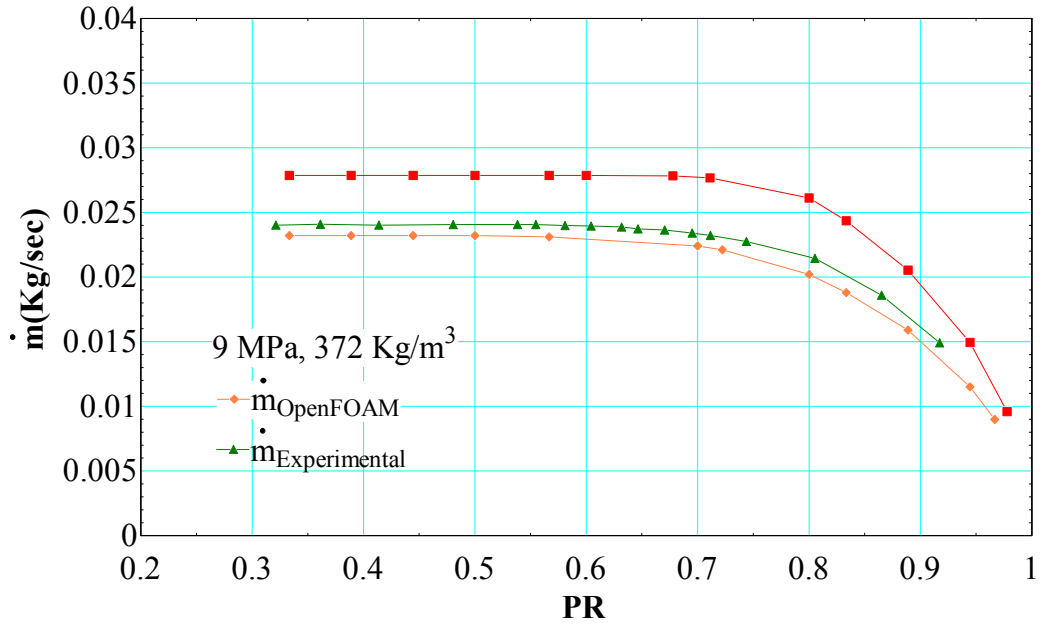

Figure 51. Leakage rate for inlet condition of 9 MPa, 372 Kg/m^3 (case 1 in Table D.3)

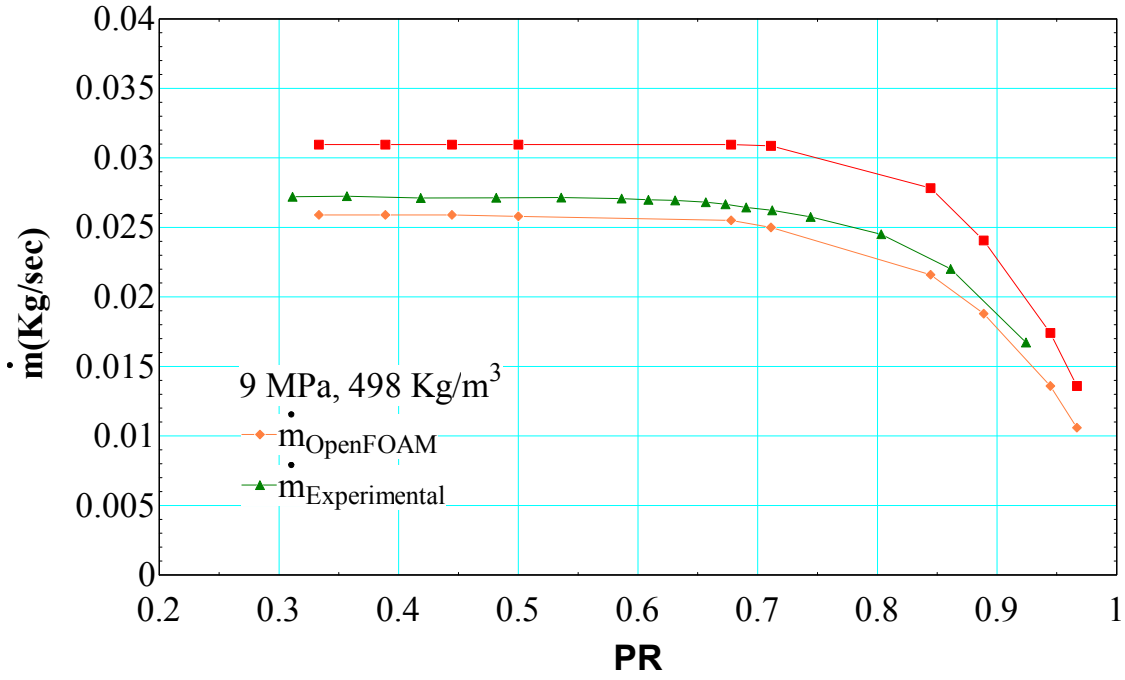

Figure 52. Leakage rate for inlet condition of 9 MPa, 498 Kg/m^3 (case 2 in Table D.3)

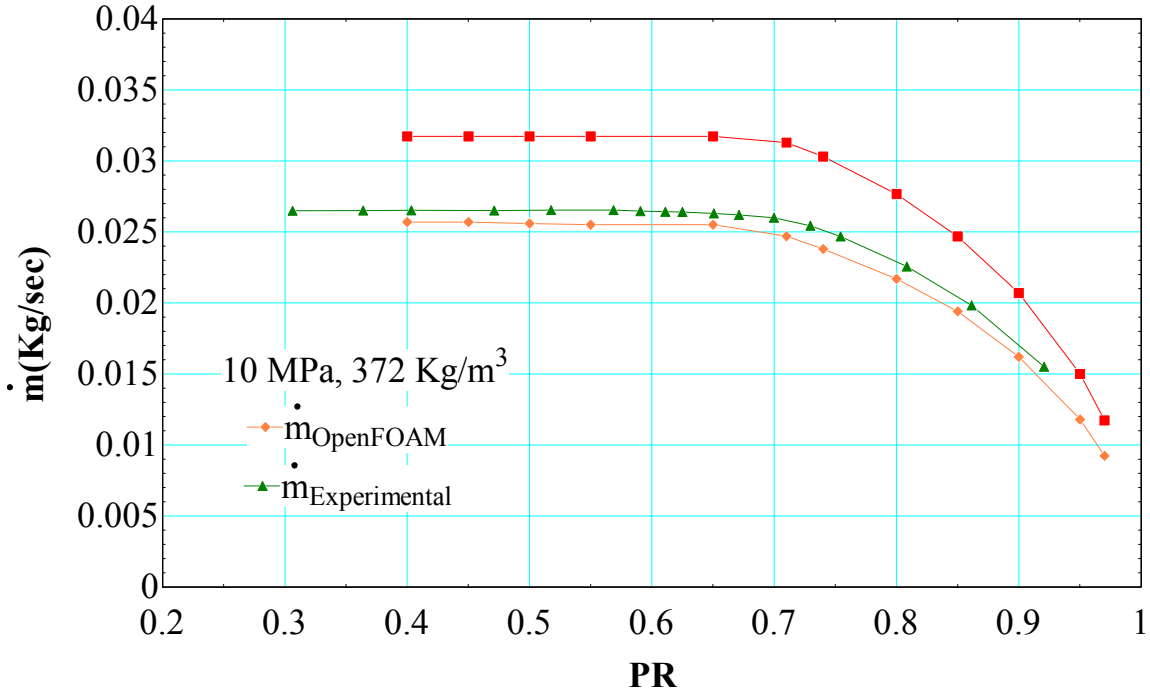

Figure 53. Leakage rate for inlet condition of 10 MPa, 372 Kg/m^3 (case 3 in Table D.3)

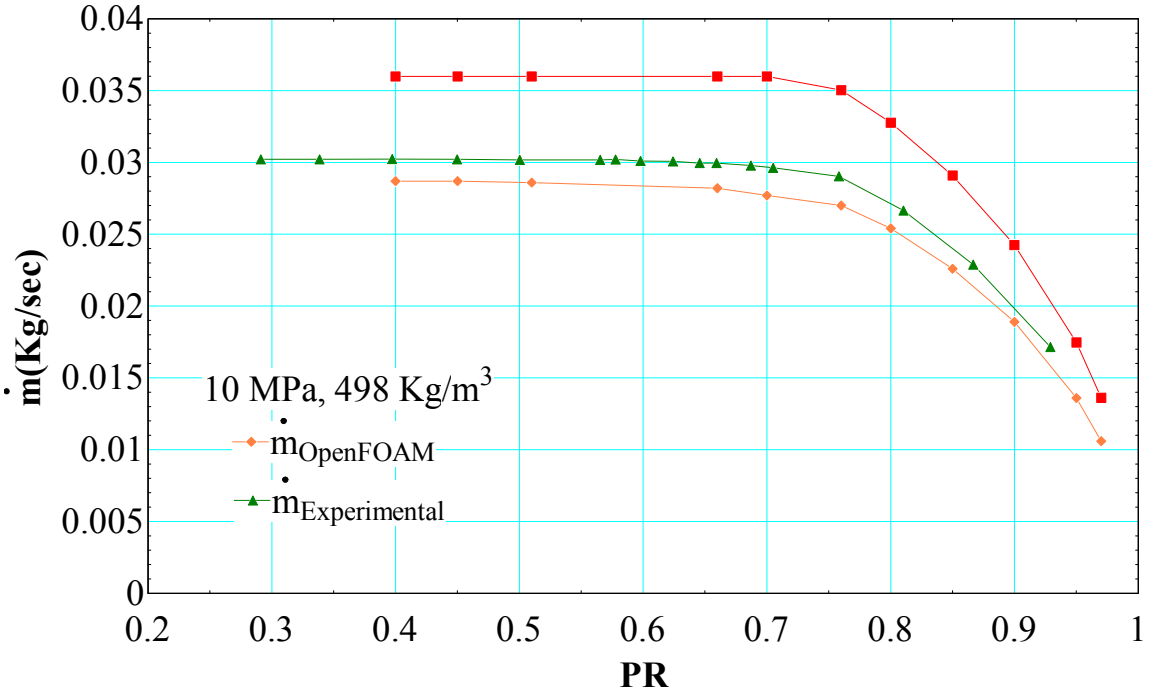

Figure 54. Leakage rate for inlet condition of 10 MPa, 498 Kg/m^3 (case 4 in Table D.3)

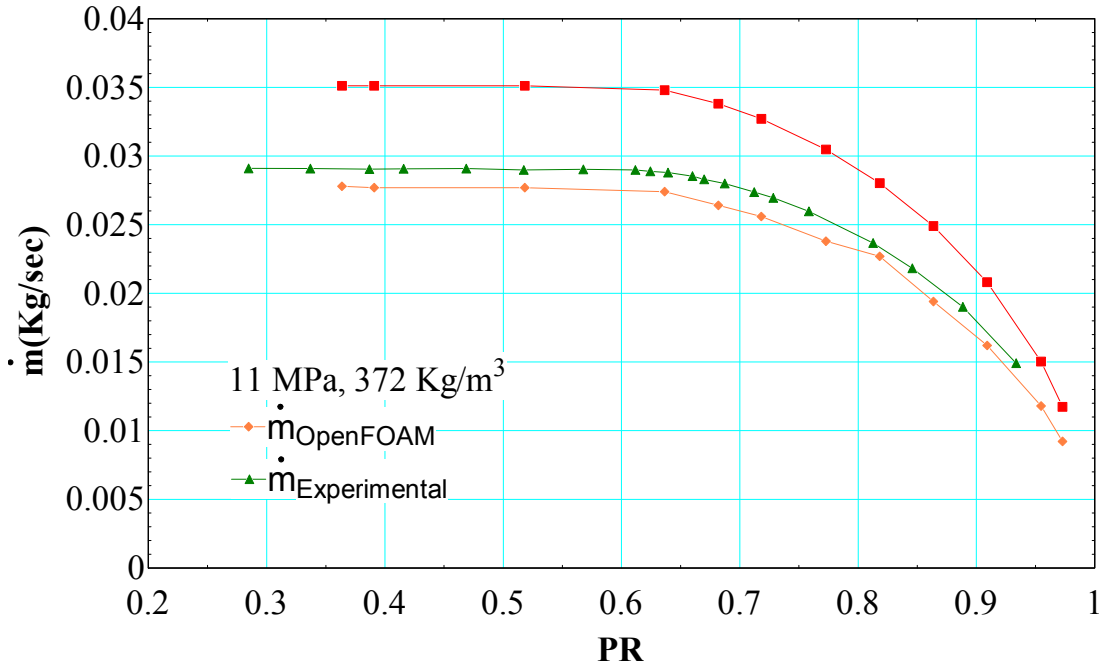

Figure 55. Leakage rate for inlet condition of 11 MPa, 372 Kg/m^3 (case 5 in Table D.3)

It can be qualitatively concluded from these Figures that OpenFOAM, is in general, capable of predicting the experimental data for all operating conditions. For each operating condition, the PR's at which experimental data is available doesn't match with that of computational data and hence, in order to facilitate a comparison, a 6^{th} order polynomial curve is fit to the experimental data and the leakage is calculated for the needed PR's. An error analysis is performed to compare the numerical simulation data with that of the experimental data and the results are plotted in Figure 56 for all operating conditions. It can be concluded from the error analysis that the majority of the simulation data for higher PR and low leakage rate are within ± 10 % of experimental values and for low PR and high leakage rate all data points are within ±10 % of experimental values with majority of the data close to a 5 % error. This slight error could be due to the fact that there are adverse property changes as S-CO_2 flows through an orifice and a refined mesh based on gradients in properties is needed to capture the flow field more accurately. Implementing an adaptive mesh refinement algorithm in OpenFOAM to refine the mesh automatically based on gradients in properties will minimize the error further and is to future work.

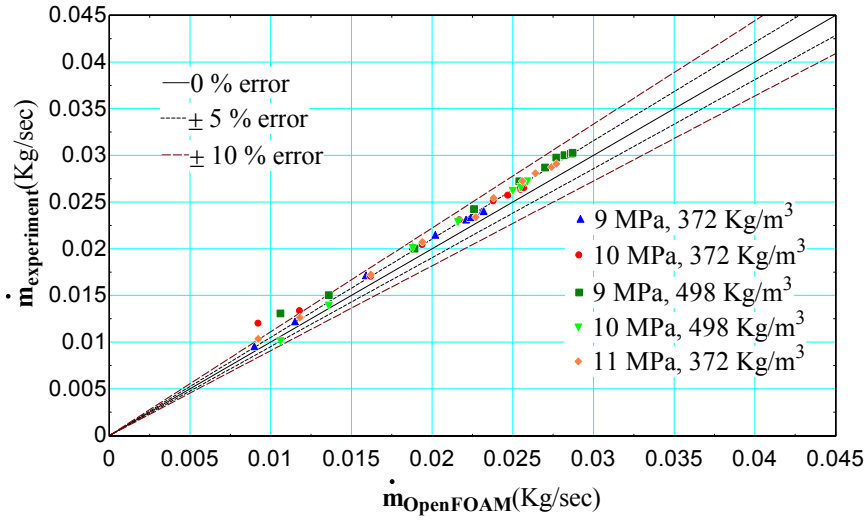

Figure 56. Error analysis for plain orifice data

5.1.1 Effect of radius of curvature

Due to flow separation at the inlet of an orifice, the area at vena contracta might change as the radius of curvature is changed. Hence, it is important to measure the radius of curvature of the inlet edge as it has a significant effect on the leakage rate as shown in Figure 57. The presence of a chamfered edge with a chamfer radius as small as 0.005 mm causes the leakage rate to increase by about 5 %. In the future, if numerical data is being compared to experimental data care has to be taken to measure the radius of curvature accurately and use it for simulations otherwise the error between simulations and experiments can be expected to be as high as 5-10 %.

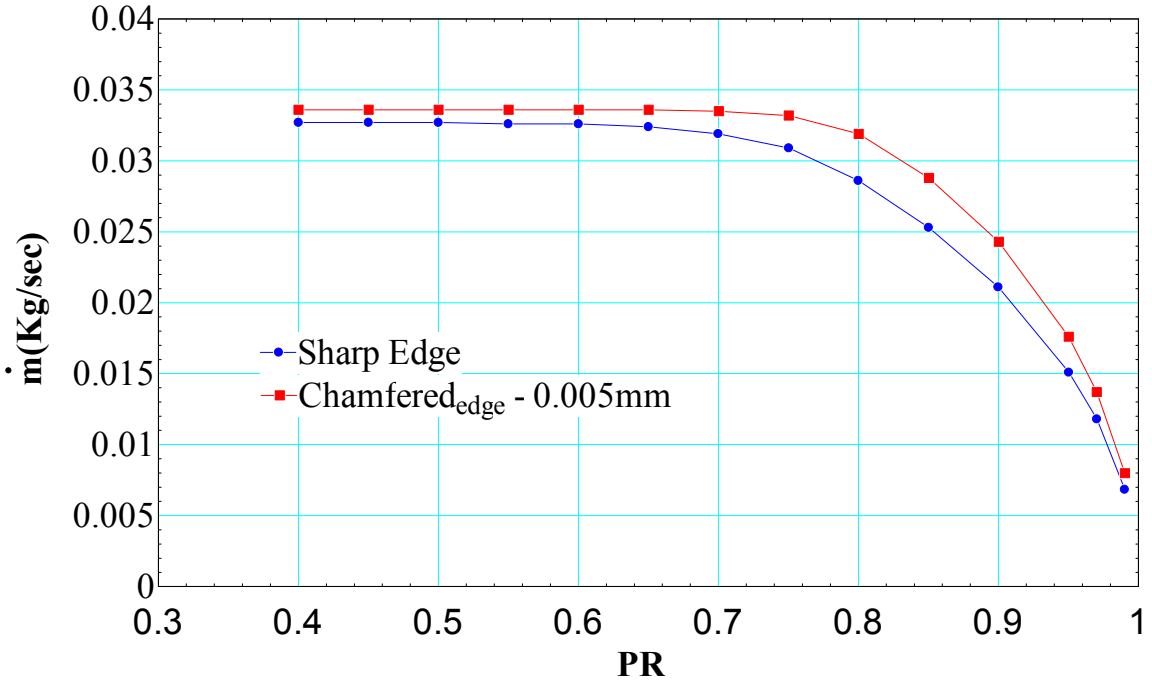

Figure 57. Effect of radius of curvature on leakage rate

5.2 Effect of geometrical parameters

There are various geometrical parameters which affects the leakage rate through orifices. Some of the important parameters which will be analyzed in this section are the effects of radial clearance, tooth width, tooth depth, inlet radius of curvature, shaft diameter.

5.2.1 Effect of Radial clearance

The first parameter that is of interest when designing seals for turbo-machines is the radial clearance. Simulations were performed for four different radial clearances (cases 1-4 in Appendix B) with the rest of the geometrical parameters held constant for all four cases. The leakage rate is calculated by integrating the mass flow at each node of the inlet and scaling the 2-D axisymmetric mass flow rate to a 3-D model. Then the discharge coefficient is predicted by calculating the ratio of this scaled mass flow rate with respect to the 1-D isentropic mass flow rate. Figures (58 and 59) present the results of the leakage rates and discharge coefficients respectively for all four cases.

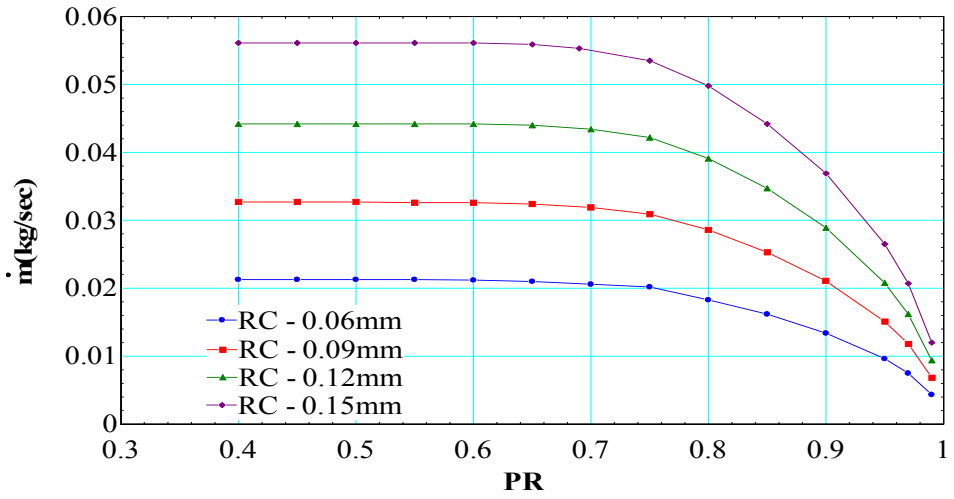

Figure 58. Variation of Leakage rate with Radial clearance

The leakage rate increases with an increase in radial clearance, which is a fairly obvious result as an increase in clearance area allows more fluid to be forced underneath the tooth. It should be noted that the inlet operating condition for all these simulations is fixed at a pressure of 10 MPa, and a density of 498 kg/m^3. Although the leakage rate increases by a magnitude of approximately 3 times between the clearances of 0.06 mm and 0.15 mm, it is interesting to note that the discharge coefficient for all the four cases doesn't vary by much.

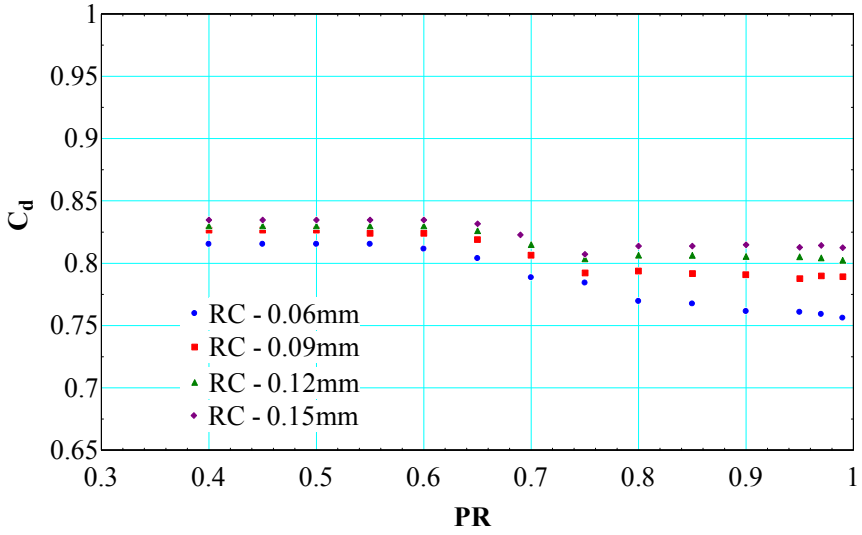

Figure 59. Variation of discharge coefficient with radial clearance

This result implies that the 1-D isentropic model is able to predict the leakage rate for all radial clearances equally well. One more interesting thing to note is how the C_d remains constant for higher PR's, increases over a certain range of PR and stays constant below the choked PR. The reason for this increase in C_d over a range of PR is due to the fact that the 1-D isentropic model and real flow choke at different PR's. In reality, the mass flow rate continues to increase even after the 1-D isentropic model chokes and hence, the C_d increases till the real flow chokes and stays constant after that.

5.2.2 Effect of Tooth width

To understand the effect of tooth width on the C_d, simulations were performed for three different tooth widths while holding rest of the geometrical parameters constant (cases 2, 5 and 6 in Appendix B). Figures (60 and 61) present the results of the leakage rates and discharge coefficients respectively for all three cases.

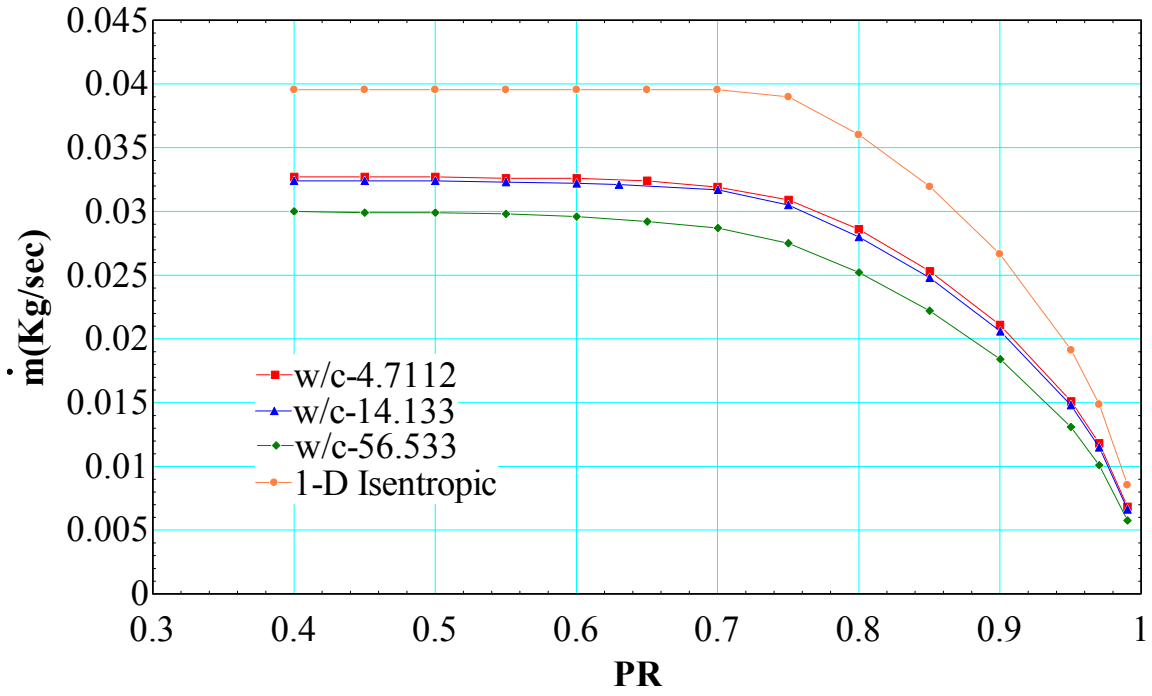

Figure 60. Variation of leakage rate with tooth width

It can be seen that smaller *w/c* (width to clearance) result in higher leakage rate and as a result, the discharge coefficients are higher for the lower *w/c* cases. As the flow enters the clearance region, fluid separates from the tooth edge and forms a recirculation zone in the clearance region until the flows reattaches back to surface. The fluid stream reaches a minimum diameter where radial velocity is zero before reattaching to the surface again. The point where fluid stream has least diameter is termed as “vena contracta”. The Coefficient of contraction (C_c) can be defined as in equation (66)

$$C_c = \frac{Area\ at\ vena\ contracta}{Area\ of\ orifice} \tag{66}$$

The typical value of C_c is 0.64 for a sharp orifice. The smaller the value of C_c, the more effective the vena contracta is. After the flow reattaches to the surface the pressure drop in the orifice can be treated equivalent to a flow through pipe. In the case of laminar pipe flow for a given pressure drop the flow rate gets smaller as the length of the pipe increases, as shown in equation (67). This can be extended to complicated turbulent flow and said that the leakage rate is inversely proportional to the tooth width.

$$Q = \frac{\pi D^4 \Delta P}{128 \mu l} \tag{67}$$

As presented in Figure 61, C_d doesn't change much for lower *w/c* cases. If the fluid reattaches to the surface of tooth very close to the downstream edge, the effect of tooth width might not be very significant, as observed for lower *w/c* cases. As *w/c* increases the effect of tooth width becomes more and more significant. In fact, while understanding the effect of radial clearance, *w/c* for the least clearance (0.06mm) case is about 7.06 whereas for the maximum radial clearance (0.15mm) case it is about 2.82 which is the reason why the discharge coefficients didn't vary much even though the leakage rates increased by 3 times between minimum and maximum clearance cases. It has been shown by many authors [18] in the past that the major non-dimensional parameter influencing the discharge coefficient is *w/c*.

In order to reassert the theory that *w/c* is the only geometrical parameter that significantly affects the discharge coefficient of an annular orifice, two simulations were performed with different widths and clearances but having the same *w/c* (cases 2 and 7 in Appendix B). Figure 62 indicates that the discharge coefficient of both the cases show nearly the same functional relationship with PR thus verifying that *w/c* is the correct non-dimensional geometrical

parameter that influences the discharge coefficient of an annular orifice. It might also be worthwhile to affirm the theory at higher *w/c* of 56.533 or above, which is left to be part of future work.

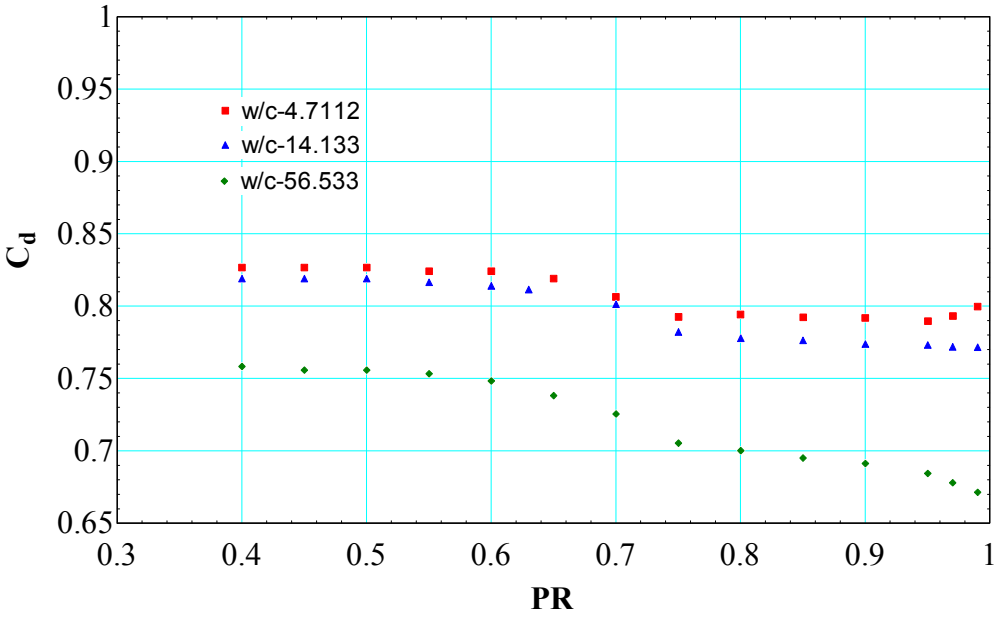

Figure 61. Variation of C_d with tooth width

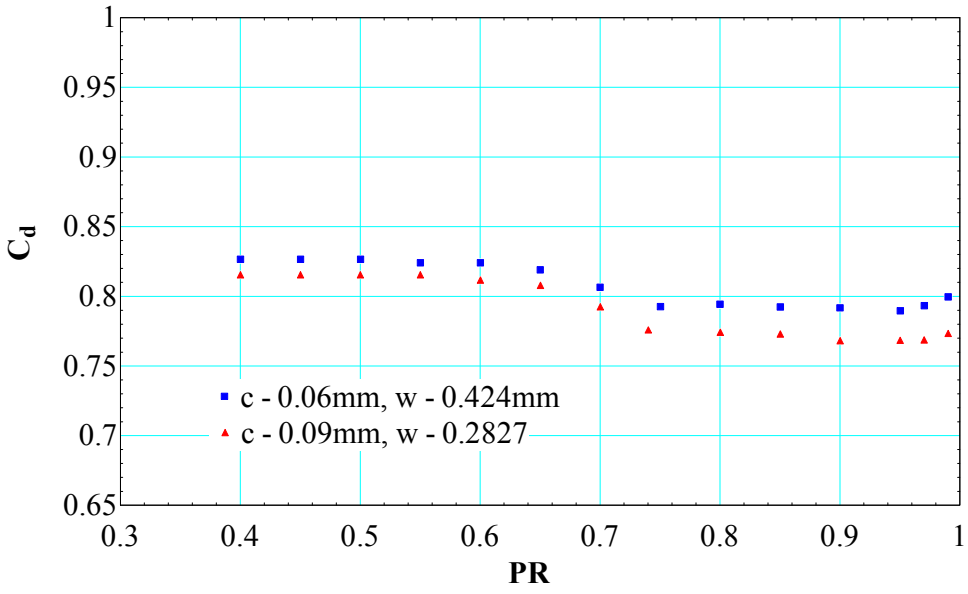

Figure 62. Cd of annular orifices having same w/c

5.2.3 Effect of tooth height

In order to examine the effects of tooth height, simulations are performed for 3 different tooth heights (cases 2, 8 and 9 in Appendix B) while holding the other geometrical parameters constant. The results for leakage rate and C_d are presented in Figures 63 and 64.

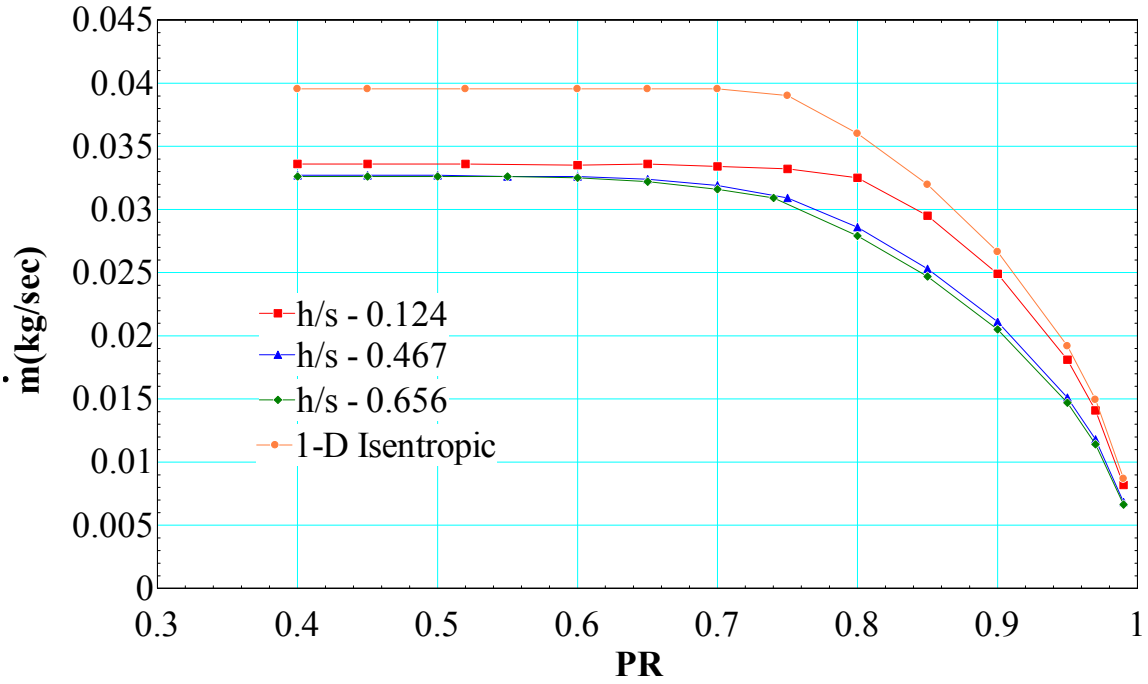

Figure 63. Variation of leakage rate with tooth height

It can be shown using the Bernoulli equation that, for an incompressible fluid as tooth height decreases, the total head loss from inlet to exit of an orifice decreases. This implies that the leakage rate will be higher for a given pressure drop. This theory can be extended to complicated turbulent flows and it can be concluded that the leakage rate increases as tooth depth decreases as seen in Figure 63. It is interesting to note that the C_d for lower tooth height case is higher for higher PR's and decreases over a certain PR and stays constant after 1-D isentropic flow chokes. This trend is quite opposite to what other cases present. This is due to the real flow choking before the 1-D isentropic flow chokes and hence isentropic flow rate keeps

increasing even after the real flow chokes. The physical reason behind why the real flow chokes before the isentropic flow is unknown at this point and requires more detailed study. As tooth height increases, discharge coefficient is nearly independent of tooth height and can be assumed that it has no effect on C_d. It has to be noted that the aspect ratio of cavities of most real world labyrinth seals is over 0.5 and rarely exceeds 1.5.

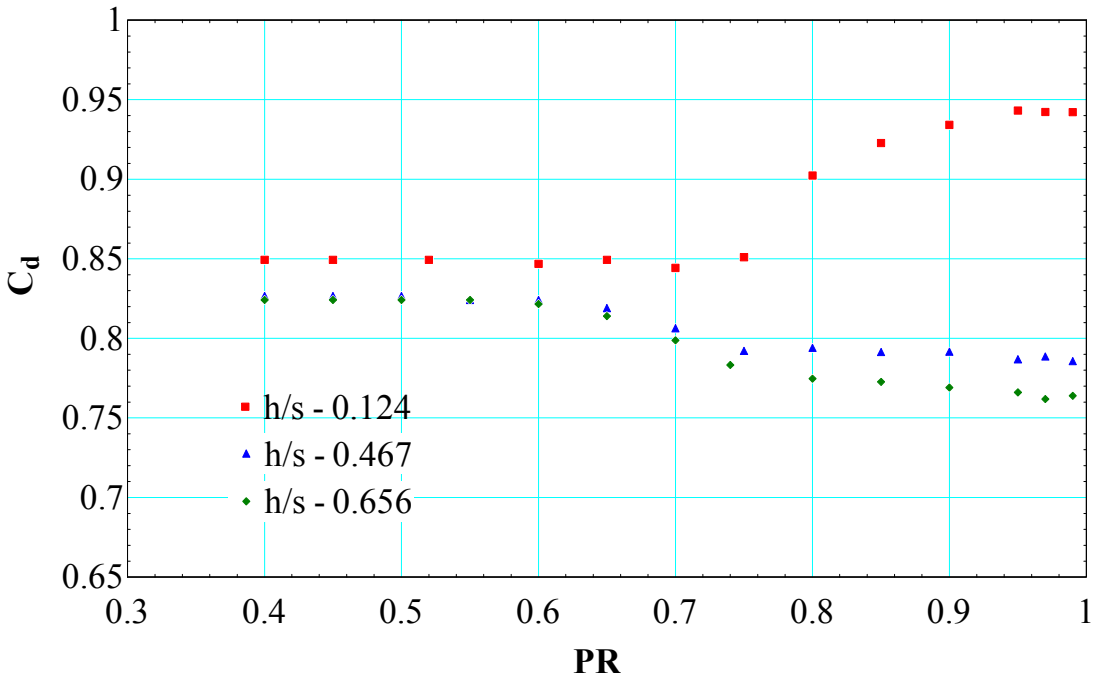

Figure 64. Variation of C_d with tooth height

5.2.4 Effect of Shaft Diameter

It can be observed from Figure 65 that the C_d of annular orifice doesn't change with shaft diameter, even after increasing the shaft diameter to 3 times the initial value (Cases 2 and 10 in Appendix B). Hence, it can be concluded that shaft diameter does not influence the value of C_d and a model which is developed for a particular shaft diameter can be applied to any shaft diameter.

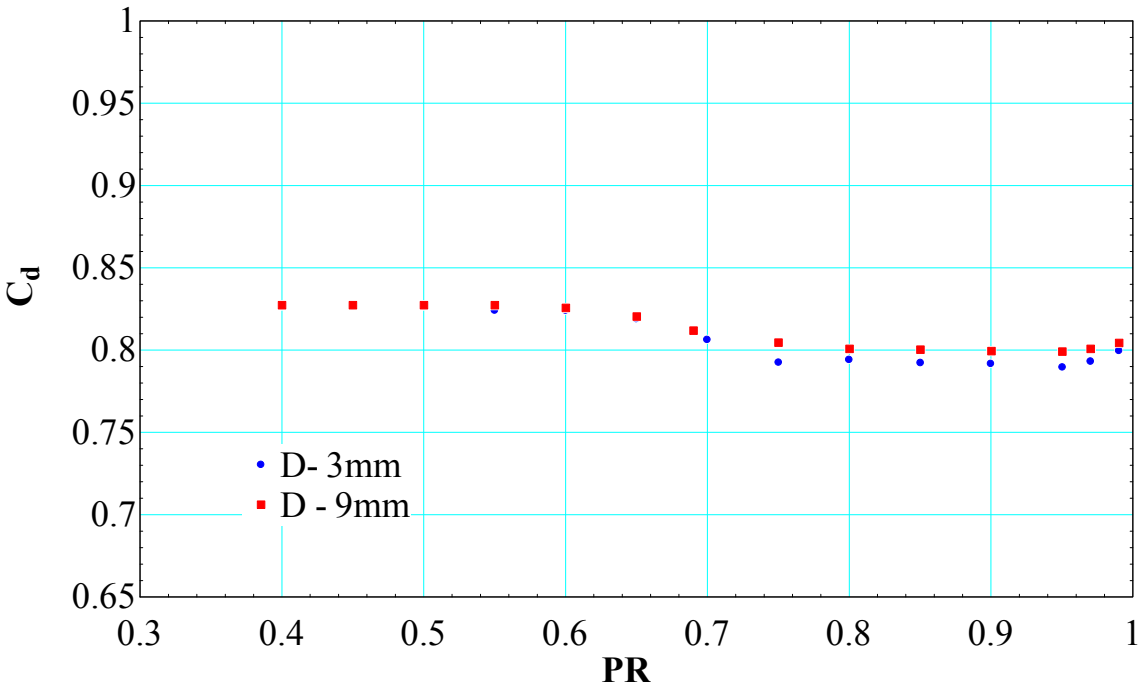

Figure 65. Variation of C_d with shaft diameter

5.2.5 Correlation for Carry over coefficient

As described by Hodkinson [18], leakage rate through a labyrinth seal can be estimated as,

$$\dot{m} = \alpha\gamma\dot{m}_{ideal} \tag{68}$$

Where $\dot{m}_{ideal}$ is the 1-D isentropic flow rate for labyrinth seals, γ is the carry over coefficient of the cavity, α is the flow coefficient similar to discharge coefficient. Following the definition presented by Hodkinson, γ is calculated as a function of the divergence angle, β, measured from the streamline separating the fluid recirculating in the seal cavity and that passing under the tooth. The carry over coefficient can be calculated based on following relationships provided by Hodkinson.

$$\gamma^2 = \frac{1}{1-\chi} \tag{69}$$

$$tan\,\beta = c\frac{(1-\chi)}{\chi s} \tag{70}$$

The divergence angle, β, is the angle made between the line connecting the lip of the upstream tooth to the point of impingement of the jet onto the downstream tooth and a line parallel to the rotor surface. Radial velocity data is collected along the downstream tooth surface and the point where radial velocity is zero is taken as the point of impingement of the jet, as shown in Figure 66. The cavity geometrical parameters are varied (single parameter is varied at a time) and model for carry over coefficient is developed to include the geometrical effects.

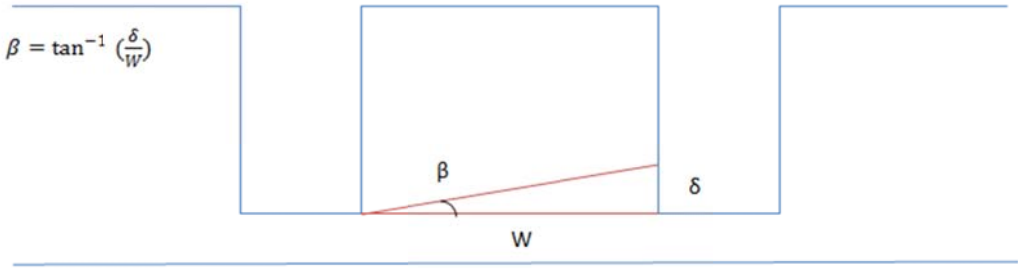

Figure 66. Measurement of divergence angle in the cavity

5.2.6 Effect of radial clearance

Hodkinson [35] used, the clearance to pitch ratio (*c/s*) as the only non-dimensional parameter to develop an empirical correlation for *γ* based on geometry. Four cases are simulated for fixed pitch but with varying clearance (cases 1-4 in Appendix C). The carry over coefficient for each of these cases is calculated and the results are presented in Figure 67. It is very important to note that γ is not a function of PR and stays constant for a fixed clearance to pitch ratio. A higher value of *c/s* results in higher carry over coefficient as, for a given jet divergence, more fluid flows under the tooth when the clearance is higher. However, increasing the clearance by a factor of

2.5 increases the carry over coefficient by only 2%. Based on these results, the carry over coefficient can be written as shown in equation (71).

$$\gamma = 0.3948\left(\frac{c}{s}\right) + 1.001 \tag{71}$$

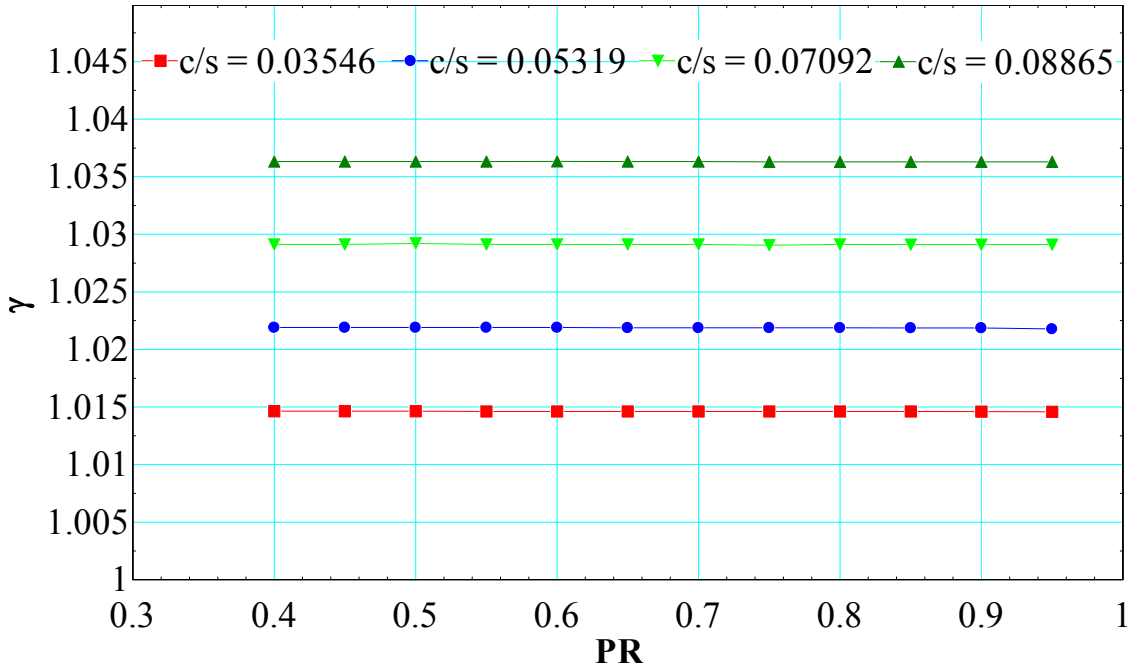

Figure 67: Effect of clearance on γ

5.2.7 Effect of Tooth Height

Changing the tooth height to pitch ratio (*h/s*) changes the aspect ratio and could possibly have some effect on recirculation in the cavity. To verify if changing the aspect ratio of the cavity affects the carry over coefficient or not, three simulations were performed by varying the cavity depth while leaving other geometrical parameters constant (cases 9, 10 and 11 in Appendix C). It can be seen from Figure 68 that the carry over coefficient is independent of *h/s*. Therefore, the conclusions from these simulations is that tooth height or cavity height has no effect on the kinetic energy carry over coefficient, which is one of the basic assumptions made by Hodkinson [18].

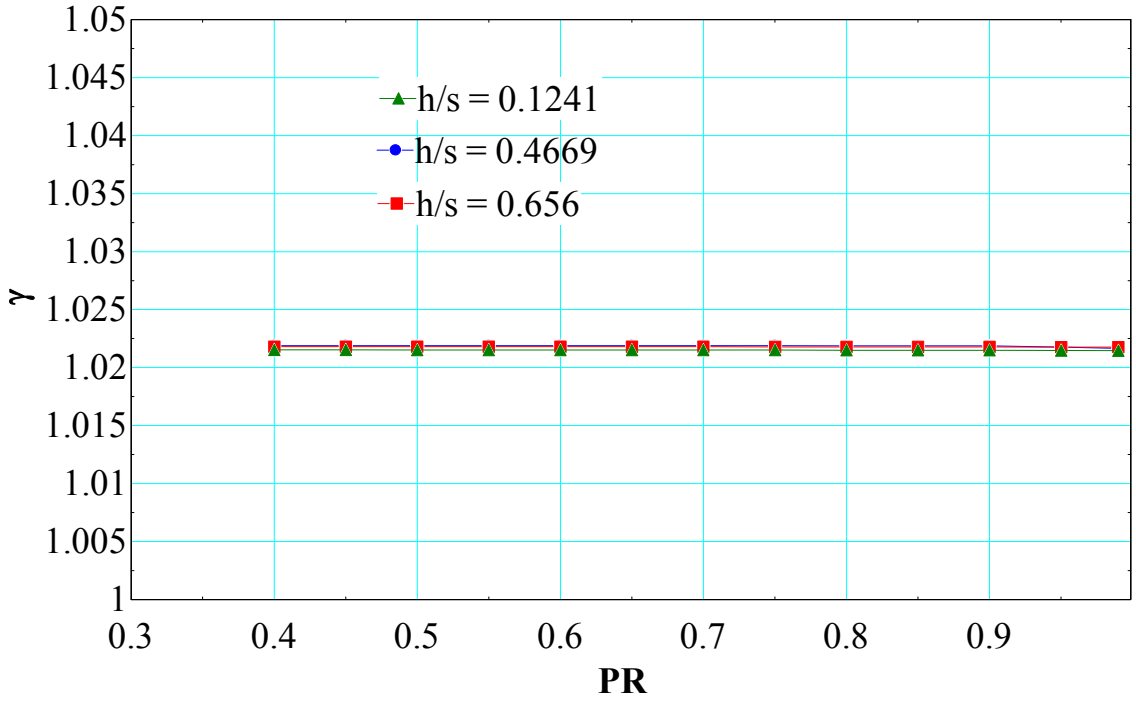

Figure 68. Effect of tooth/cavity height on γ

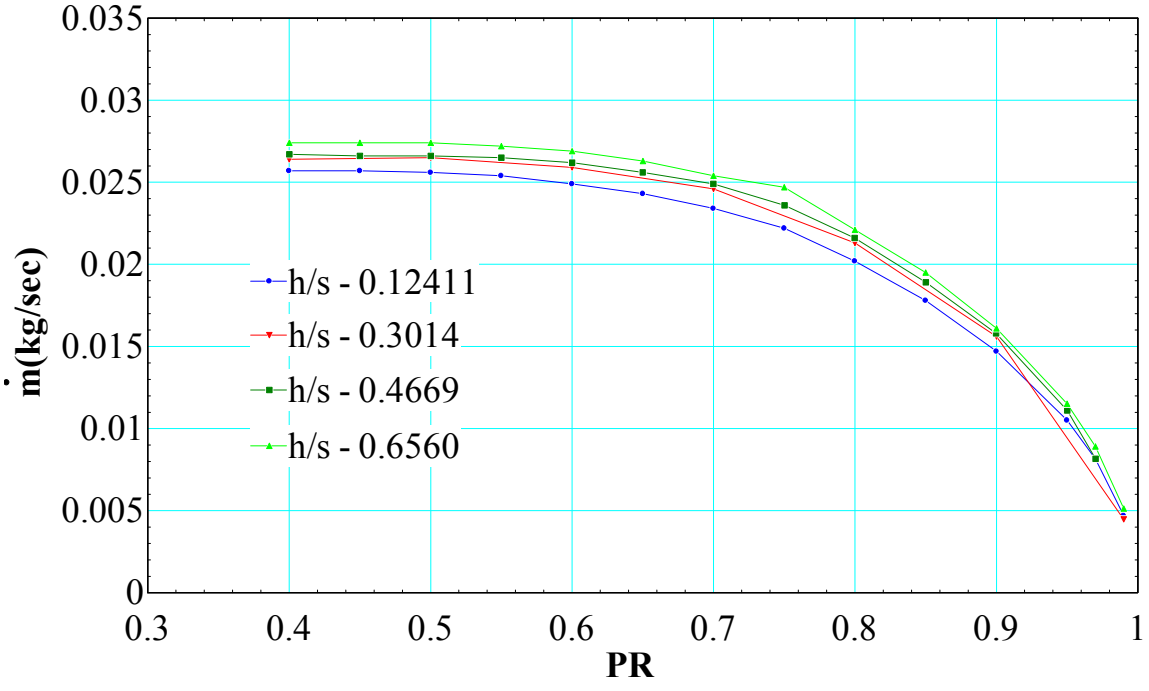

Figure 69. Effect of cavity height on leakage rate

As the cavity depth decreases it is expected that the intensity of turbulence dissipation in the cavity increases thereby decreasing the leakage rate through the seal. As shown in Figure 69 (cases 2, 9, 10 and 11 in Appendix C), the leakage rate decreases as the cavity height decreases due to the phenomenon explained above.

However, it has been shown earlier that cavity depth doesn't have any effect on carry over coefficient which would imply that the effect of change in cavity depth has to be modeled into the flow coefficient, α, described in equation (68).

5.2.8 Effect of cavity width

The vortex pattern of the flow field varies with cavity width. It is expected that, as the width of the cavity increases the intensity of the vortex pattern increases causing a reduction in the leakage rate as shown in Figure 70. (Cases 1, 5, 6, 7 and 8 in Appendix C) and Figure 71 show the variation of carry over coefficient for these cases.

It can be seen that as *w/c* increases the carry over coefficient increases whereas the leakage rate decreases. These are two contradictory results which could be due to the fact that the discharge coefficient of any tooth with a preceding cavity is different from that of a single tooth without any preceding cavity as in the case of annular orifices. So, the discharge coefficient of the first tooth in a multiple tooth labyrinth seal is similar to that of an annular orifice since it doesn't have any preceding cavity whereas the discharge coefficient from the second tooth will be a function of the discharge coefficient of the previous tooth and the carry over coefficient as shown in equation (72)

$$C_d^{n\ tooth} = f(C_d^{n-1\ tooth}, \gamma) \tag{72}$$

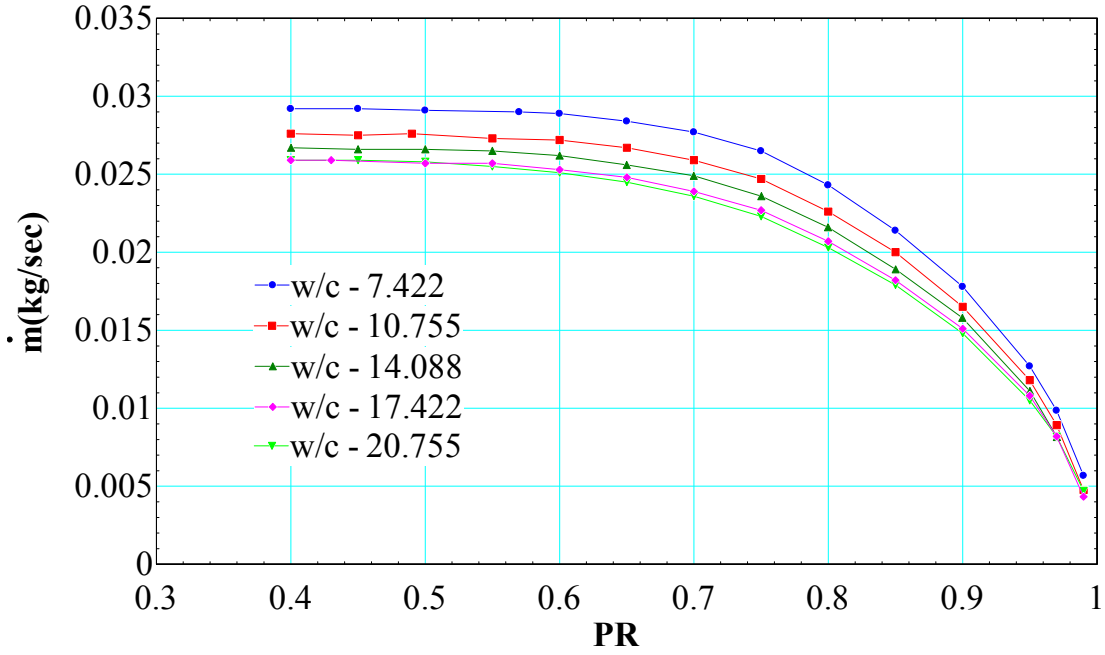

Figure 70. Effect of cavity width on leakage rate

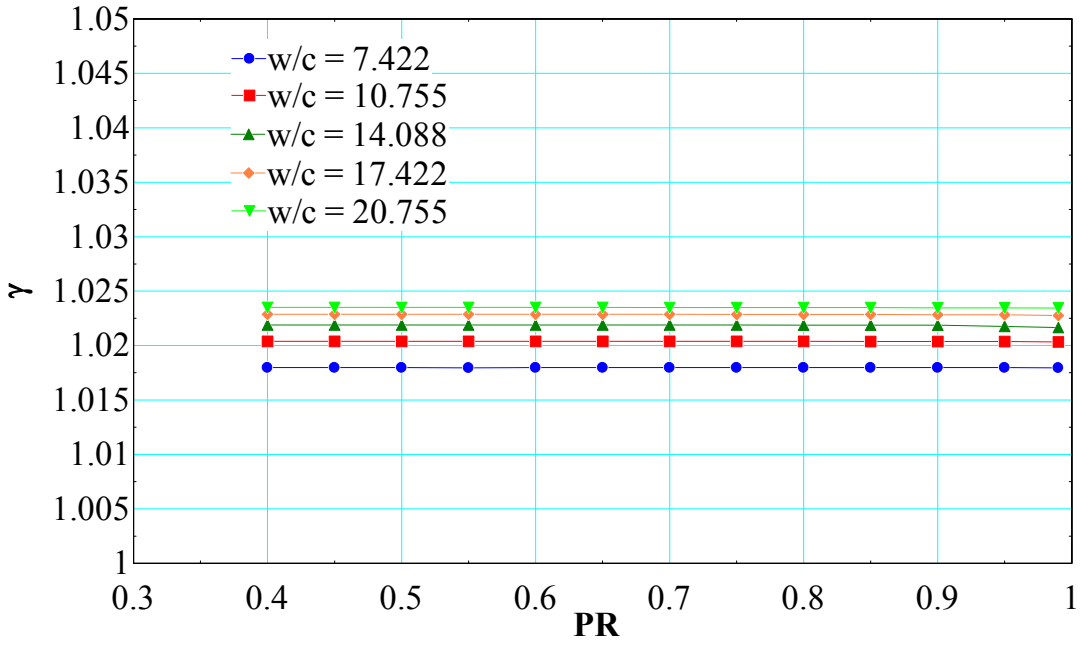

Figure 71. Variation of γ with cavity width

This can be proved by analyzing the velocity profiles at the entrance of each tooth in a three teeth labyrinth seal (Case 1 in Appendix C). Figure 72 indicates that the velocity profile at the entrance of each tooth is different. It is interesting to note that velocities at the entrance of last tooth are much higher than that of previous teeth which is due to the pressure drop being largest for the last tooth which will be shown later.

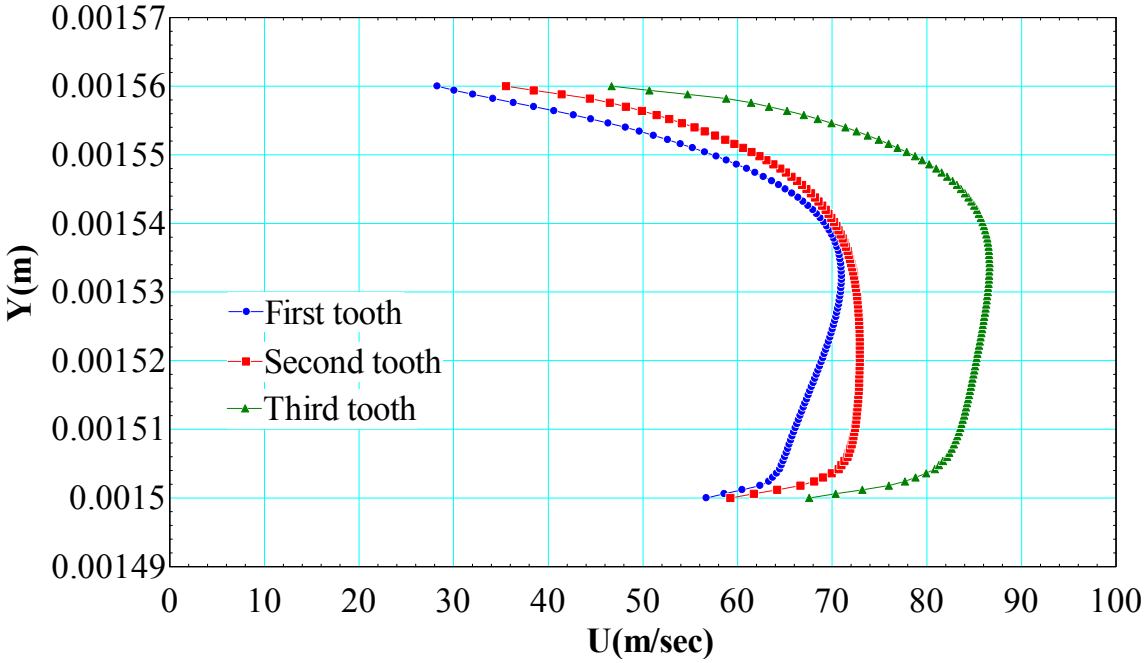

Figure 72. Velocity profile at the entrance of each tooth

Taking into account the effect of cavity width, equation (71) is modified and model for γ is developed with *c/s*, *w/c* as the non-dimensional parameters.

$$\gamma = 0.91559 + \left[0.395745 + 0.113839\left(\frac{w_{cavity}}{c}\right)\right]\left(\frac{c}{s}\right) \tag{73}$$

5.2.9 Effect of Shaft Rotation on annular orifices and labyrinth seals

A rotating shaft may change the flow pattern within the seal as it introduces swirl velocity. The speed of the shaft might influence the discharge coefficient and the carry over coefficient of flow through a labyrinth seal. Literature often presented contradictory results with some studies indicating that the shaft rotation reduced leakage rate whereas some studies showed that leakage rate increases due to shaft rotation. A report by Sandia National Laboratories (SNL) [34] indicated that shaft rotation has no influence on the leakage rate even for speeds as high as 65,000 rpm. To analyze this effect, simulations are performed for a fixed operating condition and seal geometry at different shaft speeds. First, results will be presented for discharge through annular orifices and then for labyrinth seals.

The results for annular orifices are presented in Figure 73 (cases 2, 11-16 in Appendix B) and it can be seen that for a low pressure ratio shaft rotation has nearly no influence on C_d.

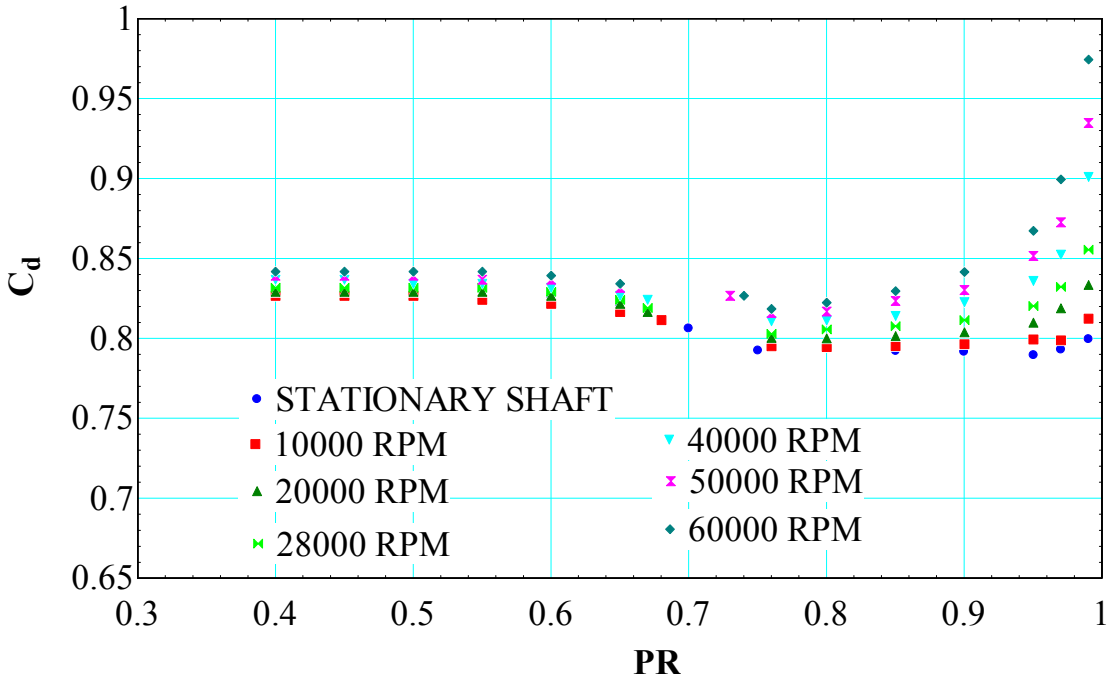

Figure 73. Influence of shaft rotation on C_d of annular orifices

This is in good agreement with the results from SNL. However, at higher PR there is a drastic increase in C_d as shown in Figure 73. The induced radial velocity due to shaft rotation increases as the shaft speed increases and is nearly independent of PR. The reason for the drastic increase in C_d might be due to the fact that induced radial velocities are comparable to axial velocities at higher PR's.

The discharge coefficient of a labyrinth seal will be a function of the C_d through an annular orifice having dimensions that of the tooth and carry over coefficient from the cavity. It has been observed that shaft rotation has no effect on the carry over coefficient as shown in Figure 74 and hence the C_d of a labyrinth seal as shown in Figure 75 (cases 2, 12-16 in Appendix C) presents a similar trend as that of an annular orifice.

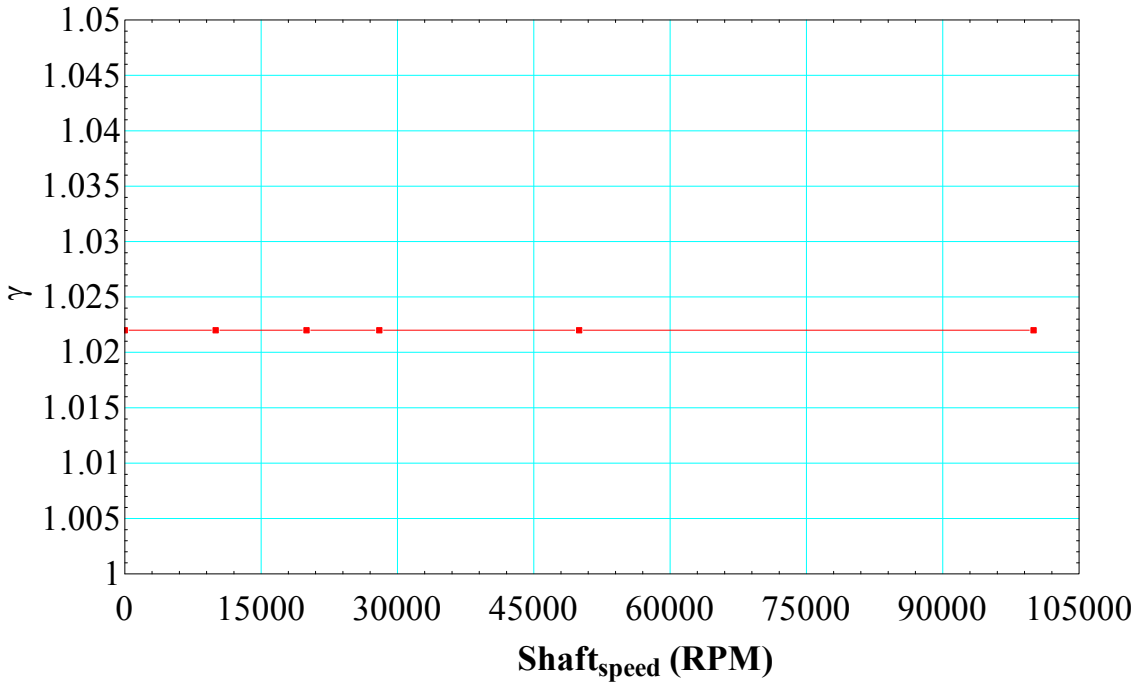

Figure 74. Variation of *γ* with shaft speed

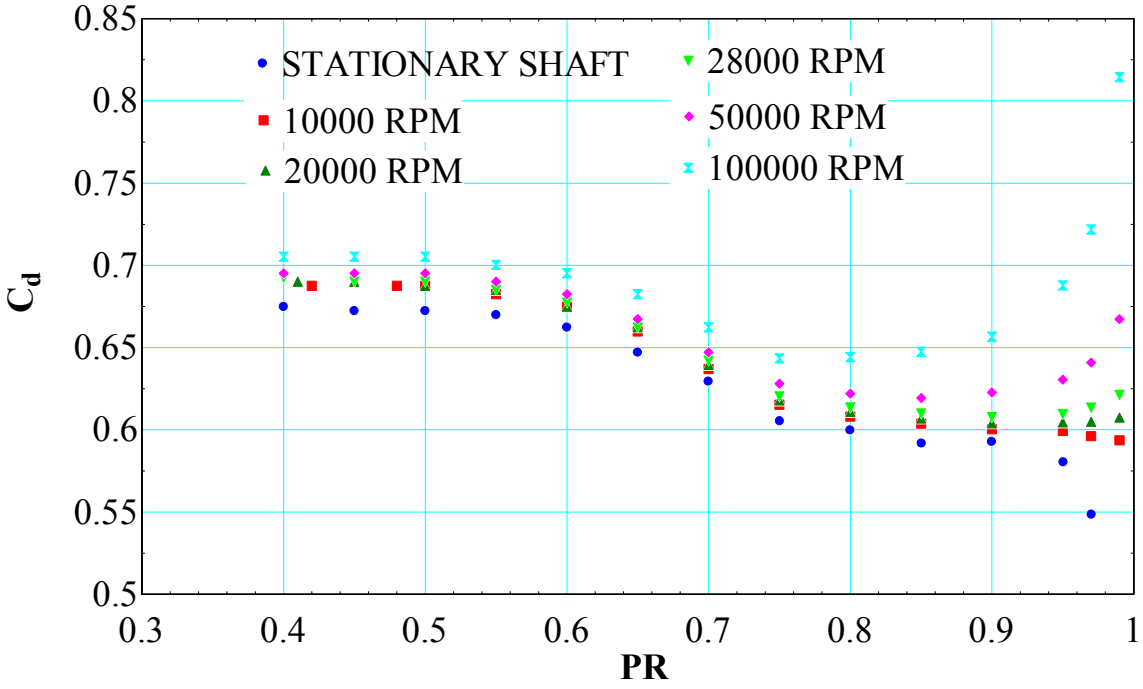

Figure 75. Variation of the C_d with shaft speed for labyrinth seals

This would imply that it is sufficient to model the influence of shaft rotation into C_d of an annular orifice. However, at these high shaft speeds, the influence of boundary layer in the θ direction might be significant and it is good practice to validate some of these results against a 3-D model or experimental data for an annular orifice, which is left as a part of future work.

To predict leakage through labyrinth seal, each tooth can be treated individually and leakage rate equation for each tooth can be written as,

$$\dot{m} = C_d|_{ntooth}\gamma\dot{m}_{isentropic} \tag{74}$$

Where C_d of the first tooth is same as that of an annular orifice and C_d from the second tooth depends on the C_d of previous tooth and γ of the cavity. For first constriction γ is equal to 1. A correlation for γ is developed earlier in this section. In future, it is proposed to develop a correlation for the discharge coefficient which can be applied to each tooth as in equation (74).

This would result in a set of equations equal to the number of teeth in a labyrinth seal. These equations can be solved simultaneously to obtain the pressure drop across each tooth and the leakage rate through the labyrinth seal. It has been found out that a 1-D isentropic model assuming that C_d = 1 and γ = 1 is good enough in predicting the leakage rate through labyrinth seals as shown below.

One Dimensional Isentropic flow model for Labyrinth seals:

The ideal leakage rate through a labyrinth seal can be calculated by assuming that the carry over coefficient ($\gamma = 1$) in cavity, which means that the kinetic energy of the jet expanding from the tooth is completely dissipated in following cavity.

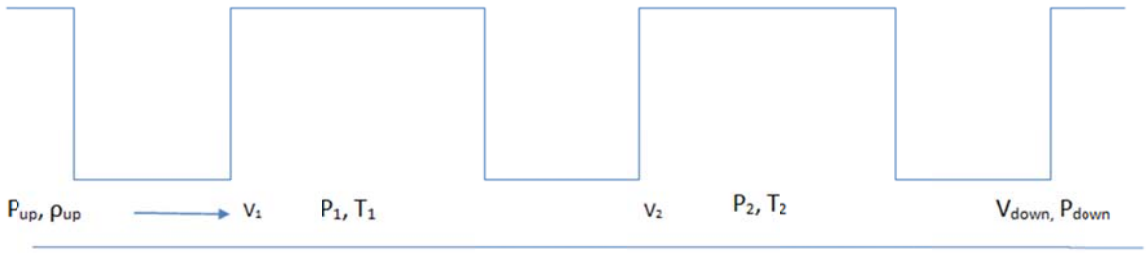

The 1-D isentropic model equations for Labyrinth seals are as follows:

$$S_{up} = S(P_{up}, \rho_{up}) \tag{75}$$

$$S_{up} = S_1 = S_2 = S_{down} \tag{76}$$

$$h_{up} = h(P_{up}, \rho_{up}) \tag{77}$$

$$h_1 = h(P_1, S_1),\ \rho_1 = \rho(P_1, S_1) \tag{78}$$

$$h2 = h(P_2, S_2),\ \rho_2 = \rho(P_2, S_2) \tag{79}$$

$$h_{down} = h(P_{down}, S_{down}),\ \rho_{down} = \rho(P_{down}, S_{down}) \tag{80}$$

$$h_{up} = h_1 + \frac{V_1^2}{2} \tag{81}$$

$$h_1 = h_2 + \frac{V_2^2}{2} \tag{82}$$

$$h_2 = h_{down} + \frac{V_{down}^2}{2} \tag{83}$$

$$\dot{m}_{ideal} = \rho_1 A_{clearance} V_1 = \rho_2 A_{clearance} V_2 = \rho_{down} A_{clearance} V_{down} \tag{84}$$

The Above set of equations are modeled in EES and solved simultaneously to obtain 1-D isentropic leakage rate for labyrinth seals without carry over. Although, the equations presented here are for three teeth cases, these equations can be extended to a labyrinth seal with any number of teeth. The behavior of this model is quite similar to that of an annular orifice model. The isentropic leakage rate increases until the choking PR and then starts decreasing. Again, these calculations are run through min/max function in EES and the modified leakage rate will be used for multiple teeth cases as well. The model assumes temperature and pressure to be constant across the cavity in the radial clearance region. The question now is: "How valid is this assumption?"

To answer this question, temperature and pressure in the radial clearance region are plotted for one of the cases (Case 1 in Appendix C). From Figure 76 it can be observed that for a pressure drop as high as 6 MPa, pressure remains fairly constant throughout the cavity. It can also be seen from Figure 77 that temperature also follows the same trend. It is also interesting to note that majority of the pressure and temperature drop occurs across the last tooth. This would imply that leakage rate through labyrinth seal is dictated by the C_d of last tooth.

The 1-D isentropic model for labyrinth seal, described above is applied to case 2 in Appendix C. From Figure 78, it can be seen that a simple 1-D isentropic model for labyrinth seals assuming the C_d and the γ are equal to 1, works reasonably well in predicting leakage through multiple constrictions. The drawback of this 1-D isentropic model is that it doesn't take into

consideration the geometrical parameters of labyrinth seals and is only dependent on the number of constrictions and radial clearance.

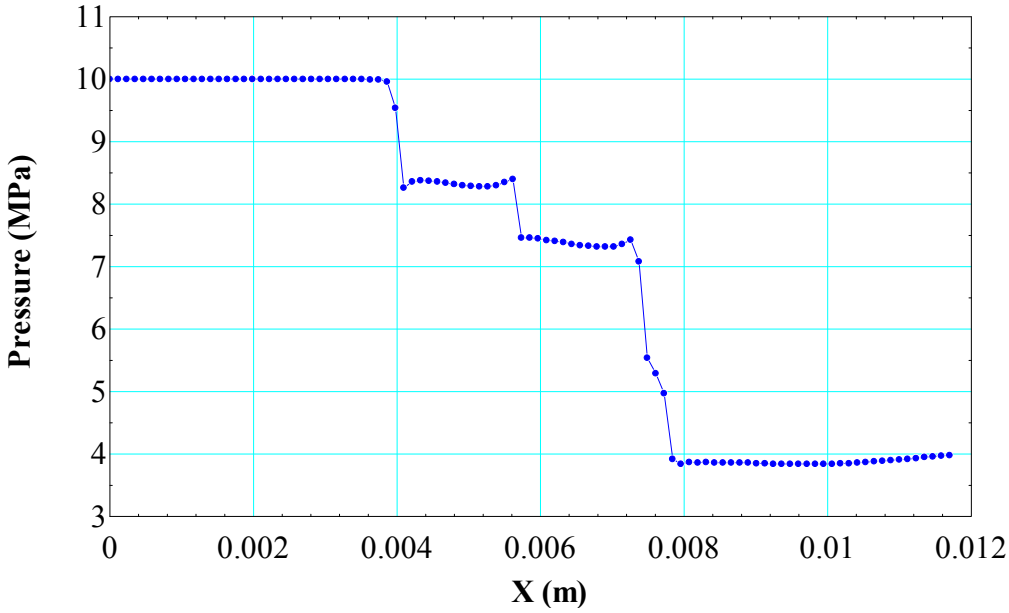

Figure 76. Pressure variation along centerline in the radial clearance region

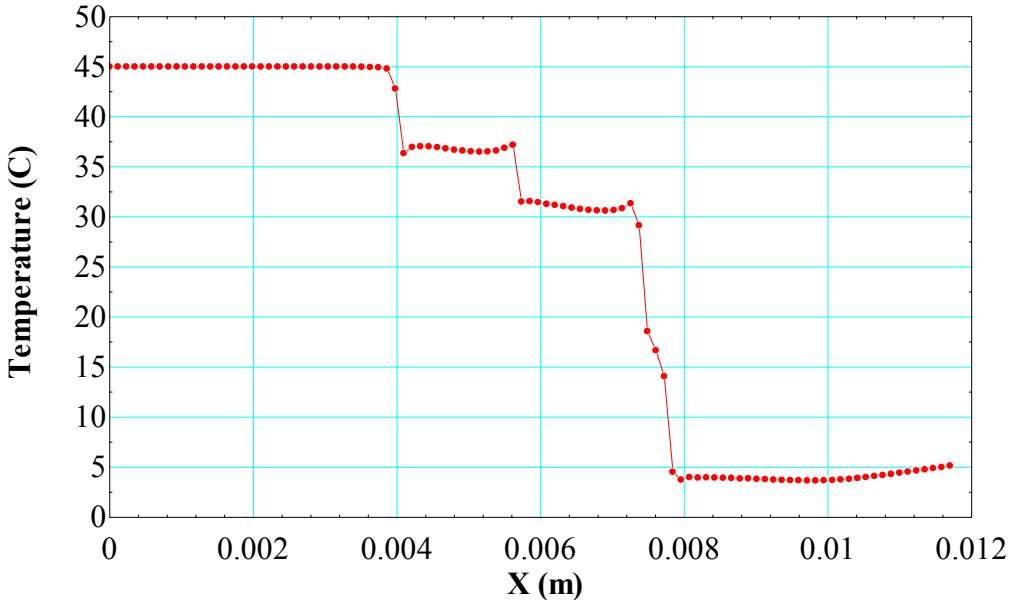

Figure 77. Temperature variation along centerline in the radial clearance region

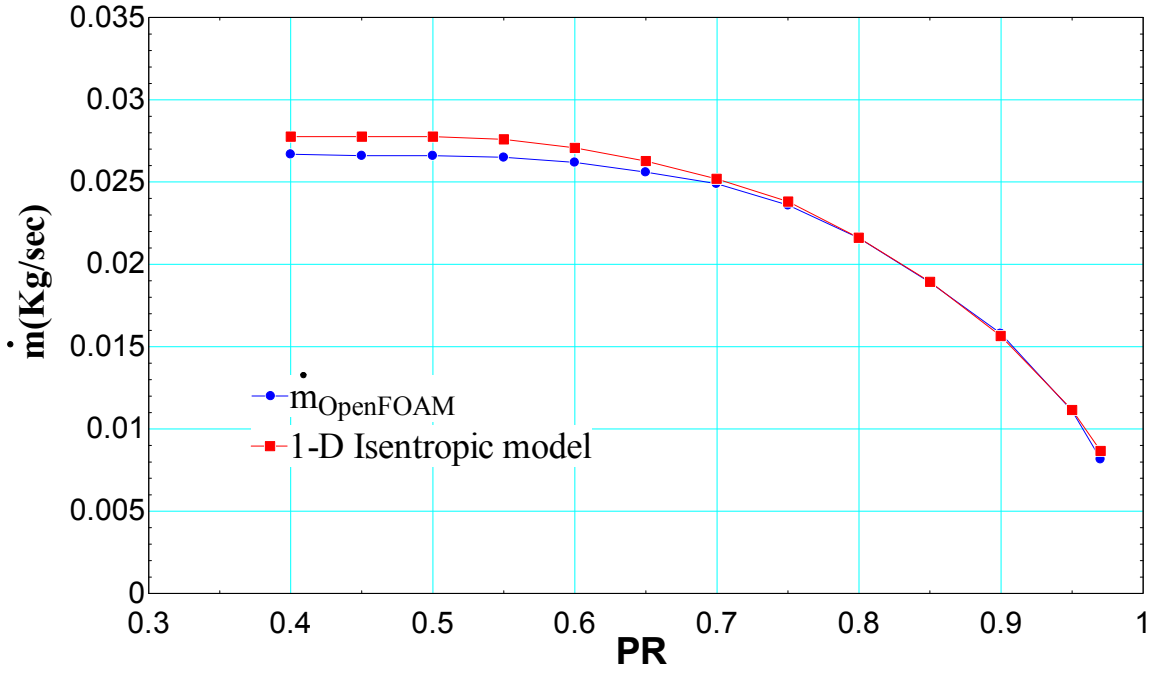

Figure 78. Leakage rate prediction using 1-D isentropic model for case 2 in Appendix C

5.3 Effect of Operating Conditions

The previous section explained the effects of geometrical parameters while holding the inlet operating condition constant at 10 MPa, 498 kg/m^3. In this section we will look at the effect of operating conditions without changing geometry. First, the effect of operating conditions on an annular orifice will be studied and then the theory will be extended to labyrinth seals. Before even performing simulations, a simple 1-D isentropic model for annular orifices is used to understand the effects of operating conditions.

According to the 1-D isentropic flow model for annular orifices,

$$\dot{m} = \rho_{down} * V_{down} * A_{clearance} \tag{85}$$

$$V_{down} = \sqrt{2(h_{up} - h_{down})} \tag{86}$$

For a given inlet condition and constant entropy condition, every variable in these equations is a function of the downstream pressure only. To find where the mass flow rate reaches its maximum value, the derivative of $\dot{m}$ with respect to P_{down} (downstream pressure) can be set to zero.

$$\frac{d\dot{m}}{dP_{down}} = \sqrt{2(h_{up} - h_{down})}\frac{d\rho_{down}}{dP_{down}} - \frac{\rho_{down}}{\sqrt{2(h_{up}-h_{down})}}\frac{dh_{down}}{dP_{down}} = 0 \qquad (87)$$

Rearranging the above equation one can obtain,

$$\frac{dh_{down}}{d\rho_{down}} = \frac{2(h_{up}-h_{down})}{\rho_{down}} \qquad (88)$$

From equation (88) it can be seen that for a given inlet condition there is a corresponding outlet pressure that will satisfy this equation and that the mass flow rate is maximum. These equations are modeled in EES and the behavior of the isentropic model is studied as inlet conditions are varied. All the inlet conditions are shown on a T-s diagram in Figure 79. Three inlet entropies and four inlet pressures are tested.

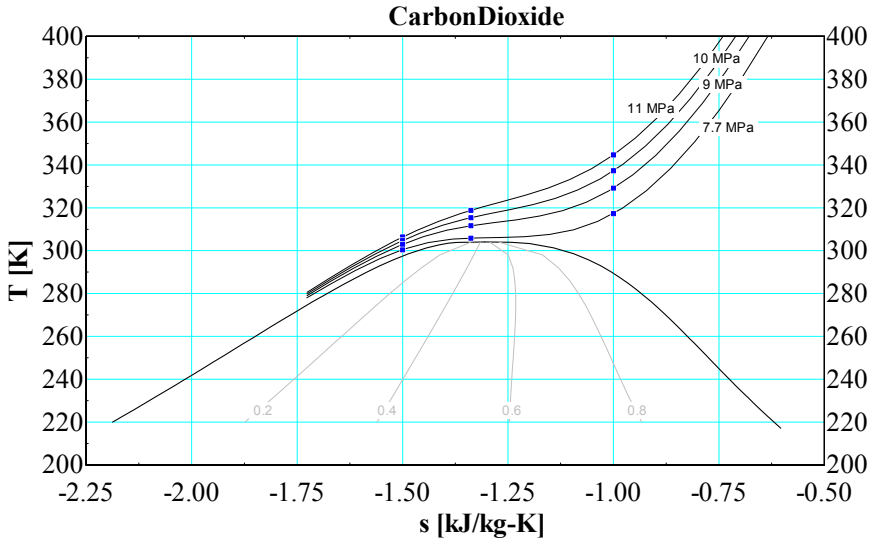

Figure 79. Inlet conditions used for testing 1-D isentropic model

The results of the1-D isentropic flow model are presented in Figures (80, 81 and 82). Some very important conclusions can be drawn from the behavior of the1-D isentropic model as inlet conditions are changed. Firstly, it can be seen that if geometry is fixed and the operating conditions are changed, the pressure at which the flow chokes changes as well as the leakage rate changes. For inlet entropy (S_{in}) = -1.0 KJ/Kg-K (right side of the two phase dome), the inlet pressures of 9 MPa and 10 MPa choke very close to the saturation pressure when the flow is expanded isentropically. Inlet pressure of 11 MPa choke before the flow enters two phase dome or chokes in superheated region for this particular entropy, whereas inlet pressure of 7.7 MPa chokes late into the two phase dome.

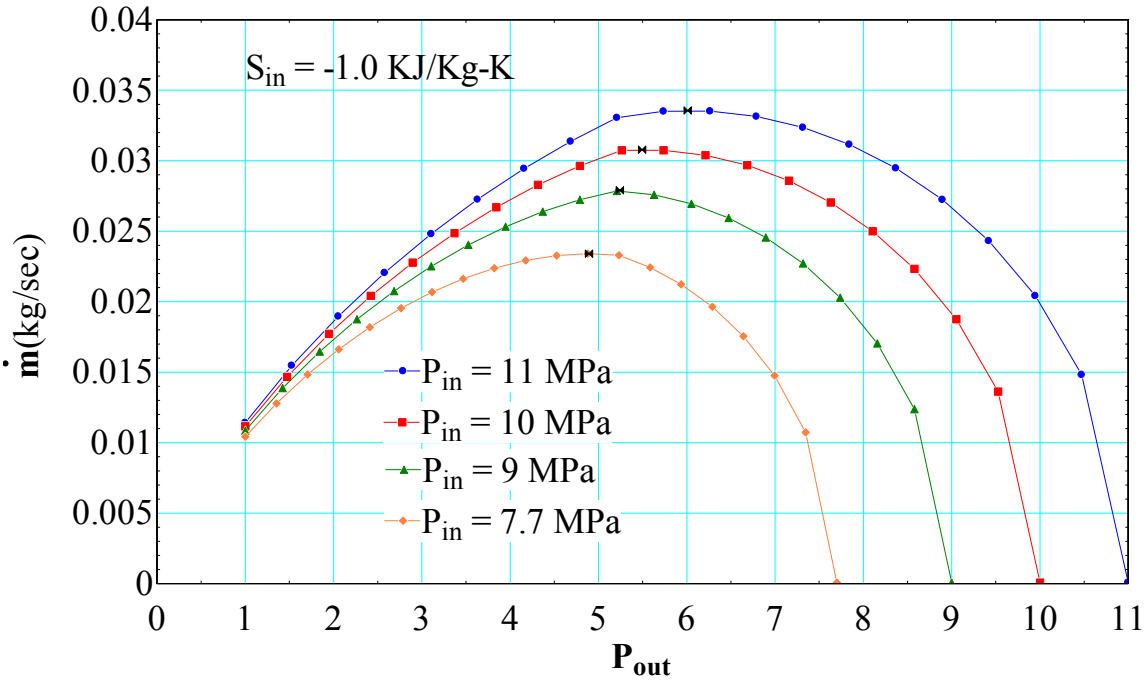

Figure 80. Isentropic flow behavior for Sin = -1.0 KJ/Kg-K

For S_{in} = -1.338 KJ/Kg-K (very close to the critical point), inlet pressures of 11Mpa and 10Mpa choke at the critical point which is very close to the saturation pressure for this entropy whereas inlet pressures of 9Mpa and 7.7Mpa choke very late into the saturation dome.

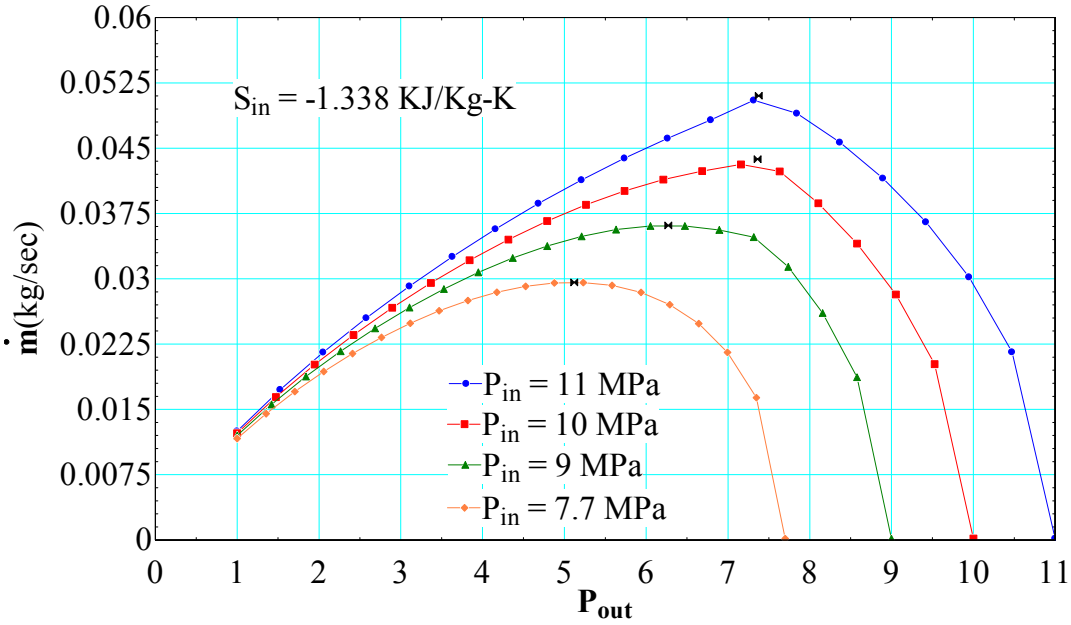

Figure 81. Isentropic flow behavior for Sin = -1.338 KJ/Kg-K

For S_{in} = -1.5 KJ/Kg-K (left side of the two phase dome), the inlet pressures of 11MPa, 10MPa, and 9MPa choke right where the flow enters the saturation dome, whereas the inlet pressure of 7.7Mpa chokes late into the saturation dome.

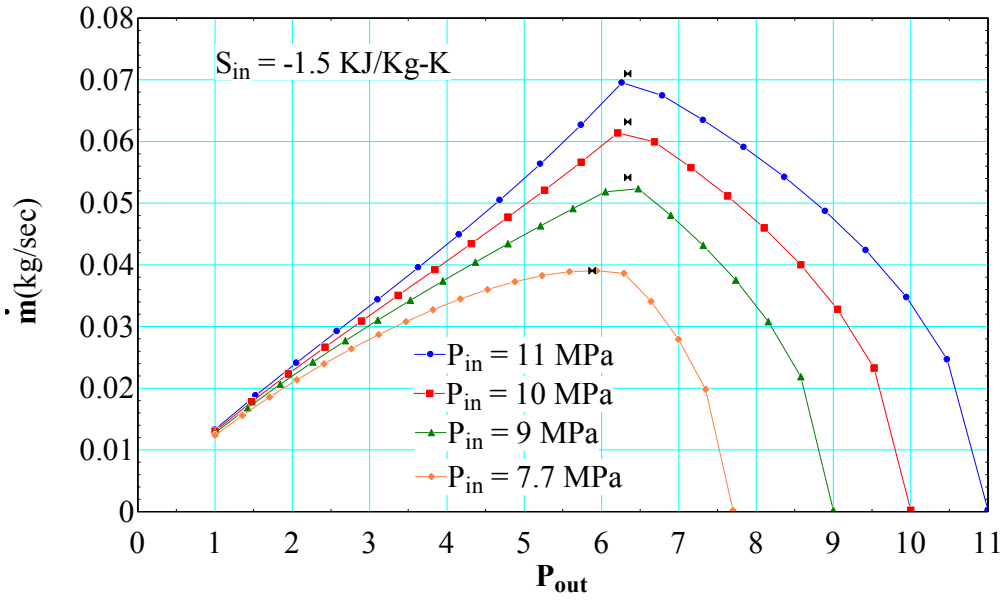

Figure 82. Isentropic flow behavior for S_{in} = -1.5 KJ/Kg-K

Table III is generated to show the choking and saturation pressures for different inlet pressures and entropy conditions. From this analysis, we can ask ourselves a very valid question: “What is determining the choking point for each operating condition?” The isentropic flow theory explained in the next few pages of this report gives an idea about the choking behavior as operating conditions are varied.

Table III Choking and saturation pressures for various operating conditions

S_{in} [KJ/Kg-K]	P_{in}[MPa]	$P_{choking}$[MPa]	$P_{saturation}$[MPa]
-1.0	11	6.011	5.243
-1.0	10	5.494	5.243
-1.0	9	5.243	5.243
-1.0	7.7	4.892	5.243
-1.5	11	6.338	6.338
-1.5	10	6.338	6.338
-1.5	9	6.338	6.338
-1.5	7.7	5.887	6.338
-1.338	11	7.376	~ critical pressure
-1.338	10	7.362	~ critical pressure
-1.338	9	6.271	~ critical pressure

-1.338	7.7	5.121	~ critical pressure

From first law of Thermodynamics for a quasi-static process,

$$dh = \delta Q + v\, dP \tag{89}$$

According to Clausius equality, for a reversible process

$$\oint \frac{\delta Q}{T} = 0 \xrightarrow{yields} \delta Q = T\, ds \tag{90}$$

Hence,

$$dh = T\, ds + v\, dP \tag{91}$$

For an isentropic flow, $ds = 0$ implies

$$\rho\, dh = dP \tag{92}$$

Equation (92) can be applied to downstream condition as,

$$\rho_{down} \frac{dh_{down}}{d\rho_{down}} = \frac{dP_{down}}{d\rho_{down}} = c^2 \tag{93}$$

Equation (93) can be rearranged as,

$$\frac{dh_{down}}{d\rho_{down}} = \frac{2(h_{up} - h_{down})}{\rho_{down}} \tag{94}$$

$$\rho_{down} \frac{dh_{down}}{d\rho_{down}} = 2\left(h_{up} - h_{down}\right) = V_{down}^2 \tag{95}$$

From equations (93 and 95), the true definition of the choking point is

$$V_{down}^2 = c^2 \tag{96}$$

To answer the question raised earlier, downstream velocity (V_{down}) and local speed of sound (c) at the exit are plotted in Figure 83 for a given inlet pressure and entropy as a function of outlet pressure. From equation (93) for a fixed inlet entropy the local speed of sound is only a function of the outlet pressure which is represented by the black curve in Figure 83. It should be noted that there is a sudden drop in local speed of sound which occurs right when the fluid enters saturation dome, which is the main criteria dictating the choking phenomenon. The homogeneous equilibrium model (HEM), as explained earlier, is assumed to calculate local speed of sound in the saturation dome. As inlet pressure increases, the downstream velocity increases for a given outlet pressure and as the outlet pressure is decreased, at a point velocity will be equal to the local speed of sound which is the choking point. The sudden change in the speed of sound occurs almost instantaneously at the saturation pressure for a given inlet entropy condition.

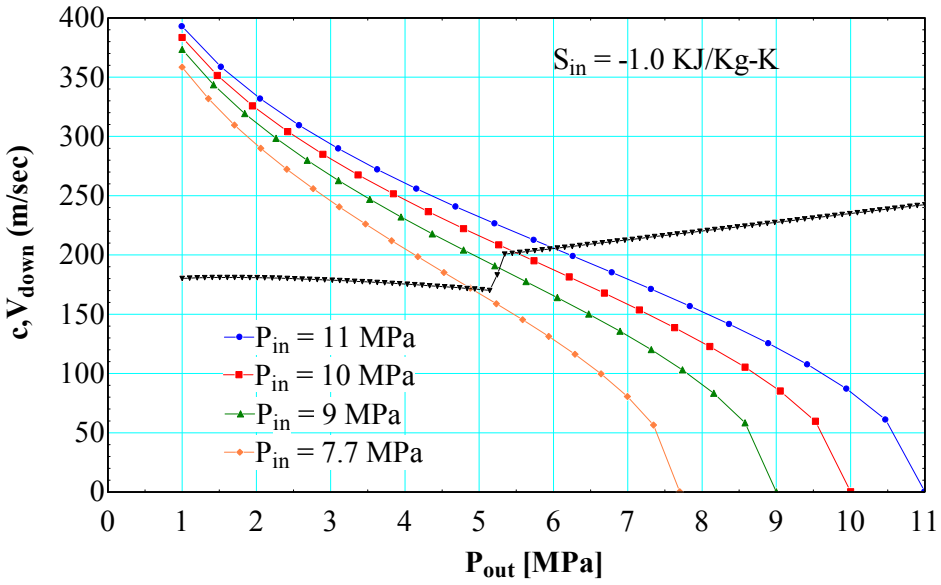

Figure 83. Downstream velocity and local sound speed of an annular orifice as a function of outlet pressure

From a general observation of Figure 83 it can be said that for a given inlet entropy condition, there exists a range of inlet pressures for which the downstream velocity intersect the sound speed curve very close to the saturation pressure. Following the above theory, inlet entropy is varied from $-0.75\frac{KJ}{Kg-K}$ to $-1.75\frac{KJ}{Kg-K}$ with an increment of $-0.05\frac{KJ}{Kg-K}$ and the upper and lower limit of inlet pressure for which the flow chokes at the saturation point is calculated for each S_{in}. The results of the above calculations are presented in Figure 84 and the following conclusions are made:

a) If the inlet condition is bounded by the two curves, the flow chokes very close to the saturation point/ when flow enters the saturation dome.

b) If the inlet condition is above both the curves, the flow chokes before it enters the saturation dome.

c) If the inlet condition is below both the curves, the flow chokes late into the saturation dome.

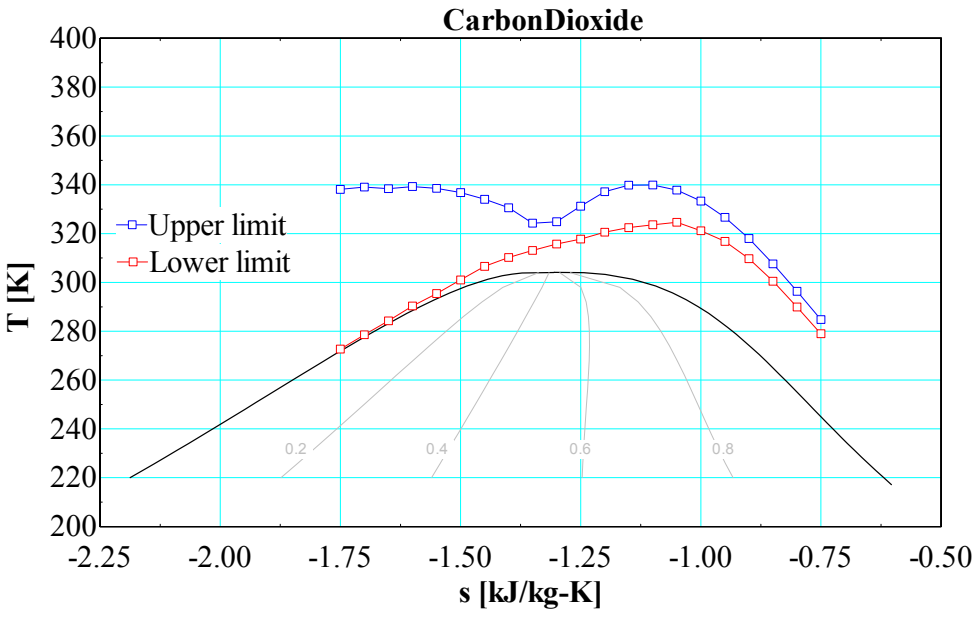

Figure 84. Choking theory for isentropic flow.

The theory derived above is based on the isentropic flow assumption. So, the next question is: "Is this model valid for a real flow situation?" To check the validity of this model simulations are performed for annular orifices holding the geometry constant and varying operating conditions as shown in (Table D.1 of Appendix D).

5.3.1 Results for Annular orifice

The geometry of the annular orifice used for these simulations is the same as the geometry of case 2 in Appendix B. Simulations are performed for two different inlet densities (372 kg/m^3 and 498 kg/m^3) at an inlet pressure of 9 MPa (cases 4 and 5 of Table D.1 in Appendix D) and the leakage rate through the annular orifice for both these operating conditions are plotted in Figures 85 and 86. It can be noted that for a fixed inlet pressure as inlet density is increased the leakage rate increases which is what one would expect to see. However, it is interesting to note that the discharge coefficient for both these cases is nearly the same for all pressure ratios as can be seen from Figure 87. The discharge coefficient stays constant at about 0.8 for higher pressure ratios before starting to increase.

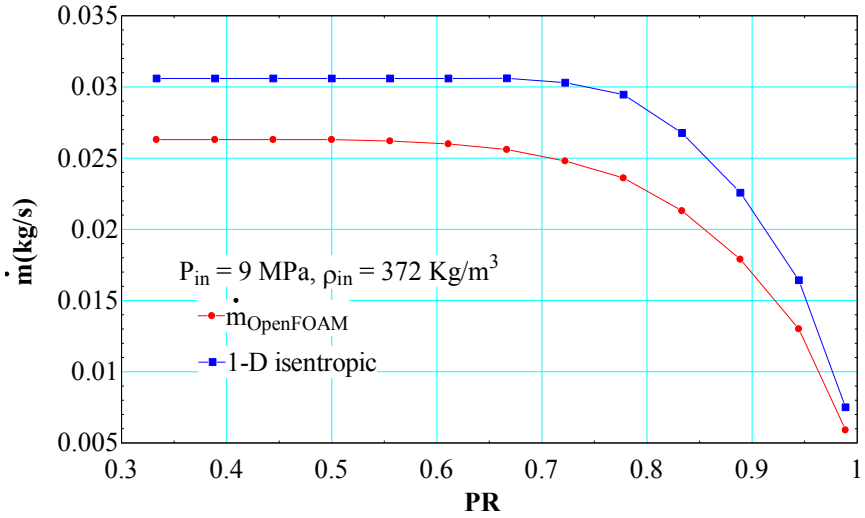

Figure 85. Leakage rate for inlet condition of 9 MPa and 372 Kg/m^3

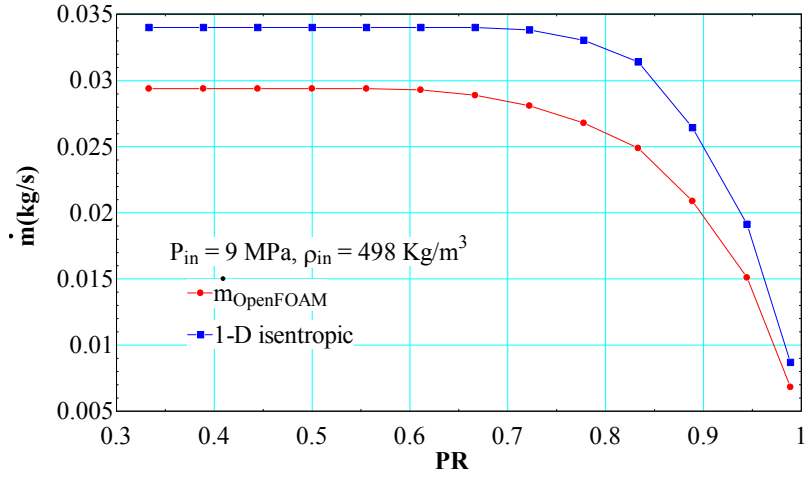

Figure 86. Leakage rate for inlet condition of 9 MPa and 498 Kg/m^3

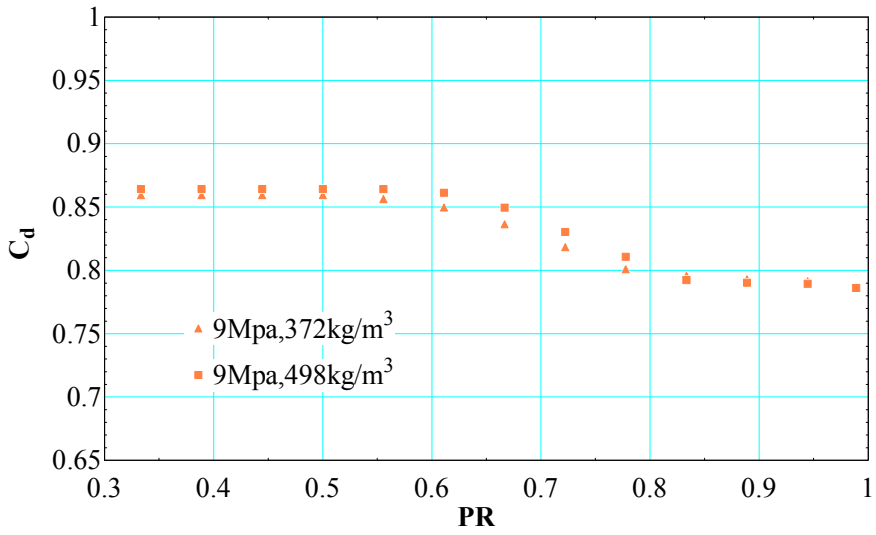

Figure 87. C_d for cases 4 and 5 in Table D.1 of Appendix D

Next, the inlet density is fixed as (372 kg/m^3 and 498 kg/m^3), the inlet pressure is increased to 10 MPa (case 3 in Table D.1 of Appendix D and case 2 in Appendix B) and the leakage rate through the annular orifice for both these operating conditions is plotted in Figures (88 and 89). Again, the leakage rate is higher for higher density case and the discharge coefficient is the same for both these cases as shown in Figure 90.

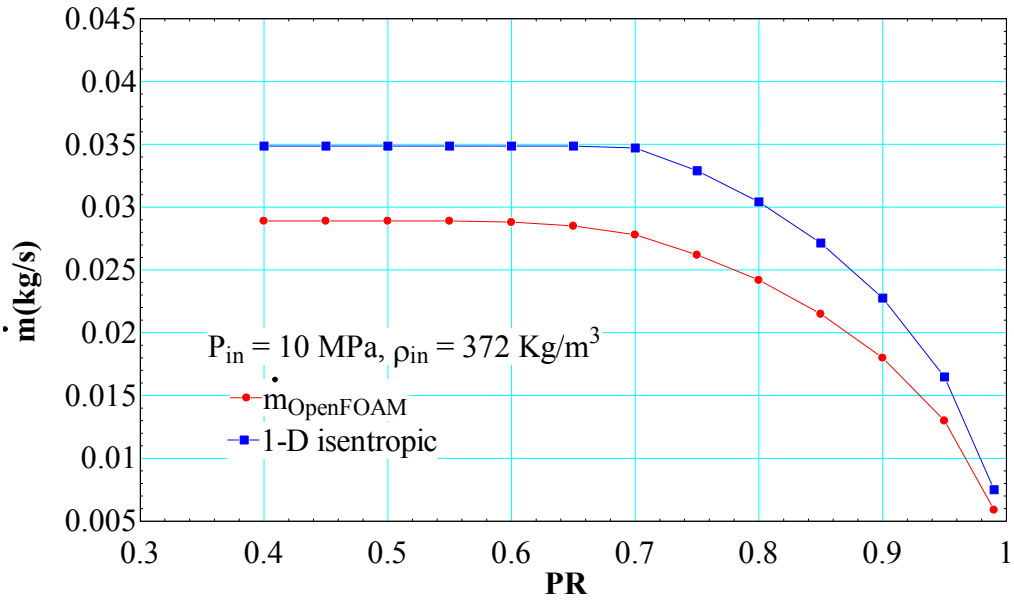

Figure 88. Leakage rate for inlet condition of 10 MPa and 372 Kg/m^3

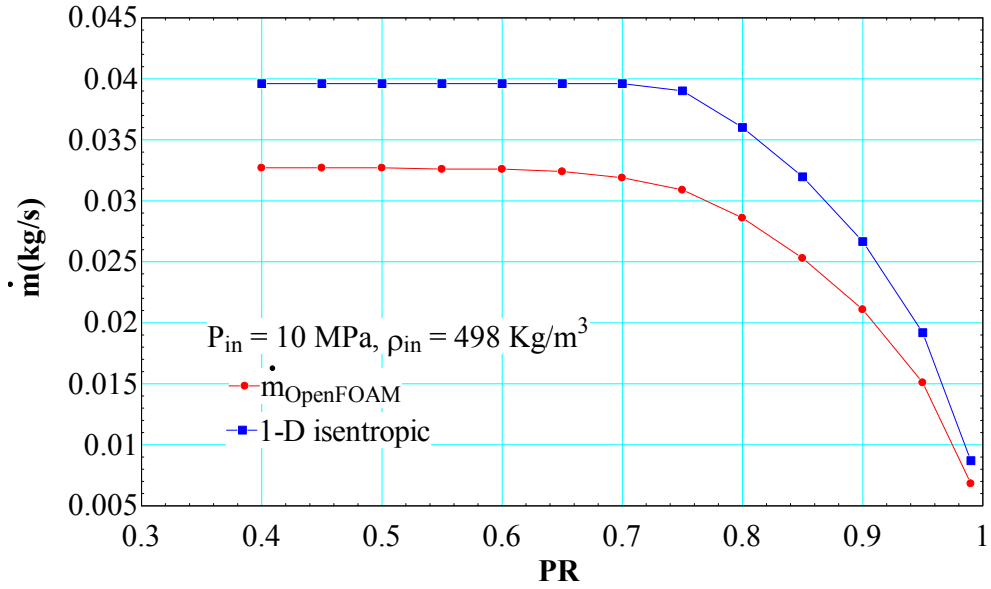

Figure 89. Leakage rate for inlet condition of 10 MPa and 498 Kg/m^3

It can be noted from a comparison of the discharge coefficient plots (Figures 87 and 90) that as pressure increases, the increase in C_d from higher PR to lower PR decreases. In other words, as the pressure increases, the discharge coefficient tends to stay constant over the whole range of

PR. In order to see if this is really true, the inlet pressure was increased to 11 MPa and simulations (Cases 1 and 2 in Table D.1 of Appendix D) are performed for two inlet densities (372 kg/m^3 and 498 Kg/m^3) and the results for leakage rate are presented in Figures (91 and 92). The discharge coefficient for these two cases is plotted in Figure 93.

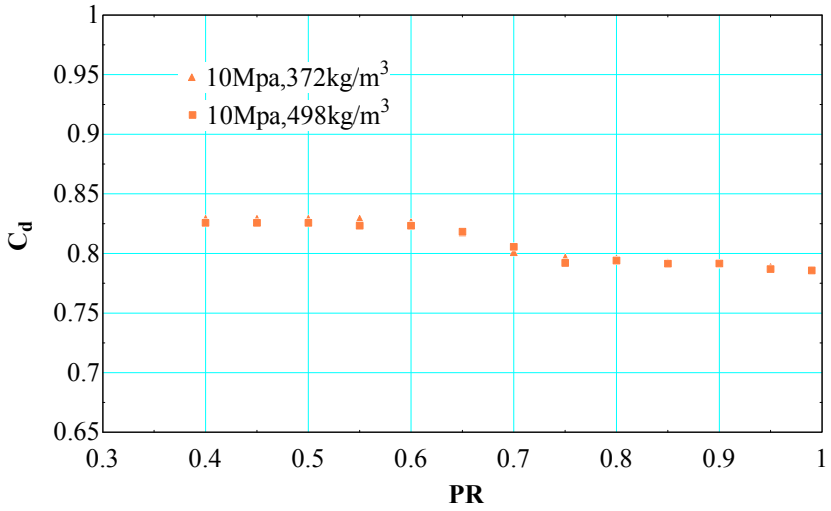

Figure 90. C_d for case 3 in Table D.1 and case 2 in Appendix B

It is interesting to note that discharge coefficient stays nearly constant at 0.8 for both these cases which would mean that choking pressure ratio predicted by the simulations and isentropic model are nearly the same.

One case very close to the critical pressure is simulated (case 6 in Table D.1). It can be seen from the C_d plot, shown in Figure 94 that spread in the C_d is much higher for this case compared to the high pressure cases (9, 10 or 11Mpa). Inlet conditions which are near the critical point are particularly hard to simulate because they are very close to the saturation dome and tend to deviate from the homogeneous equilibrium model as soon as they enter the saturation dome. As the discharge coefficient is only a function of the inlet pressure for inlet densities tested, it

might be safely assumed that for a given inlet pressure, there exists a range of inlet densities for which discharge coefficient is only a function of inlet pressure.

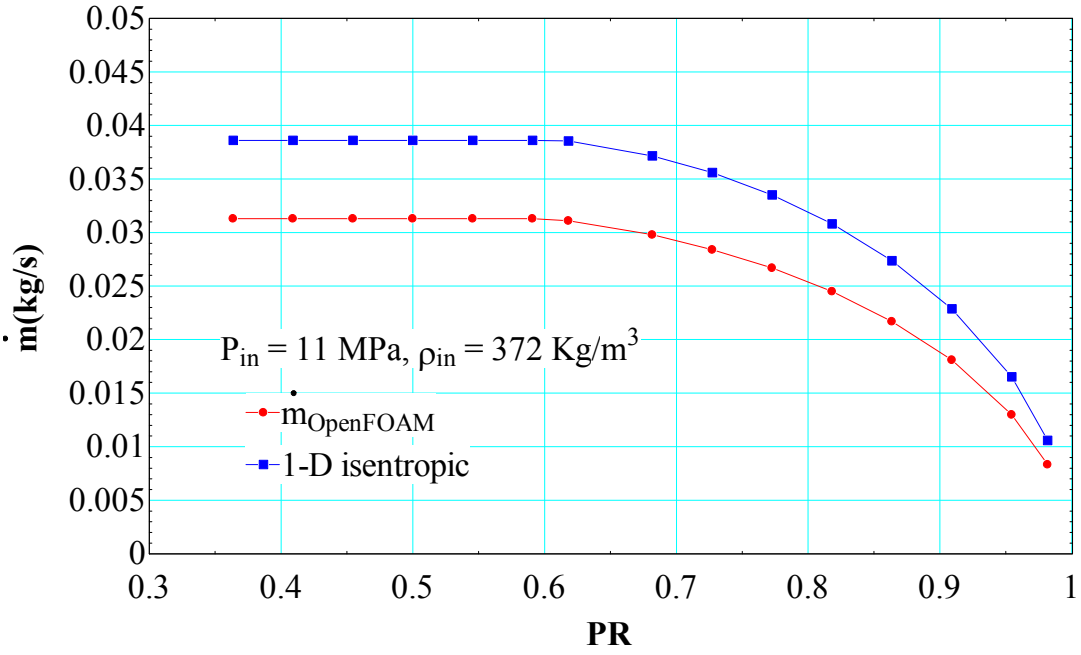

Figure 91. Leakage rate for inlet condition of 11 MPa and 372 Kg/m^3

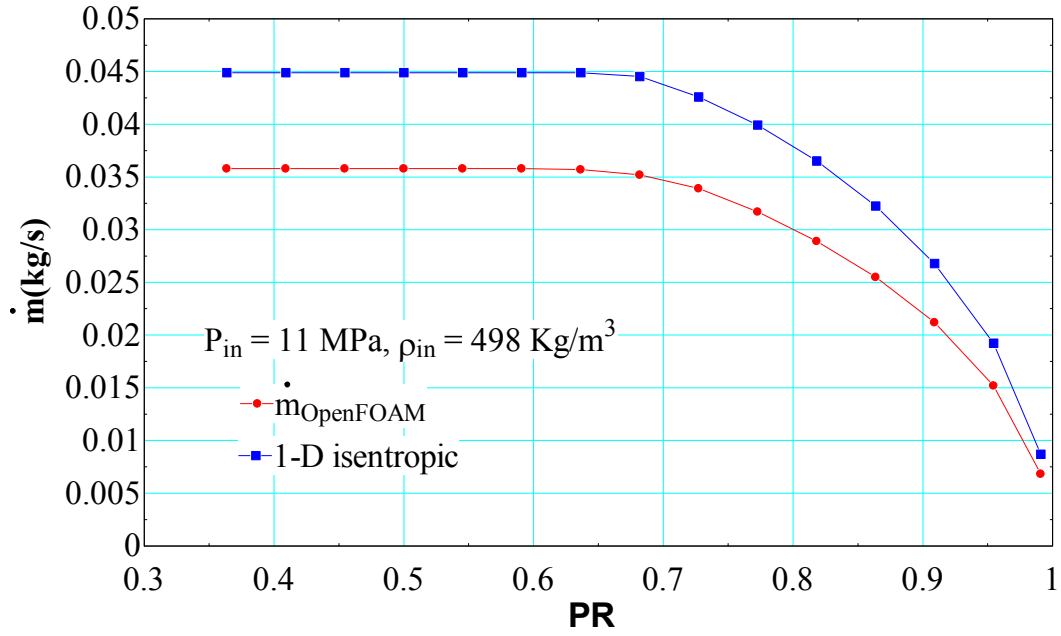

Figure 92. Leakage rate for inlet condition of 11 MPa and 498 Kg/m^3

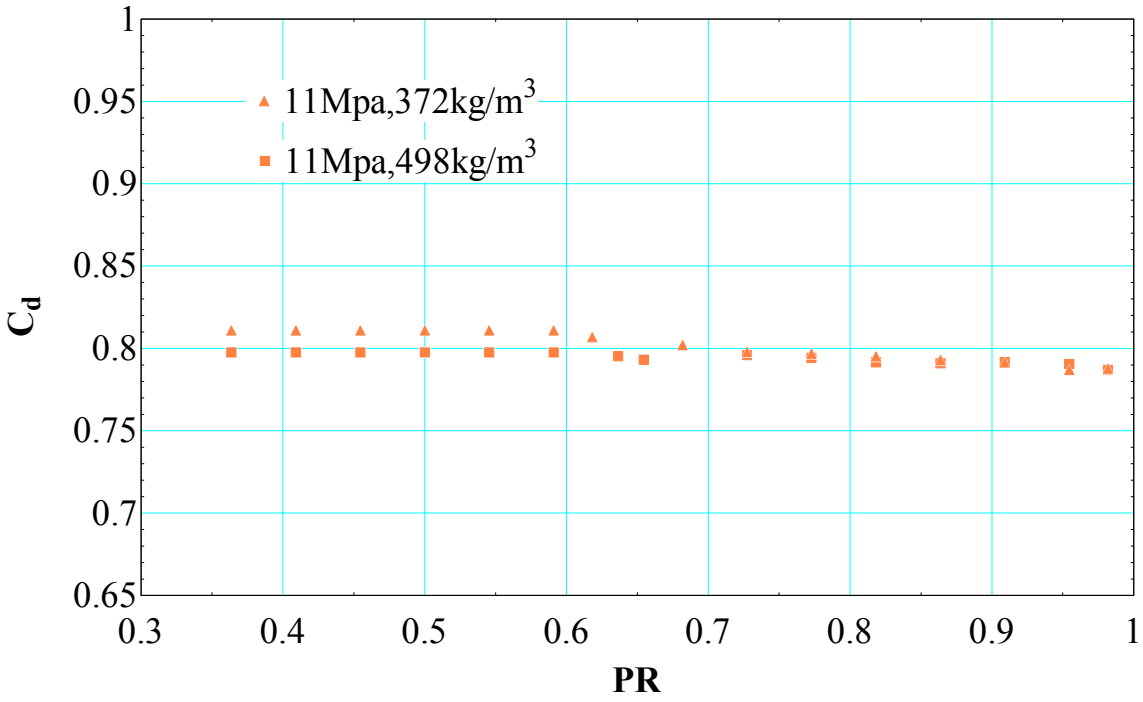

Figure 93. C_d for cases 1 and 2 in Table D.1 of Appendix D

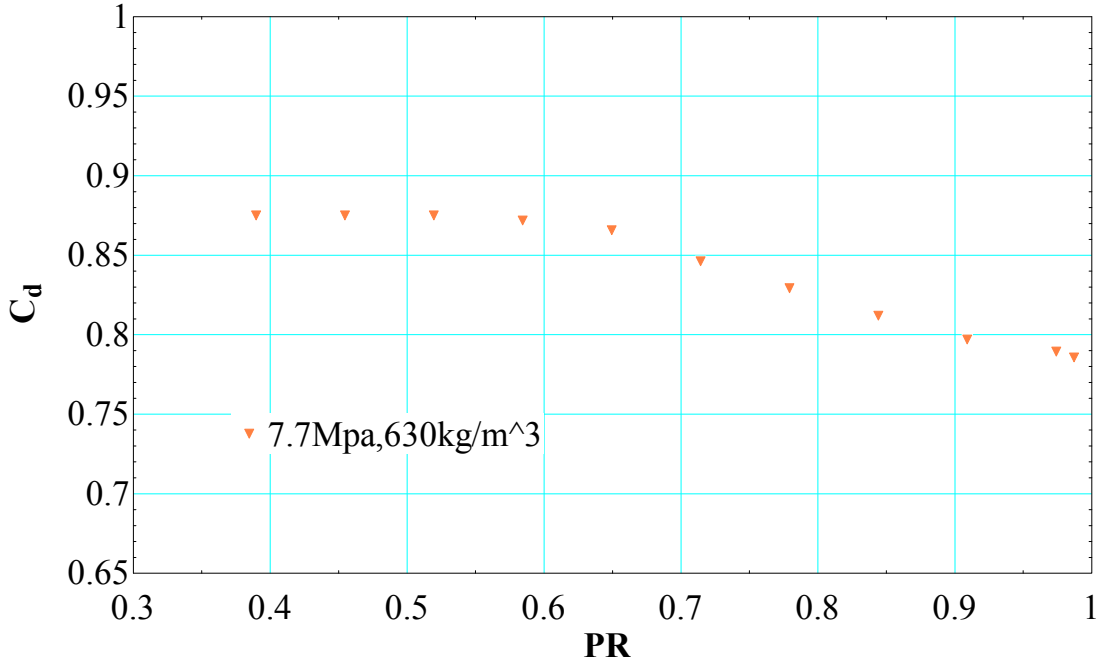

Figure 94. C_d for case 6 in Table D.1 of Appendix D

Downstream conditions from all these simulations can be calculated based upon the following equations:

$$h_{up} = h(P_{up}, \rho_{up})$$

$$h_{down} = h(P_{down}, \rho_{down})$$

$$\dot{m}_{Openfoam} = \rho_{down} * A_{clearance} * V_{down}$$

$$h_{up} = h_{down} + \frac{V_{down}^2}{2}$$

$$S_{down} = S(P_{down}, \rho_{down})$$

$$T_{down} = T(P_{down}, \rho_{down})$$

These equations can be solved simultaneously in EES to calculate downstream temperature and entropy for each pressure ratio. These results are plotted in Figure 95. For all these cases the choking point is calculated by fitting a sixth order polynomial to the leakage rate data and taking a numerical derivative of the polynomial. The pressure ratio at which the numerical derivative is zero for the first time is taken as the choking PR.

$$\frac{d\dot{m}_{curvefit}}{dPR}|_{chokedflow} = 0 \quad (97)$$

The choking PR can alternatively be calculated by plotting V_{down}, and local speed of sound versus PR. The point where these two plots intersect is the choking PR according to our definition. Technically, choking occurs at the vena contracta, which is the point of minimum area for a fluid flow through an orifice. The Vena contracta might not necessarily occur at the exit of an orifice as a result of which the true fluid velocity at the vena contracta is unknown. Hence, care must be taken while applying this method to find the choking point.

From an observation of the flow curve it can be concluded that, for inlet conditions (11MPa, 372Kg/m^3) and (11MPa, 498Kg/m3), which are bounded by the two curves, choking occurs very close to the saturation point where flow enters the two phase region. As inlet condition drifts below the two curves (10MPa, 372Kg/m^3) and (10MPa, 498Kg/m^3) choking is slightly delayed going into the two phase region. Whereas for inlet conditions which are completely below the two curves (9MPa, 372Kg/m^3), (9MPa, 498Kg/m^3), and (7.7MPa, 630 Kg/m^3) choking occurs very late into two phase dome, which is in good agreement with the theory put forward earlier. It might be interesting to test some inlet conditions that are above both the curves but this is left to future work.

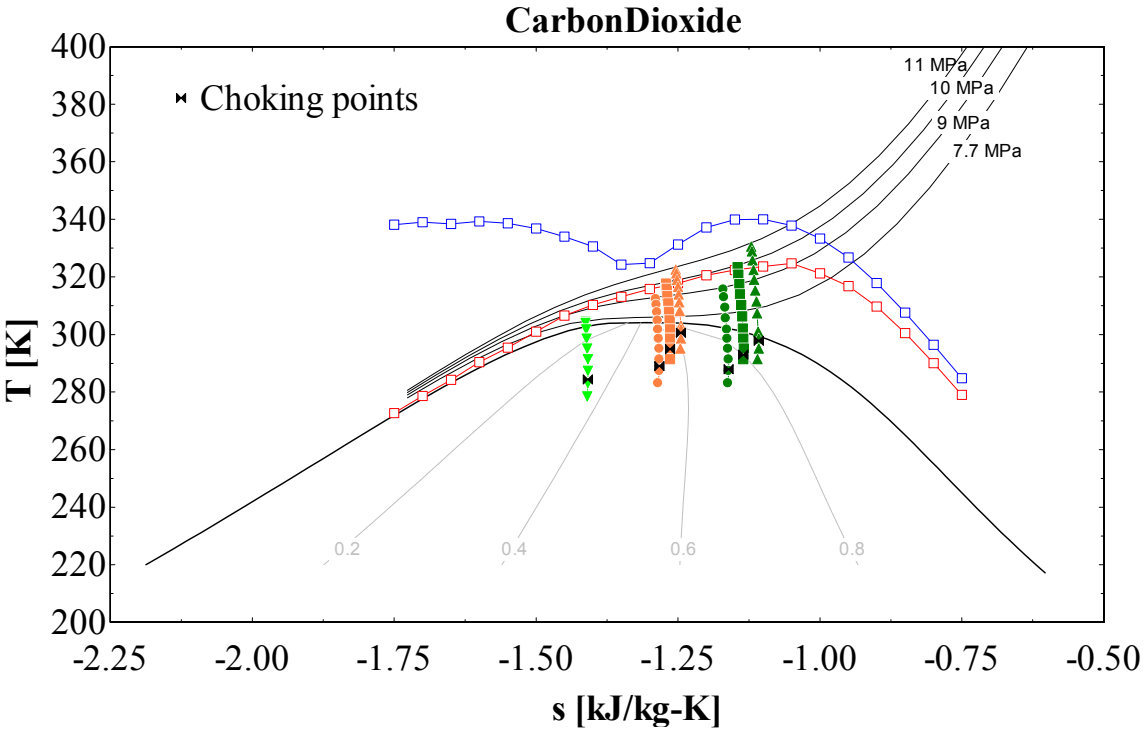

Figure 95. Choking point calculations for annular orifice (Flow curve).

One should expect that the presence of multiple teeth would cause a delay in choking as most of the times choking occurs at the exit of the last tooth where the pressure drop is maximum, as mentioned earlier. In that case we can ask ourselves a question: “Can the isentropic choking

theory which worked well for annular orifices, be applied to labyrinth seals?" To answer this question the geometry is held constant, which is the same as case 2 in Appendix C, and the inlet operating conditions are varied. The inlet conditions simulated are the same as those used for annular orifices so that a direct comparison can be made (cases 1-6 in Table D.2 of Appendix D, case 2 in Appendix C).

5.3.2 Results for Labyrinth Seal

Three inlet densities (372, 498 and 630 Kg/m^3) are simulated for an inlet pressure of 9 MPa (cases 3-5 in Table D.2 of Appendix D) and leakage rate results for these three cases are presented in Figures (96, 97 and 98).

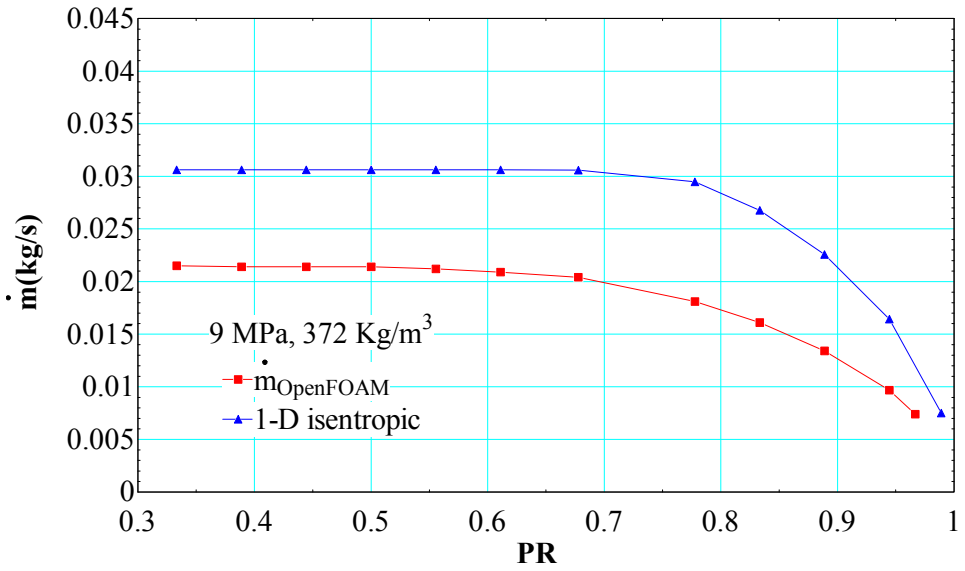

Figure 96. Leakage rate for inlet condition of 9 MPa and 372 Kg/m3

The discharge coefficient for all three cases is plotted in Figure 99. It is interesting to note that the C_d for these inlet densities is nearly the same for all pressure ratios as observed in the case of annular orifices. However, the C_d which is 0.8 for higher PR's in the case of an annular orifice is now 0.6 for three teeth labyrinth seals indicating that the leakage rate has been reduced due to the presence of multiple constrictions.

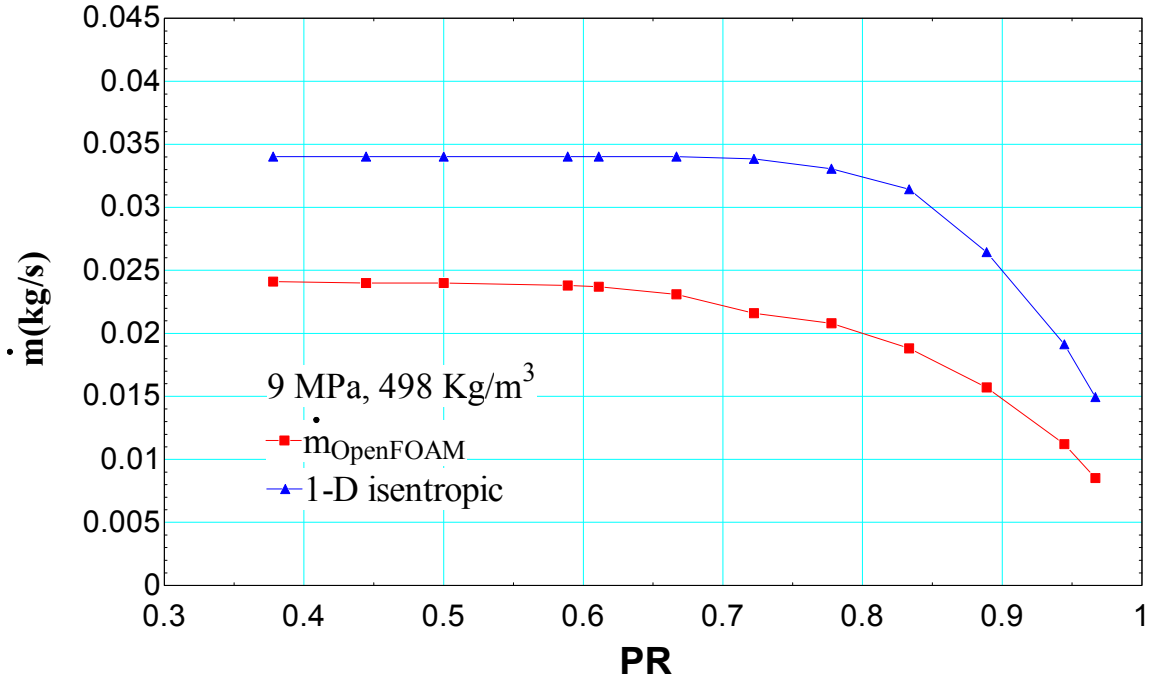

Figure 97. Leakage rate for inlet condition of 9 MPa and 498 Kg/m^3

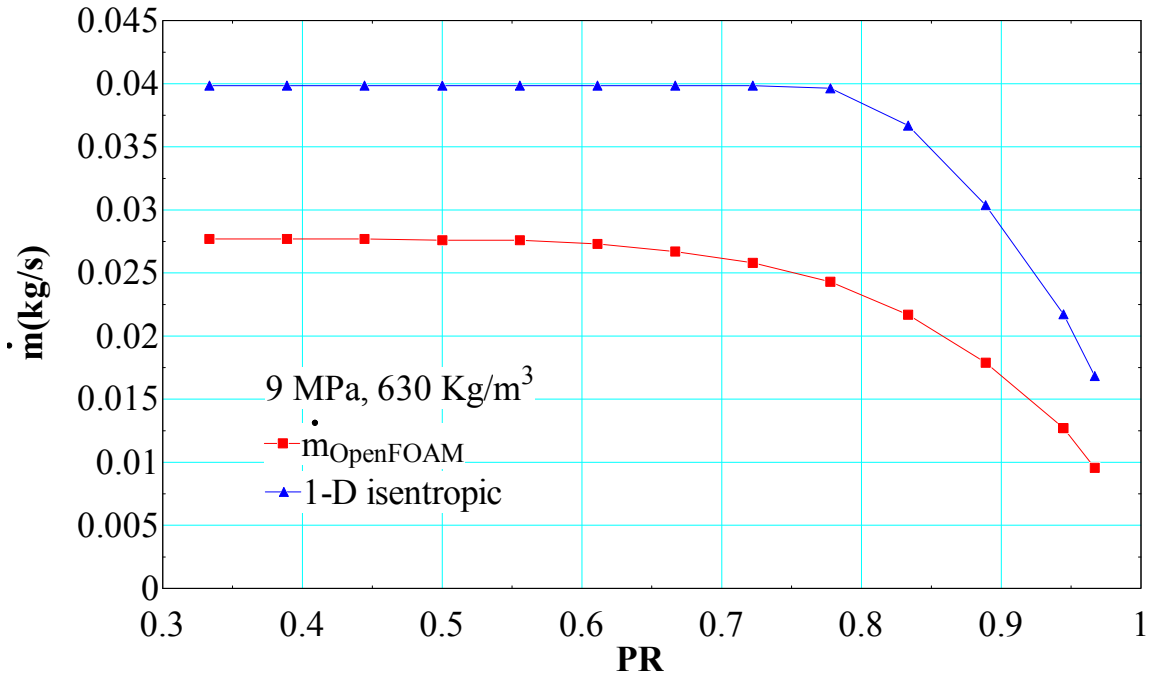

Figure 98. Leakage rate for inlet condition of 9 MPa and 630 Kg/m^3

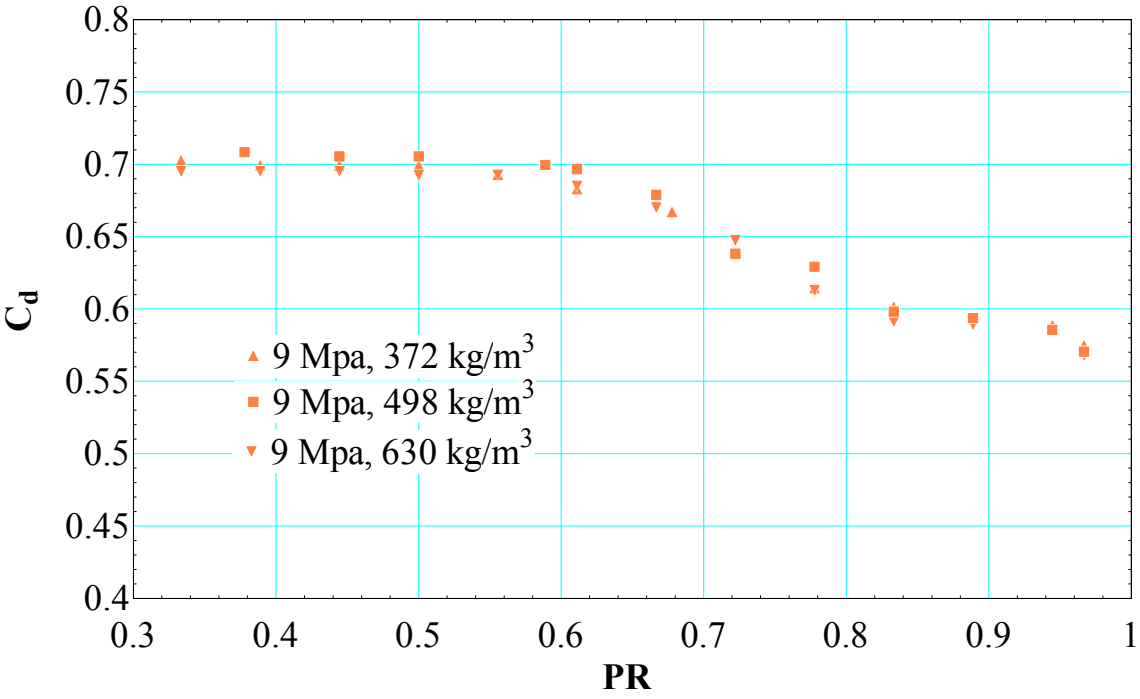

Figure 99. C_d for an inlet pressure of 9 MPa (cases 3, 4 and 5 in Table D.1)

To see if this is true for other pressures as well, the pressure was increased to 10 MPa and two inlet densities (372 Kg/m^3 and 498 Kg/m^3) are simulated (case 2 in Table D.1 and case 2 in Appendix C). Results for the leakage rates are self-explanatory and are presented in Figures 100 and 101. The C_d for both these cases, plotted in Figure 102, collapse on to each other just like in the case of annular orifices reassuring our claim that, there exists a range of inlet densities for which C_d is only a function of inlet pressure.

One simulation was performed for an inlet pressure of 11MPa and density of 498 Kg/m^3 (case1 in Table D.1 of Appendix D) to check if C_d stays constant over the whole range of PR's like in the case of an annular orifice. The C_d for this case is presented in Figure 102 and it can be seen that the C_d is not constant but is tending towards becoming constant. Further increase in pressure should result in a constant C_d over the whole range of PR.

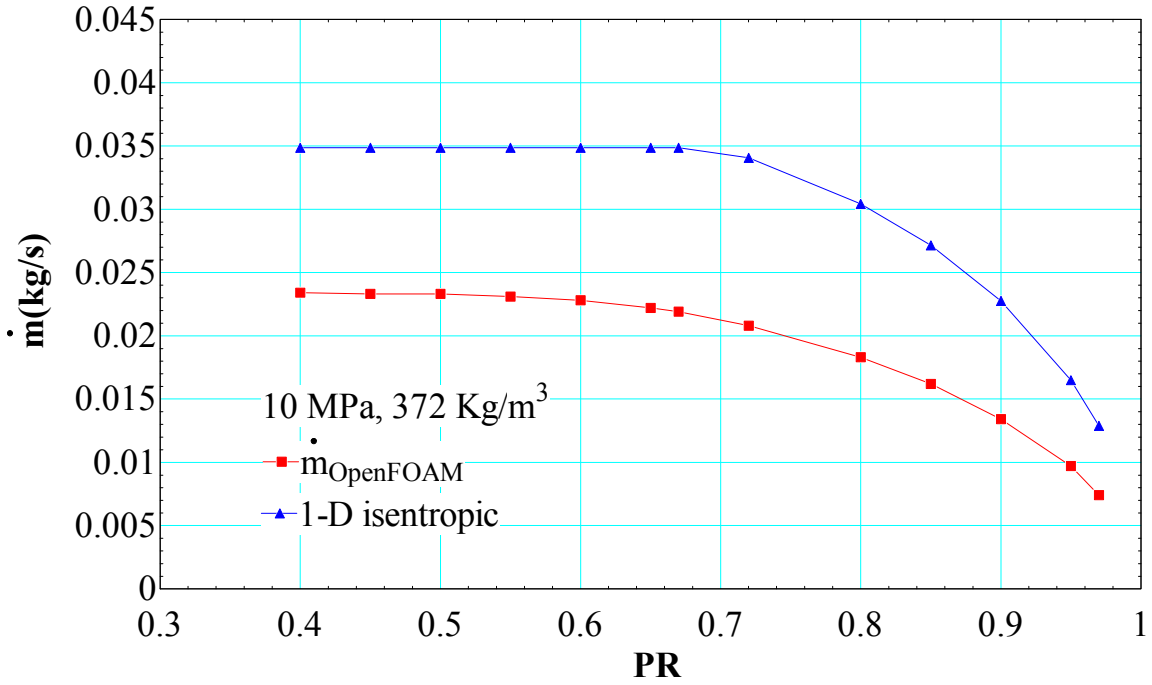

Figure 100. Leakage rate for inlet condition of 10 MPa and 372 Kg/m3

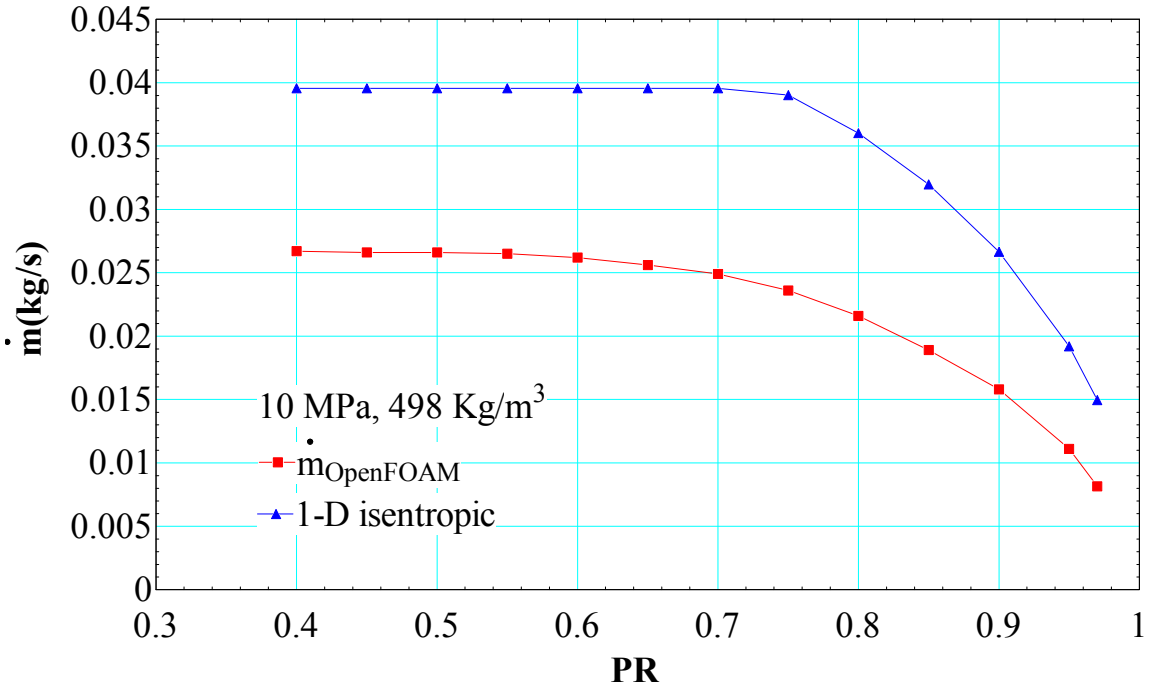

Figure 101. Leakage rate for inlet condition of 10 MPa and 498 Kg/m3

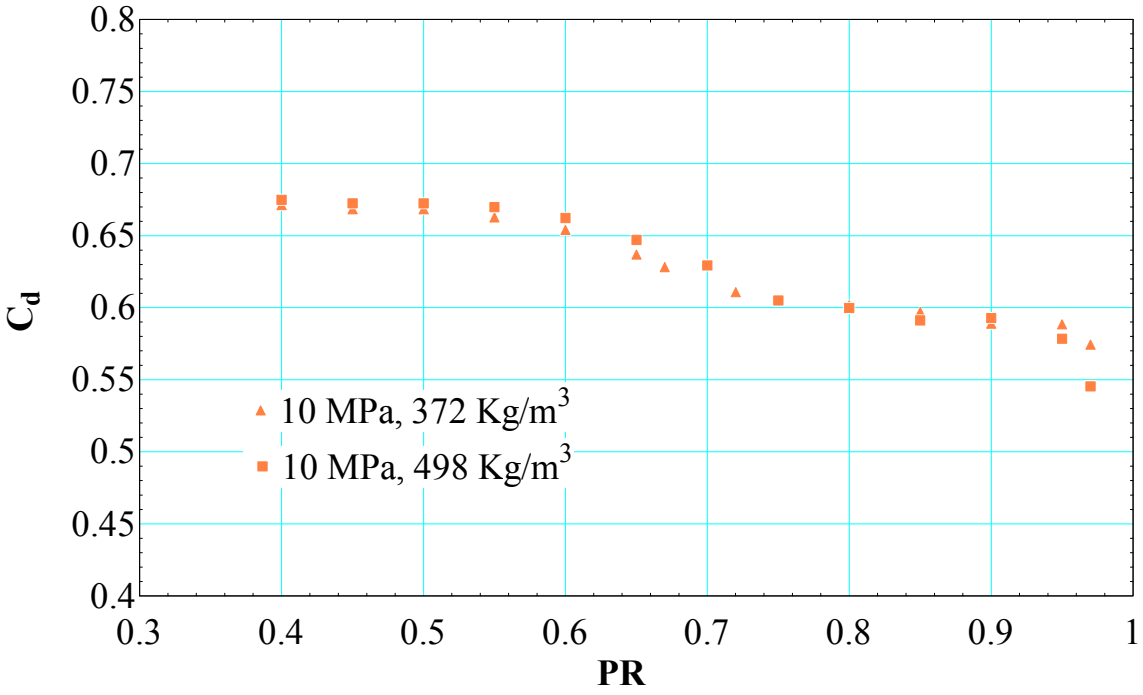

Figure 102. C_d for an inlet pressure of 10 MPa.

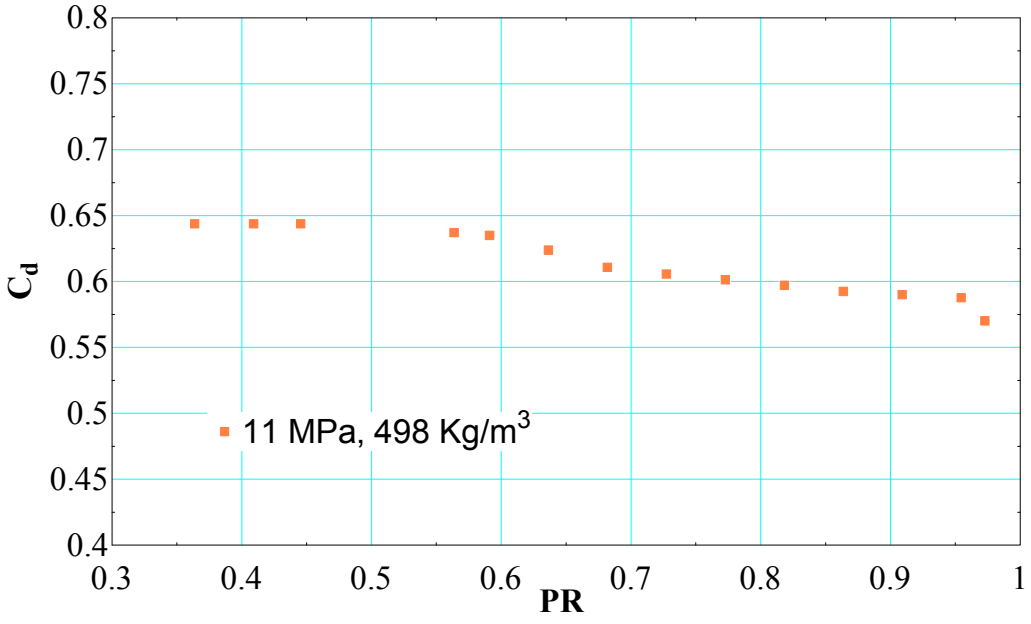

Figure 103. C_d for an inlet pressure of 11 MPa

The C_d for 7.7 MPa, 630 Kg/m^3 (case 6 in Table D.2 of Appendix B) presents some unusual behavior as shown in Figure 104. The reason why the C_d starts increasing instead of staying constant at higher PR's is unknown at this point and requires more detailed study. As for now it can be safely assumed that the unusual trend is caused due to the presence of multiple constrictions as this behavior is not observed in the case of an annular orifice for the same operating condition (Figure 94).

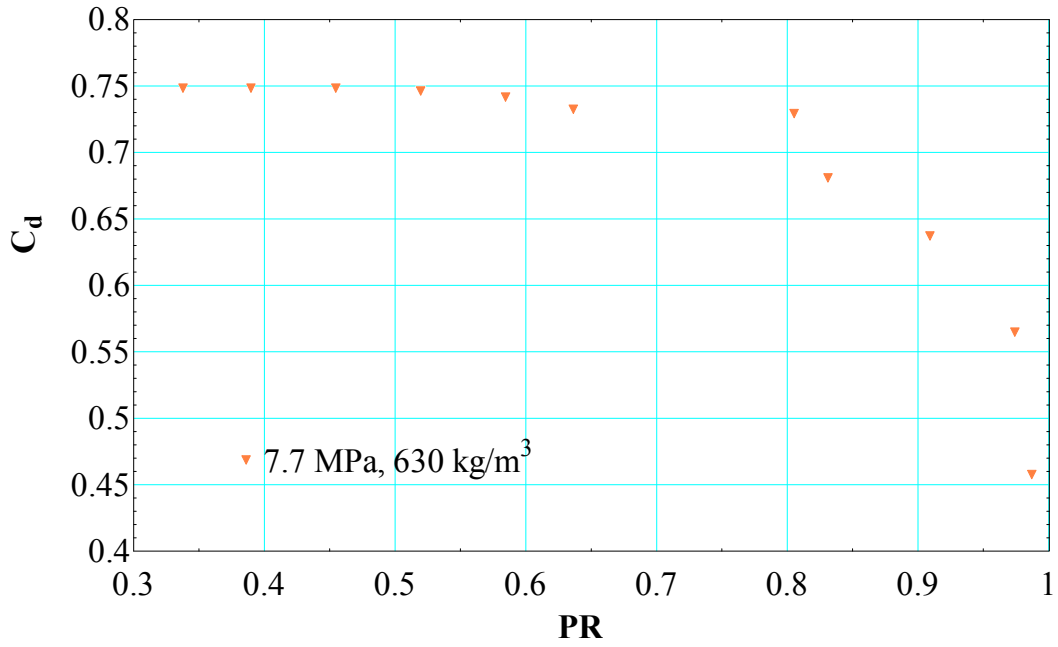

Figure 104. C_d for an inlet pressure of 7.7 MPa

From Figures (95 and 105), it can be observed that for a similar set of operating conditions choking in the case of labyrinth seals is significantly delayed compared to annular orifices. Even for an operating condition of 11Mpa, 498Kg/m^3 which is bounded by the two curves, the flow chokes late into the two phase dome suggesting that 1-D isentropic choking theory derived for annular and plain orifices cannot be extended to labyrinth seals. So, "Is there a 1-D isentropic model which can predict choking behavior of labyrinth seals?"

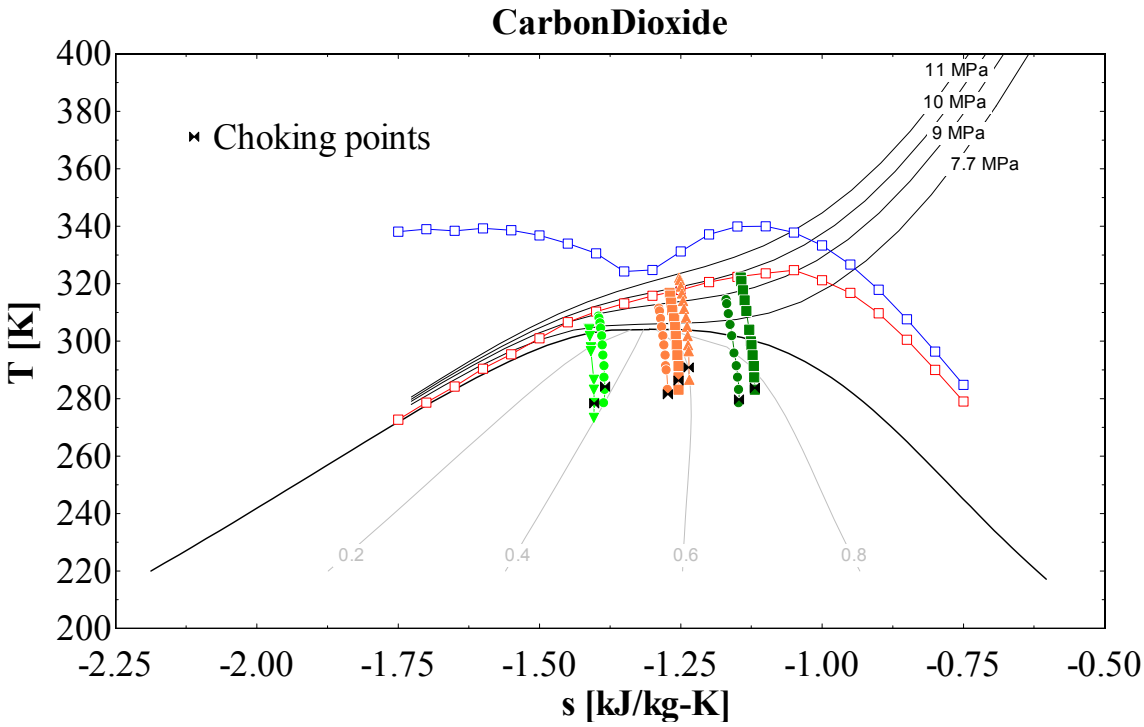

Figure 105. Choking point calculations for labyrinth seal (Flow curve).

Let us revisit the 1-D isentropic model presented for labyrinth seals. From the 1-D isentropic model the local speed of sound at the exit of a labyrinth seal is defined as,

$$\rho_{down}\frac{dh_{down}}{d\rho_{down}} = \frac{dP_{down}}{d\rho_{down}} = c^2 \tag{98}$$

From equation (98), it can be said that for a given inlet entropy condition and downstream pressure the local speed of sound at the exit is independent of upstream conditions and the geometry of the labyrinth seal. Therefore, under similar conditions the speed of sound is the same for annular orifices as well as labyrinth seals. However, the downstream velocity of the fluid will depend on the geometry and is different for annular orifices and labyrinth seals. Figure 83 presented the calculations for local speed of sound and downstream velocity as a function of upstream and downstream pressures for an annular orifice (S_{in} = -1.0 KJ/Kg-K). In the case of a

labyrinth seal, equations (75 – 84) are used to calculate the downstream velocity and the results are presented in Figure 106 for S_{in} = -1.0 KJ/Kg-K.

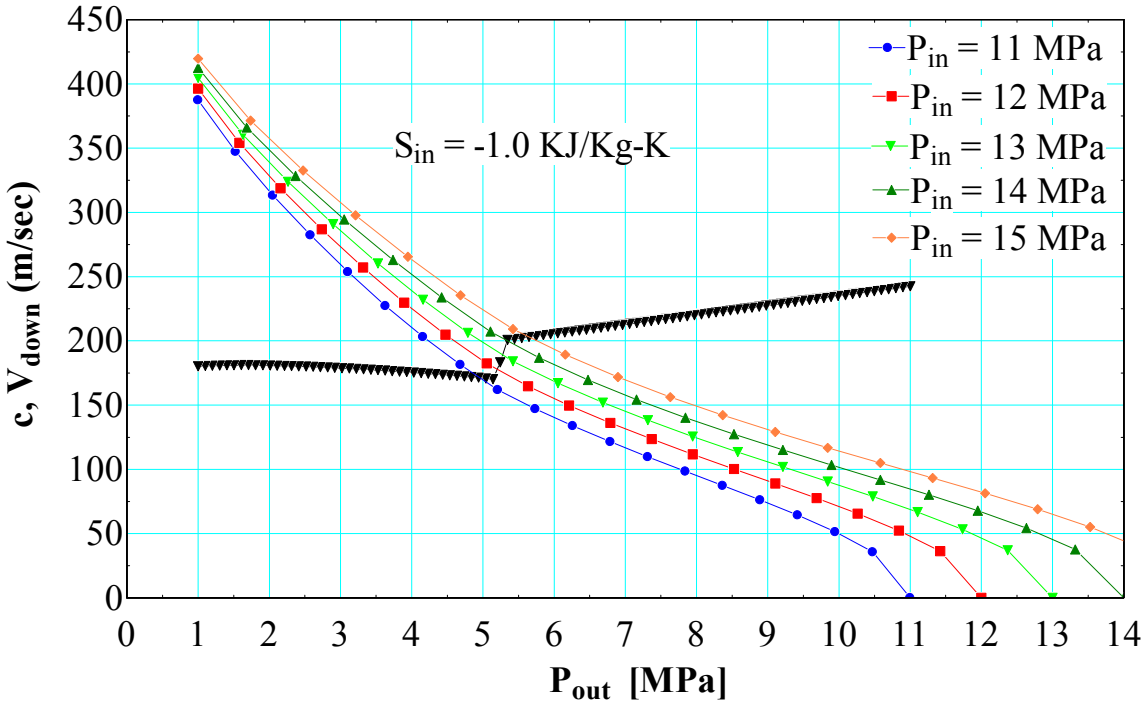

Figure 106. Downstream velocity of labyrinth seal and local sound speed as a function of outlet pressure

Figures 83 and 106 indicate that for an inlet pressure of 11MPa, the 1-D isentropic model for labyrinth seals chokes in the saturation dome and the 1-D isentropic model for an annular orifice chokes above the saturation dome. Therefore, the curves developed using 1-D isentropic choking model for annular orifices cannot be extended to labyrinth seals. However, from a general observation of Figure 106 it can be said that there exists a range of inlet pressures for which the downstream velocity curve intersects the sound speed curve very close to the saturation pressure. Following this theory, the inlet entropy can be varied and the upper and lower limit of the inlet pressure for which the flow chokes at saturation point can be calculated for each inlet entropy. This would result in two different sets of curves but the conclusions made for annular orifices are still valid in the case of labyrinth seals.

6 Heat transfer characteristics of supercritical CO_2

This chapter describes the third task of this report, which is to investigate the heat transfer characteristics of S-CO_2. The first section of this chapter provides the details of the experimental facility constructed to achieve this task. This is followed by the validation results of the facility using distilled water. Finally, the experimental results will be presented to investigate the effects on buoyancy on heat transfer characteristics of supercritical carbon dioxide.

6.1 Experimental facility overview

The schematic of the experimental facility and test section is shown in Figure 107. The loop consists of a liquid CO_2 cylinder, high pressure liquid chromatography (HPLC) pump, circulation pump, Coriolis flow meter, high pressure CO_2 preheater, test section, high-pressure CO_2 cooler, DC power supply, buffer tank, and data acquisition system.

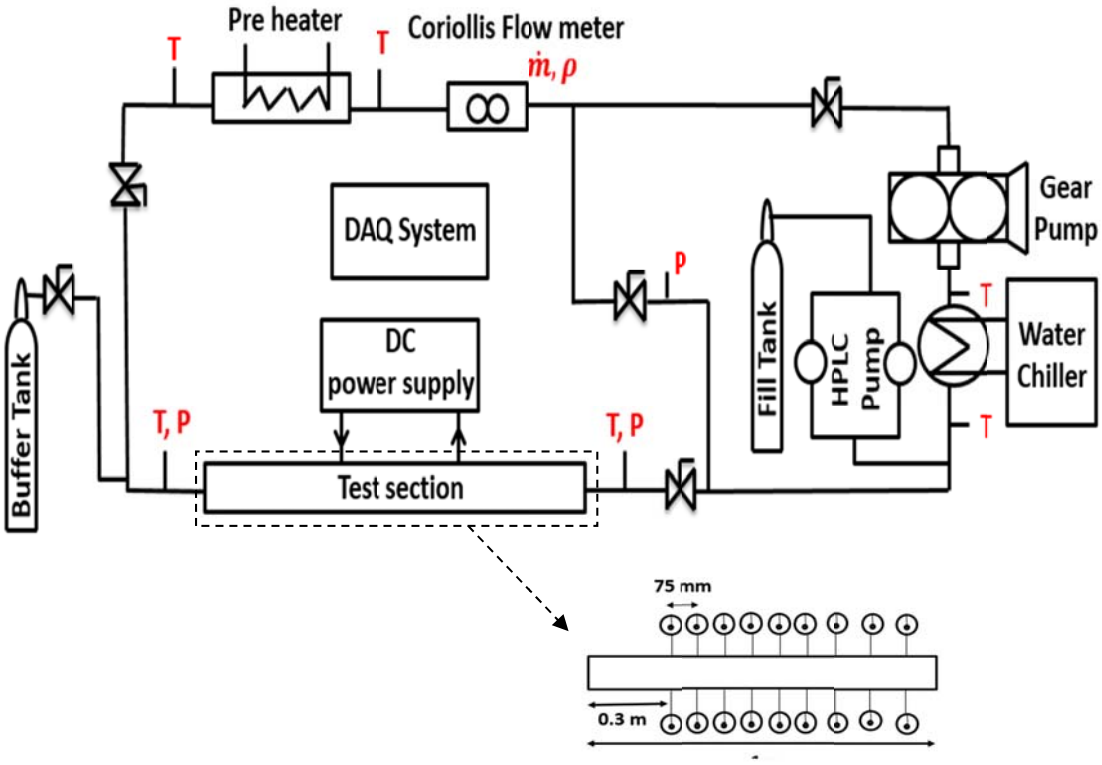

Figure 107. Schematic of the experimental facility and the test section

System operating pressure is monitored and controlled by a Scientific Systems, Inc. SFC-24, positive displacement, constant pressure HPLC pump (S10SNXP1). It is capable of pressurizing the system to 69 MPa (~10,000) psi, with an accuracy of ±2% of full scale. A buffer tank of volume ~0.5 m^3 is used to increase the system volume and minimize the pressure fluctuations in the loop due to the temperature fluctuations from the chiller.

The circulation pump is a Micropump (GLH25) magnetically driven gear pump. It is capable of handling flow rates between 0.6-7.0 GPM, a differential pressure of 0.86 MPa (~125 psi), and a maximum operating pressure of 10.35 MPa (~1500 psi). This pump is coupled to Baldor variable frequency drive and this in conjunction with a throttling valve is used to precisely control the mass flow rate in the loop.

A Micro Motion Coriolis flow meter (F025P) and transmitter are used to measure the mass flow rate in the system. The flow meter is capable of measuring flow rates up to 0.27 kg/sec with an accuracy of ±0.1% full scale. Measurements from the flow meter serve as a feedback control for the variable frequency drive.

Temperatures in the loop excluding the test section are controlled using a high-pressure CO_2 preheater and cooler. In the preheater, CO_2 splits into two tubes that run next to a 5.5 kW cartridge heater. This preheater is used to raise the temperature of CO_2 to the desired test section inlet temperature. Upon exiting the test section, the CO_2 enters into a high pressure cooler where excess heat is removed facilitating the pump to move liquid-like CO_2. The cooler is a concentric tube-in-tube heat exchanger where the chilled water and CO_2 run through the outside and inside tubes respectively. Chilled water is provided using Advantage Engineering (M1-1.5A) water chiller with a maximum cooling capacity of 1.5 refrigeration tons. Inlet and outlet temperatures to the test section are measured by Omega 3 wire platinum RTDs having

maximum uncertainty of ±0.3°C. These RTDs are calibrated against boiling water and an ice bath to quantify the systematic error. The pressure is monitored by Omega gauge pressure transducers (PX309) within a manufacturer specified accuracy of ±0.25% of full scale accuracy. Several K-type thermocouples are used in the loop to monitor the amount of energy that was being put in or removed from the flow by each component.

The test section is a stainless steel 316 circular pipe with 12.7 mm OD, 10.9 mm ID, and is 1 m long. Constant heat flux boundary condition is provided to the test section using a Magna-Power electronics TSD10-500/480 DC power supply. The heat flux to the test section is varied by adjusting the voltage between copper clamped terminals at the ends. The accuracy of voltage control is ±0.01% of full scale and current control is ±0.04% of full scale. The test section is electrically and thermally insulated from the rest of the loop by using Swagelok dielectric fittings at each end of the test section.

Outer wall temperatures of the test section are measured using 20 E type stick on thermocouples. Out of these 20 thermocouples, 10 thermocouples are mounted on the top side and 10 on the bottom side at axial locations which are 75 mm apart from each other. The first thermocouple is mounted 300 mm from the inlet side to allow for the flow to be hydrodynamically fully developed. It should be noted that the perspective of top and bottom side is with respect to horizontal orientation of the test section. These E-type thermocouples have a manufacturer specified uncertainty of ±1.0°C or 0.4% of the measurement, whichever is greater. Drift in wall thermocouples reading is minimized by performing specific in-situ calibration under no heat flux conditions.

6.2 Validation of the test facility

Experimental facility was tested under constant heat flux condition (q'' – 13.5 KW/m^2) using distilled water to check for the system operation. Experiments were conducted at fluid inlet temperature of 25^{o} C and several mass flow rates. Wall temperatures were recorded and the results were compared with the results obtained from energy balance using the empirical correlation of Dittus Boelter for calculation of the Nusselt number. The empirical correlation for fully developed turbulent flow under constant wall heat flux is given as:

$$Nu_{DB} = 0.023 Re_b^{0.8} \mathrm{Pr}_b^{0.4}$$

Theoretical wall temperature was then calculated using bulk fluid temperature calculated using an energy balance assuming constant heat flux:

$$T_{wall} = T_{bulk} + \frac{q"d}{k_b Nu_{DB}}$$

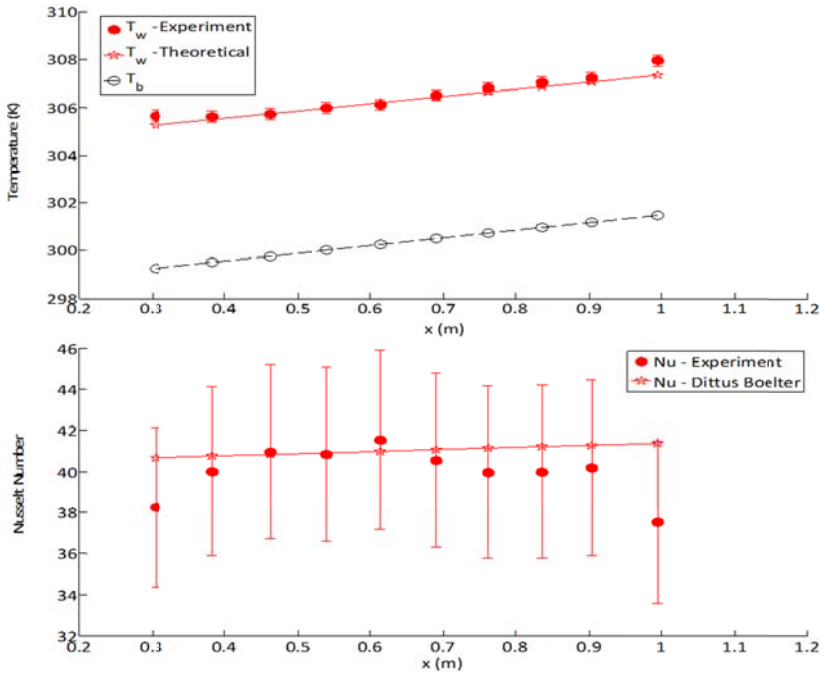

Figure 108. Wall temperature and Nusselt Number for water validation test

Figure 108 shows the measured wall temperatures and Nusselt number for mass flow rate of 0.035 *Kg/sec* compared with those calculated from the correlation. Here, measured wall temperatures and Nusselt number agree well with the estimated values. It has to be noted that the readings from first three thermocouples were neglected due to the thermally developing region.

6.3 Experimental and data analysis procedure

A series of integral experiments were performed by changing the mass flow rate and heat flux for operating pressures of 7.5, 8.1, and 10.2 MPa. The inlet temperature to the test section was varied from 20°C to 55°C to cover the whole range of bulk temperatures spanning the pseudocritical temperature. The mass flux was in the range of 150-350 kg/m^{2}s and the heat flux was in the range of 10-65 kW/m^2. Three different test section orientations namely, horizontal, upward and downward flow were tested to investigate the effects of buoyancy. During the experiments, all independent parameters such as test section inlet temperature, mass flow rate, pressure, and heat flux were monitored and controlled by NI Labview DAQ system (cDAQ-9178). For each operating condition, the system was assumed to be at steady state once the experimental parameters were constant for at least 10 minutes. Heat added, or removed to/from CO_2 in the preheater and pre-cooler was calculated by measuring the temperatures across each component and performing energy balance as,

$$Q_{CO_2} = \dot{m}(i_{in} - i_{out}) \tag{99}$$

Once the system achieved a steady state, the data was recorded for 500 s at the rate of 1Hz and the average of these data points was used for the analysis.

Heat flux to the test section, $Q"_{PS}$ is estimated as,

$$Q"_{PS} = \frac{V_{PS} I_{PS}}{\pi D L} \tag{100}$$

Outer wall temperatures are measured and inner wall temperatures are estimated by using a simple one-dimensional, steady-state conduction equation,

$$T_{wi} = T_{wo} + \frac{\dot{q}}{4k_{ss}}\left[\left(\frac{D_{out}}{2}\right)^2 - \left(\frac{D_{in}}{2}\right)^2\right] - \frac{\dot{q}}{2k_{ss}}\left(\frac{D_{out}}{2}\right)^2 \ln\left(\frac{D_{out}}{D_{in}}\right) \tag{101}$$

Where $\dot{q}$ is the volumetric heat rate (W/m^3) expressed as,

$$\dot{q} = \frac{V_{PS} I_{PS}}{\left[\frac{\pi}{4}(D_{out}^2 - D_{in}^2)L\right]} \tag{102}$$

Using the assumption of constant heat flux, the bulk fluid temperature at the locations of the thermocouples was obtained by performing an energy balance on a differential control volume, and using the following equations [41],

$$T_{b+1} = T_b + \frac{Q"_{PS}}{\dot{m} C_p} \pi D x \tag{103}$$

The local heat transfer coefficient was then defined by,

$$h = \frac{Q"_{PS}}{A(T_{wi} - T_b)} \tag{104}$$

Finally, the experimental local Nusselt number was determined as,

$$Nu_b = \frac{hD}{k_b} \tag{105}$$

6.3.1 Uncertainty analysis

Using the method proposed by Kline and McClintock [42], the uncertainty in the measurement of the heat transfer coefficient can be expressed as follows,

$$\delta h = \left[\left(\frac{\partial h}{\partial Q''_{PS}}\delta Q''_{PS}\right)^2 + \left(\frac{\partial h}{\partial T_{wi}}\delta T_{wi}\right)^2 + \left(\frac{\partial h}{\partial T_b}\delta T_b\right)^2\right]^{0.5} \quad (106)$$

Evaluating the partial differentials in equation (106), relative uncertainty in the measurement of the heat transfer coefficient can be expressed as,

$$\frac{\delta h}{h} = \left[\left(\frac{\delta Q''_{PS}}{Q''_{PS}}\right)^2 + \left(\frac{\delta T_{wi}}{(T_{wi}-T_b)}\right)^2 + \left(\frac{\delta T_b}{(T_{wi}-T_b)}\right)^2\right]^{0.5} \quad (107)$$

The uncertainty in the measurement of the wall temperatures and the heat flux was described earlier. It is clear from equation (107) that as the wall and the bulk temperature approaches each other the uncertainty in the measurement of heat transfer coefficient increases. This generally occurred close to the pseudocritical point at sufficiently high mass flow rate and low heat flux.

The dielectric fittings are made of Polyamide-imide insulation material. This material has a very low thermal conductivity (~0.26 W/m-K) and hence, minimized the heat loss from test section to the rest of the loop. As a result, the only significant source of heat loss is the natural convection from the outer tube wall to the atmosphere. The estimation of heat loss based on natural convection was less than 5% without insulation. The test section as well as the whole loop is well insulated with flexible ceramic fiber glass insulation and hence, the heat loss to the atmosphere is assumed to be negligible under such conditions and was not included in the uncertainty analysis.

6.4 Results and Discussion

6.4.1 Effect of operating pressure

The effect of operating pressure was investigated by comparing the test results for downward flow at three different operating pressures, 7.5, 8.1, and 10.2 MPa, for a mass flux of 195

kg/m^{2}s, and a heat flux of 13.5 kW/m^2. The heat transfer coefficients and wall temperatures are plotted against the normalized bulk-fluid temperature as shown in Figure 109. It can be seen that the wall temperature increases as the operating pressure is increased. When the bulk-fluid temperature (T_b) is lower than the pseudocritical temperature (T_{pc}), heat transfer coefficients are higher for the lower operating pressures with maximum enhancement observed slightly below the pseudocritical temperature. However, when the T_b is higher than the T_{pc}, the heat transfer coefficients are higher for the higher operating pressures. This dependence of the heat transfer coefficient on the pressure and temperature can be attributed to the variation of isobaric Prandtl number. These results were observed to be true for upward and horizontal flows as well provided that the mass flux is sufficiently high compared to the heat flux, and the buoyancy effects are negligible.

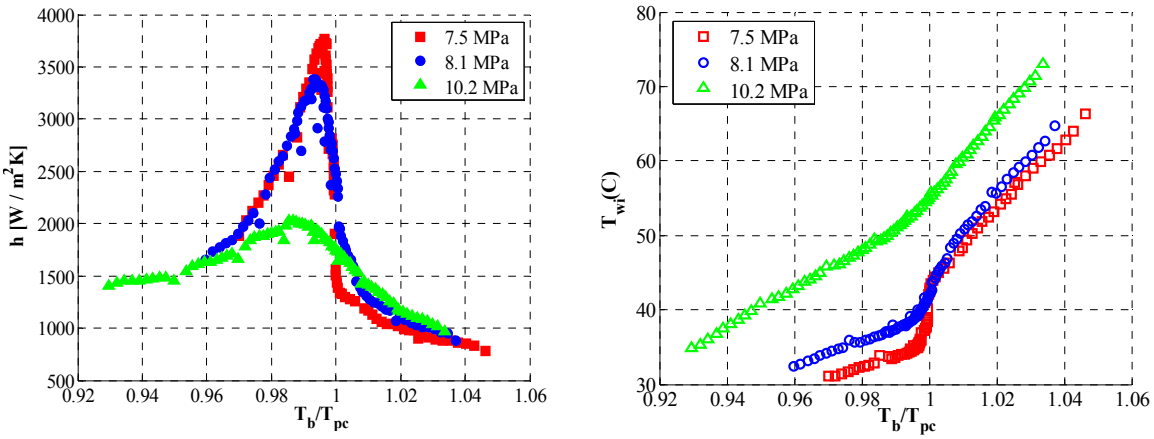

Figure 109. Effect of operating pressure on heat transfer for downward flow, G – 195 kg/m^{2}s, Q"$_{PS}$ – 13.5 kW/m^2

6.4.2 Effect of flow configuration

In order to investigate the effect of buoyancy on heat transfer, the test results at operating pressure of 10.2 MPa for horizontal, upward, and downward flows are compared for a mass flux of 195 Kg/m^{2}s, heat flux of 24 kW/m^2, and an inlet temperature of 46°C. It should be noted that

this inlet temperature is close to the pseudocritical temperature for 10.2 MPa. Figure 110 shows the variation of heat transfer coefficient and wall temperature along the length of the tube.

In the case of horizontal flow, it has been observed that the wall temperatures on the top side are significantly higher than the wall temperatures on the bottom side indicating that there is a circumferential variation in the wall temperature. This was particularly true when $T_b < T_{pc} < T_w$. Under these conditions, the density of CO_2 near the wall is significantly lower than the density of CO_2 in the bulk of the flow and hence, the buoyancy effects become prominent. This density gradient causes the low density CO_2 to rise from the bottom side of the tube thereby, enhancing the heat transfer on the bottom side whereas the top side is covered by a blanket of CO_2 having low thermal conductivity deteriorating the heat transfer on the top side. This phenomenon has been experimentally observed in previous horizontal flow studies on supercritical water [43-45] and supercritical CO_2 [46]. The circumferential variation in wall temperature was observed to be more pronounced at low mass flux and high heat flux.

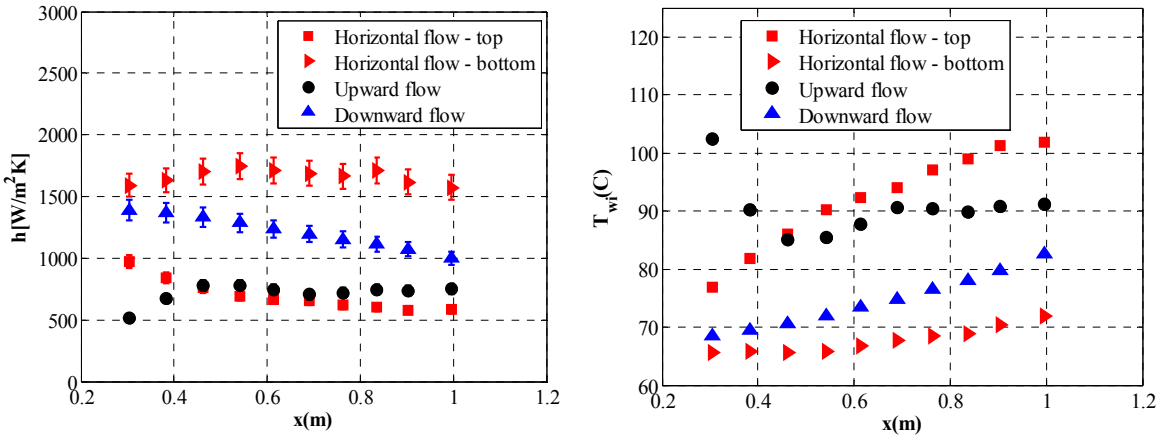

Figure 110. Effect of flow configuration on heat transfer for p – 8.1 MPa, G – 195 kg/m^{2}s, Q"$_{PS}$ –24 kW/m^2, T$_{in}$ – 46°C

In the case of upward flow, localized peaks in the wall temperature were observed as can be seen from the wall temperature profile of upward flow in Figure 110. This severe localized deterioration was observed initially by Shitsman [47], Ackerman [48], and was originally believed to be similar to the film boiling phenomenon at subcritical pressures. However, experiments [49], [50] showed occurrence of localized peaks even when the wall temperature was well below the pseudocritical temperature. These conditions should result in a liquid like blanket in the near wall-region and hence, does not support the theory of film boiling.

These localized peaks often referred to as “buoyancy peaks” occur as a result of modification of turbulent shear stress by the buoyancy forces acting on the flow [51]. It is believed that, as the fluid is heated along the tube, the density difference between the near wall region and the bulk flow increases as a result of which the boundary layer experiences a buoyancy force due to its reduced density. In case of upward flow, this buoyancy force opposes the wall shear stress reducing the turbulence production. As the boundary layer grows, for a particular boundary layer thickness, there might occur a situation where the wall shear stress is balanced by the buoyancy force and at this point the bulk flow is de-coupled from the wall causing the wall temperature to spike. As the buoyancy force increases further, a region of negative shear stress develops resulting in formation of an “M-shaped” velocity profile restoring turbulence production and hence, the wall temperature decreases after the spike.

Experimental evidence of the “M-shaped” velocity profile was provided [52-55] using pitot tubes and micro thermocouples. Bourke and Pulling [53], showed formation of “M-shaped” profile after the spike in wall temperature, whereas Kurganov et al. [55] found that the “M-shaped” profile occurred at the spike in wall temperature.

In the case of downward flow, the buoyancy force acts in the direction of wall shear stress increasing the turbulence production and thereby, enhancing the heat transfer compared to the values where buoyancy is absent. As can be seen from Figure 110, wall temperatures for the downward flow don't exhibit any localized peaks and are significantly lower than that of the upward flow.

6.4.3 Effect of inlet temperature

It is expected that the effect of buoyancy on heat transfer is influenced by the inlet temperature due to variation in both radial and axial properties. In order to investigate this effect, wall temperatures are recorded for different inlet temperatures at operating pressure of 7.5 MPa, mass flux of 320 kg/m^{2}s, and heat flux of 24 kW/m^2 are compared. These plots are shown in Figure 111 for horizontal, upward, and downward flows.

In the case of horizontal flow, for inlet temperature below the pseudocritical temperature (for instance, T_{in}=20°C), it has been observed that the wall temperatures on the top side are significantly higher than the wall temperatures on bottom side as discussed in the previous section. However, when the inlet temperature was raised above the pseudocritical temperature (for instance, T_{in}=36.5°C), the difference between the top and bottom surface temperatures reduced as can be seen from Figure 111. This is because as the T_b moves away from the T_{pc}, the CO_2 bulk density nearly approaches the value of density at the wall and the buoyancy effects are minimized [45]. It is expected that with further increase in the inlet temperature, the temperature difference between top and bottom sides will nearly be zero. However, due to limitations of the current test facility, this phenomenon could not be tested but was experimentally proven for supercritical water by Bazargan et al. [45].

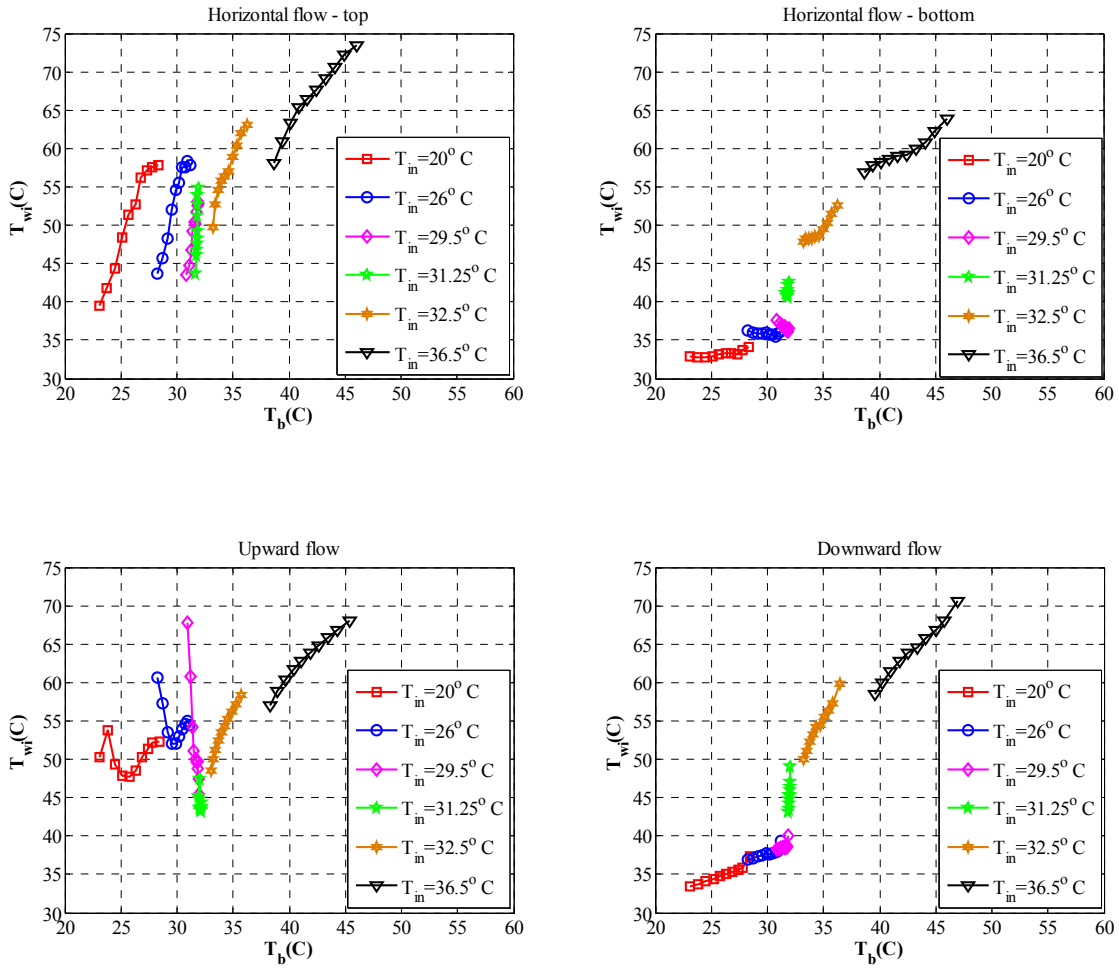

Figure 111. Effect of inlet temperature on the wall temperatures for p – 7.5 MPa, G – 320 kg/m^{2}s, Q"$_{PS}$ –24 kW/m^2

It is also interesting to note that as the inlet temperature is changed, severe discontinuity in the wall temperature was observed. This effect was more pronounced on the top side than on the bottom side. It is believed that this could be due to the effect of thermal entry length which is not well defined in the case of supercritical fluids. For constant property fluids, thermal entry length is defined as the tube length required to achieve constant radial temperature distribution. From this perspective, the thermal entry length in the case of supercritical fluids can be very long or in some cases impossible to achieve due to continuous radial and axial variation in thermophysical properties along the tube length [56]. The effect of thermal

entrance length was less pronounced as the bulk temperature moves away from the pseudocritical temperature due to less variation in properties.

In the case of upward flow, sharp localized peaks are observed for inlet temperature below the pseudocritical temperature as discussed earlier. However, when the inlet temperature was raised above the pseudocritical temperature (for instance, T_{in}=32.5°C), there was no evidence of localized peaks. In this case, the density of bulk CO_2 is nearly the same as density of CO_2 in the near wall region. As a result of this, the boundary layer doesn't experience significant opposing buoyancy force and hence, the turbulence production is not affected irrespective of flow direction. In fact, the wall temperatures for both upward and downward flows were observed to be similar as can be seen from Figure 111. It can also be seen that the location of localized peaks can be readily changed by varying the fluid inlet temperature. For instance, spike in wall temperature for inlet temperature of 20°C occurred at the location of second thermocouple whereas for inlet temperature of 26°C it occurred at the location of first thermocouple. Hence, as the inlet temperature increases, the localized peaks in wall temperature appear to move towards the inlet of the tube. This can again be attributed to the thermal entrance length effects [57], [58] and was observed to be true for all the test cases.

It is also interesting to note the steep increase in wall temperature in the case of downward flow for inlet temperatures close to the pseudocritical temperature. This was also observed on the bottom side of the tube in the case of horizontal flow under similar conditions. This could be due to a phenomenon which is similar to film boiling at subcritical pressures and is often referred to as "pseudo-film" boiling phenomenon in literature [48].

6.4.4 Effect of heat flux

In order to investigate the effect of heat flux and pseudo-film boiling phenomenon further, tests were conducted for downward flow at operating pressure of 7.5 MPa, mass flux of 195 Kg/m^{2}s for varying heat fluxes. The results are presented in Figure 112 in the form of the wall temperatures and heat transfer coefficients versus the bulk temperatures for different heat fluxes.

For low heat flux cases (Q''_{PS} – 13.5, and 24 kW/m^2), the energy input to the test section was not sufficient to span the pseudocritical region. As a result, inlet temperature was changed to span the pseudocritical region and hence, it was initially believed that the sharp increase in wall temperature was due to the thermal entrance length effects. However, for high flux cases (Q''_{PS} – 50, and 62.5 kW/m^2), the energy input to the test section is high enough to span the pseudocritical region and the sharp increase in wall temperature was still observed as can be seen from Figure 112.

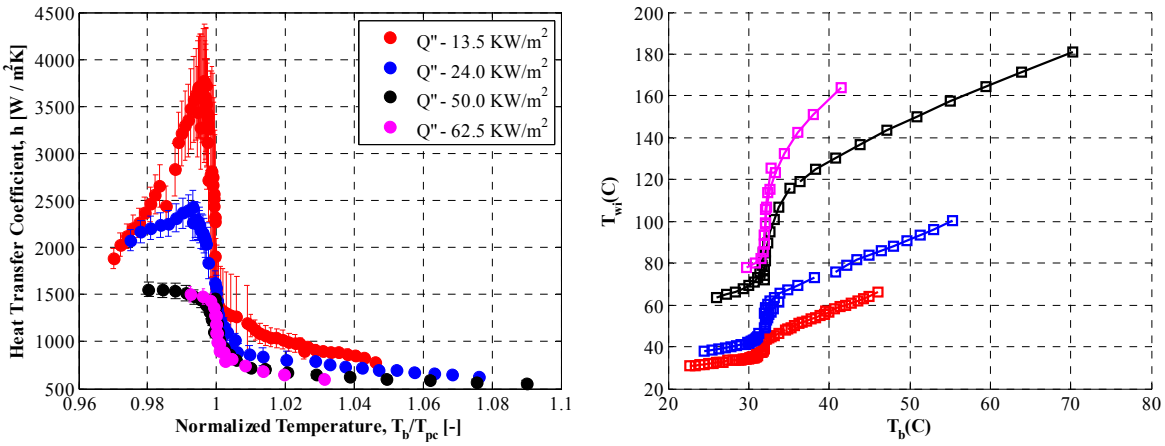

Figure 112. Effect of heat flux on downward flow heat transfer for p – 7.5 MPa, G- 195 kg/m^{2}s

This indicates that the phenomenon is due to pseudo-film boiling and not due to the thermal entrance length or buoyancy effects. It should also be noted that the heat transfer enhancement reduces with increase in heat flux. As the heat flux increases, the region of the maximum specific heat moves away from the boundary layer and hence, it is easier to overcome the region of highest specific heat. In other words, the area integrated values of specific heat decrease near the pseudocritical region causing a reduction in enhancement.

6.4.5 Buoyancy criteria

As seen in previous sections, the heat transfer to supercritical CO_2 is quite different than that of heat transfer to constant property fluids. One of the reasons for this unusual heat transfer can be associated with the effect of buoyancy due to large variations in axial and radial density profiles. Hence, it is important to identify the conditions for which the effects of buoyancy are significant and also differentiate these effects from other unusual heat transfer phenomenon. The effects of buoyancy can be effectively quantified based on Grashof number which represents the ratio of buoyancy forces to viscous forces and is defined as,

$$Gr = \frac{g\beta(T_w - T_b)D^3}{v_b^2} \tag{108}$$

Buoyancy parameters based on the variants of Grashof number are suggested in literature both for horizontal and vertical flows. In order to investigate the influence of buoyancy, experimentally determined Nusselt numbers are normalized with respect to Jackson's correlation [59] and compared with the existing buoyancy criteria. Jackson's correlation as shown in equation (109) is proven to best capture the heat transfer to S-CO_2 under forced convection conditions in the absence of buoyancy effects or any sort of deterioration.

$$Nu_{jackson} = 0.0183 Re_b^{0.82} Pr_b^{0.5} \left(\frac{\rho_w}{\rho_b}\right)^{0.3} \left(\frac{C_{av}}{C_{pb}}\right)^n \tag{109}$$

Where the subscript *n* is proposed as,

$$n = 0.4, \text{ for } T_b < T_w < T_{pc} \text{ and } 1.2T_{pc} < T_b < T_w$$

$$n = 0.4 + 0.2\left(\frac{T_w}{T_{pc}} - 1\right), \text{ for } T_b < T_w < T_{pc}$$

$$n = 0.4 + 0.2\left(\frac{T_w}{T_{pc}} - 1\right)\left(1 - 5\left(\frac{T_b}{T_{pc}} - 1\right)\right), \text{ for } T_{pc} < T_b < 1.2T_{pc}$$

Jackson [58] suggested a buoyancy parameter, Bu, for vertical flows which was derived from boundary layer theory taking into account the property variations:

$$Bu = C_B Bo_b F_{VP1} F_{VP3} F_{VP4} \tag{110}$$

Corresponding terms in equation (110) are defined as,

$$Bo_b = \frac{Gr_b}{Re_b^{2.625} Pr_b^{0.4}}$$

$$F_{VP1} = \left(\frac{\mu_{av}}{\mu_b}\right)\left(\frac{\rho_{av}}{\rho_b}\right)^{-0.5}$$

$$F_{VP3} = \left(\frac{Pr_{av}}{Pr_b}\right)^{-0.4}$$

$$F_{VP4} = \frac{\rho_b - \rho_{av}}{\rho_b - \rho_w}$$

It was suggested that for C_B value of 4600, the flow can be assumed to be in forced convection regime if the parameter suggested in equation (110) is less than 0.04. This criterion was investigated for our upward and downward flow data. The results are presented in Figure 113, where the normalized Nusselt numbers obtained from the experiments were plotted against the Jackson's non-dimensional buoyancy parameter, *Bu*. The red (circle), blue (square), and green

(triangle) data from here on correspond to the data for operating pressures of 7.5, 8.1, and 10.2 MPa respectively.

In the case of upward flow, three heat transfer regions were identified, namely: regions I, II, and III as shown in Figure 113. In region I, the normalized Nusselt number (*Nu*) was almost linearly dependent on the buoyancy parameter and the flow could be characterized as the one similar to the natural convection regime. In this region, the Reynolds number was practically constant and hence, the change of *Bu* was mainly due to change of Gr_b. As a result of this, the linear decreasing trend of *Nu* with *Bu* in this region is a principle of natural convection [60]. As the T_b approaches the T_{pc}, the normalized *Nu* reaches a minimum value at *Bu* value of approximately 0.4. This is where the transition between regions I and II occurred and in terms of a global view. This can also be viewed as the point where the velocity profile is altered into an "M-shaped" velocity profile as discussed earlier. The minimum value of Normalized *Nu* was also observed to be dependent on the operating pressure. The transition from region I to II did not occur along a single path but was dependent on the flow conditions as can be seen from wide scattering in region II especially for the lower operating pressure case. Bae et al. [60] attributed this wide scattering to the thermal entrance length effects and flow history. As the T_b moves away from the T_{pc}, the transition from region II to III occurs and this is where the normalized *Nu* is independent of the *Bu* and the flow can be characterized as the one similar to the forced convection regime. In this region, the *Nu* determined from the Jackson's correlation, equation (109), is nearly the same as the experimental *Nu*.

In the case of downward flow, it can be expected that the buoyancy forces will enhance the turbulence production and hence, the normalized *Nu* should be greater than one for $Bu > 0.04$ [58]. This was found to be true for the present data as shown in Figure 113. It is interesting to

note the region I for downward flow, where deterioration was observed, contrary to the generally understood belief that deterioration does not occur in a downward flow. Most of the data in this region is the data having T_b close to the T_{pc} and operating pressure of 7.5 MPa.

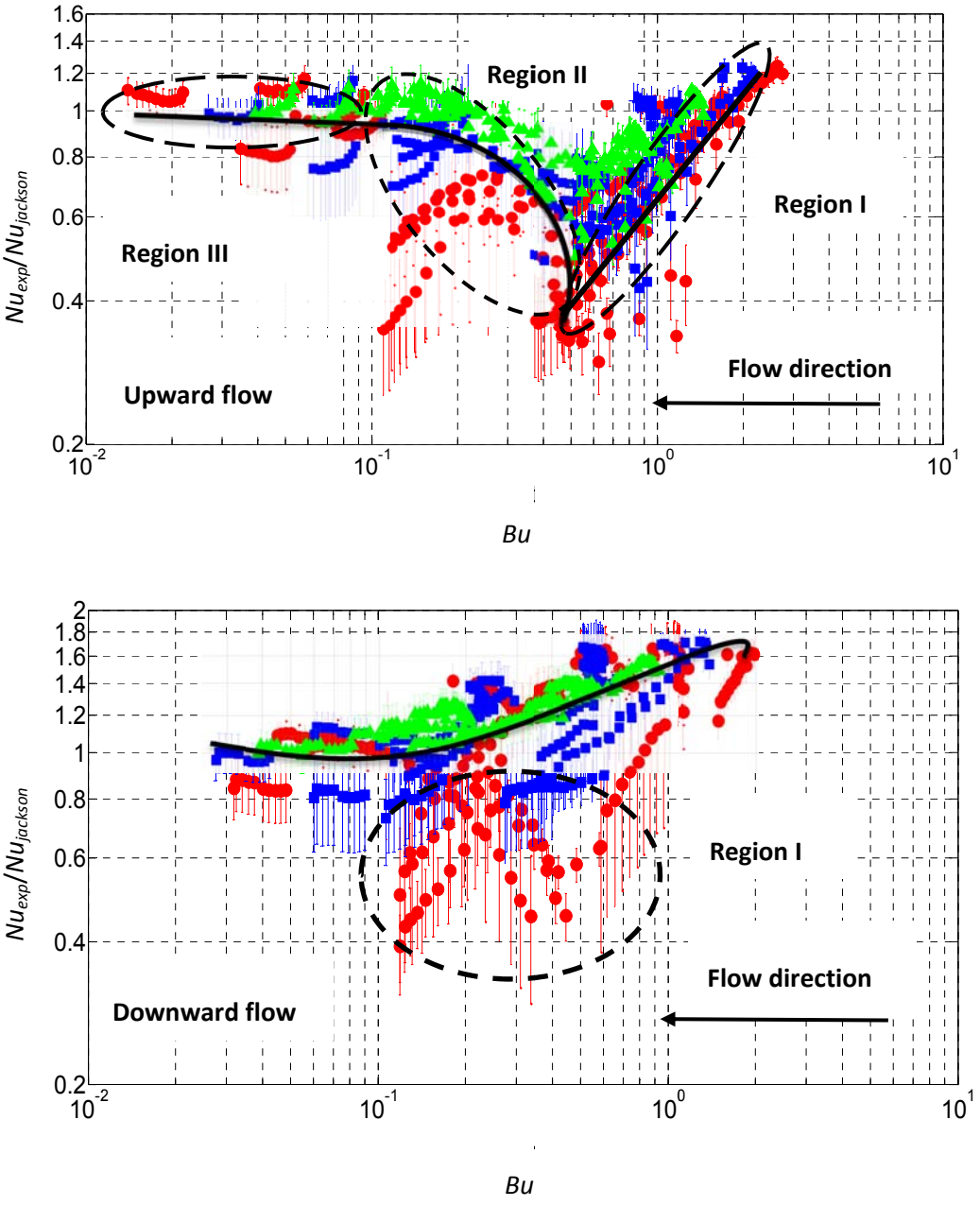

Figure 113. Normalized Nusselt number versus Jackson's buoyancy parameter, *Bu*

Hence, this data can be classified as the deterioration data for downward flow due to the pseudo-film boiling phenomenon as discussed earlier. This deterioration was not observed for higher operating pressures as can be seen from gradual increase in wall temperature around the pseudocritical region in Figure 109. Hence, excluding region I, it can be safely assumed that the Normalized *Nu* monotonically increases with *Bu*.

Recently a global parameter based on Froude number (*Fr*) was developed by Seo et al. [61] to study the influence of buoyancy.

$$\frac{1}{Fr} \sim \frac{1}{\rho_b}\left(\frac{\rho_b - \rho_w}{T_w - T_b}\right)\left(\frac{\overset{"}{Q}_{PS} D}{k_b}\right)\left(\frac{gD^3}{v_b^2}\right)\left(\frac{1}{Re_b^{2.8} Nu_b}\right) \tag{111}$$

It was suggested by Licht et al. [62] that for inverse Froude number < 0.1, the buoyancy effects are negligible. This criterion was verified using the current data for upward and downward flows. It has been found out that the criterion can satisfactorily predict the influence of buoyancy just like the Jackson's criterion for vertical flows.

For horizontal flows, Jackson [46] proposed a criterion to neglect the buoyancy effects and is in the form of,

$$Bo_j = \frac{Gr_b}{Re_b^2}\left(\frac{\rho_b}{\rho_w}\right)\left(\frac{x}{D}\right)^2 < 10 \tag{112}$$

This criterion was tested by plotting the normalized *Nu* versus the Bo_j for both the top and bottom sides of the test section as shown in Figure 114. For the top side, two regions of heat transfer were identified, namely: regions I and II. In region I, the flow is dominated by natural convection and the change of Reynolds number was found to be relatively small compared to the change in Gr_b and normalized *Nu* was found to almost linearly increase with decrease in the Bo_j on a log-log plot.

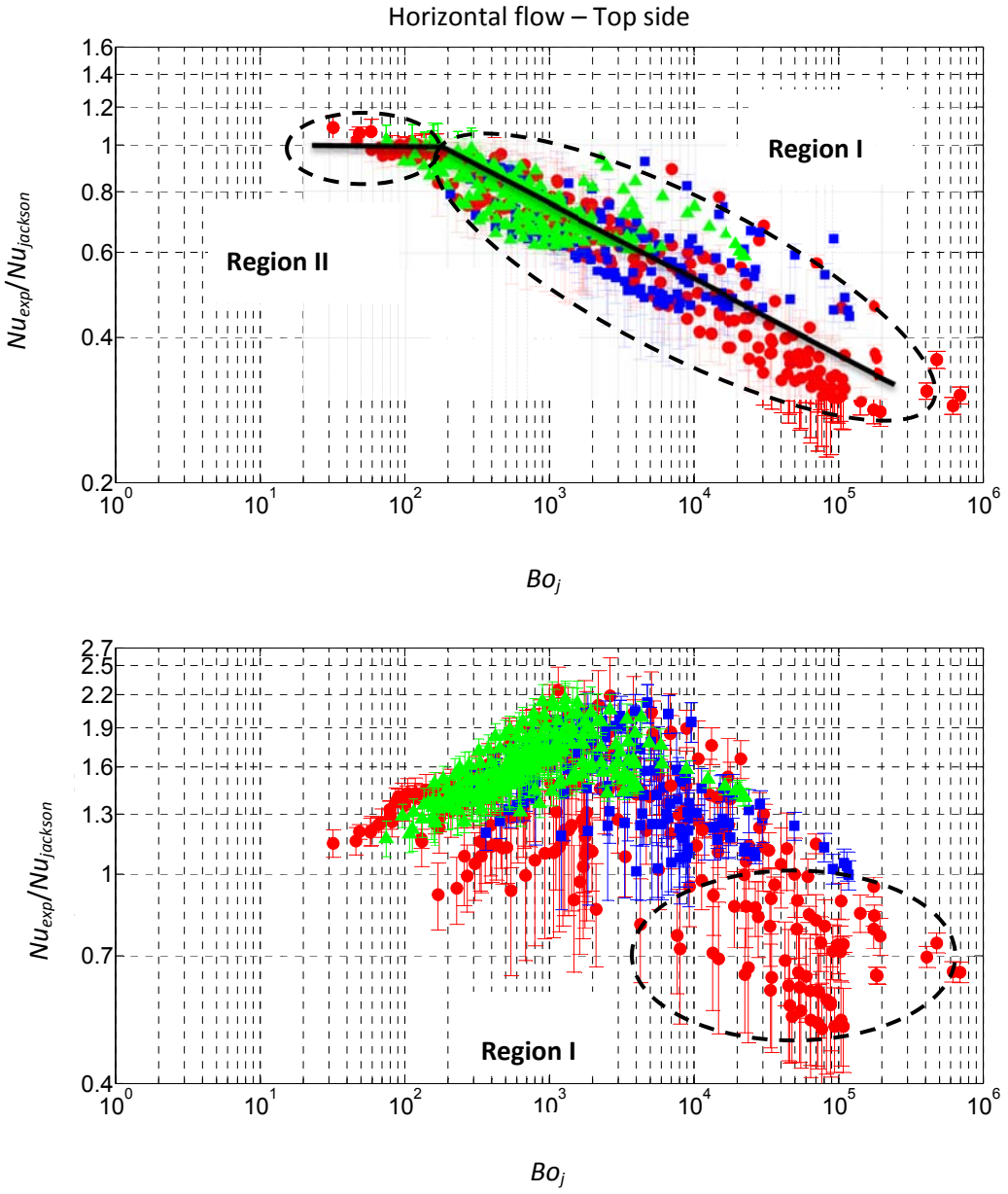

Figure 114. Normalized Nusselt number versus Jackson's buoyancy parameter, Bo_j

Transition from region I to II occurred at a Bo_j value of approximately 100. In region II, the T_b is greater than the T_{pc} and the effects of buoyancy are minimized resulting in forced convection heat transfer. The normalized *Nu* in this region is independent of the Bo_j values and the *Nu* values predicted by the Jackson's correlation are nearly the same as the experimental values.

For the bottom side, no clear trend in normalized *Nu* was observed with respect to the Bo_j. However, as the Bo_j is approaching 10, the normalized *Nu* values are approaching towards one

as suggested by Jackson [46]. Similar to the downward flow, a region of deteriorated heat transfer was observed for the bottom side. This region, marked as region I, consists of data close to the pseudocritical region for operating pressure of 7.5 MPa. This can again be attributed to pseudo-film boiling phenomenon.

Petukhov et al. [63] studied horizontal flows and derived a threshold value of Grashof number, Gr_{th}, above which the buoyancy effect can be neglected. Gr_{th} is defined as,

$$Gr_{th} = 3e-5Re_b^{2.75}\overline{Pr}^{0.5}\left[1+2.4Re_b^{-\frac{1}{8}}\left(\overline{Pr}^{\frac{2}{3}}-1\right)\right] \tag{113}$$

Where,

$$\overline{Pr} = \frac{i_w - i_b}{T_w - T_b}\left(\frac{\mu_b}{k_b}\right)$$

They also defined a Grashof number based on heat flux as,

$$Gr_q = \frac{g\overline{\beta}\overset{"}{Q}_{PS}D^4}{v_b^2 k_b} \tag{114}$$

Where,

$$\overline{\beta} = \frac{1}{\rho_{film}}\left(\frac{\rho_b-\rho_w}{T_w-T_b}\right)$$

Petukhov et al. [63] stated that the flow is completely dominated by forced convection for $Gr_q < Gr_{th}$. When this criterion was applied to the present data, no clear trend in the data was observed for either top or bottom sides. Although the criterion was not violated, Gr_q was found to be greater than Gr_{th} for all the data points indicating that the buoyancy cannot be neglected

for any of the flow conditions. Hence, this criterion can be considered as a stringent test for predicting the influence of buoyancy.

6.4.6 Evaluation of existing correlations

In this section, widely accepted correlations for supercritical fluids in literature will be evaluated. Mokry et al. [64] proposed a correlation (equation (115)) for supercritical water using data obtained in a vertical bare tube for upward flow at the Institute for Physics and Power engineering (Russia).

$$Nu_{Mokry} = 0.0061 Re_b^{0.904} \overline{Pr_b}^{0.684} \left(\frac{\rho_b}{\rho_w}\right)^{0.564} \quad (115)$$

Although this correlation was developed with supercritical water, it performs equally well for supercritical carbon dioxide as can be seen in Figure 115.

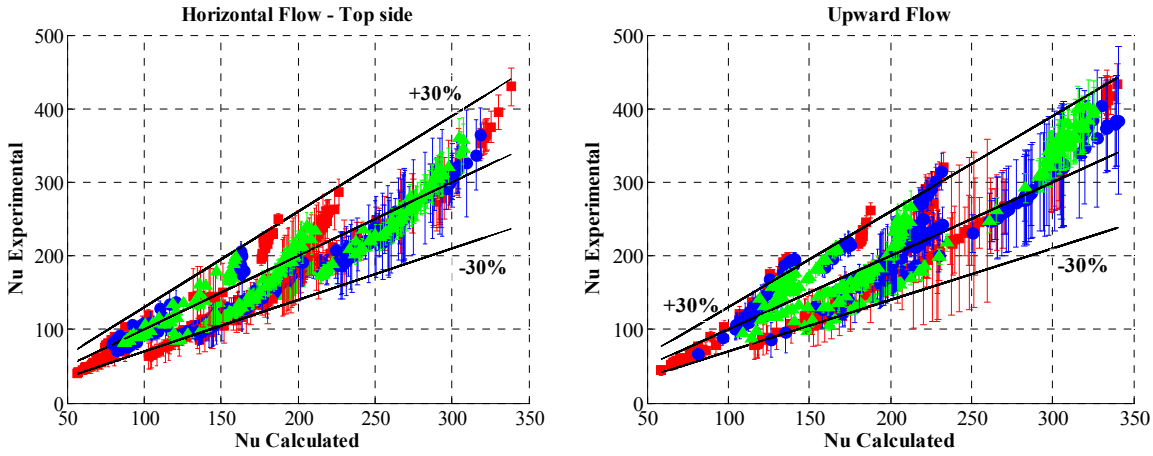

Figure 115. Calculated Nusselt number using Mokry et al. correlation

The correlation was able to capture over 95% of the data within ±30% accuracy for both upward flow and the top side of horizontal flow. Extremely good agreement was observed at lower Nusselt numbers, or the region of deteriorated heat transfer. Slightly higher standard deviation

was observed at higher Nusselt numbers where the data is dominated by forced convection. The standard deviation was much higher when the same correlation was used to predict the Nusselt numbers for downward flow and the bottom side of horizontal flows.

Swenson et al. [65] suggested a correlation (equation (116)) for upward flow of supercritical water. This correlation is based on the wall properties and was reported that the correlation performs equally good for supercritical CO_2 as well. No evaluation of this correlation was reported for downward flows. As can be seen in Figure 115, the Swenson et al. correlation was able to capture over 90% data of the within ±30% accuracy.

$$Nu_{swenson} = 0.0459 Re_w^{0.923} \overline{Pr_w}^{0.613} \left(\frac{\rho_w}{\rho_b}\right)^{0.231} \quad (116)$$

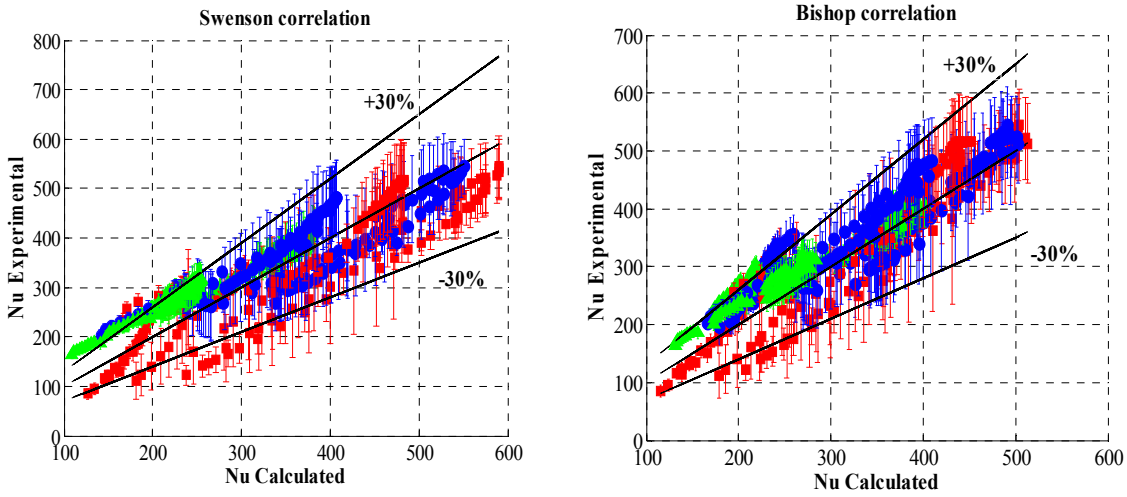

Figure 116. Calculated Nusselt number for downward flow

Bishop et al. [66] suggested a correlation (equation (117)) based on bulk properties for upward flow of supercritical water. It was reported that the correlation could be used for supercritical CO_2 as well [60]. As can be seen in Figure 116, this correlation was able to capture over 95% of the data within ±30% accuracy.

$$Nu_{bishop} = 0.0069 Re_b^{0.9} \overline{Pr_b}^{0.66} \left(\frac{\rho_w}{\rho_b}\right)^{0.43} \left(1 + 2.4\left(\frac{D}{x}\right)\right) \quad (117)$$

It should be noted that the Swenson et al. correlation which is based on the wall properties over predicted majority of downward flow data, whereas, the bishop et al. correlation which is based on the bulk properties performed much better than the Swenson et al. correlation.

7 Wet Cooling tower option for S-CO_2 Cycle

This chapter describes the final task of this report, which is to investigate the use of indirect wet cooling tower option for an S-CO_2 cycle. To perform this task a code was developed in Engineering Equation Solver (EES) to estimate the tower dimensions, power and water consumption, and to perform economic analysis. The first two sections of this chapter will provide brief introduction to cooling towers and cooling tower theory. Third section will explain the details of the code developed at Argonne National Laboratory (ANL) and finally results of the investigation will be discussed.

7.1 Introduction to cooling towers

7.1.1 Classification of cooling towers

Cooling towers can be classified into different categories as follows [67]:

Based on heat transfer mode

a) Dry towers in which the working fluid, in this case S-CO_2, flows through finned coiled sections and the air is blown over the coils. Hence, the working fluid is cooled totally by the sensible heat transfer as there is no direct contact between air and the working fluid. In such towers, the theoretically possible lowest temperature that can be achieved is equal to the dry bulb temperature of ambient air.

b) Wet cooling towers or simply evaporative cooling towers operate on the principle of evaporation. Heat from the working fluid is rejected to the circulating water in the cooler and ultimately heat from the water is rejected to atmosphere through a wet cooling tower. In a wet cooling tower, theoretically, the water can be cooled down to the wet bulb temperature of ambient air.

c) Fluid coolers are hybrid towers in which the working fluid is passed through a tube bundle, upon which water is sprayed and a fan-induced draft applied. The resulting heat transfer performance is closer to that of a wet cooling tower.

Based on the air circulation

a) Natural draft towers are the large hyperbolic towers in which the air flow is produced by the density differential between the heated air in the tower and the relatively cool ambient air outside the tower. These towers have a very high capital costs due to their large size and operate efficiently only in the regions of high relative humidity.

b) Mechanical draft towers use either single or multiple fans to provide required volumetric flow rate of air through the tower. These towers are in general smaller than the natural draft towers and the presence of fans provide a means of better regulating air flow to compensate for changing atmospheric and load conditions. These towers can be sub-categorized as forced draft and induced draft towers. Forced draft towers have the fan located in the ambient air stream entering the tower and are characterized by high air entrance velocities and low exit velocities. Due to low air exit velocities, these towers are more susceptible to recirculation, thereby, altering the entering air stream conditions. Induced draft towers have the fan located in the exit air stream and are characterized by low air entrance velocities and high exit velocities.

Based on the flow configuration

a) Cross flow in which the air flow is perpendicular to the water flow. Air enters the cooling tower through one or more vertical faces to meet the fill material and the water flows vertically downward through the fill due to gravity.

b) Counter flow in which the air flows opposite to the water flow. Air enters the cooling tower from the bottom side and the water is sprayed onto the fill from top using nozzles. Counter flow configuration is more effective than the cross flow as it requires less cooling tower volume for the same amount of heat load. Disadvantage of the counter flow configuration is that it uses nozzles to distribute the flow and hence, the required pump head increases compared to the cross flow configuration.

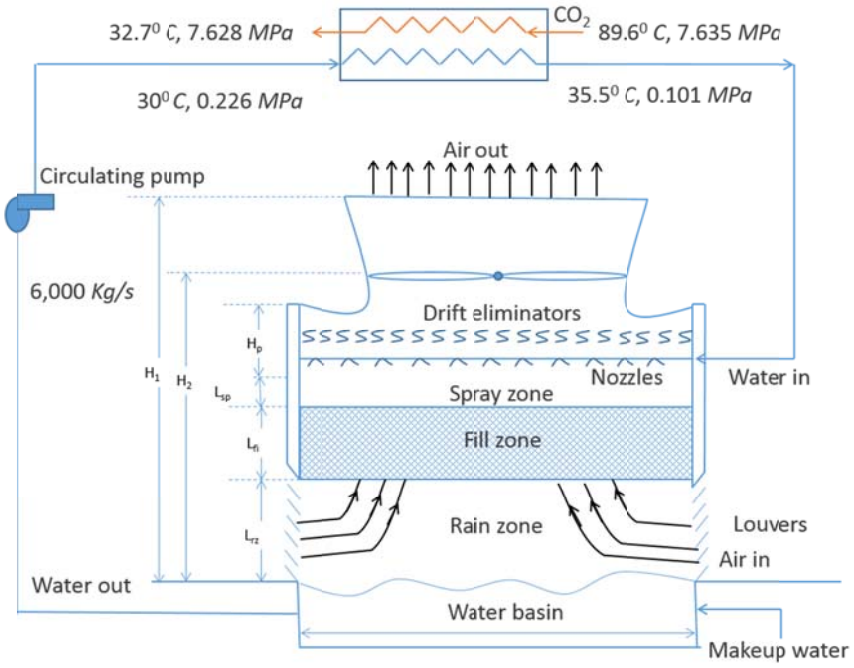

Figure 117. Proposed schematic of the cooler and induced draft cooling tower

Considering the advantages and disadvantages for each type of tower, counter flow induced draft cooling towers are identified to be most suitable for use with the proposed plants. A

simple schematic of the cooler and selected cooling tower is shown in Figure 117. Also shown in the Figure are the key components of a cooling tower which include fill material, water-basin, drift eliminators, louvers, nozzles, fans, and circulating pump.

7.1.2 Components of a cooling tower

A brief explanation of the key components of a cooling tower is provided below.

Fill material is the key component of a cooling tower and is an area of active research for cooling tower manufacturers. The purpose of the fill material is to enhance the heat transfer by increasing the area and time of contact between water and air. A proper design of the fill material can reduce the required fill volume significantly. Two common types of fills are identified in literature [69]:

1) Splash fill – Water splashes over successive layers of horizontal or inclined splash bars, continuously breaking the water into small droplets, while also wetting the fill surface as shown in Figure 118. Most commonly used materials for splash bars are wood and plastic. Plastic splash fills are known to promote better heat transfer than wood splash fills.
2) Film fill – Is the most commonly used fill type nowadays because of its ability to expose greater water surface within a given packed volume. Water flows in the form of a thin film over vertically oriented sheets of corrugated pattern fill as shown in Figure 118. With the use of film fill same amount of cooling can be achieved within a smaller volume compared to the splash fill. Plastic is the most common material used for film type fills.

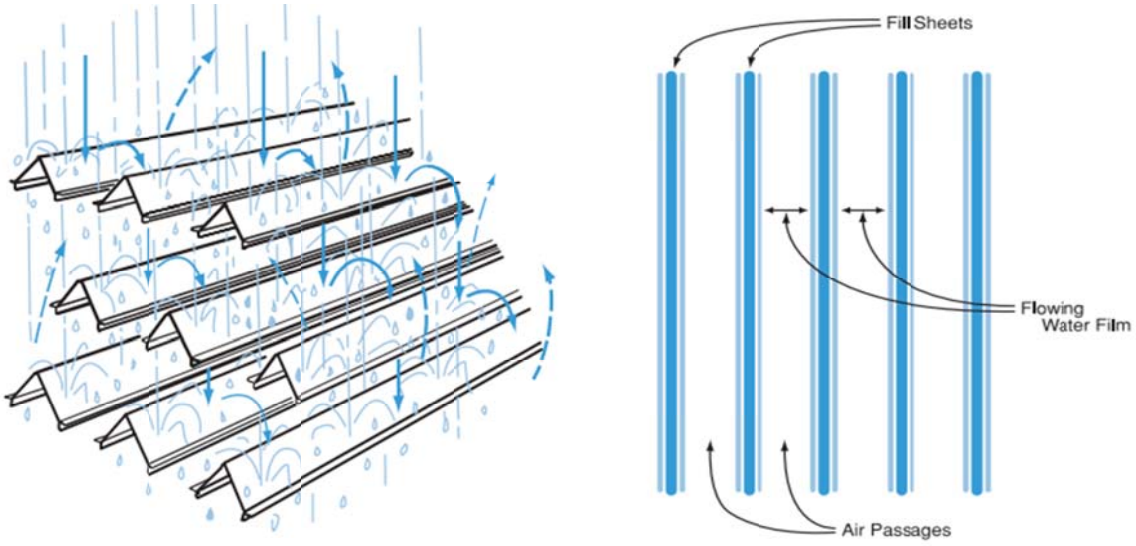

Splash type fill Film type fill

Figure 118. Concept of different fill types

Cold-water basin is located at or near the bottom of the cooling tower, and it is used to collect the cooled water that flows through the fill. The capacity of cold water basin should be large enough to provide the required water flow. This is also the point of water exchange between the cooling tower and external water bodies like pond, river etc.

Drift eliminators capture the water droplets entrapped in the air stream by providing a tortuous path for the air out. These water droplets should not be confused with the evaporated water and would be lost to the atmosphere if not captured, thereby, increasing the makeup water requirements. Promoting better design of drift eliminators will limit the drift losses to 0.2 - 0.5% of the total water flow.

Louvers are used to equalize the air flow in the tower and retain the water within the cooling tower. Louvers are commonly used for cross-flow towers and many counter flow tower designs do not require louvers.

Nozzles are used to distribute or spray water onto the fill. It is important to ensure that the water distribution is uniform at the top of fill to achieve proper wetting of the entire fill surface.

Fans can be of either axial or centrifugal type. Axial fans are generally used in induced draft towers and centrifugal fans are more common in forced draft towers. These fans should be equipped with either adjustable pitch blades or variable frequency drives so that the air flow can be varied due to the change in load and atmospheric conditions.

Circulating pump is used to transport the water between the cooling tower and the cooler. The water is pumped from the cold-water basin through to the cooler, where it is used as cooling medium. The hot water then returns back to the nozzle distribution system for evaporative cooling in the cooling tower. Hence, the pump should be able to overcome the pressure losses in the cooler, piping, and the tower.

7.2 Cooling tower theory

Heat and mass transfer in the cooling tower occurs in three zones namely; spray zone, fill zone, and the rain zone as shown in Figure 117. More than 90% of the heat transfer occurs in the fill zone and it has been reported [70] that the error in prediction of tower volume due to exclusion of spray and rain zones is about 6.5%. When the spray and rain zones are included in the model the error was reduced to 2.65% compared to the full scale 3-D modeling of the tower. Hence, the spray and rain zones are not explicitly modeled in the current study. The governing equations in the fill zone of a counterflow cooling tower are derived by making certain simplifying assumptions. Water droplets are assumed to be surrounded by a thin film of saturated air at water temperature. Heat and mass transfer between this thin layer and the surrounding air occur due to temperature and humidity ratio difference respectively. Figure 119shows a control volume in the fill of a counterflow cooling tower.

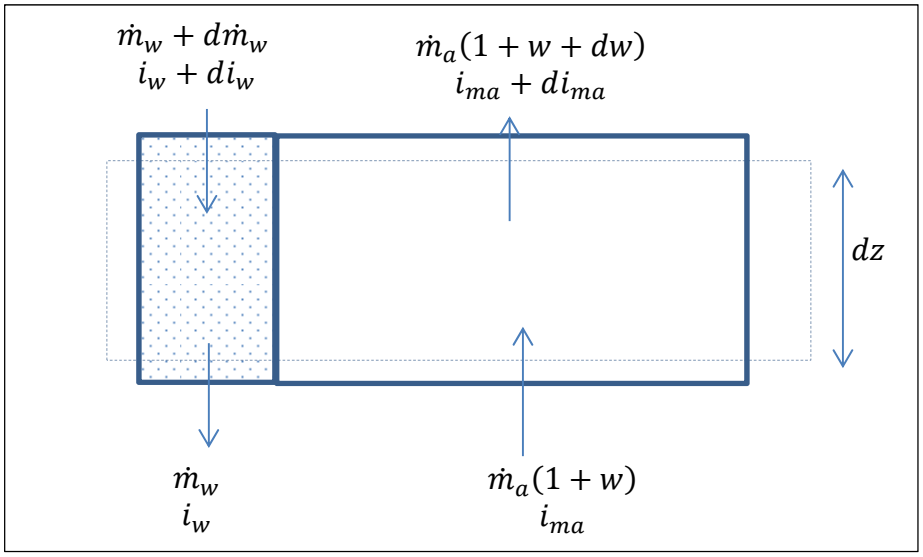

Figure 119. Control volume of counterflow fill configuration

Overall mass and energy balance for the control volume yields,

$$d\dot{m}_w = \dot{m}_a dw \tag{118}$$

$$\dot{m}_a di_{ma} - \dot{m}_w di_w - i_w d\dot{m}_w = 0 \tag{119}$$

Substitute equation (118) into equation (119) and use $di_w = C_{pw} dT_w$ to arrive at,

$$dT_w = \frac{\dot{m}_a}{\dot{m}_w}\left(\frac{1}{C_{pw}} di_{ma} - T_w dw\right) \tag{120}$$

Consider the air side control volume as shown in Figure 120. An energy balance at the interface yields,

$$dQ = dQ_m + dQ_c \tag{121}$$

Where, dQ_c is the sensible heat transfer due to the difference in temperature and dQ_m is the enthalpy transfer due to difference in humidity ratio between the saturated air film and the surrounding mean air stream.

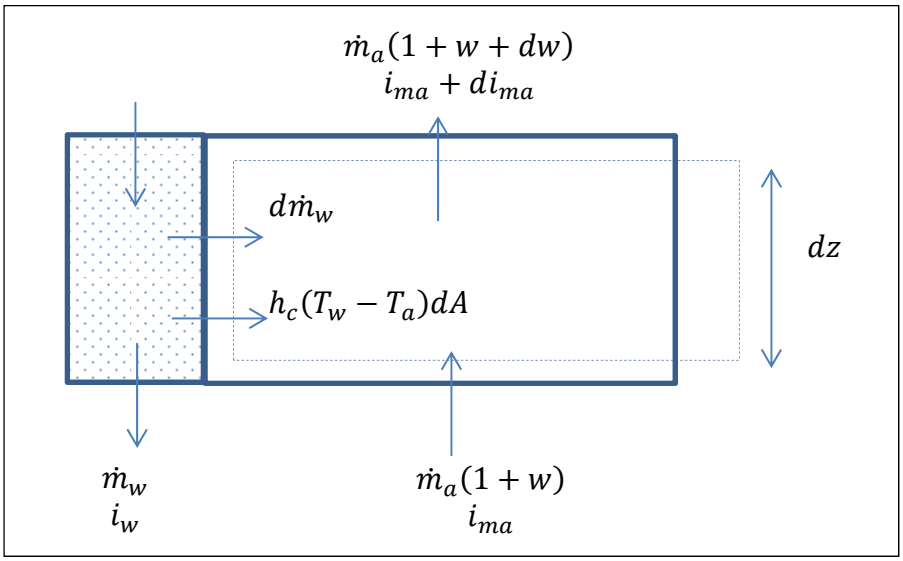

Figure 120. Air side control volume

The convective heat transfer in equation (121) can be expressed as,

$$dQ_c = h_c(T_w - T_a)dA \tag{122}$$

The mass transfer at the interface is given by,

$$dm_w = h_d(w_{sw} - w)dA \tag{123}$$

The corresponding enthalpy transfer due to the mass transfer in equation (123) is

$$dQ_m = i_v h_d(w_{sw} - w)dA \tag{124}$$

Where, i_v, is the enthalpy of the water vapor evaluated at the bulk water temperature.

The temperature differential in equation (122) can be expressed in terms of enthalpy difference as follows,

$$T_w - T_a = \frac{((i_{masw} - i_{ma}) - (w_{sw} - w)i_v)}{c_{pma}} \tag{125}$$

Substituting equation (122) and (124) into equation (121) and using equation (125) will result in,

$$dQ = h_d[Le(i_{masw} - i_{ma}) + (1 - Le)i_v(w_{sw} - w)]dA \quad (126)$$

Where, Le is the Lewis factor and is defined as shown in equation (127). It is an indication of the relative rates of heat and mass transfer during evaporation process.

$$Le = \frac{h_c}{C_{pma}h_d} \quad (127)$$

From equation (126) enthalpy transfer to the air stream can be expressed as,

$$di_{ma} = \frac{h_d dA}{\dot{m}_a}[Le(i_{masw} - i_{ma}) + (1 - Le)i_v(w_{sw} - w)] \quad (128)$$

Since, the current study deals with one dimensional model of the cooling tower, the available area for heat and mass transfer is assumed to be the same at any horizontal cross-section through the fill, the transfer area for a section dz is expressed as,

$$dA = a_{fi}A_{base}dz \quad (129)$$

Where, a_{fi}, is the area density of the fill. In other words, it is the wetted area divided by the volume of the fill.

Hence, equation (128) can be written as,

$$\frac{di_{ma}}{dz} = \frac{h_d a_{fi} A_{base}}{\dot{m}_a}[Le(i_{masw} - i_{ma}) + (1 - Le)i_v(w_{sw} - w)] \quad (130)$$

Equation (130) together with equation (120) describes the change in the enthalpy of air-water vapor mixture and the change in water temperature. It is clear that these equations need to be solved using numerical integration techniques with an additional humidity ratio differential

equation. However, Merkel [71] made simplifying assumptions to reduce these equations to simple hand calculations. These assumptions are as follows:

1) The evaporation losses are neglected, i.e. $dw = 0$ in equation (120). Depending on the conditions, this assumption might result in over-prediction of the tower size since the energy transfer due to mass transfer is neglected.
2) Lewis factor is assumed to be equal to 1. Lewis factor is typically measured to be in the range of 0.85-0.9 [76].
3) To estimate the air outlet conditions and make-up water requirements, it is assumed that the air exiting the tower is saturated (100% relative humidity).

Implementing these simplifying assumptions, equations (130) and (120) will reduce to

$$\frac{di_{ma}}{dz} = \frac{h_d a_{fi} A_{base}}{\dot{m}_a}(i_{masw} - i_{ma}) \tag{131}$$

$$\frac{dT_w}{dz} = \frac{\dot{m}_a}{\dot{m}_w}\frac{1}{C_{pw}}\frac{di_{ma}}{dz} \tag{132}$$

Finally, these equations can be combined into a single governing equation known as the Merkel equation,

$$Me = \frac{h_d a_{fi} L_{fi}}{G_w} = \int_{T_{wo}}^{T_{wi}} \frac{C_{pw} dT_w}{(i_{masw} - i_{ma})} \tag{133}$$

In cooling tower practice, Me is often referred to as the number of transfer units (NTU) and is a measure of difficulty of the cooling task [72]. Merkel equation (equation (133)) is the cooling tower design equation and can be used to estimate the cooling tower dimensions if the mass transfer coefficient (h_d) and area density of the fill (a_{fi}) are known. Mass and heat transfer occur on the wetted surface of fill and on the surface of drops. Hence, it is practically impossible

to measure h_d and a_{fi} individually. Fortunately, these two exist as a product in equation (133) and individual values are not needed for design calculations. Fill and cooling tower vendors don't release the values of $h_d a_{fi}$. However, empirical correlations are available in literature which can used to estimate fill dimensions.

Cooling process in the fill can be represented on an enthalpy-temperature diagram as shown in Figure 121. As the water is cooled flowing downwards, the saturated air film enthalpy follows the saturation curve AB. The air operating line is represented by CD. The linear nature of air operating line is due to the fact that the solution of equation (132) is linear. The slope of the air operating line equals the liquid to gas ratio, $\dot{m}_w/\dot{m}_a$. BC represents the initial enthalpy driving force and the projected length of CD on to the temperature axis represents the range of the cooling tower.

$$Range = T_{wi} - T_{wo} \tag{134}$$

The cooling tower approach is the difference between the cold water temperature leaving the tower and the ambient air wet bulb temperature. From economic standpoint, a cooling tower should be designed such a way that the approach is greater than 5^0F or 2.2^0C. For fixed water conditions, the water operating curve will always be AB, whereas, the air operating line can be adjusted by changing $\dot{m}_w/\dot{m}_a$ or the ambient wet bulb temperature. An increase in the ambient wet bulb temperature shifts the air operating line upward and to the right to establish equilibrium conditions. It can also be seen from Figure 121 that as the $\dot{m}_w/\dot{m}_a$ increases the potential enthalpy difference within the tower decreases and for $\dot{m}_w/\dot{m}_a$ > 2.5, energy transfer can occur from air to water in part of the tower. This undesirable situation should be avoided, but sometimes is necessary when the wet bulb temperature of the ambient air is extremely low

like in the winter months. Typically, mechanical draft counter flow cooling towers are designed for $\dot{m}_w/\dot{m}_a$ ranging from 0.5 to 1.75 [73].

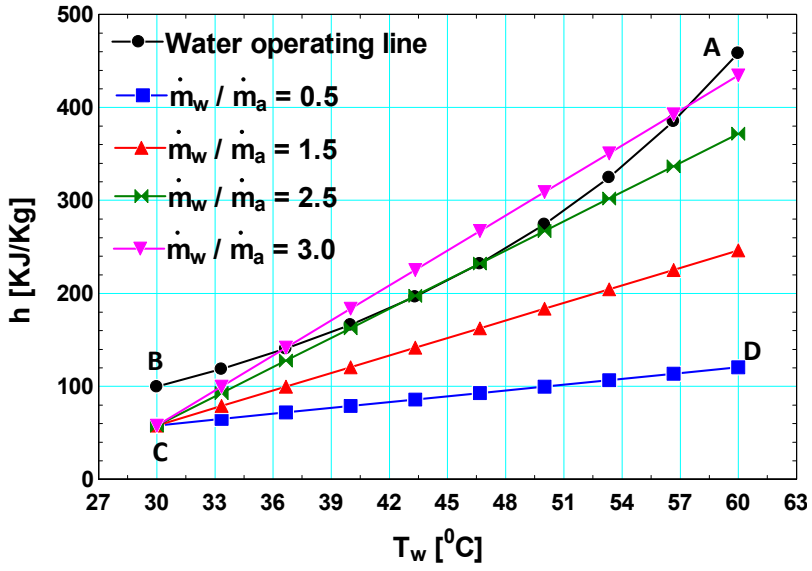

Figure 121. Counterflow cooling diagram

7.3 Design procedure

In this study, the cooling tower design analysis was carried out for an S-CO_2 cycle developed for the AFR-100 and ABR-1000 reactor applications. The reactor power of the AFR-100 is 250 MW_{th}, for net cycle efficiency of 42.27% results in 104.8 MW_e. The reactor power of the ABR-1000 is 1000 MW_{th} and for net cycle efficiency of 40.26% results in 400.3 MW_e. Reference cooler design water conditions for both these power plants are tabulated in Table IV and these conditions are selected for the base case cooling tower design. The effect of changing the water conditions on cooling tower and cooler size design will be presented later.

Table IV. Reference cooler design conditions for AFR-100 and ABR-1000 plants

Power plant	AFR-100	ABR-1000
Reactor power (MW_{th})	250	1000
Electrical output (MW_e)	104.8	400.3
CO_2 inlet temperature (^0C)	89.6	87.3
CO_2 outlet temperature (^0C)	32.8	32.7
CO_2 pressure drop (MPa)	0.007	0.009
Cycle efficiency (%)	42.27	40.26
Water inlet temperature (^0C)	30	30
Water outlet temperature (^0C)	35.5	36.8
Water flow rate (kg/s)	6,000	20,000
Water pressure drop (MPa)	0.125	0.104
Cooler thermal load (MW)	137.2	569.2

Cooler conditions

7.3.1 Estimation of optimum $\dot{m}_w/\dot{m}_a$

For a given set of cooling tower design conditions an optimum value of $\dot{m}_w/\dot{m}_a$ exists. This optimum $\dot{m}_w/\dot{m}_a$ will result in minimum construction and operating costs. As a rule of thumb [74], to find the optimum $\dot{m}_w/\dot{m}_a$, air outlet temperature is taken as the average of hot and cold water temperature entering and exiting the tower.

$$T_{ao} = \frac{T_{wi}+T_{wo}}{2} \tag{135}$$

It has been reported [74] that the approximated air outlet temperature is very close to the actual optimal design temperature. For a given water flow rate, air flow rate can be estimated within ±10% of the actual optimum design flow rate. Once the optimum air outlet conditions are known, $\dot{m}_w/\dot{m}_a$ can be calculated according to,

$$\frac{\dot{m}_w}{\dot{m}_a} = \frac{i_{mao}-i_{mai}}{C_{pw}(T_{wi}-T_{wo})} \tag{136}$$

7.3.2 Merkel number

The tower Merkel number, *Me*, from equation (133) can be solved numerically using the Chebyshev four point numerical integration method [73] as follows:

$$Me\ or\ NTU = C_{pw}\int_{T_{wo}}^{T_{wi}} \frac{dT_w}{(i_{masw}-i_{ma})} = \frac{C_{pw}(T_{wi}-T_{wo})}{4}\left(\frac{1}{\Delta i_1}+\frac{1}{\Delta i_2}+\frac{1}{\Delta i_3}+\frac{1}{\Delta i_4}\right) \tag{137}$$

where,

Δi_1 = value of $i_{masw} - i_{ma}$ at $T_{wo} + 0.1Range$

Δi_2 = value of $i_{masw} - i_{ma}$ at $T_{wo} + 0.4Range$

Δi_3 = value of $i_{masw} - i_{ma}$ at $T_{wo} + 0.6Range$

Δi_4 = value of $i_{masw} - i_{ma}$ at $T_{wo} + 0.9Range$

Table V presents an example of calculation of the Merkel number for AFR-100. Calculations are performed in engineering equation solver (EES) [75]. Plotting several values of *Me* as a function of $\dot{m}_w/\dot{m}_a$ produces the tower demand curves. The tower characteristic curve is then found for design $\dot{m}_w/\dot{m}_a$ by field testing under variable flow and atmospheric conditions.

Table V. Tower Merkel number calculation example

Water side			Air side		Enthalpy difference
Description	**T_w (^{0}C)**	**i_{masw} (J/kg)**	**Description**	**i_{ma}(J/kg)**	**$1/(i_{masw} - i_{ma})$**
$T_{wo} + 0.1Range$	32.5	56647.8	$i_{mai} + 0.1\left(\frac{\dot{m}_w}{\dot{m}_a}\right)Range$	45571.7	0.0903e-3
$T_{wo} + 0.4Range$	35	63342.6	$i_{mai} + 0.4\left(\frac{\dot{m}_w}{\dot{m}_a}\right)Range$	51214.7	0.0825e-3
$T_{wo} + 0.6Range$	36.67	68259.1	$i_{mai} + 0.6\left(\frac{\dot{m}_w}{\dot{m}_a}\right)Range$	54976.7	0.0753e-3
$T_{wo} + 0.9Range$	39.17	76401.3	$i_{mai} + 0.9\left(\frac{\dot{m}_w}{\dot{m}_a}\right)Range$	60619.7	0.0634e-3
$\sum 1/(i_{masw} - i_{ma})$					0.3114e-3
Merkel number (Me) = $\sum 1/(i_{masw} - i_{ma}) * Range * C_{pw}/4$					1.1677

7.3.3 Estimation of floor area

Instead of using a single large cooling cell it is common to use a certain number of small cells to provide better temperature control as well as reduce the total power consumption. Table VI shows the different cell types used by a manufacturer [79]. These cells are classified based on

the cell dimensions and the blower horsepower required for certain range of volumetric flow rate through the cell. On this basis, seven cells are identified and are color coded in the table. Choosing different cell sizes will result in different floor area as well as power consumption. Using the smallest cell size (towers 1-4) will increase the total floor area of the cooling tower but will reduce the power consumption. Using the largest cell size (towers 22-24) will reduce the total floor area but will increase the power consumption.

Table VI. Manufacturer data for different cell types

Tower	Flow rate (cfm)	Blower power (HP)	Length	Width	Height
1	70,800	10	7'9 5/8"	18'1 1/4"	10'2 3/4"
2	80,750	15	7'9 5/8"	18'1 1/4"	10'2 3/4"
3	88,300	20	7'9 5/8"	18'1 1/4"	10'2 3/4"
4	95,000	25	7'9 5/8"	18'1 1/4"	10'2 3/4"
5	99,400	15	9'9 1/4"	20'1 1/4"	10'2 3/4"
6	108,700	20	9'9 1/4"	20'1 1/4"	10'2 3/4"
7	116,550	25	9'9 1/4"	20'1 1/4"	10'2 3/4"
8	123,550	30	9'9 1/4"	20'1 1/4"	10'2 3/4"
9	124,450	20	11'9 3/4"	20'7 1/4"	10'2 3/4"
10	133,450	25	11'9 3/4"	20'7 1/4"	10'2 3/4"
11	142,200	30	11'9 3/4"	20'7 1/4"	10'2 3/4"

12	143,800	30	11'9 3/4"	20'7 1/4"	11'6"
13	157,550	40	11'9 3/4"	20'7 1/4"	11'6"
14	166,050	30	11'9 3/4"	22'1 1/4"	13'3 5/8"
15	181,800	40	11'9 3/4"	22'1 1/4"	13'3 5/8"
16	195,000	50	11'9 3/4"	22'1 1/4"	13'3 5/8"
17	193,800	40	11'9 3/4"	22'1 1/4"	15'11 5/8"
18	207,800	50	11'9 3/4"	22'1 1/4"	15'11 5/8"
19	220,150	60	11'9 3/4"	22'1 1/4"	15'11 5/8"
20	221,550	50	11'9 3/4"	22'1 1/4"	18'7 5/8"
21	235,000	60	11'9 3/4"	22'1 1/4"	18'7 5/8"
22	255,400	50	13'11 7/8"	24'1 1/4"	18'7 5/8"
23	270,700	60	13'11 7/8"	24'1 1/4"	18'7 5/8"
24	290,050	75	13'11 7/8"	24'1 1/4"	18'7 5/8"

Several years ago a quotation was obtained from Delta cooling towers Inc. for one similar (but lower power) design condition and the cell used by the company has dimensions very close to that of the cell used for towers 1-4 in Table VI. Hence, cell #1 is chosen for this particular study. Later in this report it is concluded that using the smallest cell size is more economical to the plant and this justifies the use of cell #1. Two extreme options are possible for a selected cell type:

1) Lowest power consumption – In this option, lowest possible air flow rate per cell is selected from the table. For cell #1 this value is 70,800 *cfm*. This will reduce the power consumption per cell but will increase the total number of cells required to achieve the desired performance. Overall, this option will result in least power consumption and largest cooling tower size. Number of required cells is estimated as,

$$Number\ of\ cells = \frac{\dot{Q}_{ao}}{70800} \tag{138}$$

2) Lowest footprint – In this option, highest possible air flow rate per cell is selected. For cell #1 this value is 95,000 *cfm*. This will increase the blower power consumption per cell but will decrease the total number of cells. This option will result in highest power consumption and smallest tower footprint/cost. Number of required cells is calculated as,

$$Number\ of cells = \frac{\dot{Q}_{ao}}{95000} \tag{139}$$

Total volumetric flow rate of air required for all the cells is calculated from the known air mass flow rate in section 7.3.1 as,

$$\dot{Q}_{ao} = \frac{\dot{m}_a}{\rho_{ao}}\ [cfm] \tag{140}$$

Once the number of required cells is calculated for each option, the required floor area is calculated as,

$$A_{floor} = Number\ of\ cells * A_{cell} \tag{141}$$

Where, A_{cell} is the area of one cell and is equal to 7'9 5/8" X 18'1 1/4" for cell #1. Figure 122 shows the one cell plan of Delta cooling towers Inc. [80].

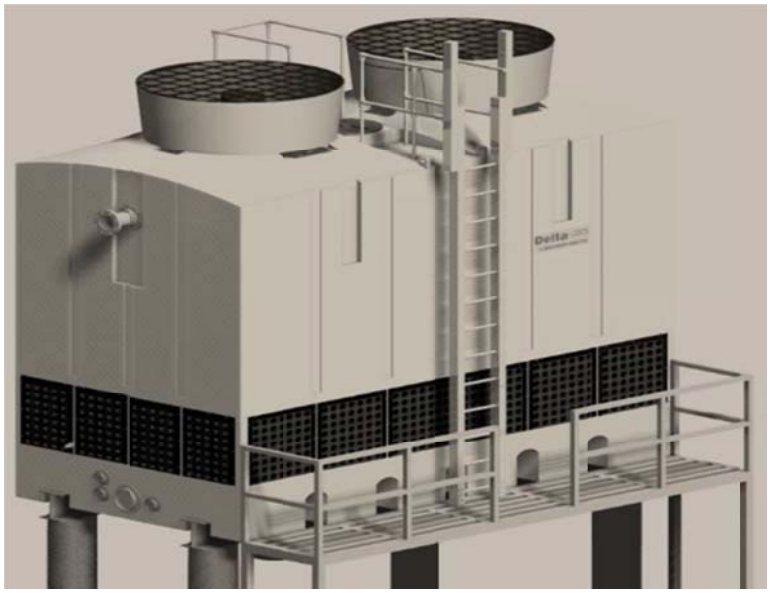

Figure 122. Delta cooling towers Inc. one cell plan [80]

It should be noted that the outlet air density is used to estimate the required volumetric flow rate of air in equation (140) because the fan is located at the exit for an Induced draft cooling tower. If these calculations are being performed for a forced draft cooling tower, inlet air density has to be used and this will change the required floor area and number of cells accordingly.

7.3.4 Estimation of fill height

As explained in the introduction section, there are different types of fills and use of better fill design will reduce the size of fill significantly. Empirical correlations for different fill types are available in literature and can be used to estimate the size of cooling fill. Kloppers *et al* [76] performed experiments to investigate different types of fill and proposed correlations to predict *NTU* for splash, trickle (film fill with round channels), and film type (with rectangular channels) fills.

Once the optimum $\dot{m}_w/\dot{m}_a$ and floor area are calculated, the water and air mass fluxes are defined as,

$$G_w = \frac{\dot{m}_w}{A_{floor}}$$

$$G_a = \frac{\dot{m}_a}{A_{floor}}$$

NTU for a splash type fill is given as,

$$\frac{NTU}{L_{fill}} = 0.249013 G_w^{-0.464089} G_a^{0.653578} \quad (142)$$

NTU for a trickle fill is given as,

$$\frac{NTU}{L_{fill}} = 0.817071 G_w^{-0.581055} G_a^{0.670746} \quad (143)$$

NTU for a film fill is given as,

$$\frac{NTU}{L_{fill}} = 0.996604 G_w^{-0.469512} G_a^{0.790386} \quad (144)$$

NTU is estimated using numerical integration technique as mentioned in section 7.3.2. Hence, for varying water and air conditions required fill height for each type of fill can be calculated using the equations specified above.

Once the fill height is known, as a rule of thumb [74], length of the rain zone is assumed to be equal to that of fill length. Similarly, length of spray zone is assumed to be equal to be half of the fill length.

$$L_{rz} = L_{fill}$$

$$L_{sp} = 0.5 L_{fill}$$

7.3.5 Water consumption rate

There are three major water losses in a wet cooling tower:

1) Evaporation Losses – As the water is cooled in the cooling tower, portion of water gets evaporated into the air stream. The difference between amount of water vapor in the entering and exiting air streams will provide the quantity of water evaporated.

$$E = \dot{m}_a(w_o - w_i) \tag{145}$$

2) Blow-down Losses – As the water evaporates, solids and chemical matter concentrate in the cooling water. If this is ignored, it will result in severe corrosion and chemical build up affecting the performance of tower in long run. Hence, some amount of circulating water needs to be replaced by fresh water to avoid solids/chemical build up. The amount of water which needs to be replaced can be estimated as,

$$B = \frac{E}{COC-1} \tag{146}$$

Where, COC is known as cycles of concentration and is defined as,

$$COC = \frac{Concentration\ of\ solids\ in\ the\ cooling\ tower\ water}{Concentration\ of\ solids\ in\ the\ cooling\ tower\ makeup\ water} \tag{147}$$

Cycles of concentration is typically limited from 3-7. Value of 3 is used in this report for an upper estimate of blow-down losses.

3) Drift Losses – As the air flows in the cooling tower, some of the water droplets get carried away by the air stream. With the use of drift eliminators, these losses can be minimized to within 0.2-0.5% of the total water flow rate.

$$W = 0.005\dot{m}_w \tag{148}$$

Total water consumption rate is estimated as the sum of evaporation, blow-down, and drift losses.

7.3.6 Power requirements

Power required to operate the cooling tower comprises of two parts – water pump power and the air blower power. The power required to operate the pump is estimated as,

$$P_{pump} = \frac{\dot{m}_w H_p g}{\eta_{pump}} \tag{149}$$

Where, H_p is the net required pump head and is equal to the sum of required head in the cooling tower and the cooler.

$$H_p = H_{coolingtower} + H_{cooler} \tag{150}$$

The net cooling tower head is equal to the head required to raise the water from the water basin to the nozzle sprays,

$$H_{coolingtower} = L_{sp} + L_{fill} + L_{rz} = 2.5L_{fill}$$

An additional head of 10*ft* is added to the cooling tower head to compensate for the assumptions made and to better match the vendor quotations.

The net cooler head is the head required to overcome the water side pressure drop across the cooler, expressed in the units of height of water column.

$$H_{cooler} = \delta P_{cooler}[\mathrm{m}]$$

Efficiency of the pump is assumed to be 90%.

Blower power for the lowest footprint option is calculated as,

$$P_{blower} = 10[\text{HP}] * Number\ of\ cells \quad (151)$$

Blower power for the lowest power consumption option is calculated as,

$$P_{blower} = 25[\text{HP}] * Number\ of\ cells \quad (152)$$

7.3.7 Estimation of cooling tower cost

Delta cooling towers Inc. quoted $448,439 for 12 cells. Hence, the price of each cell is calculated to be $37,370. Total cost of the cooling tower is then estimated as,

$$Tower_{cost} = Cost\ per\ cell * Number\ of\ cells \quad (153)$$

Alternatively, Zanker *et al* [74] proposed an empirical correlation in 1967 for the estimation of cooling tower construction cost:

$$\$_{1967} = \frac{Q_{load}\left[\frac{BTU}{hr}\right]}{C*A+39.2R-586} \quad (154)$$

Where, *R* and *A* are range and approach in Fahrenheit respectively. C in equation (154) is defined as,

$$C = \frac{279}{[1+0.0335(85-WBT)^{1.143}]} \quad (155)$$

Where, *WBT* is the design wet bulb temperature in Fahrenheit. It should be noted that the above correlation was proposed in 1967 when the material and fabrication costs were different compared to the present day. Due to inflation rate, $1 in 1967 has the same buying power as $7.08 in 2014 [77]. These statistics are based on change in average consumer price index from 1967 to 2014. Hence, the value estimated from equation (154) is multiplied by a factor of 7.08 to estimate the cost of tower in 2014.

$$Cost_{tower} = 7.08 * \$_{1967} \quad (156)$$

7.3.8 Factors affecting cooling tower size

There are several factors which affect the design of a cooling tower. Some of the important variables are mentioned below:

1) Heat load is dependent on the cycle conditions and for steady state design calculations it is assumed to be constant (137.2 MW for AFR-100, and 569.2 MW for ABR-1000). In general, if other variables are held constant, heat load is directly proportional to the mass flow rate of water according to the heat balance equation,

$$Q_{load} = \dot{m}_w C_{pw}(T_{wo} - T_{wi}) \quad (157)$$

   Hence, the tower volume increases linearly with the heat load as shown in Figure 123.

2) Range – If other variables (i.e., heat load, approach, and wet bulb temperature) are held constant, tower volume varies inversely with the range as shown in Figure 124. This is primarily due to two reasons. First, increasing the range at a constant heat load requires the water flow rate to be lowered. Second, increasing the range will increase the enthalpy difference between the entering hot water temperature and the entering wet bulb temperature of air.
3) Approach – Tower volume varies inversely with the approach, provided that other variables are held constant. A longer approach requires smaller tower as shown in Figure 125. It can be seen that the tower volume starts to increase asymptotically for approach lower than 2.2^0C. For this reason, it is not economical to design cooling towers for any approach values of less than 5^0F or 2.2^0C.

4) Wet bulb temperature – Tower size varies inversely with wet bulb temperature as shown in Figure 126. In a hypothetical situation, for fixed heat load, approach, and range, reducing the design wet bulb temperature will increase the size of the tower. This is due to the fact that the ability of air to absorb moisture reduces with temperature.

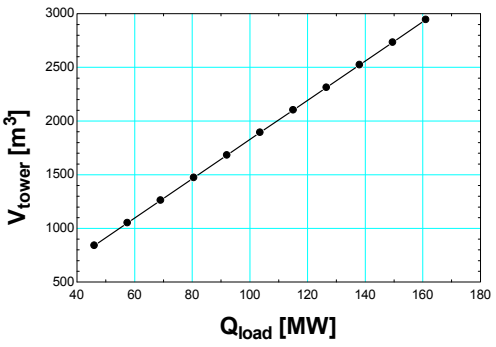

Figure 123. Effect of heat load

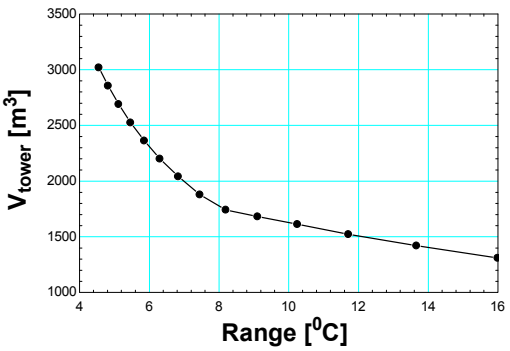

Figure 124. Effect of range

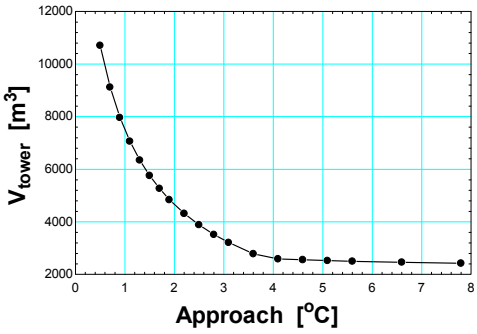

Figure 125. Effect of approach

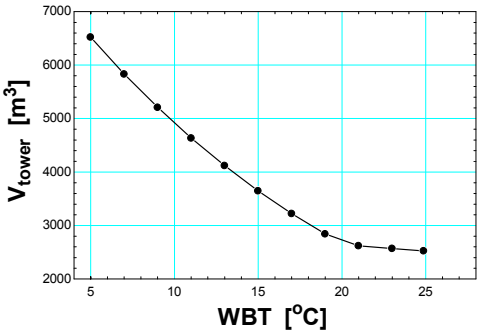

Figure 126. Effect of wet-bulb temperature

7.4 Design Calculations

Equations described in section 7.3 are modeled in EES [75] to perform design calculations. The code is verified by comparing the calculations to the vendor quotation. Later in this section, effect of air ambient conditions and water conditions on the cooling tower and cooler design will be described. The original idea was to develop the cooling tower code in FORTRAN and integrate it with ANL Plant Dynamics Code to perform the calculations. However, cooling tower calculations require psychrometric properties which are not readily available in FORTRAN. Due

to the limited time this project, EES was used instead to perform the calculations since the psychrometric properties are readily available. The current code developed in EES will be modified into FORTRAN in the near future.

7.4.1 Verification of the code

The code is verified by comparing the estimated power requirements, tower dimensions, and tower cost to the quotation obtained from Delta cooling towers, Inc. for the conditions specified in their quotation. These calculations are presented in Table. VII.

It should be noted that the quotation obtained from Delta cooler towers Inc. is for the lowest footprint option and the values are close to the code predictions. The required blower and pumping power are slightly underestimated by the code. The manufacturer used a 30HP fan per cell whereas the code uses 25HP fan per cell, which explains why the code underestimates the required blower power. To compensate for the underestimation of pumping power, an additional 10ft of head is added (to the values in Table. VII) to the total pump head as mentioned in section 7.3.6. Required number of cells and the floor area matches extremely close to the vendor quotation indicating that the assumption made regarding the optimum $\dot{m}_w/\dot{m}_a$ is valid. The table also compares the different fill types described in section 7.3.4. As can be seen from the table, the fill height and hence, the pumping power are much smaller for the film fill type compared to splash or trickle type fills. Moreover, predictions using the film type fill are closer to the manufacturer specifications. Therefore, film type fill is used for all the calculations from here on. The table also compares the lowest power consumption and lowest footprint options. For the described conditions, the required number of cells, floor area, and tower cost for lowest horse power option are about 33% more than the lowest footprint option whereas, the power consumption is about 40% less compared to the lowest footprint option.

Hence, it is important to understand which option is economical for the plant. This is explained in more detail in the plant optimization section. Cost estimation using Zanker *et al* correlation mentioned in the section 7.3.7 is closer to the lowest footprint option. It should be noted that the correlation doesn't differentiate between the two options as it is only a function of heat load, approach, and range which are same for both the options. Hence, for accurate cost estimate the cost per cell method is used throughout this report.

Table VII. Comparison of calculations to the manufacturer quotation

Variable	**Delta**	**Calculated (Lowest footprint)**			**Calculated (Lowest Power)**
Number of cells	84	83			111
Water flow rate [kg/s]	4,900	4,900			4,900
T_{in} [^{0}C]	35.78	35.78			35.78
T_{out} [^{0}C]	28.88	28.88			28.88
T_{wbt} [^{0}C]	25.55	25.55			25.55
		Splash	Trickle	Film	Film
P_{blower} [MW]	1.88	1.545	1.545	1.545	0.8295
P_{pump} [MW]	0.182	0.7415	0.2634	0.1588	0.1712
L_{fill} [m]	~ 1.3	5.553	1.973	1.167	1.282
A_{floor} [m^2]	1147	1088	1088	1088	1459

Cost [$]*$10^6$	3.139	3.1017	4.148
Cost[$]*$10^6$ – Zanker *et al*		2.8977	2.8977

7.4.2 Effect of ambient air conditions

Since ambient air conditions (wet and dry bulb temperature) depend on the location and time of the year, design calculations are performed for three possible locations of the power plant to investigate the effect of air conditions.

1) Chicago, IL
2) Las Vegas, NV
3) Idaho Falls, ID

For all the calculations presented in this section and next section, water conditions are held constant at the reference conditions described in Table IV.

At these three locations, monthly design temperature data is extracted from the ASHRAE climatic design conditions online software (http://ashrae-meteo.info/) and is presented in Table. VIII. The ambient conditions for each location do not exceed the values in the table for more than 5% of the time each month. Calculations are performed for all the months to identify the maximum requirements for the whole year at each location.

Monthly variation of the requirements at each of these locations for optimum design condition ($\dot{m}_w/\dot{m}_a$) are shown in Figure 126 for an AFR-100 power plant. It can be seen that the required tower volume, total power consumption, and make-up water requirements are highest for the month of July at all the locations.

Table VIII. Monthly design ambient air conditions

Chicago

Data	Jan	Feb	Mar	Apr	May	June	July	Aug	Sep	Oct	Nov	Dec
WBT (^{0}C)	4	5.33	11.72	15.66	20.11	22.77	24.88	24.11	21.61	16.94	12.83	6.66
DBT (^{0}C)	5.44	7.55	15.44	20.72	24.33	28.16	30.16	28.33	25.66	20.61	15.05	8.33

Las Vegas

Data	Jan	Feb	Mar	Apr	May	June	July	Aug	Sep	Oct	Nov	Dec
WBT (^{0}C)	11.94	13.16	14.66	16.33	19.83	22.5	23.88	23.5	22.38	17.94	14.66	11.33
DBT (^{0}C)	16.66	21.83	27.44	31.72	37.83	39.5	39.27	37.16	32.16	30.83	22.11	16.94

Idaho Falls

Data	Jan	Feb	Mar	Apr	May	June	July	Aug	Sep	Oct	Nov	Dec
WBT (^{0}C)	3.88	6.66	8.88	11.88	15.27	17.83	20.22	19.11	17.16	12.33	8.94	4.88
DBT (^{0}C)	6.11	10.77	16.11	23.83	26.27	29.38	30.27	30.16	26.44	22.5	12.66	7.55

Comparing these plots to the wet bulb temperature data in Table. VIII, it can be concluded that the requirements are higher for higher wet bulb temperatures. The main purpose of this study is to identify the maximum requirements and hence, from here on, calculations presented will be

for the month of July. It is also interesting to note that the total required volume and power consumption are smaller in Las Vegas compared to Chicago for the month of July. The weather in Las Vegas is extremely hot and dry resulting in a lower wet bulb temperature than Chicago in the summer. This means that the cooling tower in Las Vegas consume more water but less power as can be seen in Figure 127.

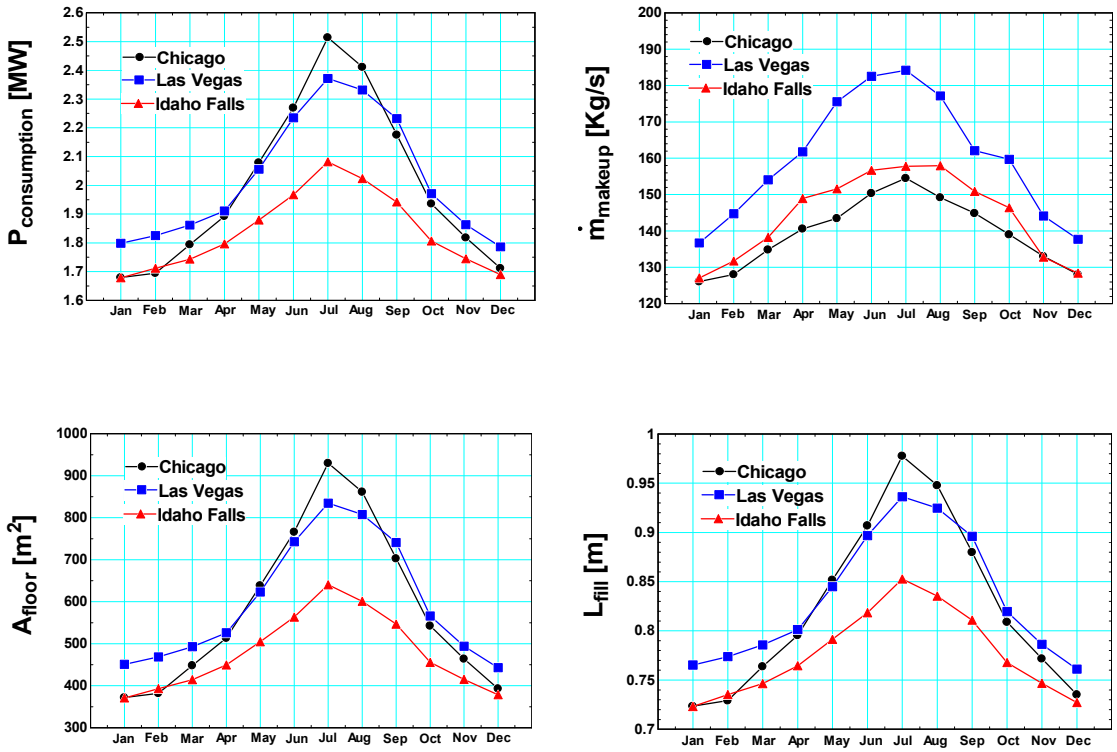

Figure 127. Variation of requirements for AFR-100 at optimum $\dot{m}_w/\dot{m}_a$ conditions

7.4.3 Control of water conditions

It is extremely important to maintain the water temperature and flow rate at design conditions in order to achieve the desired cycle efficiency. Once the tower dimensions are fixed, in absence of any sort of temperature control, the water temperature can change drastically due to changes in ambient air conditions on daily as well as monthly basis, thereby, severely affecting the efficiency of the cycle. This section provides an example of how to control the water

conditions. These calculations are performed for Chicago but similar curves can be generated for other locations as well. The curves shown in Figure 128 are generated using the Merkel equation. The right hand side of the equation (133) is only a function of water and air conditions. Therefore, a series of NTU curves can be generated for changing ambient conditions. These curves are known as “tower demand curves” in cooling tower theory. However, the left hand side of the equation (133) is always the same independent of air conditions and can be seen as the linear curve on the log-log NTU plot shown in Figure 128. This curve is also known as the “tower characteristic curve” and is a function of fill type used. Film type fill is used in this case to generate the tower characteristic curve. Typically, the cooling tower manufacturers provide the tower characteristic curve during the purchase. However, the characteristic curve can also be generated during field testing of the cooling tower under varying air and water conditions.

The point where the tower characteristic curve intersects the tower demand curve will provide the required $\dot{m}_w/\dot{m}_a$ for that particular ambient air condition. Then the $\dot{m}_w/\dot{m}_a$ value needs to be adjusted to achieve constant water temperature. Makeup water requirements also change with the air conditions. Once the required $\dot{m}_w/\dot{m}_a$ is obtained, the makeup water plot in Figure 128 can be used to estimate the amount of water to be added to maintain a constant water flow rate. As mentioned earlier, the wet bulb temperature exceeds the design value only for 5% of the time in month of July. This corresponds to less than 36 hours for the whole year. Excluding these 36 hours, the value of $\dot{m}_w/\dot{m}_a$ will always be higher than the designed value and this will increase the required $\dot{m}_w/\dot{m}_a$ and reduce the make-up water consumption rate.

Value of $\dot{m}_w/\dot{m}_a$ in a cooling tower can be adjusted by adopting two methods: adjusting the water flow rate or air flow rate per cooling cell.

1) Adjusting water flow rate – Temperature control is achieved by switching on/off the water flow to one or multiple cells as the air conditions change. The water flow rate per changes while air flow rate per cell is maintained constant, thereby, adjusting $\dot{m}_w/\dot{m}_a$.

2) Adjusting air flow rate – In this technique variable frequency drives (VFDs) are used to adjust the fan speed and hence, air velocity through one or multiple cells to account for changing ambient conditions. The water flow rate is maintained constant and air flow rate per cooling cell changes, thereby, adjusting $\dot{m}_w/\dot{m}_a$.

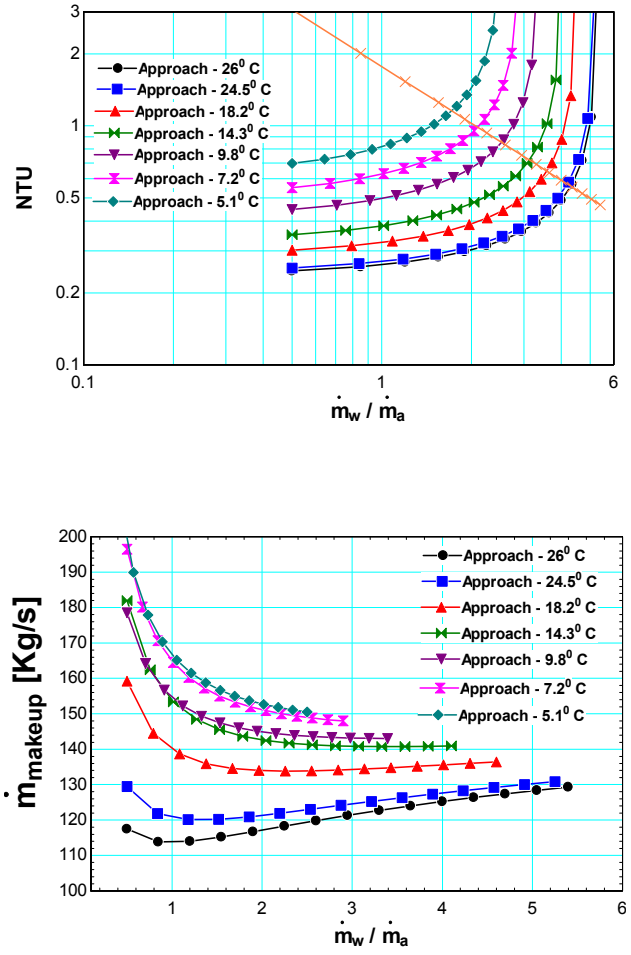

Figure 128. Effect of $\dot{m}_w/\dot{m}_a$ on the power consumption and make-up water requirements

Each technique has its advantages and disadvantages. Adjusting water flow rate will eliminate need of variable frequency drives (VFDs), however, accurate control of water temperature is difficult to achieve. Adjusting air flow rate will provide almost accurate temperature control but will increase the operation cost of the tower.

7.4.4 Effect of design water conditions

The calculations performed in the previous sections were for a constant design water temperature and flow rate as shown in Table IV. However, for a fixed heat load, infinite combinations of water temperature and mass flow rate are possible. Changing the water temperature and flow rate will affect both the cooling tower as well as the cooler design. This section describes the effect of water conditions on both the cooler as well as cooling tower variables. Plant Dynamics Code (PDC) developed at ANL [67] is used for the cooler calculations. Due to corrosion issues, range of the tower should not exceed 22^0C [80] and this limits the lowest possible water flow rate to 1,500kg/s for an AFR-100 plant and 6,200kg/s for an ABR-1000 plant.

The minimum water temperature that can be achieved is limited to 22.5^0C in Idaho Falls. This limitation is due to the restriction that the approach of the cooling tower has to be greater than 2.2^0C as explained in section 7.3.7. Effect of series of water flow rates and water temperatures on cooler design is presented in Figure 129.

The water inlet and outlet temperatures to the cooler are related according to equation (157). Hence, for all the water flow rates slope of the equation is always close to 1. However, the intercept of the equation is inversely proportional to the water flow rate. Hence, as the water flow rate increases the intercept decrease asymptotically. This can be seen in Figure 129, for the same water inlet temperature, the difference in water outlet temperatures become smaller as

the water flow rate increases. This is also reflected in the required cooler length and minimum approach plots.

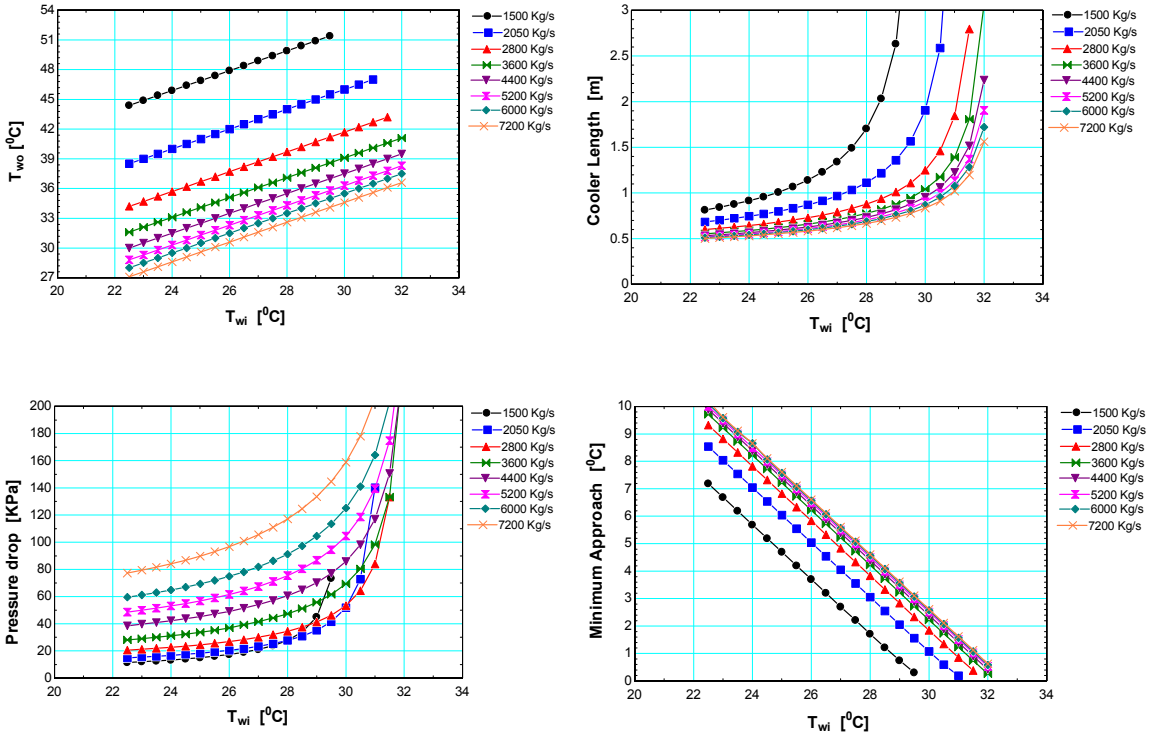

Figure 129. Effect of water conditions on the cooler variables

Approach of the cooler, which is defined as the minimum difference in temperature of cold and hot streams increases as the water temperature decrease or the water flow rate increase. For this reason, a longer cooler is needed if the flow rate is decreased or the water temperature is increased. It should be noted that the required cooler length starts to increase asymptotically as the water inlet temperature get close to the CO_2 outlet temperature in the cooler. Similar behavior can be observed for the water pressure drop as it is proportional to the cooler length and water flow rate. Changing the water flow rate and temperature will also affect the size of cooling tower, power consumption as well as the cost. Figure 130 presents how the required floor area changes with the water conditions for both the lowest power consumption and lowest footprint options.

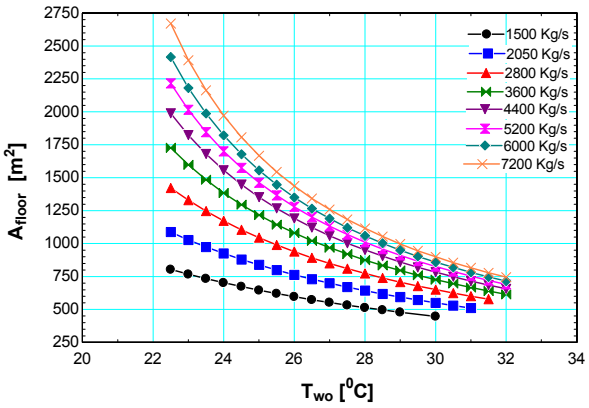

Lowest power consumption option

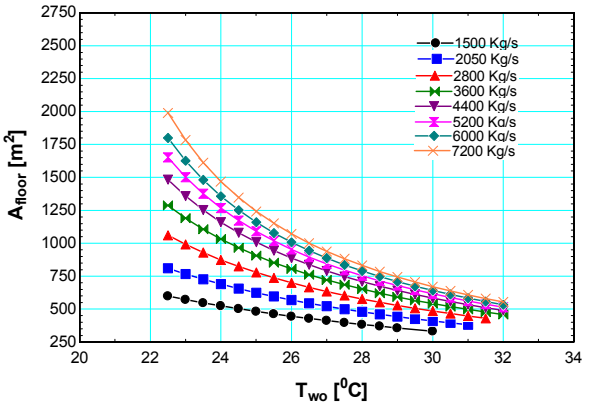

Lowest footprint option

Figure 130. Effect of water conditions on the tower floor area in Idaho Falls

All these calculations are performed for constant air conditions (month of July) in Idaho Falls. For constant air and water temperature the optimum $\dot{m}_w/\dot{m}_a$ is always the same irrespective of the water flow rate. Hence, as the water flow rate decreases the required volumetric flow rate of air decreases leading to a total reduction of floor area as can be seen in Figure 130 for both the options. Obviously, the required floor area increases as the cold water temperature approaches the wet bulb temperature as is evident from these plots. It is also worthwhile to note again that the required floor area for lowest power consumption option is significantly

higher than lowest footprint option for all the water conditions. Figure 130 presents the fill height calculations for both the options. As can be seen, the required fill height increases with decrease in water outlet temperature. This is exactly opposite to the effect of water temperature on the cooler length. This is expected because an increase of approach in the cooler leads to decrease in the approach of the cooling tower and vice versa. However, the effect of water flow rate on the fill height is similar to what has been observed in the case of the cooler and is due to the fact that overall driving enthalpy decreases with decrease in flow rate. Just like the required floor area, the required fill height is higher for the lowest power consumption option than the lowest footprint option.

The effect of water conditions on the total power consumption to operate the cooling tower and the cooler is presented in Figure 132. For both the options, it is clearly evident that there is an optimum water temperature for each flow rate that results in least power consumption. This is expected because a decrease of pumping head in the cooler will lead an increase of pumping head in the cooling tower as explained earlier. Also, the total power consumption decreases with water flow rate due to lower blower power consumption. It should be noted that the total power consumption for the lowest power consumption option is significantly lower than the lowest footprint option for all the water conditions.

Although the results presented here are for Idaho Falls, similar conclusions can be drawn about other locations as well. The only change would be the optimum water temperature at each flow rate. In general, it has been observed that as the design wet bulb temperature of the ambient air increases the optimum water temperature move slightly towards hotter conditions (see Table IX in the next section for details). The effect of water conditions on cooling tower cost is

presented in Figure 133 for both the options. And the trend is similar to the required floor area as the floor area dictates the total number of cells and in turn, the total cost of the tower.

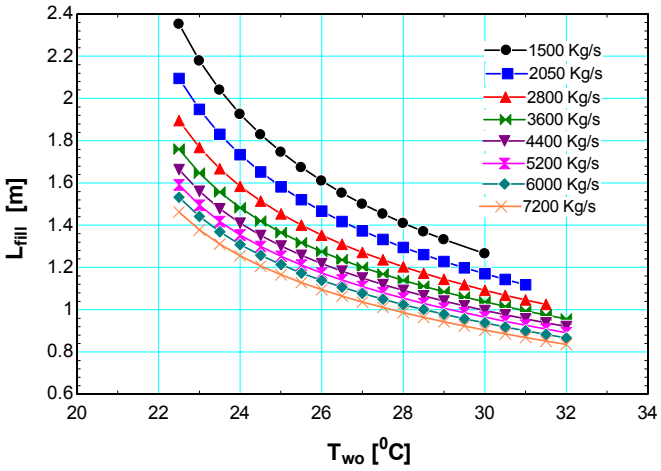

Lowest power consumption option

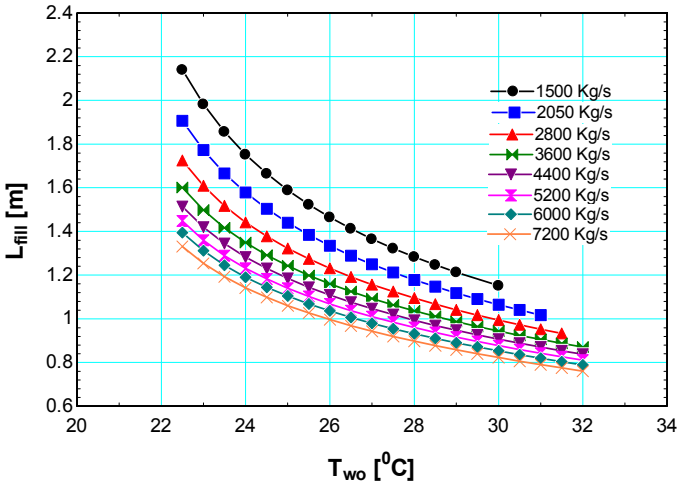

Lowest footprint option

Figure 131. Effect of water conditions on the fill height in Idaho Falls

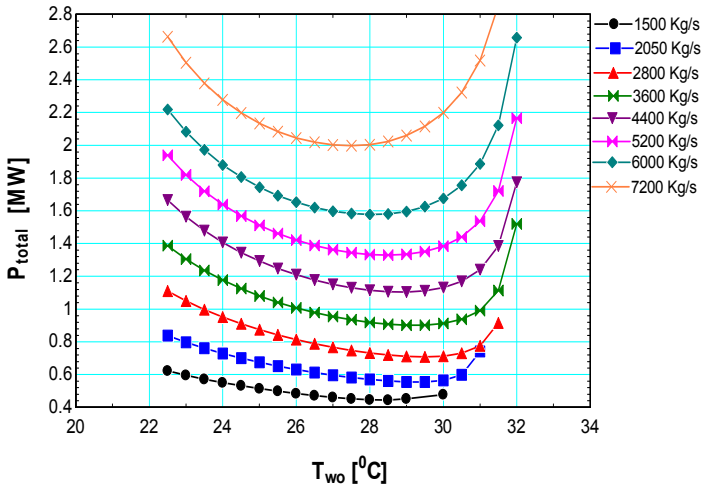

Lowest power consumption option

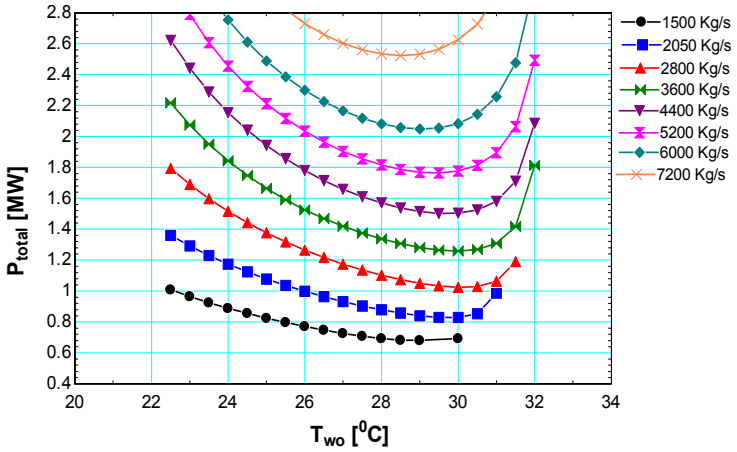

Lowest footprint option

Figure 132. Effect of water conditions on the total power consumption in Idaho Falls

It is also important to understand the effect of water conditions on cooler cost to study the plant economics. The proposed coolers for the S-CO_2 cycles use printed circuit heat exchanger (PCHE) technology and are fabricated in stainless steel 316 (SS-316) blocks which are welded together. The total cost of the cooler is calculated by adopting the following procedure [78].

1) The volume of each PCHE block is calculated from the Plant Dynamics Code and the total material required to fabricate the block is calculated as,

$$Mass_{block} = Volume_{block} * SS316\ density\ @\ 20^0\ C$$

2) The cost of SS316 material as per the current market is 8.48 $/kg and the total material cost of one PCHE block is calculated.

3) The fabrication cost to chemical etch the channels and perform diffusion bonding is estimated to be $48,480 per block.

4) The total cost of each block is estimated by adding up the material cost and the fabrication cost of each block and the total cost of the cooler is calculated as,

$$Cost_{cooler} = Cost_{block} * Number\ of\ blocks$$

5) Number of PCHE blocks is assumed to be fixed at the reference design conditions at 72 for AFR-100 and 288 for ABR-1000 plants.

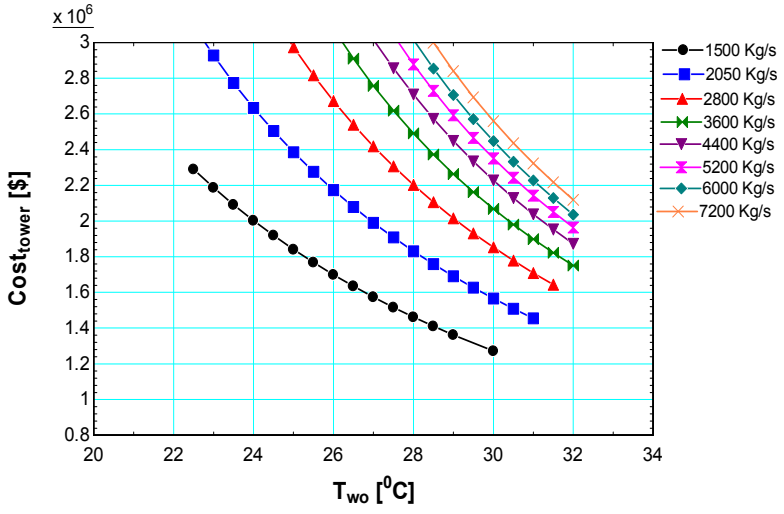

Lowest power consumption option

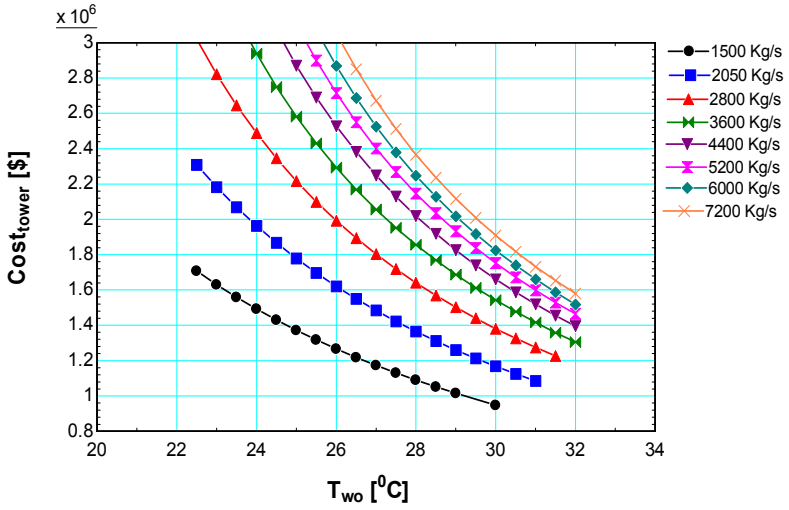

Lowest footprint option

Figure 133. Effect of water conditions on the cooling tower cost in Idaho Falls

Figure 134 shows how the cooler cost changes with the water conditions for an AFR-100 plant and these results don't depend on the location as the ambient air conditions have no influence on the cooler design. It is obvious that the cost of the cooler has a similar trend to the cooler length as it is the only variable changing during the calculations from the PDC.

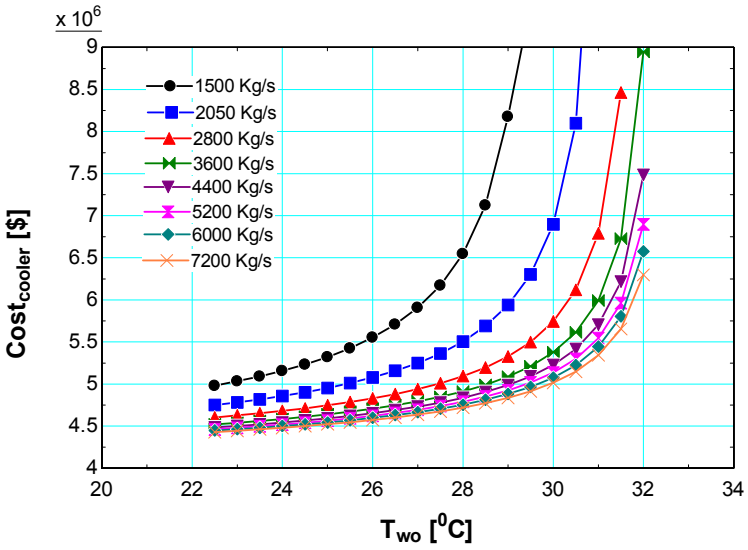

Figure 134. Effect of water conditions on the cooler cost

7.5 Cost based optimization

In the previous section it has been concluded that the water conditions which reduce the cost of cooler will increase the cost of cooling tower and vice versa. Also, any attempt to reduce the total cost of cooling tower and cooler tend to increase the total power consumption. Hence, it is important to improve the plant economics by taking into consideration both cost as well as power consumption. This section explains the procedure employed to perform the optimization as well as the optimization results for AFR-100 and ABR-1000 plants. Previously, simplified version of the cost analysis was developed for the S-CO_2 cycle components [78]. The components capital cost was compared to the rest-of-the-plant capital cost and the effect on the plant capital cost per unit net electrical output ($/KWe) is investigated for varying water operating conditions. Several assumptions need to be made for this procedure and are kept consistent with the previous studies [67, 78]. The assumptions are listed as follows:

1) The capital cost of the plant, including the cooler and cooling tower, is assumed to be equivalent to 5,395 $/KWe for reference water conditions, month of July in Chicago, and lowest footprint option.
2) The capital cost of the plant, excluding the cooler and cooling tower, is calculated for the reference conditions mentioned above and is assumed to be constant for all other conditions and locations. This value is calculated to be 5,192 $/KWe for AFR-100 plant and 5,204 $/KWe for ABR-1000 plant.

With these assumptions, the plant capital cost per unit electrical output will depend on the water conditions according to,

$$\frac{\$}{KWe} = \frac{Rest\ of\ plant\ capital\ cost + Cooling\ tower\ cost + Cooler\ cost}{P_{elec} - P_{pump} - P_{blower}} \tag{158}$$

This optimization technique is a powerful tool and allows for the plant optimization using any plant component as the variable. For the current study, it should be noted that the cooling tower and cooler are the selected components. The results of the capital cost calculations are presented in Figure 135 for lowest footprint and lowest power consumption options in Idaho Falls for AFR-100. The results will be explained in detail for the AFR-100 plant and will be summarized for the ABR-1000 plant. The goal of this technique is to find the optimum water mass flow rate and temperature which results in the least plant capital cost. Not surprisingly, there is an optimum water temperature for each flow rate which results in least plant capital cost. The plant capital cost also reduces with the water flow rate. Interestingly, the plant capital cost is smaller for the lowest power consumption option compared to the lowest footprint option. This indicates that, it is more economical to have more number of cooling cells (or smaller cooling cell for fixed floor area), which reduces the total power consumption. This also justifies the use of cell #1 in section 7.3.3. It also seems like the optimum water temperature for the lowest footprint option is slightly higher than the lowest power consumption option.

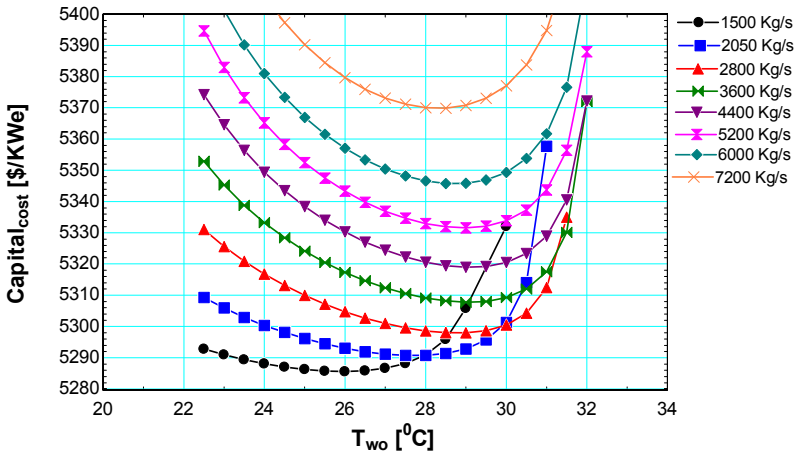

Lowest power consumption option

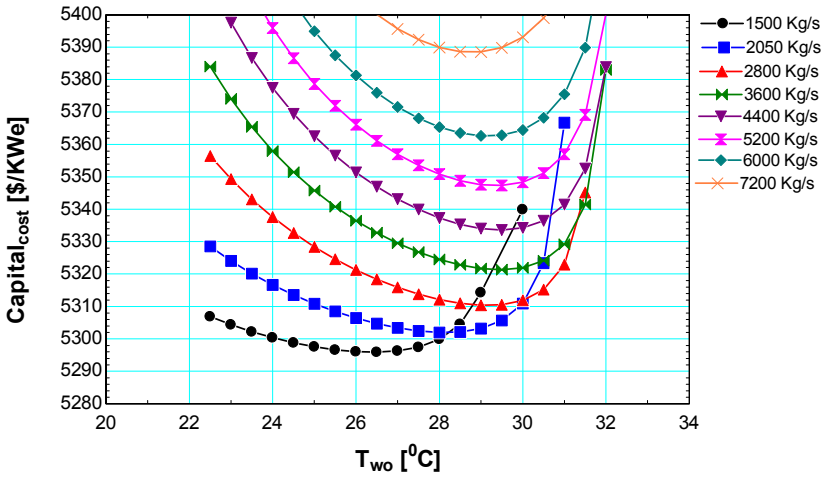

Lowest footprint option

Figure 135. Effect of water conditions on plant capital cost in Idaho Falls

These results were also found to be true for other locations as well. Hence, Figure 136 compares the optimization results of lowest power consumption option for all three locations. It should be noted that the minimum water temperature at each location is dictated by the design wet bulb temperature for that particular location. For this reason, the minimum water temperature in Chicago and Las Vegas is selected as 26^0 C instead of 22.5^0 C as in the case of Idaho Falls.

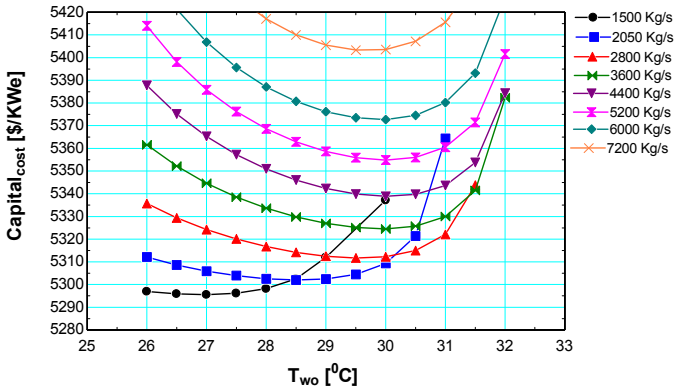

Chicago

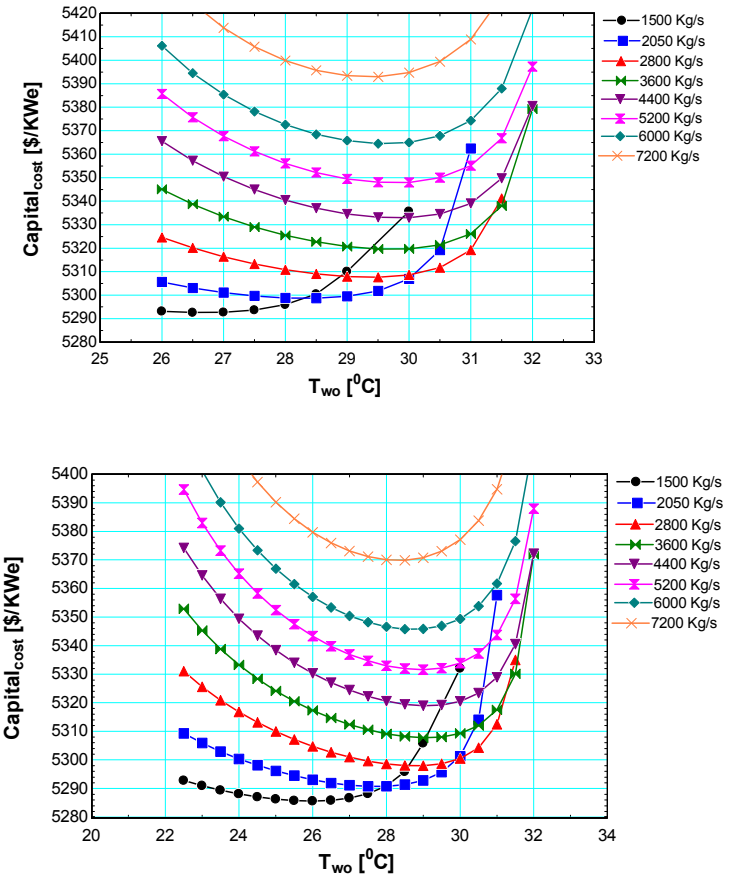

Figure 136. Effect of water conditions on plant capital cost for all three locations

The plant capital cost and the optimum water temperature are highest in Chicago for all the water flow rates. This indicates that the plant capital cost and optimum water temperature increases as the design wet bulb temperature increases. In Idaho Falls, the plant capital cost per unit electrical output can be reduced from 5,350 $/KWe to 5,286 $/KWe by changing the water operating conditions from (6,000kg/s, 30^{0}C) to (1,500kg/s, 26^{0}C). This corresponds to about 6.7 million dollars reduction in total plant capital cost and goes on to show the importance of this optimization study. Table IX summarizes the optimum water conditions and the corresponding cooler and cooling tower variables for both AFR-100 and ABR-1000 plants. Close observation of the table shows that the optimization results for ABR-1000 are not very different from that of AFR-100 and hence, the conclusions made for AFR-100 are also valid for ABR-1000. Only

difference being that the power consumption, water consumption rate, and heat rejection cost (cooling tower + cooler costs) are scaled according to the heat load, which is higher for ABR-1000.

Table IX. Cost-based optimization results for AFR-100 and ABR-1000 plants

	AFR-100			ABR-1000		
Location	Chicago	Las Vegas	Idaho Falls	Chicago	Las Vegas	Idaho Falls
Number of cells	53	52	46	227	223	196
Water flow rate [kg/s]	1,500	1,500	1,500	6,200	6,200	6,200
T_{in} [^{0}C]	48.86	48.36	47.86	48.44	47.94	47.44
T_{out} [^{0}C]	27	26.5	26	26.5	26	25.5
Design WBT [^{0}C]	24.88	23.88	20.22	24.88	23.88	20.22
A_{floor} [m^2]	685.1	675.7	596.5	2,971	2,925	2,566
L_{fill} [m]	2.219	2.056	1.61	2.46	2.231	1.676
Blower power [MW]	0.3984	0.3841	0.3391	1.688	1.663	1.459
Pump power [MW]	0.1757	0.1655	0.1446	0.7642	0.7132	0.6097
Peak water consumption [kg/s]	126.1	144.1	130	524.1	602.3	540.8
Cooler PCHE volume [m^3]	34.78	31.86	29.55	131.3	121.5	113.6

Tower cost [$]*$10^6$	1.951	1.925	1.699	8.462	8.34	7.31
Cooler cost [$]*$10^6$	5.98	5.71	5.553	23.1	22.44	21.9
Plant capital cost [$/KWe]	5,296	5,293	5,286	5,315	5,312	5,304

As explained in the introduction section, there are multiple ways to reject heat from these plants. An attempt to compare these cooling options has been made in Table X. Clearly, direct water cooling option has the least plant capital cost per unit electrical output. However, the water consumption rate is 12,000 kg/s and it is not possible to meet such water demand at locations where the water resources are scarce. Even if the water resources are abundant, hot water being dumped into the water bodies will severely affect the aquatic life, especially at temperatures as high as mentioned in the table. Hence, there are stringent environmental policies in place to prevent dumping hot water into water bodies. It should be noted that the water flow rate of 12,000 kg/s reported for the direct water cooling option is found to be the optimum value for water inlet temperature of 30^0C. The optimization results for direct water cooling option are reported in Appendix A. Previous study [67] aimed at investigating the dry air cooling option as a replacement for the direct wet cooling option. For reference compressor inlet conditions (7.4MPa, 31.25^0C), it has been realized that in order to have a reasonable power consumption of about 5% of the plant output the cooler volume has to be increased by about 100 times compared to the water cooled PCHE. This is primarily due to the fact that the specific heats of air and S-CO_2 are quite different. PCHE size can be reduced by increasing the minimum CO_2 temperature in the cooler. This will force to increase the compressor inlet pressure to take advantage of high density CO_2 along the pseudo-critical region. Optimization was previously performed along the pseudo-critical region and it has been found out that increasing the

minimum CO_2 temperature to 40^0C is beneficial for air cooling. Unfortunately, even for the optimized conditions mentioned in the table, the plant capital cost and power consumption are significantly higher compared to the direct water cooling. Although feasible, at least a 40% increase in the electricity price is expected from implementation of air cooling option [67]. From Table X, it is clear that the cooling tower option is a much more feasible option compared to the dry air cooling. When compared to the direct water cooling option, there is about ~1% increase in the plant capital cost per unit electrical output but at only a small fraction of the water consumption. It should be noted that there is still scope of optimization as far as the cooling tower option is concerned. Further optimization can be performed along the pseudo-critical region by altering the compressor inlet conditions. This study will be performed in future.

Table X. Comparison of different cooling options for ABR-1000

Cooling option	Direct water cooling	Dry air cooling	Cooling tower
Fluid flow rate [kg/s]	12,000	30,000	6,200
Peak water consumption rate [kg/s]	12,000	-	540.8
Cooler inlet temperature [^{0}C]	30	30	25.5
Cooler outlet temperature [^{0}C]	41.34	49.7	47.44
Compressor inlet temperature [^{0}C]	31.25	40	31.25
Compressor inlet pressure [MPa]	7.4	8.864	7.4
Cycle efficiency [%]	40.26	38.05	40.26
Blower power [MW]	-	24.04	1.459

Pump power [MW]	0.7843	-	0.6097
Cooler PCHE volume [m^3]	126.7	3290.4	113.6
Heat rejection cost [$]*$10^6$	22.7	603.4	29.21
Plant capital cost [$/KWe]	5,271	7,670	5,304

Conclusion

With the growing energy concern in the world it is important for the research into alternative means of power processing to be continued. As a result of relatively high efficiencies and low capital costs, the S-CO_2 Brayton Cycle is a promising technology for power production. To do this, research must be performed to better understand S-CO_2 as a working fluid within advanced turbomachinery designs. The objective of this work was to focus on different challenging aspects of the cycle and to gain working experience with supercritical fluids.

The first task was to experimentally measure leakage through annular and labyrinth seal geometries to evaluate one-dimensional models and provide data for the optimization of seal design within S-CO_2 flow conditions.

The effect of eccentricity on flow through small diameter annuli was found to be minimal for the lengths typically found in labyrinth type shaft seals. The variation in fluid friction between eccentric and concentric shaft placements is the driving parameter behind the increase in flow due to shaft eccentricity and at the short lengths typical of shaft seals this is not seen. An increase in flow rate of 3% was observed for short length annular orifices. This effect was increased to 8.5% when the orifice length was increased passed the developing entrance length and frictional effects became dominant.

Flow rate measurements for a straight through labyrinth seal with three teeth were made at inlet pressure of 7.7, 10, and 11 MPa at inlet densities of 325, 475, and 630 kg/m^3. Various labyrinth seal leakage models were applied to the data calculated to compare applicability. Among the one dimensional models that assume ideal and incompressible flow the equation described by Esser and Kazakia performed the best. Their equation is a modification of the Neumann equation applying a

constant flow coefficient and performs within 30% for all the conditions tested. The flow coefficient used in this formula was experimentally determined from a geometry that was most similar to the geometry tested here. This similarity in the geometry used to determine the flow coefficient allowed the Esser and Kazakia equation to outperform the other models based on Neumann's equation which predicted the flow within 40%.

Empirical discharge coefficients were defined for all geometries tested to be applied to the Homogeneous Equilibrium Model (HEM). With an experimentally determined discharge coefficient the HEM predicted the mass flow rate with less than 5% error for the higher pressure cases of 10 and 11 MPa and less than 14% error for the lower pressure case of 7.7 MPa. The HEM works well when the inlet condition chokes prior to entering the two phase region and begins to deviate when two-phase effects become more prevalent. In the low inlet pressure case of 7.7 MPa where this was prevalent two discharge coefficients were defined for two pressure ratio ranges. Using these values within their respective ranges allowed the predicted mass flow rate to remain within 10%.

A Stepped labyrinth seal was designed to mimic the geometry used within the research loop at Sandia National Laboratories. This provided a more complex geometry to further test the capabilities of the facility and validate models. Three-tooth and four-tooth cases were tested at an inlet pressure of 10 MPa with a corresponding inlet density of 325 kg/m^3. It was found that increasing the tooth number decreased the flow by 5% from the three-tooth case to the four-tooth case. Inlet pressure was varied for a constant inlet density of 640 kg/m^3 and outlet pressure of 3.62 MPa to determine a probable inlet pressure seen for the SNL leakage results. The results predicted a seal inlet pressure closer to the compressor outlet pressure of 13.8 MPa. The results showed that the data could be used to scale to larger diameters and apply to more practical geometries. This is an important result as it shows that operating conditions can be duplicated in a controlled environment to better understand the conditions

experienced by seals and orifices within the more complex facilities. The data and models described here are useful for creating and validating models that will be used in next generation plant dynamics code. This data can be used as a starting point for the validation of models for more complex geometries such as pocket damper seals and dry liftoff seals.

The second task was to develop a computational model and to understand the flow behavior of S-CO_2 through labyrinth seals. An Open source CDF software OpenFOAM was used to perform a series of simulations for S-CO_2 flows through annular orifices, labyrinth seals and some plain orifices. To accurately model the properties of S-CO_2, a FIT (Fluid Interpolation Tables) algorithm was implemented in OpenFOAM which is based on biquintic spline interpolation resulting in an error of about ~0.01%. To solve the Navier-Stokes equations in the saturation dome, HEM is assumed to be valid. A parametric study was performed which was divided into two parts:

The first part explained about the effect of geometrical parameters on leakage rate through seals while holding operating condition constant. (Appendix B and C)

Conclusions that can be drawn from study of geometrical parameters are as follows:

1) W_{tooth}/c (Tooth width to clearance ratio) is the only major geometrical parameter influencing discharge coefficient of an annular orifice.
2) There exists a certain range of W_{tooth}/c for which C_d is independent of W_{tooth}/c.
3) Except for very low h/s (tooth height to pitch ratio) tooth depth has no significant effect on C_d.
4) The carry over coefficient, γ as defined by Hodkinson is independent of pressure ratio and stays constant for a fixed geometry of a seal.
5) The major geometrical parameters influencing γ is c/s (clearance to pitch ratio) and to some extent W_{cavity}/c (Cavity width to clearance ratio).

6) Based on the results from numerical simulations a model for *γ* has been developed. This model is developed for constant tooth width and needs modification in the future to include effect of tooth width.

$$\gamma = 0.91559 + \left[0.395745 + 0.113839\left(\frac{W_{cavity}}{c}\right)\right]\left(\frac{c}{s}\right)$$

7) Shaft rotation has no effect on C_d of an annular orifice at lower PR's but has a significant effect for a smaller pressure drop and needs further validation to develop a model for the same.
8) Shaft rotation has no influence on the carry over coefficient.
9) To predict leakage through a labyrinth seal, each constriction can be treated individually and leakage rate equation for each constriction can be written as,

$$\dot{m} = C_d|_{ntooth}\gamma\dot{m}_{isentropic}$$

Where the C_d of the first tooth is same as that of an annular orifice and C_d for the following tooth depends on the C_d of previous tooth and γ of the cavity. For first constriction γ is equal to 1.

10) A simple 1-D isentropic model for labyrinth seals assuming C_d and γ equal to 1, works reasonably well in predicting leakage through multiple constrictions.

The second part explained about the effect of operating conditions on the leakage rate and choking through a seal while holding the geometry constant.

Conclusions that can be drawn from study of operating conditions are as follows:

1) Changing the inlet operating condition changes leakage through seals significantly depending on inlet density and pressure.
2) A 1-D isentropic choking theory has been put forward which predicts that there exist a range of inlet pressures for which the flow chokes at the saturation point for a given inlet entropy

condition. Based on this theory, two curves are presented for an annular orifice. These two curves control choking based on inlet operating condition as follows:

   a. If the inlet condition is bounded by the two curves, the flow chokes very close to the saturation point when the flow enters the saturation dome.
   b. If the inlet condition is below both the curves, flow chokes late into the saturation dome.
   c. If the inlet condition is above both the curves, the flow chokes before it enters the two phase dome.

3) The 1-D isentropic choking theory developed is applied to simulations performed on annular orifices for a range of operating conditions (Table D.1) and it has been observed that the theory works reasonably well for all the cases.
4) From simulations performed on annular orifices and labyrinth seals (Table D.1 and D.2) it has been shown that, for a given inlet pressure there exist a range of inlet densities for which the discharge coefficient is independent of density and is only a function of inlet pressure.
5) At high enough inlet pressures where properties are not sensitive to temperature changes, S-CO_2 behaves more like an incompressible fluid and the discharge coefficient stays constant over the whole range of PR's. This inlet pressure increases as the number of constriction in a labyrinth seal increases.
6) It has been concluded that the 1-D isentropic choking model is in general valid for any labyrinth seal geometry but the upper and lower pressure limit curves depend on the number of constrictions present in the labyrinth seal. As number of constrictions increases these two curves move farther away from the critical point.

The third task of this project was to investigate the effects of buoyancy on heat transfer to supercritical CO_2. This task was achieved by performing systematic experiments for horizontal, upward, and downward flows under similar conditions. When the bulk temperature is less than and the wall temperature is greater than the pseudocritical temperature, significant influence of buoyancy was observed for all three flow orientations. Enhancement and deterioration in the heat transfer was observed on the bottom and top sides respectively for horizontal flow leading to a circumferential variation in wall temperature. Turbulent shear stress was modified by buoyancy forces for both downward and upward flows. For upward flow, the buoyancy forces act to reduce the turbulent shear stress resulting in localized spikes in wall temperature. For downward flow, buoyancy forces act to enhance the turbulent shear stress enhancing the heat transfer compared to cases with no influence of buoyancy. The effect of buoyancy was observed to be most severe near the pseudocritical region and pressures closer to the critical pressure. When both the bulk and wall temperatures are above the pseudocritical temperature, the effect of buoyancy was greatly minimized due to presence of more gas like CO_2 in both the bulk and near wall regions. The only mode of heat transfer deterioration for downward flow was observed to be due to the pseudo-film boiling phenomenon. Buoyancy parameters suggested in literature were investigated by normalizing the experimental Nusselt numbers with that of a forced convection correlation suggested by Jackson and Hall. For vertical flows, the buoyancy criteria suggested by Jackson (*Bu*), and Seo et al. (*1/Fr*) were able to correctly predict the influence of buoyancy on heat transfer. For horizontal flows, the buoyancy criterion suggested by Jackson (Bo_j) performed satisfactorily. Existing correlations proposed for supercritical water were evaluated for supercritical CO_2. The correlation suggested by Mokry et al. performed well for upward flow whereas the correlations suggested by Swenson et al., bishop et al. performed well for downward flow.

The final task of this project was to investigate the possibility of using wet cooling tower option for S-CO_2 cycle as opposed to direct water cooling or dry air cooling. Two plants namely AFR-100 and ABR-1000

were selected as a part of investigation. A thorough literature survey was performed to explore different types of cooling towers and their advantages and disadvantages were analyzed in detail. Finally, a counter flow induced draft tower was chosen for investigation as it is believed to be most suitable for the current application.

Counter flow cooling tower can be modeled using one dimensional heat and mass transfer equations. However, nonlinear governing equations in the original form require simultaneous solutions of water temperature, air humidity ratio and air enthalpy to obtain detailed temperature profile of water inside the tower. Since, the purpose of this study is just to look at the design aspects of the cooling tower and not to predict the detailed temperature distributions, certain reasonable assumptions were made to simplify the governing equations and a code was developed which can predict the size of the tower, water consumption as well as the power consumption rate. Two extreme options namely lowest power consumption and lowest footprint were identified. As the names suggest, lowest power consumption option will result in the largest plant footprint and least power consumption. And, lowest footprint option will result in the smallest footprint and highest power consumption.

The results from the code were verified by comparing them to a vendor quotation for lowest footprint option. After verification, the effect of ambient air conditions on the cooling tower variables was investigated for fixed water conditions. Since, the ambient air conditions depend on the geographical locations as well as the time of the year, three possible plant sites namely Chicago, IL, Las Vegas, NV, and Idaho Falls, ID were selected. The design ambient conditions at each of these locations were extracted from the ASHRAE climatic design software for all the months in a year. It has been realized that the size of the tower, power consumption as well as the water consumption rate are maximum for the highest wet bulb temperature. Hence, the cooling tower was designed for the month of July at all the locations.

An example was demonstrated to provide an insight about the accurate control of the water conditions to account for the changing ambient air conditions. Next, effect of water conditions on the cooler and cooling tower variables was investigated for fixed ambient air conditions. It has been realized that the water conditions have opposite effect on the cooling tower and cooler. For example, decreasing the water temperature lead to a decrease in the size as well as the cost of the cooler but an increase in the cooling tower size and cost. Similar effect was observed as far as the water flow rate is concerned. Also, total power consumption was found to be minimum for particular optimum water conditions. Hence, a cost-based optimization procedure was employed to determine the optimum water conditions at all three locations which would result in least plant capital cost per unit electrical output. For optimized conditions, direct wet cooling, cooling tower, and dry air cooling options for ABR-1000 were compared and it can safely be concluded that the wet cooling tower option is a much more feasible and economical option than the dry air cooling option. Moreover, replacing the direct water cooling option with the cooling tower option would increase the plant capital cost per unit electrical output by only ~1% and consumes only a fraction of water. Hence, at locations where the water resources are scarce and/or stringent environmental policies are in place, cooling tower option is a better option than the direct water cooling option. Further optimization can be possibly performed by modifying the compressor inlet conditions and this will be undertaken as a part of the future work.

References

[1] "A Technology Roadmap for Generation IV Nuclear Energy Systems," U.S. DOE Nuclear Energy Research Advisory Committee and the Generation IV International Forum2002.

[2] T. Conboy, S. Wright, J. Pasch, D. Fleming, G. Rochau, and R. Fuller, "Performance Characteristics of an Operating Supercritical CO2 Brayton Cycle," *Journal of Engineering for Gas Turbines and Power,* vol. 134, 2012.

[3] V. Dostal, P. Hejzlar, and M. J. Driscoll, "High-Performance Supercritical Carbon Dioxide Cycle for Next-Generation Nuclear Reactors," *Nuclear Technology,* vol. 154, pp. 265-282, 2006.

[4] R. J. Allam, M. R. Palmer, G. W. Brown Jr., J. Fetvedt, D. Freed, H. Nomoto*, et al.*, "High Efficiency and Low Cost Electricity Generation from Fossil Fuels while Eliminating Atmospheric Emissions, Including Carbon Dioxide," *Energy Procedia,* vol. 37, pp. 1135-1149, 2012.

[5] T. Held, M. Persichilli, A. Kacludis, and E. Zdankiewicz, "Supercritical CO2 Power Cycle Developments and Commercialization: Why SCO2 Can Displace Steam," presented at the Power-Gen India and Central Asia, New Delhi, India, 2012.

[6] V. Dostal, P. Hejzlar, and M. J. Driscoll, "The Supercritical Carbon Dioxide Power Cycle: Comparison to Other Advanced Power Cycles," *Nuclear Technology,* vol. 154, pp. 283-301, 2006.

[7] Yuan, H. "Simulations of Supercritical Fluids Flow through Complex Geometries," University of Wisconsin-Madison, 2014.

[8] J. P. Edlebeck, “Measurements and Modeling of the Flow of Supercritical Carbon Dioxide,” University of Wisconsin-Madison, 2013.

[9] S. Klein and G. Nellis, *Thermodynamics*. New York, NY: Cambridge University Press, 2012.

[10] N.A.V. Piercy, M.S. Hooper, H.F. Winny. “Viscous Flow through Pipes with Cores,” *London Journal. of Science*, vol. 15-99, pp. 647-676, 1933.

[11] Tao, L.N., and Donovan, W.F., 1955, “Through-Flow in Concentric and Eccentric Annuli of Fine Clearance With and Without Relative Motion of the Boundaries”, Transactions of the ASME, Vol. 77, pp. 1291-1299.

[12] White, F.M., 2006, Fluid Mechanics. McGraw-Hill.

[13] V.K. Jonsson, E.M. Sparrow. “Experiments on turbulent-flow phenomena in eccentric annular ducts,” *Journal of Fluid Mech.* vol. 25, part 1, pp.64-86, *1966*.

[14] K. Velusamy, V. K. Garg. “Entrance flow in eccentric annular ducts,” *J. Num. Meth. in Fluids, vol. 19(6), pp. 493-512, 1994.*

[15] Vennard, J. K. and Street, R. L., 1982, Elementary Fluid Mechanics, John Wiley & Sons, New York

[16] Shultz, R. R., 1996, “Analytical and Experimental Investigation of a Labyrinth Seal Test Rig and Damper Seals for Turbomachinery,” M.S. thesis, Mechanical Engineering Department, Texas A&M University, College Station, TX

[17] Egli, A., 1935, “The Leakage of Steam through Labyrinth Seals,” Transactions of the ASME, 57, pp. 115-122

[18] Hodkinson, B., 1939, “Estimation of the Leakage through a Labyrinth Gland,” Proceedings of the Institution of Mechanical Engineers 141, pp. 283–288

[19] Vermes, G., 1961 (April), “A Fluid Mechanics Approach to the Labyrinth Seal Leakage Problem,” ASME Transactions - Journal of Engineering for Power, 83(2), pp. 161-169

[20] Childs, D. W. and Hale, K., 1994, “A Test Apparatus and Facility to Identify theRotordynamic Coefficients of High-Speed Hydrostatic Bearings,” ASME Journal of Tribology, 116, pp. 337-344

[22] Scharrer, J., 1988, “Theory Versus Experiment for the Rotordynamic Coefficient of Labyrinth Gas Seals: Part I – A Two Control Volume Model,“ Journal of Vibration, Acoustics, Stress and Reliability in Design, 110, pp. 270-280

[23] Esser, D. and Kazakia, J. Y., 1995, “Air Flow in Cavities of Labyrinth Seals,” International Journal of Engineering Science, 33 (15), pp. 2309-2326 [24]

[24] Kurohashi, M., Inoue, Y., Abe, T., and Fujikawa, T., 1980, “Spring and Damping Coefficients of the Labyrinth Seals,” Vibrations in Rotating Machinery, pp. 215-

[25] Sriti, M, Agouzoul, M., Ouazar, D., and Micheau, P., 1997 (May), “Simulation Numerique D’Ecoulement Compressible dans les Joints Labyrinthe,” Journal De Physique, III, 7 (5), pp. 1025-1037

[26] M. L. Corradini. (1997). *Fundamentals of Multiphase Flow*.

[27] G. B. Wallis, *One-dimensional Two-phase Flow*: McGraw-Hill, Inc., 1969.

[28] S. A. Klein, "Engineering Equation Solver," ed. Madison, WI: F-Chart Software, 2013.

[29] "Instruction Manual-Hydro-Pac LX Compressor," ed. Fairview, PA: Hydro-Pac, Incorporated, 2010.

[30] *Duo-Tape Heavy Insulated Tape*. Available: http://www.heatingtapes.com/Duo_All.pdf

[31] "SITRANS P, Series DIII Transmitter," 4 ed: Siemens Energy and Automation, 2004.

[32] "Cubemass DCI-Coriolis mass flow measuring system," ed. Reinach, Switzerland: Endress+Hauser, 2010.

[33] "NewView 7300 Specifications," ed. Middlefield, CT: Zygo Corporation, 2013.

[34] Steven A. Wright, et al., 2010. "Operation and Analysis of a Supercritical Carbon Dioxide Brayton Cycle", Albuquerque, New Mexico: Sandia National Laboratories

[35] Benvenuti, E., Ruggeri, G. & Tomasini, E., 1981. "Analytical and experimental development of labyrinth seals for process centrifugal compressors. ASME, Volume 32, pp. 21-35.

[36] OpenFOAM, 2012. "User Guide 2.1.1". [Online] Available at: http://www.openfoam.org/docs/user/userch1.php

[37] CFD, [Online] Available at http://www.cfd-online.com/Wiki/Two_equation_turbulence_models

[38] Span, R. & Wagner, W., 1996. "A New Equation of State for Carbon Dioxide Covering the Fluid Region from the Triple-Point Tempearture to 1100 K at Pressures up to 800 MPa". American Institute of Physics and American Chemical Soceity, 25(6), pp. 1509-1596.

[39] Dyreby, J., Northland Numerics. [Online] Available at: http://www.northlandnumerics.com/

[40] Wilcox, D., 1993. "Turbulence Modeling for CFD". DCW Industries, Inc.

[41] Incropera, F.P., A.S. Lavine, and D.P. DeWitt, *Fundamentals of heat and mass transfer*. 2011: John Wiley & Sons.

[42] Kline, S.J. and F. McClintock, *Describing uncertainties in single-sample experiments.* Mechanical engineering, 1953. **75**(1): pp. 3-8.

[43] Belyakov, I., Krasyakova, L. Y., Zhukovskii, A. V., and Fefelova, N. D., *Heat-transfer in vertical risers and horizontal tubes at supercritical pressure.* Thermal Engineering, 1972. **18**(11): pp. 55-59.

[44] Yamagata, K., Nishikawa, K., Hasegawa, A., Fujii, T., Yoshida, S., *Forced convective heat transfer to supercritical water flowing in tubes.* International Journal of Heat and Mass Transfer, 1972. **15**(12): pp. 2575-2593.

[45] Bazargan, M., D. Fraser, and V. Chatoorgan, *Effect of buoyancy on heat transfer in supercritical water flow in a horizontal round tube.* Journal of heat transfer, 2005. **127**(8): pp. 897-902.

[46] Adebiyi, G. and W. Hall, *Experimental investigation of heat transfer to supercritical pressure carbon dioxide in a horizontal pipe.* International Journal of Heat and Mass Transfer, 1976. **19**(7): pp. 715-720.

[47] Shitsman, M., *Impairment of the heat transmission at supercritical pressures(Heat transfer process examined during forced motion of water at supercritical pressures).* High temperature, 1963. **1**: pp. 237-244.

[48] Ackerman, J., *Pseudoboiling heat transfer to supercritical pressure water in smooth and ribbed tubes.* Journal of Heat transfer, 1970. **92**(3): pp. 490-497.

[49] Vikhrev, Y.V., Y.D. Barulin, and A. Kon'Kov, *A study of heat transfer in vertical tubes at supercritical pressures.* Thermal Engineering, 1967. **14**(9): pp. 116-119.

[50] Alferov, N.S., Balunov, B.F., Rybin, R.A., *Features of heat transfer due to combined free and forced convection with turbulent flow.* Heat Transfer–Soviet Research, 1973. **5**(4): pp. 57-59.

[51] Jackson, J. and W. Hall, *Influences of buoyancy on heat transfer to fluids flowing in vertical tubes under turbulent conditions.* Turbulent forced convection in channels and bundles, 1979. **2**: pp. 613-640.

[52] Wood, R.D. and J. Smith, *Heat transfer in the critical region—temperature and velocity profiles in turbulent flow.* AIChE Journal, 1964. **10**(2): pp. 180-186.

[53] Bourke, P. and D. Pulling, *An Experimental Explanation of Deterioration in Heat Transfer to Supercritical Carbon Dioxide*. 1971: Atomic Energy Research Establishment.

[54] Miropol'skiy, Z. and V. Baigulov. *Investigation in heat transfer, velocity and temperature profiles with carbon dioxide flow in a tube over the nearly critical region of parameters*. in *Proceedings of the Fifth International Heat Transfer Conference*. 1974.

[55] Kurganov, V., V. Ankudinov, and A. Kaptilnyi, *Experimental study of velocity and temperature fields in an ascending flow of carbon dioxide at supercritical pressure in a heated vertical pipe.* High Temperature, 1986. **24**(6): pp. 811-818.

[56] Hall, W., J. Jackson, and A. Watson. *Paper 3: A Review of Forced Convection Heat Transfer to Fluids at Supercritical Pressures*. in *Proceedings of the Institution of Mechanical Engineers, Conference Proceedings*. 1967. SAGE Publications.

[57] Shiralkar, B. and P. Griffith, *The effect of swirl, inlet conditions, flow direction, and tube diameter on the heat transfer to fluids at supercritical pressure.* Journal of heat transfer, 1970. **92**(3): pp. 465-471.

[58] Jackson, J., *Fluid flow and convective heat transfer to fluids at supercritical pressure.* Nuclear Engineering and Design, 2013. **264**: pp. 24-40.

[59] Jackson, J. and W. Hall, *Forced convection heat transfer to fluids at supercritical pressure.* Turbulent forced convection in channels and bundles, 1979. **2**: pp. 563-611.

[60] Bae, Y.Y., *Mixed convection heat transfer to carbon dioxide flowing upward and downward in a vertical tube and an annular channel.* Nuclear Engineering and Design, 2011. **241**(8): pp. 3164-3177.

[61] Seo, K.W., Kim, M.H., Anderson, M.H., Corradini, M.L., *Heat transfer in a supercritical fluid: classification of heat transfer regimes.* Nuclear technology, 2006. **154**(3): pp. 335-349.

[62] Licht, J., M. Anderson, and M. Corradini, *Heat transfer to water at supercritical pressures in a circular and square annular flow geometry.* International Journal of Heat and Fluid Flow, 2008. **29**(1): pp. 156-166.

[63] Petukhov, B.S., Polyakof, A.F., Kuleshov, V.A., Sheckter, Y.L., *Turbulent flow and heat transfer in horizontal tubes with substantial influence of thermo-gravitational forces*. in *Proc. of Fifth Int. Heat Transfer Conference*. 1974.

[64] Mokry, S., Pioro, I., Farah, A., King, K., Gupta, S., Peiman, W., Kirillov, P., *Development of supercritical water heat-transfer correlation for vertical bare tubes.* Nuclear Engineering and Design, 2011. **241**(4): pp. 1126-1136.

[65] Swenson, H., J. Carver, and C.d. Kakarala, *Heat transfer to supercritical water in smooth-bore tubes.* Journal of Heat Transfer, 1965. **87**(4): pp. 477-483.

[66] Bishop, A., R. Sandberg, and L. Tong, *Forced-convection heat transfer to water at near-critical temperatures and supercritical pressures*. 1964, Westinghouse Electric Corp., Pittsburgh, Pa. Atomic Power Div.

[67] Moisseytsev, A., & Sienicki, J. J. (2013). Investigation of a Dry Air Cooling Option for an S-CO2 cycle.

[68] John, H. C. (2009). Cooling Tower Fundamentals . Kansas: SPX Cooling Technologies, Inc.

[69] SPX Technologies,. Retrieved from spxcooling.com/pdf/CTII-2

[70] Qureshi, A. B., & Zubair, M. S. (2006). A complete model of wet cooling towers with fouling in fills. Applied Thermal Engineering , 1982-1989.

[71] Merkel, F. (1925). Verdunstungskuhlung VDI Forschungsarbeiten., (p. 275). Berlin.

[72] Braun, J., Klein, S., & Mitchell, J. (1989). Effectiveness models for cooling towers and cooling coils. ASHRAE Transactions, 164-174.

[73] ASHRAE. (1996). ASHRAE Handbook - HVAC Systems and Equipment. American Society of Heating, Refrigerating, and Air-Conditioning Engineers Inc.

[74] Leeper, S. A. (1981). "WET COOLING TOWERS: 'RULE-OF-THUMB' DESIGN AND S IMULATION" . Idaho National Engineering Labratory: U.S. Department of Energy.

[75] Klein, S. A. Engineering Equation Solver . F- Chart Software.

[76] Kloppers, J., & Kroger, D. (2005). Refinement of the Transfer Characteristic Correlation of Wet-Cooling Tower Fills. Heat Transfer Engineering, 35-41.

[77] DollarTimes. Retrieved fromhttp://www.dollartimes.com/calculators/inflation.htm

[78] Moisseytsev, A. and Sienicki, J. J., "Cost-Based Optimization of Supercritical Carbon Dioxide Cycle Equipment," Transactions of the American Nuclear Society, Americal Nuclear Society 2011 Winter Meeting, Washington, DC, October 30-November 3, 2011

[79] Lilly, D. E. (1998). *Analysis and Performance of Gas-Electric Hybrid Chiller Systems.* Atlanta: Georgia Institute of Technology.

[80] Delta Cooling Towers, *TM Series Cooling Tower - Installation, Operation and Maintainance Manual.*

Appendix A

8 Uncertainty Analysis

The instrumentation utilized in the design of this test facility was selected to minimize the uncertainty of key variable at test conditions. The test section mass flow rate, test section inlet density, test section inlet pressure, and test section outlet pressure were the conditions used to define the state experienced by the seal geometry tested. A description of the components used to measure these variables and their relative uncertainties is given here.

8.1 Pressure Transducers

Siemens SITRANS P 7MF4332 [31] pressure transducers are used in this experiment to measure the inlet and outlet pressure at the test section. These transducers output a current range of 4-20mA which is passed through a 250 Ohm resistor. This allows the voltage to be measured by a National Instruments NI 9216 computer DAQ for a range up to 17.2 MPa. This is done via the National instruments Measurement and Automation Explorer (MAX) which is conFigured to read a voltage signal from 1V to 5V. This configuration provides a 1.07 kPa/bit resolution compared to the transducer uncertainty of 17 KPa. This information is detailed in Table XI.

Parameter	Value
Siemens Absolute Pressure Transducer	
Device Accuracy	0.08%
Full Span	40 MPa
Application Full Span	17.2 MPa
Sensor Output	1V to 5V

NI 9215 DAQ Card	
Bits	16
Range	-10V to 10V
NI MAX	
Full Span	17.2 MPa
Limits	1V to 5V
Summary	
Transducer Uncertainty	17 kPa
Bit Change	305 µV/bit
DAQ Card Limitation	1.07 kPa/bit

Table XI. Pressure transducer uncertainty and configuration summary.

As can be seen from Table XI the NI card used provides ample resolution for the instrumentation uncertainty from the Siemens pressure transducers. The pressure transducers were calibrated using a dead weight oil tester. This allowed for a known pressure to be applied to the pressure transducer to calibrate the 1V to 5V output signal measured using MAX. The pressure was varied from 0.41 MPa to 12.4 MPa and a line was fit using EES. The calibration equation is shown in Equation (159). This equation is then used to calculate the actual pressure from the pressure measured by the transducer.

$$P_{Actual} = 1.20931 + 1.00003 \cdot P_{Measured} \tag{159}$$

8.2 Temperature

Thermocouples are used to monitor and record the temperature throughout the facility. Type E thermocouples are used throughout the facility as they offer high resolution and work well at temperature below 0^{o}C. The pertinent information regarding the thermocouples is listed in Table XI which describes the expected error. Type K thermocouples are also described in Table XII as they are used to control the temperature of the heaters used in the system to control the inlet condition.

Parameter	Value
Type E-Thermocouples	
Resolution	68μV/°C
Temperature range	-40 to 800 °C
Type-K Thermocouples	
Resolution	41μV/°C
Temperature Range	0 to 1100 °C
NI 9213	
Bits	24
Range	-78.125 mV to 78.125 mV
Expected Error (Type E)	0.1 °C

Table XII. Temperature uncertainty and configuration summary.

8.3 Mass Flow Rate and Density

The mass flow rate and density at the inlet of the test section were measured using an Endress Hauser Coriolis Flow Meter and Cubemass DCI combo unit. This allowed for the inlet conditions to be accurately recorded in a single phase environment. The unit is not designed to measure flow rate in a two-phase environment and cannot be placed downstream of the test section. The problems that arise from this are demonstrated in the flow rate measurements of the SNL research facility results detailed in the Background section. The flow rate measured for this study was taken downstream of the seal where the fluid was in a two phase state. The flow rate measured here oscillated back and forth and needed to be averaged to account for the oscillations. The uncertainties achieved in this facility for the mass flow and density measurements are detailed in Table XIII. The Endress Hauser unit outputs a 4-20 mA signal and was converted to a 1V-5V signal by reading across a 250 Ohm resistor with the MAX utility.

Parameter	Value
Mass Flow Rate Accuracy	0.10%
Flow Rate Full Span	0.1 kg/s
Sensor Output	4-20mA

NI 9215 DAQ	
Bits	16
Bit Change	305µV/bit
Mass Flow Rate Uncertainty	1.0E-4 kg/s
Flow Rate Quantization	0.0075 kg/s/mA
DAQ Card Limitation	2.2E-06 kg/s
Density Uncertainty	1.0 kg/ m^3
Density Quantization	200 kg/ m^3/V
DAQ Card Limitation	0.061 kg/m^3/bit

Table XIII. Mass flow and density uncertainties and configuration summary.

8.4 Discharge Coefficient Uncertainty

An important result from this work is the empirical discharge coefficients calculated for used with the HEM. The method for calculating the uncertainty for the discharge coefficient shall be described here. The discharge coefficient is defined as the ratio of the measure mass flow rate to the calculated mass flow as shown in Equation (30) repeated here.

$$C_d = \frac{\dot{m}_{measured}}{\dot{m}_{HEM}} \tag{160}$$

Performing propagation of uncertainty on Equation (160) yields Equation (161).

$$\sigma_{C_d} = \sqrt{{\sigma_{\dot{m}_{measured}}}^2 \cdot \left(\frac{1}{\dot{m}_{HEM}}\right)^2 + {\sigma_{\dot{m}_{HEM}}}^2 \left(\frac{-\dot{m}_{measured}}{{\dot{m}_{HEM}}^2}\right)^2} \tag{161}$$

The uncertainty in the measured mass flow rate, Equation (162), is a combination of the instrument uncertainty and the uncertainty due to variations in the pressure ratio.

$$\sigma_{\dot{m}_{measured}} = \sqrt{{\sigma_{instrument}}^2 + {\sigma_{PR}}^2} \tag{162}$$

The instrument uncertainties involved here are calculated from the steady state data measurements. The equation used to calculate the HEM mass flow rate is shown in Equation (163).

$$\dot{m}_{HEM} = A_{annular} \cdot \rho_{in} \cdot v \tag{163}$$

Where $A_{annular}$ is the measured annular flow area, ρ_{in} is the measured inlet density, and v is the calculated fluid velocity through the orifice. The combination of the uncertainties is shown in Equation (164).

$$\sigma_{\dot{m}_{HEM}} = \sqrt{{\sigma_{A_{annular}}}^2 \cdot (\rho_{in} \cdot v)^2 + {\sigma_{\rho_{in}}}^2 (A_{annular} \cdot v)^2 + {\sigma_v}^2 (A_{annular} \cdot \rho_{in})^2} \tag{164}$$

The value in Equation (164) is the value reported for all discharge coefficient plots with respect to pressure ratio. The uncertainty of the empirical discharge coefficients determined are found when the result of Equation (164) is then combined with the uncertainty in averaging the discharge coefficients across a range of pressure ratios. This is shown in Equation (165).

$$\sigma_{C_d,Total} = \sqrt{{\sigma_{C_d}}^2 + {\sigma_{C_d,Average}}^2} \tag{165}$$

The dominant uncertainty in this analysis is the standard deviation of the average discharge coefficient. This uncertainty cannot be reduced and is a result of the models ability to predict the measured flow rate.

8.5 Uncertainty Summary

Care was taken to accurately measure the inlet and outlet conditions experienced by the seal geometry tested. This allows for models to be accurately evaluated using the data acquired. The uncertainties with respect to the key variable are summarized in Table XIV.

Measurement	Instrument	Range	Uncertainty
Inlet Pressure	Siemens Sitrans P	0-17.2 MPa	17 kPa
Outlet Pressure	Siemens Sitrans P	0-17.2 MPa	17 kPa
Inlet Density	Endress Hauser Cubemass DCI	0-1000 kg/ m^3	1.0 kg/ m^3
Mass Flow Rate	Endress Hauser Coriolis Flow	0-0.1 kg/ m^3	1E-04 kg/s

Table XIV. Summary of key variable uncertainties.

APPENDIX B

Annular Orifice simulations – Geometrical Parameters @ 10Mpa, 498kg/m^3

Case #	No. of Teeth	Clearance (mm)	Tooth width (mm)	Tooth Height (mm)	Shaft Diameter (mm)	Shaft Speed (rpm)
1	1	0.06	0.424	0.79	3	0
2	1	0.09	0.424	0.79	3	0
3	1	0.12	0.424	0.79	3	0
4	1	0.15	0.424	0.79	3	0
5	1	0.09	1.272	0.79	3	0
6	1	0.09	5.088	0.79	3	0
7	1	0.06	0.2827	0.79	3	0
8	1	0.09	0.424	1.11	3	0
9	1	0.09	0.424	0.21	3	0
10	1	0.09	0.424	0.79	9	0
11	1	0.09	0.424	0.79	3	10,000
12	1	0.09	0.424	0.79	3	20,000
13	1	0.09	0.424	0.79	3	28,000
14	1	0.09	0.424	0.79	3	40,000

15	1	0.09	0.424	0.79	3	50,000
16	1	0.09	0.424	0.79	3	60,000

APPENDIX C

Labyrinth seal simulations – Geometrical Parameters @ 10Mpa, 498kg/m^3

Case #	No. of teeth	Clearance (mm)	Tooth width (mm)	Cavity/Tooth height (mm)	Pitch (mm)	Shaft Diameter (mm)	Shaft Speed (rpm)
1	3	0.06	0.424	0.79	1.692	3	0
2	3	0.09	0.424	0.79	1.692	3	0
3	3	0.12	0.424	0.79	1.692	3	0
4	3	0.15	0.424	0.79	1.692	3	0
5	3	0.09	0.424	0.79	1.092	3	0
6	3	0.09	0.424	0.79	1.392	3	0
7	3	0.09	0.424	0.79	1.992	3	0
8	3	0.09	0.424	0.79	2.292	3	0
9	3	0.09	0.424	0.21	1.692	3	0
10	3	0.09	0.424	0.51	1.692	3	0

11	3	0.09	0.424	1.11	1.692	3	0
12	3	0.09	0.424	0.79	1.692	3	10,000
13	3	0.09	0.424	0.79	1.692	3	20,000
14	3	0.09	0.424	0.79	1.692	3	28,000
15	3	0.09	0.424	0.79	1.692	3	50,000
16	3	0.09	0.424	0.79	1.692	3	100,000

APPENDIX D

Table D.1 Annular Orifice simulations – Operating Conditions for Case 2 in Appendix B

Case #	Inlet Pressure (MPa)	Inlet Density (Kg/m^3)
1	11	372
2	11	498
3	10	372
4	9	372
5	9	498
6	7.7	630

Table D.2 Labyrinth seal simulations – Operating Conditions for Case 2, Appendix C

Case #	Inlet Pressure (MPa)	Inlet Density (Kg/m^3)
1	11	498
2	10	372
3	9	372
4	9	498
5	9	630
6	7.7	630

Table D.3 Plain orifice simulations – Operating Conditions for L/D ~ 5

Case #	Inlet Pressure (MPa)	Inlet Density (Kg/m^3)
1	9	372
2	9	498
3	10	372
4	10	498
5	11	372